Developing Spectroscopic Serum Diagnostics Towards Clinical Translation: The Detection and Stratification of Brain Tumours

James M. Cameron

A thesis presented to the Department of Pure and Applied Chemistry, University of Strathclyde, in fulfilment of the requirements for the degree of Doctor of Philosophy

July 2020

This thesis is the result of the authors original research. It has been composed by the author and has not been previously submitted for examination which has led to the award of a degree.

Signed:  Date: 26/06/2020

Acknowledgements

Firstly, I would like to express my sincere gratitude to my PhD supervisor, Dr. Matthew Baker, for his guidance and support over the past three years. I feel privileged to have developed such a pleasant working relationship with you and the rest of the group - I certainly wouldn't have envisaged being in this position today when you were examining me in my undergraduate viva! Thank you for all your enthusiasm and encouragement, and for offering me the opportunity to complete such a rewarding project.

A massive thank you must go to the rest of the Spectral Analytics Research group, for making my time here far more enjoyable than I ever anticipated. Holly Jean Butler, thanks for the daily insults/'friendly' banter and advice when things weren't quite going to plan! Thanks to my big mate Chris for the chats about footy over coffee, and my favourite Frenchman JuJu – merci pour tout le café et les discussions de gym, mon ami! I'd also like to show my appreciation to Mark, Dave and the rest of the ClinSpec Dx team; Ben and Justin for the computational guidance; Ewan for the health economics support, and for the advice of our clinical collaborators, specifically Paul and Michael. Research is easier when you are surrounded by people who know what they are talking about!

Ultimately, I want to thank and dedicate this thesis to my amazing family, who have been my biggest fans throughout this whole process. My lovely girlfriend Melissa, thank you for your love and encouragement, always telling me how great I'm doing and at least pretending to be interested when I am practicing my presentations with you! My sister Amy and her husband – my new bro Jamie G – thanks for always brightening up our week at Sunday dinners with your love, humour and happiness. To the best Mum and Dad a boy could ask for, your love and support has allowed me to achieve things I never thought possible. I honestly cannot thank you both enough, and I will be forever grateful for everything that you do for me. I can't forget my two best mates, Maxi and Poppy, who have genuinely kept me sane over the past few months! A special mention goes to my Granda who sadly passed away recently, I'm sure he would have loved to have been here to see me finish off my PhD thesis. This is for you guys; I hope I can make you all proud.

Abstract

The diagnostic pathway for brain tumour patients is currently ineffective. As there are no methods in place for the early detection of brain cancer, the affected patients' average life expectancy is reduced by 20 years, which is the highest of all cancer types. Thus, the development of rapid, low-cost platforms in primary care to triage patients for medical imaging may reduce diagnostic delay, whilst potentially providing cost-effective infrastructures for health care providers. Attenuated total reflection Fourier transform infrared (ATR-FTIR) spectroscopy has demonstrated the ability to diagnose a wide range of pathologies with high accuracies, but the technique is yet to make it into a clinical setting as a regulated spectroscopic test. Recently, innovative high-throughput accessories have been developed which could accelerate clinical translation. The research described in this thesis focuses on the development of the technique by examining the diagnostic ability for the detection and stratification of brain tumours.

Initially, the novel high-throughput ATR-FTIR technology was validated in one of the largest spectroscopic studies to date, by separating brain cancer and non-cancer patients with balanced accuracies of 90%, which is comparable to traditional fixed diamond crystal methodology. Distinguishing brain tumour types with serum spectroscopy would be useful for neurologists, as some are difficult to discriminate through medical imaging alone. For example, the highly aggressive glioblastoma and primary cerebral lymphoma (PCNSL) can appear similar on magnetic resonance imaging scans. The differentiation between glioblastoma and PCNSL patients achieved a sensitivity and specificity of 90.1% and 86.3%, respectively. Several

other types of brain lesions were then distinguished with balanced accuracies >80%. A reliable blood serum test capable of stratifying brain tumours may avoid the need for surgery in some cases, and could speed up time to definitive treatment.

Rapid determination of a glioma patient's *IDH1* status facilitates vital neurosurgical decisions, such as pursuing with resection or opting for alternative therapeutics. Synchrotron-based infrared light has been utilised to probe brain tumour tissue microarrays and differentiate between *IDH1*-mutated and *IDH1*-wildtype glioma, at a sensitivity and specificity of 82.4% and 83.4%, respectively. Additionally, centrifugal filtration of patient serum was examined, with the aim of detecting the global epigenetic and metabolic changes associated with mutations in the *IDH1* enzyme. The filtration step ultimately improved the classification performance, by delivering a balanced accuracy of 69.1%.

Finally, a health economic evaluation was carried out to examine the associated costs and benefits of the blood serum test in clinical practice. Based on recent prospective clinical data, it was found that test costs up to £100 would likely be considered cost-effective, whilst primary care tests set at £75 would be cost-saving to the health services. When comparing the additional costs required for implementing a brain tumour subtype test, the cost-consequence analysis reported an estimated saving of ~£138,075 per 10,000 patients, equating to a potential saving of ~£568 per individual cancer case. Furthermore, this could prevent up to 8 unnecessary surgeries, per 100 patients. Therefore, a brain cancer diagnostic test that can also stratify tumour type would have a profound impact for patients, as well as the health services.

Publications and Awards

Peer reviewed publications

First author:

Biofluid spectroscopic disease diagnostics: A review on the processes and spectral impact of drying
James M Cameron, Holly J. Butler, David S. Palmer, Matthew J. Baker
J. Biophotonics, (2018) e201700299. https://doi.org/10.1002/jbio.201700299.

Vibrational spectroscopic analysis and quantification of proteins in human blood plasma and serum, in: Vibrational Spectroscopy in Protein Research
James M. Cameron, Clément Bruno, Drishya Rajan Parachalil, Matthew J. Baker, Franck Bonnier, Holly J. Butler, Hugh J. Byrne
Elsevier, (2020), 269-314. https://doi.org/10.1016/B978-0-12-818610-7.00010-4.

Developing infrared spectroscopic detection for stratifying brain tumour patients: glioblastoma multiforme vs. lymphoma
James M. Cameron, Holly J. Butler, Benjamin R. Smith, Mark G. Hegarty, Michael D. Jenkinson, Khaja Syed, Paul M. Brennan, Katherine Ashton, Timothy P. Dawson, David S. Palmer, Matthew J. Baker
Analyst, 144 (2019) 6736–6750. https://doi.org/10.1039/C9AN01731C.

Exploring pre-analytical factors for the optimisation of serum diagnostics: progressing the clinical utility of ATR-FTIR spectroscopy
James M. Cameron, Holly J. Butler, David J. Anderson, Loren Christie, Lily Confield, Stuart Murray, Duncan Finlayson, Katie E. Spalding, Zanib Panni, Christopher Rinaldi, Alexandra Sala, Ashton G. Theakstone, Matthew J. Baker
Vibrational Spectroscopy, 109 (2020) 103092.
https://doi.org/10.1016/j.vibspec.2020.103092.

Stratifying brain tumour histological sub-types: the application of ATR-FTIR serum spectroscopy in secondary care
James M. Cameron, Christopher Rinaldi, Holly J. Butler, Paul M. Brennan, Michael D. Jenkinson, Khaja Syed, Katherine Ashton, Timothy P. Dawson, David S. Palmer, Matthew J. Baker
Cancers, 12 (7), (2020) 1710; https://doi.org/10.3390/cancers12071710

Interrogation of *IDH1* status in gliomas by Fourier transform infrared spectroscopy
James M. Cameron, Justin J.A. Conn, Christopher Rinaldi, Alexandra Sala, Paul M. Brennan, Gianfelice Cinque, David S. Palmer, Matthew J. Baker
In draft for submission to Analyst (2020)

Co-author:

Development of high-throughput ATR-FTIR technology for rapid triage of brain cancer
Holly J. Butler, Paul M. Brennan, James M. Cameron, Duncan Finlayson, Mark G. Hegarty, Michael D. Jenkinson, David S. Palmer, Benjamin R. Smith, Matthew J. Baker
Nat. Commun. 10 (2019) 4501. https://doi.org/10.1038/s41467-019-12527-5.

Biofluid Diagnostics by FTIR Spectroscopy: A Platform Technology for Cancer Detection
Alexandra Sala, David J. Anderson, Paul M. Brennan, Holly J. Butler, James M. Cameron, Michael D. Jenkinson, Christopher Rinaldi, Ashton G. Theakstone, Matthew J. Baker
Cancer Lett. 477 (2020) 122-130. https://doi.org/10.1016/j.canlet.2020.02.020.

Shining a light on clinical spectroscopy: Translation of diagnostic IR, 2D-IR and Raman spectroscopy towards the clinic
Holly J. Butler, James M. Cameron, Cerys A. Jenkins, Gordon Hithell, Samantha Hume, Neil T. Hunt, Matthew J. Baker
Clinical Spec. 1 (2019) 100003. https://doi.org/10.1016/j.clispe.2020.100003

Early economic evaluation to guide development of a spectroscopic liquid biopsy for the detection of brain cancer
Ewan Gray, James M. Cameron, Holly J. Butler, Michael D. Jenkinson, Mark G. Hegarty, David S. Palmer, Paul M. Brennan, Matthew J. Baker
Submitted to International Journal of Technology Assessment in Health Care (2020).

Patent Applications
Infra-Red Spectroscopy System March 2017
Matthew J. Baker, Holly J Butler, James M. Cameron, Duncan Finlayson, Angela Flack, Mark Hegarty, David Palmer, Benjamin Smith and Katie Spalding.
PE958329GB

Discerning Brain Cancer Type 2019
James M. Cameron, Matthew J. Baker, Holly J. Butler, Mark Hegarty, David S. Palmer.
PE959914GB

Awards
The Analyst Oral Presentation Prize
7th Analytical Biosciences Early Career Researchers Meeting 2020

ScotCHEM Postgraduate and Early Career Researcher Exchanges Travel Award 2018

Abbreviations

ATR	Attenuated total reflection
CEA	Cost effectiveness analysis
CNS	Central nervous system
CT	Computed tomography
DNA	Deoxyribonucleic acid
DTGS	Deuterated triglycine sulphate
EMSC	Extended multiplicative signal correction
FPA	Focal plane array
FT	Fourier transform
FTIR	Fourier transform infrared spectroscopy
GBM	Glioblastoma multiforme
GP	General Practitioner
H & E	Haematoxylin and eosin
HEA	Health economic assessment
HMWF	High molecular weight fraction
HTA	Health technology assessment
ICER	Incremental cost-effectiveness ratio
IDH	Isocitrate dehydrogenase
IR	Infrared
IRE	Internal reflection element
LMWF	Low molecular weight fraction
LDA	Linear discriminant analysis
MCT	Mercury cadmium telluride

MRI	Magnetic resonance imaging
NHS	National Health Service
NICE	National institute of Clinical Excellence
NPV	Negative predictive value
PC	Principal component
PCA	Principal component analysis
PCNSL	Primary central nervous system lymphoma
PET	Positron emission tomography
PLA	Polylactic acid
PLS	Partial least squares
PLS-DA	Partial least squares-discriminant analysis
PPV	Positive predictive value
QALY	Quality-adjusted life-years
RF	Random forest
SOP	Standard operating procedure
SIRE	Silicon internal reflection element
SMOTE	Synthetic minority over-sampling technique
SNR	Signal-to-noise ratio
SR	Synchrotron radiation
SVM	Support vector machine
TP	True positive
UK	United Kingdom
USA	United States of America
WHO	World Health Organization

List of Figures

List of Tables

List of Equations

Table of Contents

Chapter 1

1. Introduction

1.1 Cancer

The term ‘cancer’ refers to a disease that is caused by uncontrolled cell division in the human body. It arises from genetic mutations in a person’s DNA, which disrupts normal cell behaviour. These mutations can happen by chance, be caused by external factors - such as tobacco smoke and chemicals - or can be inherited [1]. The body normally maintains a healthy balance of cells, where cell division and cell death occur simultaneously. The regular life cycle of a cell can be described by a four stage process: the cell prepares for DNA synthesis (G1), the nucleic material is synthesised (S), the duplicated nucleic content is condensed and arranged for cell division (G2), then finally mitosis occurs which divides the cell into two new daughter cells (M). In cancer patients the genetic mutation overstimulates the cell cycle, meaning cells begin to divide uncontrollably and form a cluster of cells known as a tumour [2]. These tumours can be either cancerous (malignant) or non-cancerous (benign). Benign tumours are generally slow-growing, thus do not cause as many issues as they do not invade other body tissues. Following surgical removal, they rarely form again and are not usually life-threatening [3]. Conversely, malignant tumours grow much more quickly (Figure 1.1). They often damage nearby tissues and spread to other parts of the body through the bloodstream or lymphatic system forming secondary tumours by a process called ‘metastasis’.

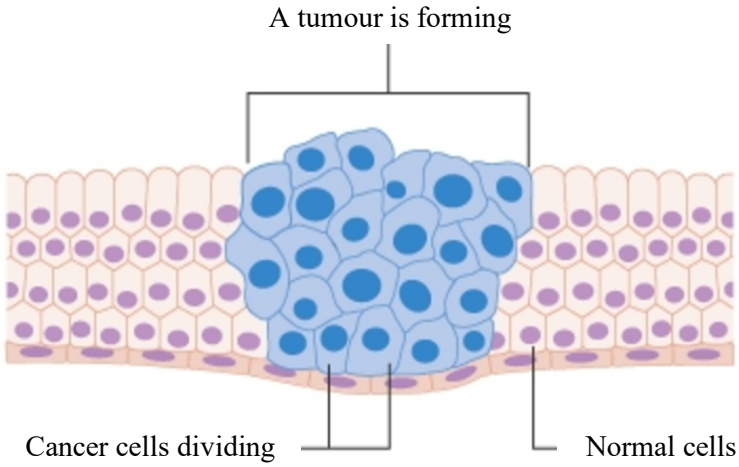

Figure 1.1 – Example of a tumour growth. Adapted from ref [4].

There are five main categories of cancer which can be grouped depending on where they originate: carcinoma, sarcoma, leukaemia, lymphatic system cancers and central nervous system (CNS) cancers [5]. The most common category is carcinoma, which originate in the epithelial tissues; these are found on the skin and line the body cavities and all the organs inside the body. Sarcomas are a group of rare cancers that differ to carcinoma as they arise from a different kind of tissue, originating in connective tissues such as bones, muscle, cartilage and tendons. Leukaemia occurs in bone marrow and result in an abnormal build-up of white blood cells in the blood. Lymphoma and myeloma are lymphatic system cancers; lymphoma starts from cells in the lymph glands, lymphatic vessels and the spleen, whereas myeloma originates in plasma cells. Finally, CNS cancers are those that start in the cells of the brain or the spinal cord.

1.1.1 Tumour Development

The development of a tumour is a multistage process; initiation, promotion and progression (Figure 1.2). The point at which the DNA becomes damaged or mutated is the initiation stage. During promotion, these irreversible genetic mutations begin to form a benign tumour through clonal expansion of the altered cells. As the cells proliferate, the tumour expands and transforms into a malignant lesion. Thus, the levels of oxygen and nutrients available to the healthy cells become limited causing cell death, allowing the tumour to break through nearby tissues.

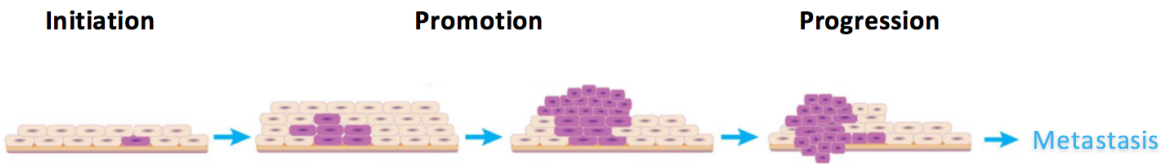

Figure 1.2 – Carcinogenesis. Adapted from ref [6].

Naturally, normal cells can exhibit self-destruct behaviour when their genes are damaged in a process known as programmed cell death (PCD). One of the major PCD mechanisms is described as apoptosis, which eliminates unhealthy cells from the body [7]. Apoptosis is a highly complex process, but current research suggests it can occur through two distinct pathways: extrinsic or intrinsic. The extrinsic pathway is initiated by a death-inducing signal complex, which forms in response to the interaction of extracellular ligands, such as fatty acid synthase (FAS), and the cell surface receptors. The intrinsic pathway involves stimuli producing intracellular signals that cause changes in the inner mitochondrial membrane, releasing proteins that activate the apoptotic pathway, such as cytochrome *C* [8]. Each require specific

triggering signals to activate their own initiator caspase (protease enzyme), which will go on to activate caspase-3 and the execution pathway. Following the cleavage of caspase-3, the cytoskeletal and nuclear proteins start to degrade, the DNA cells occurs [9].

However, cancer cells have the ability to override these physiologic signals that instruct them to undergo apoptosis, allowing them to continue to grow faster and become more aggressive [4]. There are a variety of mechanisms that allow them to disable the apoptotic pathways. Cancer cells can suppress the accumulation of pro-apoptotic proteins, such as *Bax*, or stimulate the overexpression of anti-apoptotic proteins, namely *BCL-2* [10]. The expression of both *Bax* and *BCL-2* are controlled by the tumour suppressor gene, *p53*, and a mutation or loss in the *p53* gene can give rise to a stable mutant protein. The accumulation of this mutant *p53* protein is regarded as a hallmark of cancer cells, as it is found in around 50% of malignant tumours [11,12].

1.1.2 Metastasis

In an ideal scenario cancer would be detected at the earliest stage of formation, and the patient would have a much better chance of survival. Although in reality, many cancers are not diagnosed until a later stage by which point the primary tumour may have spread to a secondary site to form another tumour – this development is called metastasis [13]. Metastatic cancer is far more difficult to treat as it is often hard to locate the original primary tumour, thus cannot determine the optimal treatment. Metastasis occurs when the primary tumour breaks into nearby tissues, releasing

single cancer cells that travel around the body through the bloodstream or lymphatic system [14]. These cells stop in small blood vessels and move into surrounding tissue at the 'secondary' location, dividing and growing into a new tumour. New blood vessels begin to grow around the newly formed tumour, supplying the nutrients required for expansion. Cancer can spread to any part of the body, but some sites are more common than others. For example, primary bowel cancer often spreads to the liver (Figure 1.3), whereas brain metastases commonly arise from primary lung or breast cancer [15]. It is thought that small attractant molecules – called chemokines – are involved in directing tumour cells to their preferred metastatic sites [16].

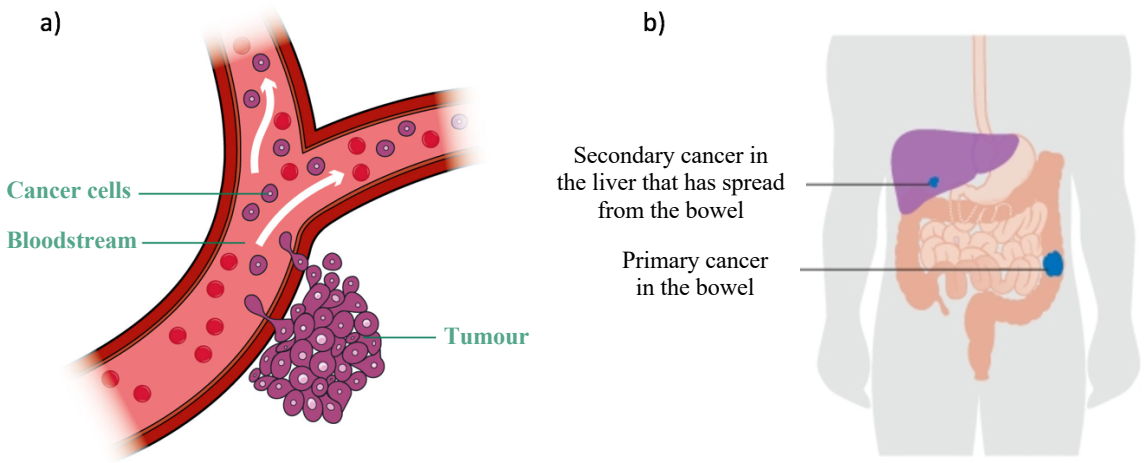

Figure 1.3 – Metastasis: a) cancer cells moving through the bloodstream and b) metastatic liver cancer. Adapted from refs [17,18].

1.1.3 Cancer Staging

There are many staging systems relating to different cancer types. Most of these are based on location and size of tumour, cell type, metastasis and tumour grade [19]. The TNM staging system is the most widely used, as it can account for the majority of common cancers, with the exception of CNS cancers and leukaemia [20]. Within this system, the T describes the size and extent of the tumour, N refers to the nearby lymph nodes that have cancer and M describes the presence of metastasis. Each of these categories are given a value, e.g. Tx Ny Mz, and are then combined to provide an overall stage of 0-IV (Table 1.1) [19].

Table 1.1 – Generic cancer staging.

Stage	Meaning
0	Known as carcinoma in situ, not yet cancer. Abnormal cells present but have not spread to nearby tissue
I, II and III	Cancer is present. The larger the tumour and the more it has spread into nearby tissues, the higher number assigned
IV	The cancer has spread to other parts of the body (metastasis)

1.1.4 Tumour Grading

Tumours are assigned a ‘grade’ as an indication of how quickly it is likely to grow and spread. By removing part of the lesion through a biopsy, doctors can examine the tissue under a microscope. The tumour grades are classified on the appearance of the cancerous cells and how similar they are to the normal, healthy cells. In some cancers, the tumour grade becomes extremely important when deciding which

treatment would be best suited, therefore some of the more complex cancers have their own specific grading system, i.e. prostate, breast and brain cancer [21]. In general, tumours are graded as 1, 2, 3 or 4 depending on the severity. Low grade tumours (grade 1) often grow and spread slowly, and appear similar to normal cells and tissue under microscopy examination – described as well-differentiated. High grade tumours (3 and 4) have abnormal cells and tissue structures and are known as poorly differentiated or undifferentiated - these grow aggressively and spread much faster than low grade tumours [22].

1.1.5 Statistics

There are over 100 different types of cancer, some of which are more common than others [23]. In 2014 in the UK, there were approximately 357,000 new cases of cancer diagnosed, equating to roughly 980 a day. More than half of all new cases were represented by only 4 cancer types; breast (15%), prostate (13%), lung (13%) and bowel (11%). Some cancers are more difficult to diagnose, mainly due to lack of early symptoms. Therefore, almost half of all cases were diagnosed at a late stage, which makes it less likely for the patients to survive. There were around 163,000 deaths caused by cancer in 2014, and it now causes more than a quarter of all deaths in the UK [24]. The cancer with the highest mortality rate in adults in the UK is lung cancer, whereas in children and teenagers, deaths from brain and other central nervous system cancers are more prevalent [25]. The number of people living with cancer in the UK is said to be increasing by 3% every year, and it has been projected by Macmillan that by the year 2030 - based on the increasing and aging population - there will be approximately 4 million people living with cancer in the UK [26].

1.1.6 Risk Factors

One of the main risk factors for cancer is increasing age. It is thought that over time there is an increase in the damage to DNA, i.e. replication errors, and with more gene mutations comes a higher likelihood of tumour development [27]. Incidence increases with age for the majority of cancer types, and likewise mortality rates. Cancer Research UK [28] reported that between the years of 2012-2014, only around 1% of cases in the UK were found from children and young adults aged 0-24. Adults aged 25-29 accounted for a tenth of all new cancer cases. As expected, incidence rates are far higher for adults over the age of 50, with 50-74 and 75+ year olds contributing 53% and 36% of all new cases, respectively (Figure 1.4).

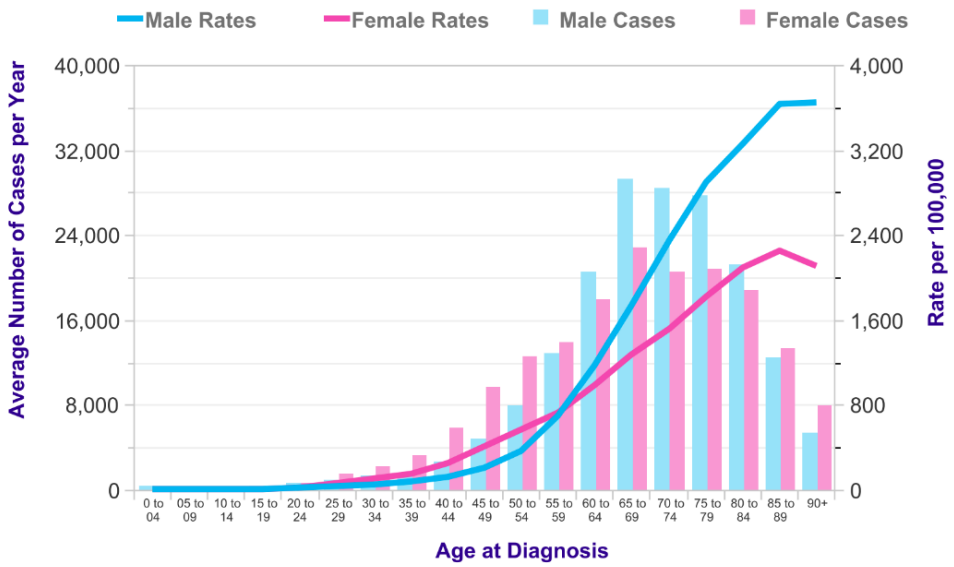

Figure 1.4 – Cancer incidence by age in the UK (2012-2014).
Duplicated from ref [28].

Family history is another major factor related to the progression of cancer, with gene mutations being passed through familial generations. There has been a vast amount of research into hereditary deposition of cancer. Lynch syndrome is a hereditary

condition that is caused by a mutation in one of the mismatch repair (MMR) genes; such as *MLH1, MSH2, MSH6, PMS1* and *PMS2.* Those who inherit this condition are at high risk of developing various different cancers, including bowel, brain and pancreatic cancer. It is thought that if a person has Lynch syndrome, their close relatives will have a 50% chance of having the same mutation [29]. Likewise, Li-Fraumeni syndrome (LFS) is caused by an alteration in the tumour suppresser gene *p53*, and has been linked to bone, breast and brain cancer, as well as soft tissue sarcoma and acute leukaemia [30].

There are various external influences that are also thought to contribute to cancer causation: tobacco smoke; chemical and radiation exposure; viruses and bacteria; alcohol; obesity and lack of physical exercise [31]. These are the elements that are described as 'general' cancer causes but some types of cancer have specific risk factors that are more relatable. For example, a lung cancer diagnosis would be more likely for a person who smokes cigarettes; liver cancer would be a higher threat for those who consume a large amount of alcohol on a daily basis; whereas melanoma skin cancer would be more probable for people who expose themselves to large amount of UV radiation – e.g. sun exposure or tanning beds.

1.2 Brain Cancer

1.2.1 Statistics

Brain cancer kills more children and adults under the age of 40 than any other cancer [32]. In 2014, there were around 11,000 new cases of brain tumours in the UK, which were the cause of approximately 5,200 deaths [33]. As brain cancer has a relatively low incidence rate compared to other cancers, such as breast and lung cancer, it leads to lower overall mortality rates which masks its true deadliness. The average number of years of life lost (AYLL) is a measure of burden of cancer to the patient, and out of all cancer types, brain tumour patients have the highest at 20.1 years [34].

1.2.2 The Central Nervous System

The brain is one of the most complex and remarkable organs in the human body, being responsible for the vast majority of the body's functions [35]. The large jelly-like organ contains millions of nerve cells and is protected by the skull (cranium). The central nervous system (CNS) is comprised of the brain and the spinal cord. The nerve network within the spinal cord allows efficient communication between the brain and rest of the body. Small layers of tissue, called meninges, cover and protect the brain and spinal cord, and cerebrospinal fluid (CSF) assists by cushioning the brain [36]. The brain is split into four main parts; cerebrum, cerebellum, brain stem and pituitary gland. The cerebellum, located at the back of the brain, controls coordination and balance. The brain stem is responsible for heart rate and breathing, and the pituitary gland manages hormone production. The cerebrum is the largest

part of the brain, consisting of two hemispheres – the right half controls the left-hand side of the body and vice versa. Each hemisphere can be split further into four sub-sections; frontal lobe, temporal lobe, occipital lobe and parietal lobe (Figure 1.5) [37].

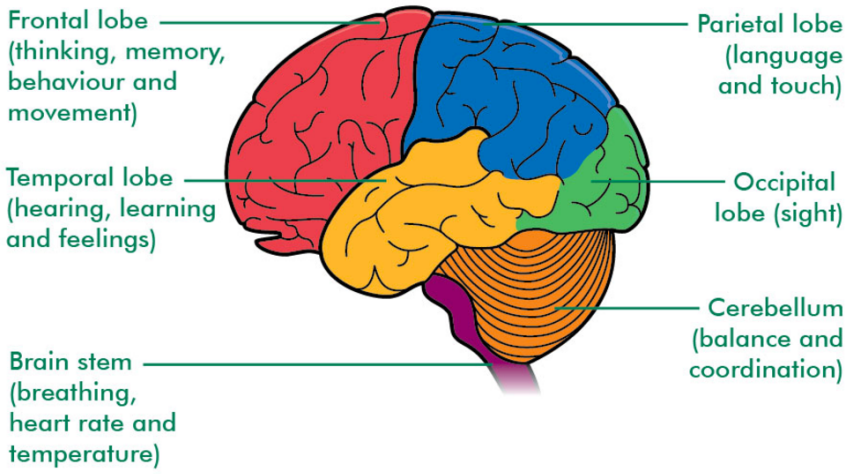

Figure 1.5 – Lobes and functions in the brain. Duplicated from ref [37]

1.2.3 Primary Brain Tumours

Abnormal growths that originate in the brain are known as primary brain tumours. There are over 130 different types of primary brain tumours, as classified by the World Health Organisation (WHO) [38]. As a general rule, the neoplasms are classified according to the type of cell they started from and its location in the brain [39].

1.2.3.1 Glioma

The majority of primary brain tumours arise in the glial tissue that surround nerve cells in the brain. These lesions are usually malignant and are known as gliomas. Gliomas can be further separated depending on which type of cell the tumour originated (Figure 1.6). For example; an astrocytoma arises from the brain's supportive cells (astrocytes), an ependymoma develops from the ependymal cells that line the cavities in the brain, and an oligodendroglioma arises from the cells that produce fatty covering of nerves (oligodendrocytes).

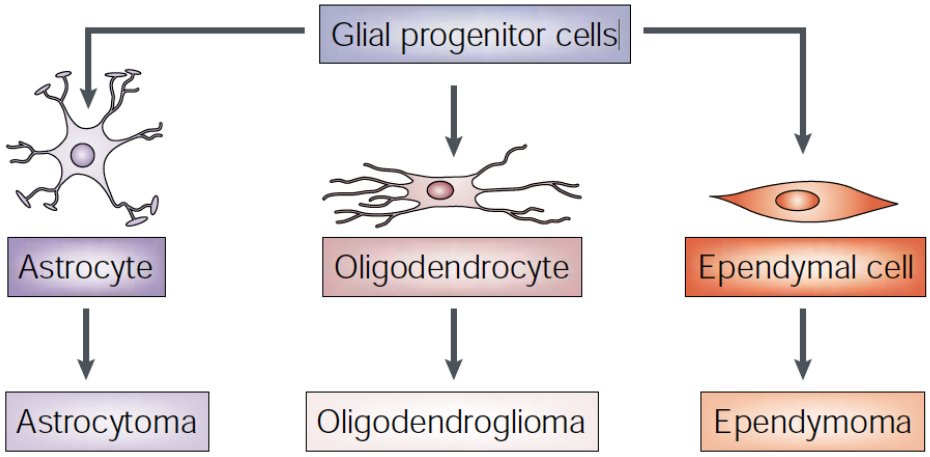

Figure 1.6 – The different types of glial cells and their distinct glioma tumour types. Replicated from ref [40].

The most common, and most aggressive, primary neoplasm found in adults is an astrocytic tumour called glioblastoma (GBM). Around 90% of diagnosed GBMs are primary tumours that have formed through carcinogenesis, the remainder are secondary tumours originating from lower-grade neoplasms [41]. Examples of common gliomas are listed in Table 1.2, with their corresponding WHO grade – I and II grow slowly and are known as 'low-grade' gliomas, whereas grade III and IV are described as 'high-grade' and are more fast-growing [42].

Table 1.2 – Types of gliomas with their corresponding WHO grades [42].

WHO Grade	**Glioma Types**		
I	Pilocytic Astrocytoma	Ganglioglioma	Subependymoma
II	Diffuse Astrocytoma	Oligodendroglioma	Ependymoma
III	Anaplastic Astrocytoma	Anaplastic Oligodendroglioma	Anaplastic Ependymoma
IV	Glioblastoma		

The complexity of CNS tumours is far greater than those found at other sites of the body, therefore WHO have derived a classification system specific to brain tumours [38]. Neoplasms were originally classified by their histological appearance (grade I-IV) and their cell type. However, in 2016 a new classification system was established that includes sub-classes with molecular parameters, such as mutations in the isocitrate dehydrogenase (*IDH*) gene [43]. This aimed to assist treatment planning, as some molecular biomarkers have been shown to improve response to chemotherapy, leading to a greater patient prognosis [44–46].

1.2.3.2 Meningioma

Meningiomas are primary CNS tumours deriving from arachnoidea cells – located in the meninges. They represent the most common benign intracranial neoplasm, with over 90% of meningiomas deemed to be non-cancerous [47]. Atypical (abnormal cells) and malignant meningiomas are much less common; 5-7% and 1-3%, respectively. However, they are extremely aggressive, and after resection the probability of recurrence is high (~60%) [48].

1.2.3.3 Other Central Nervous System Tumours

There are various other types of CNS tumours that are much less common. Medulloblastoma (MB) is a malignant tumour that starts in the cerebellum. MB neoplasms are rarely found in adults, but are the most frequently diagnosed malignancy in children [49]. The exact cause of this unusual trend is currently unknown, but recent studies have suggested that childhood and adult MB are genetically different diseases, with more mutations arising in children than adults [50]. Tumours originating in the pineal gland, such as germinoas and teratomas, are also quite rare, but are more often found in those aged 10-20. Haemangioblastomas are slow-growing, develop in the lining of blood vessels and are usually benign. Acoustic neuroma and pituitary adenoma are also both usually non-cancerous [51].

1.2.4 Metastatic Brain Tumours

Brain metastases are tumours that originate in a primary site outside the CNS, and then spread into the brain via the bloodstream. Metastatic neoplasms in the brain are much more common than primary brain tumours and it has been reported than there are 10 times the amount of brain metastases than primaries [52]. A variety of different malignancies can metastasise to the brain, but it generally depends on the location of the primary site. The majority come from primary tumours in the lung (40-50%) or breast (20-30%), although melanoma, gastrointestinal and prostate cancer have also been known to metastasise to the brain [53]. Metastasis only occurs once the cancer has progressed significantly, hence by the time it has spread to the brain the prognosis for the patient is often dismal [54].

1.3 Current Diagnosis Procedure

1.3.1 Brain Tumour Symptoms

As symptoms are generally non-specific to brain tumours, it's often difficult to diagnose patients early. The list of apparent symptoms is rather extensive, but one of the most common symptoms is intracranial pressure which is an increased pressure on the skull due to the growing neoplasm. As the skull cannot expand to allow more space for the tumour to grow, it presses against the cranium, which can lead to persistent headaches, nausea and convulsions. Other symptoms are dependent on the location of the tumour within the CNS, summarised in Table 1.3 [55].

Table 1.3 – Common brain tumour symptoms [55,56].

Location	**Symptoms**
Brain stem	Uncoordinated walking, double vision, facial weakness
Cerebellum	Uncoordinated walking and speech, nystagmus, stiff neck, vomiting,
Frontal lobe	Loss of smell, paralysis on one side of body, personality changes, vision loss
Occipital lobe	Gradual loss of vision in one or both eyes
Temporal lobe	Impaired speech and loss of memory
Parietal lobe	Impaired mental ability, lack of recognition, inability to write

Unfortunately, there will be many people worldwide living with a brain tumour that are not yet aware of their condition. In many cases tumours are asymptomatic, meaning patients are diagnosed in emergency presentations. It has recently been reported that over 900,000 people are thought to be living with an asymptomatic brain tumour in the USA [57]. For those who do become symptomatic, these effects are usually only displayed when the tumour has progressed to a late stage, making it

difficult for early diagnosis. It has been documented that 70% of brain tumour patients have shown signs of persistent headaches [58]. Yet it is uncommon for isolated headaches to be the presenting symptom of a brain tumour, meaning general practitioners (GP) only refer 2-3% for a consultation with a neurologist [59]. This leads to patients returning to their GPs multiple times before a referral is made, by which time the tumour may have progressed causing a worsened prognosis. If a reliable, quick, non-invasive diagnostic test could be implemented into the clinic, it could enable earlier detection and ultimately save lives.

1.3.2 Magnetic Resonance Imaging

When a GP suspects a brain tumour, they will refer the patient for a number of medical imaging examinations for confirmation. Magnetic resonance imaging (MRI) is one of the more commonly used techniques. MRI uses a combination of magnetic fields and radio waves to produce a three-dimensional image of the brain. It is a valuable technique as MRI is highly sensitive to any abnormalities, bone is transparent, and no ionizing radiation is used. Examples of the resulting MRI images from brain tumour patients are shown in Figure 1.7. The main downside of MRI is that the scans are costly - a single MRI scan costs the UK's National Health Service (NHS) on average £165 [60]. They are also time consuming with full body scans lasting over an hour, and false positives have proven to be an issue [61]. One study reported that 11% of brain tumour patients received a false positive result of either primary or metastatic cancer, when tested solely by MRI [62]. Furthermore, it's often difficult to distinguish between various types of brain lesions by MRI alone. For example, GBM, primary central nervous system lymphoma (PCNSL) and brain

metastases have been confused in various cases [62,63]. Functional MRI (fMRI) scanners have recently been reviewed, which have the additional benefit of detecting areas of the brain with increased blood flow. This technique tracks oxygen in the brain, and many studies have suggested implementing fMRI into standard practice could be highly beneficial in preoperative planning, with the potential to reduce post-operative morbidity [64,65].

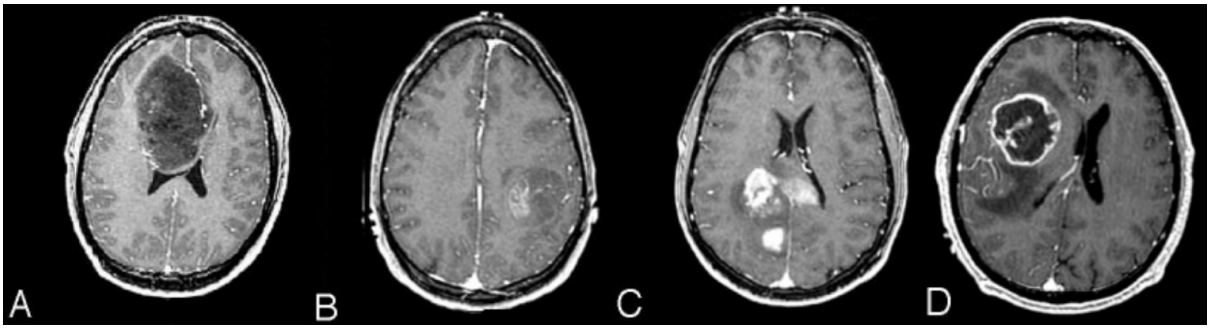

Figure 1.7 – MRI scans of various brain tumours; A: Grade II Astrocytoma, B: Grade III Astrocytoma, C: Grade IV Astrocytoma and D: Glioblastoma Multiforme. Adapted from ref [66].

1.3.3 Computed Tomography

Another common imaging technique – often used in unison with MRI – is computed tomography (CT). This technique uses computer processed x-rays to create tomograms of the human body, which are essentially images of bones, tissues and blood vessels. It can be advantageous as analysis is faster and cheaper than MRI – on average around £85 per scan - but the patients are exposed to higher amounts of radiation, which has caused some concern in the diagnostics field [67–69]. It is thought to be more of a health issue for those of a younger age, as they have an increased risk of low-dose radiation [70].

1.3.4 Other Imaging Techniques

A more specialised imaging technique that provides details of the complete chemistry and metabolic activity of the human body is positron emission tomography (PET). PET uses short-lived radioactive substances, such as fluorodeoxyglucose (FDG), to produce 3D images of the area of concern [71]. This is often used after an initial MRI or CT scan in preparation for biopsy. PET scans are useful for focusing on a specific region of interest, aiding full resection of the tumour, without the unnecessary removal of healthy tissue. Hybrid instruments allow the use of two techniques in a single instrument – PET is usually coupled with CT however integrated PET/MRI has recently become an area of active research [72]. Gamma (γ) emitting radioactive substances are used in single-photon emission computed tomography (SPECT). These radioactive tracers are injected into the patient's bloodstream, which provides a 3-dimensional description of cerebral blood flow when linked to a CT scanner. SPECT has been shown to be helpful in distinguishing between grades of astrocytomas [73]. MR spectroscopy measures the levels of metabolites in the body, which can be helpful in diagnosing tumour type and aggressiveness. The blood flow into the tissues can be examined by perfusion MRI, which can be of use when assessing tumour grade, and can differentiate between dead tumour tissue and a recurrent neoplasm [74,75].

1.3.5 Biopsy and Histopathology

Histopathology is used to determine whether the tumour present is benign or malignant. Normally a small section of the neoplasm is removed during a biopsy, and the resected tissue is examined. Tumour histology provides information on the type and grade of the tumour, and the molecular features present [76]. The preferred method for removal of the tissue is a stereotactic brain biopsy as it is the least invasive. In this procedure, CT and MRI scans linked with 3-D imaging technology targets the tumour location, allowing accurate incision near the area of interest. A tiny hole is drilled into the skull and sample of tumour tissue is removed with a thin biopsy needle. Removal of non-diagnostic tissue is common, thus repeats are often necessary [77]. Stereotactic biopsies are not always possible depending on the location or severity of the tumour, and in reality, more invasive open biopsies are the most common. During an open biopsy a piece of bone is removed from the skull while the patient is under general anaesthetic, exposing the brain and allowing tumour removal. This is of higher risk compared to the stereotactic method and patient recovery time is generally much longer [78]. Once the sample of tumour tissue has been removed, it is examined under a microscope. The histopathological examination will determine what type of cells are present and enables tumour grade assignment [79]. The tumour tissue is stained with haematoxylin and eosin (H&E), which allows the analyst to clearly view the nuclei in a deep blue/purple colour (Figure 1.8). The nuclei exhibit both cell and cancer specific patterns, therefore are diagnostically valuable [80].

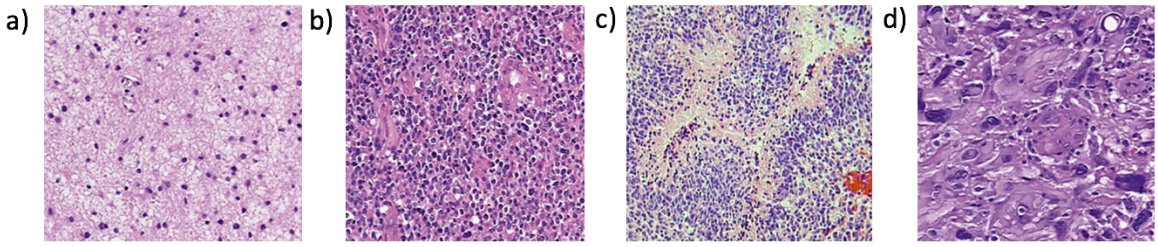

Figure 1.8 – Examples of microscopic features of diffuse gliomas: a) low-grade astrocytoma, b) anaplastic oligodendroglioma, c) small cell variant of glioblastoma with pseudo-palisading necrosis and d) large cell glioblastoma. All images stained with H&E. Adapted from ref [81].

Over the last few decades, the standard way of classifying brain tumours has been through their microscopic similarities and their levels of differentiation, based on the recommendations of WHO [42]. Lesions with low proliferative potential are termed grade I, which are commonly cured with surgery. Grade II tumours are well-differentiated, exhibit rather low levels of proliferation, and start to become infiltrative. Grade III are often termed anaplastic, and they show clear signs of nuclear atypia (abnormal looking cell nuclei). In grade IV, such as GBM, there are an abundance of malignant cells which reproduce rapidly, and the formation of new blood vessels are often visible [82]. It is still often challenging to determine the exact cancer grade and stage solely through histopathology, mainly due to the lack of consensus between pathologists, and with intra- and inter-observer errors fairly common [83,84].

1.3.6 Biological Markers

A biological marker, or biomarker, has been defined by the National Cancer Institute as, “a biological molecule found in blood, other body fluids, or tissues that is a sign of a normal or abnormal process, or of a condition or disease” [85]. Biomarkers can

be used in various ways in oncology: estimating risk of cancer, screening, tumour differentiation, prognosis determination and predicting response to therapy [86]. They can be of great value in diagnosis when combined with medical imaging techniques, but when used as a stand-alone diagnostic they are not always reliable, due to the high frequency of false positives [87]. Currently, biomarker analysis is used in the clinic to identify specific types of cancer, including prostate and ovarian cancer. The list of potential biomarkers for brain cancer is broad (Table 1.4): proteins, nucleic acids, antibodies and gene mutations all exist as valuable biological indicators. Specifically in blood serum, it is thought that various oncoproteins, metabolites and a host of inflammatory markers may be elevated in brain cancer patients – such as pro- and anti-inflammatory cytokines.

Table 1.4 – Genetic mutations and their clinical associations [74,90–94]**.**

Genetic mutation	**Current Associations**
IDH1/2 mutations	Oligodendroglial tumours, Positive prognostic factor
1p/19q co-deletion	Oligodendroglial tumours
MGMT promotor methylation	Alkylating agents e.g. TMZ
ATRX deletion	Astrocytic tumours, Not seen with 1p/19q deletion
PTEN deletion	Small cell phenotype of GBM with *EGFR* amplification and 10q loss
EGFR amplification	Reported in approx. 40% of GBM
H3-K27M mutation	Common paediatric glioma, poor prognosis
BRAF	Favourable prognosis in paediatric and young adult low grade gliomas

Various studies have emphasised potential target biomarkers as an efficient diagnostic and prognostic tool; human cartilage glycoprotein-39 (*YKL-40*), matrix metallopeptidase-9 (*MMP-9*), glial fibrillary acid protein (*GFAP*) and receptor tyrosine phosphatase β (*RPTPβ*) have all been documented as potential biomarkers for glioma, but are not currently used in the clinic [88]. Research has shown that the loss of function of *TP53* is frequent in secondary GBM, whereas primary GBMs can be characterized by *PTEN* and *EGFR* alterations [89].

Recently there has been small number of biomarker tests introduced to neuropathology laboratories [95]. Currently one of the main analyses for brain tumours looks at the promoter hypermethylation of the O^6–methylguanine-DNA-methyltransferase (*MGMT)* gene – the *MGMT* methylation test [96]. Promoter methylation of the *MGMT* gene compromises DNA repair and allows alkylating agents, such as temozolomide (TMZ), to effectively harm the cancerous cells [97]. Hence, it is believed that those who possess methylated *MGMT* will benefit more from chemotherapeutic treatment. The 1p/19q test is aimed at differentiating between different types of oligodendrogliomas; the co-deletion of both the 1p and 19q chromosomes in tumour cells has been associated with a better outcome [98]. The IDH1/2 test may be conducted for glioma patients, as those with mutations in the isocitrate dehydrogenase (*IDH1* and *IDH2*) enzyme are often predicted to have a greater prognosis than those with *IDH*-wildtype (non-mutated) lesions [99]. The BRAF test can be of use for patients diagnosed with an astrocytoma, to determine whether it is a grade I tumour (pilocytic astrocytoma) or a higher grade astrocytoma [95]. The WHO recently published a revised edition of their 2007 classification

guidelines. Now tumours are classified based on both their histological appearance, and their molecular pathology. This allows differentiation between tumours of the same grade and origin that have molecular alterations. For example, genetic mutations in the R132H-*IDH1* enzyme [43]. The presence of R132H-*IDH1* can be established through immunohistochemistry (IHC) by applying the *mIDH1R132H* antibody to resected glioma tissue, as described in Figure 1.9 [100].

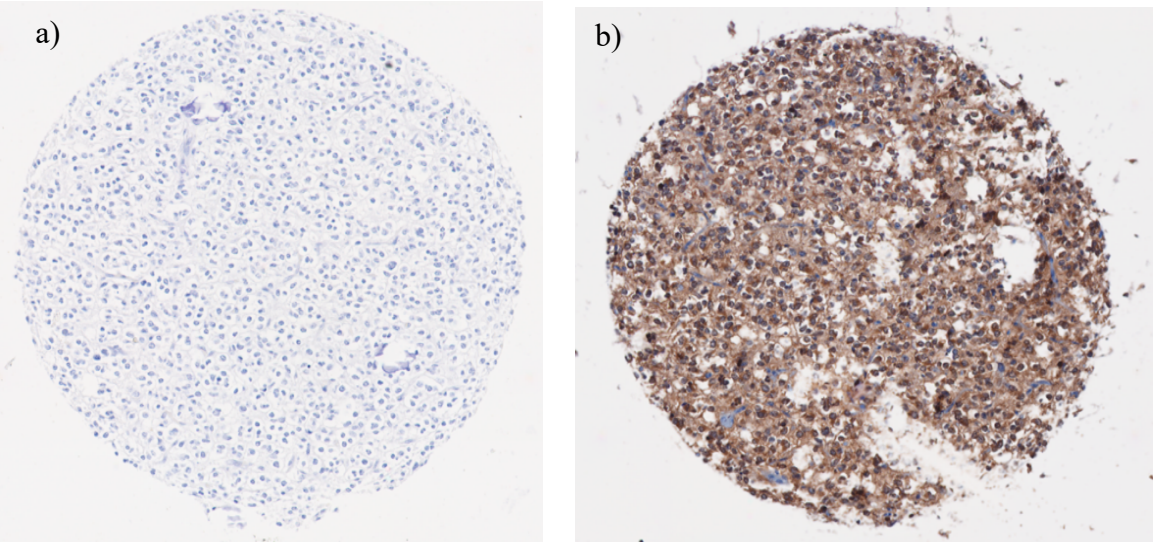

Figure 1.9 – Microscope images of tissue microarray sections of an oligodendroglioma tumour with: a) standard H&E staining and b) stained with *mIDH1R132H* antibody, where *IDH1*-mutated cells exhibit a dark brown colour.

However, the R132H-*IDH1* expression is only present in a fraction of tumour cells in some diffuse gliomas, thus several sections of brain tissue are generally removed during biopsy to increase the chances of a reliable result. The addition of molecular parameters to the classifications should aid clinicians in treatment planning, and therefore provide patients with a greater prognosis. The current histopathology decision pathway (Figure 1.10) signifies the importance reliable detection of molecular signatures for the accurate diagnosis of gliomas.

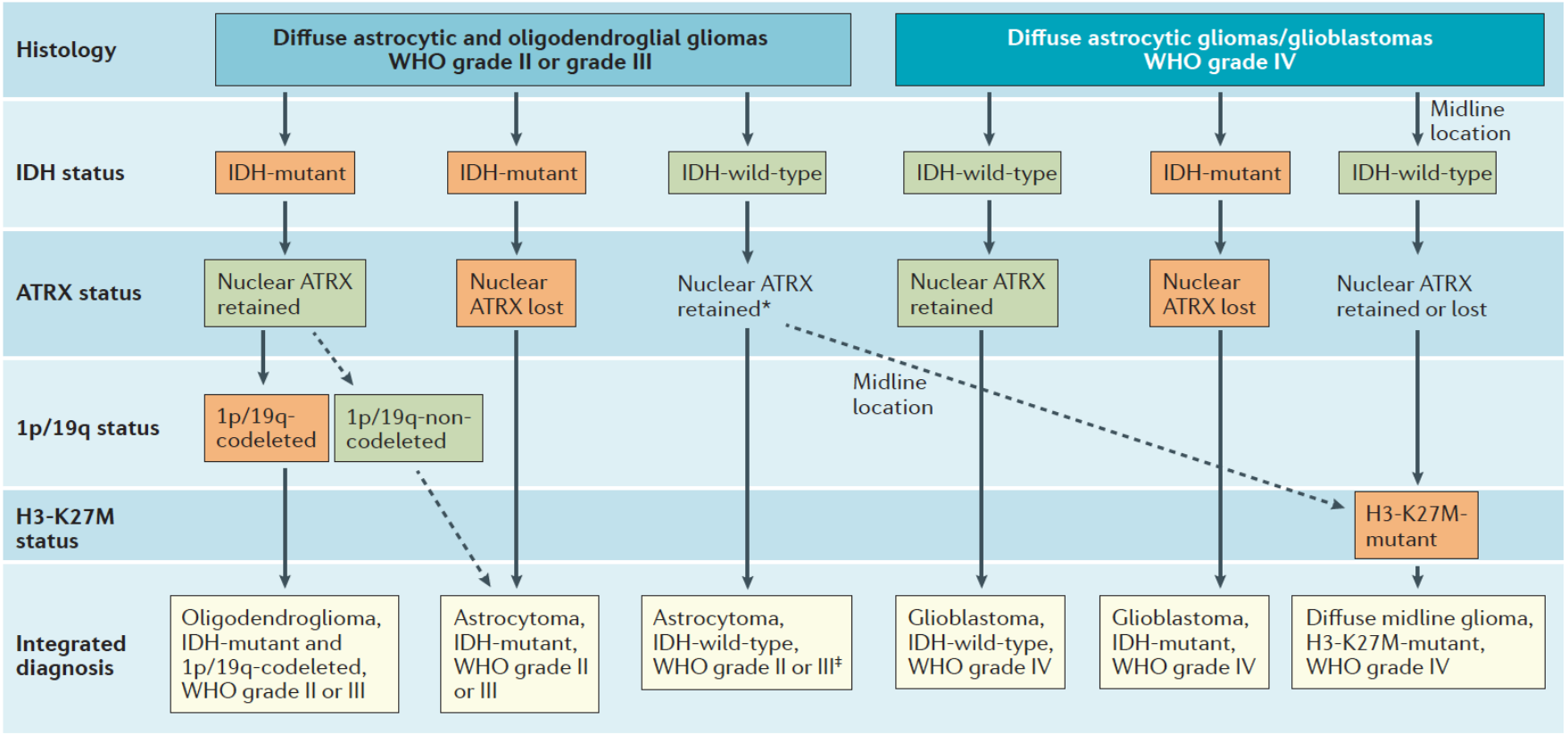

Figure 1.10 - Diagnostic approach for the histological and molecular classification of diffuse gliomas according to the *2016 WHO Classification of Tumours of the Central Nervous System.* Replicated from ref [101].

1.3.7 Current Pathway Issues

The diagnostic pathway for the majority of brain tumour patients begins with a visit to their GP, where they can be referred to a oncology specialist for further examination within a two week period, if they meet current NICE guidelines, of sub-acute progressive loss of neurological function [102]. That said, a reported 38% of patients living with a brain tumour visited their GP with headaches on 5 or more occasions before being finally diagnosed. With time being such a vital factor in tumour development, this statistic alone implies the current pathway is vastly ineffective. The severe lack of brain cancer-specific symptoms undoubtedly makes early detection more challenging. During the early stages of tumour development, symptoms can be minor at best, with many patients being asymptomatic. They become more evident with high-grade neoplasms, where seizures and vision impairment become more common, but by this point the tumour is already at an advanced stage. GP consultations are common for patients that are experiencing symptoms, but unfortunately in many cases diagnoses are made following emergency presentations. The Brain Tumour Charity has reported that 62% of patients are diagnosed in an emergency. Other routes to diagnosis include opticians, outpatient appointments and NHS walk-in centres [103]. One study reported the one year survival rate was significantly lower for those who presented as an emergency [104]. A typical timeframe of the current diagnostic pathway for brain tumours is illustrated in Figure 1.11, which highlights the significant wait that a symptomatic patient may have before receiving brain imaging. Even from this stage a full diagnosis may take a further 5 weeks [60], which is not ideal as an earlier diagnosis can have a huge impact on the effectiveness on treatment [103].

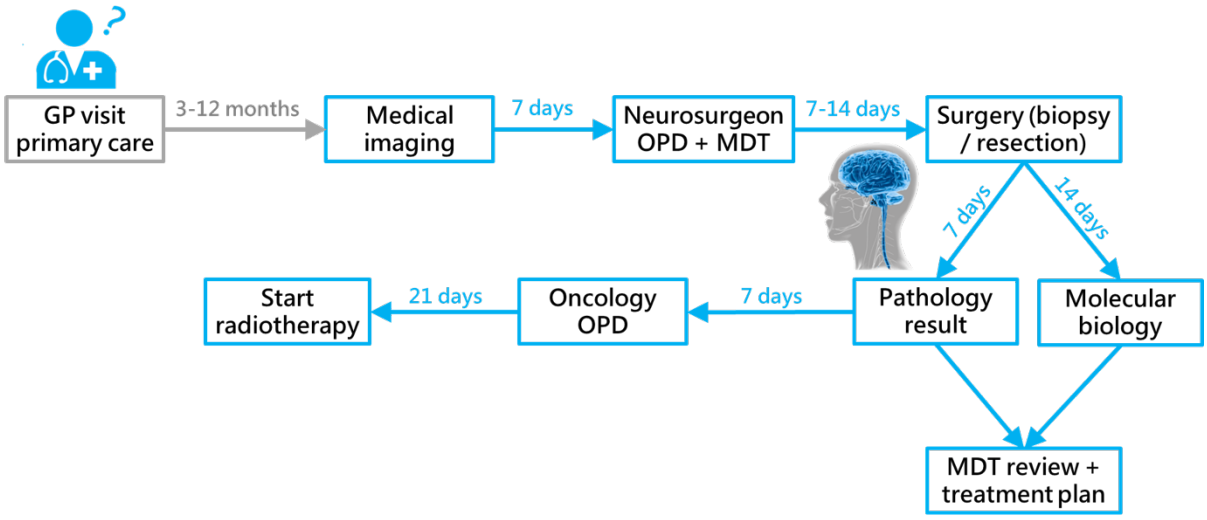

Figure 1.11 – The diagnostic pathway for brain tumours. GP, general practitioner; MDT, multidisciplinary team; OPD, outpatient department. Replicated form ref [60].

Medical imaging techniques, such as MRI and CT, can be extremely beneficial for finding the exact location of tumours, but are a significant cost burden to the NHS. They are also prone to both false negatives and positives as they are subject to the experience and competency of the radiographer performing the scan [105]. Despite histopathological examination being the gold standard in confirmatory testing, it has also been found to exhibit some errors [106].

Ultimately, the main issue in the current pathway is late diagnosis. For cancer detection in general, it is widely accepted that an early diagnosis can greatly increase the chance for successful treatment and improve the patient's outlook. Beyond the direct effects of increased survival rates, there is also the knock-on effect on quality of life. Earlier detection means the disease will be less advanced, so the patient has a better chance of being treated effectively and the outcome is more promising [107].

This might not have the benefits of allowing the patient to live much longer, but it could mean the remainder of their lives are spent in relative comfort.

The stress on NHS resources and cost of MRI and CT scans and may incentivise a GP to send away a patient complaining of headache for the first time, rather than referring them to a specialist for a full examination. Interestingly, a recent study found GP's were of the opinion that ~30% of diagnostic delays experienced by patients in primary care may have been preventable, whilst one fifth of GP's advocated that tools allowing timely clinical assessment may have benefited patients [108]. Thus, development of rapid, low-cost platforms in primary care to triage patients for medical imaging may reduce diagnostic delay whilst potentially providing cost-saving or cost-effective infrastructures for health care providers.

1.4 Infrared Biomedical Spectroscopy of Biofluids

Biomedical vibrational spectroscopy is an emerging field in the quest for early disease diagnosis [109–113]. Over the past decade, there has been a rapid increase of proof of concept publications, highlighting its potential for progression into the clinical environment [114–116]. Spectroscopic techniques have become of great interest to medical researchers for various reasons: analysis is rapid, cheap and non-invasive, instruments are easy to operate, but more importantly, they have the ability to characterise the presence of biomolecules and generate a biochemical fingerprint [117]. It has also been shown that imbalances in these biomolecules can give an indication of disease states. Therefore, rather than striving to detect specific biomarkers which exist in extremely low concentrations, a culmination of markers

can be probed with spectroscopy to detect a global change in biomolecular content caused by the systemic response to cancer [118].

In infrared (IR) spectroscopy, a sample is irradiated with infrared light which causes atomic displacements and molecular vibrations. Various types of modalities can be used, as the IR radiation can be transmitted, internally reflected or transflected [119]. The absorption of this light excites vibrational transitions of molecules, producing spectra that contain a vast amount of chemical and biological information [120]. A typical IR spectrum of a biological sample can quantify the levels of lipids, proteins, carbohydrates and nucleic acids present within the sample, and when coupled with data analysis, can differentiate between healthy and diseased samples [121]. Fourier Transform IR (FTIR) spectroscopy is thought to have the potential to be effectively translated to the clinic when combined with multivariate analysis techniques, due to the rapid acquisition times and high spectral quality [122,123].

The majority of the publications in the biomedical vibrational spectroscopy field have been based on the analysis of human tissue, with pilot studies showing it is possible to differentiate between healthy and cancerous tissue, as well as benign and malignant tumours [124]. Malignancies from various organs - such as breast, lung, colon, prostate and cervical tissues - have previously been studied which has provided a platform of promising results [125–131]. Despite the high volume of published research, the technique has yet to make a successful transition into the clinic [132]. More recently there has been further interest in biofluid spectroscopy due to the ease of collection and handling, and minimal sample preparation is

required. Blood components such as serum and plasma are commonly analysed in clinical tests, as they carry information regarding both intra- and extra-cellular events. Biobanks exist as a valuable stock both serum and plasma, with the ability to repeat analysis or monitor treatment or disease progression [133]. More specifically, blood serum perfuses all body organs, gaining proteomes from surrounding tissues and cells, thus contains over 20,000 different proteins [134]. Within a typical blood serum sample, there are a plethora of molecules that represent biochemical changes associated with malignancy and tumour growth, hence it represents an attractive sample medium for the early identification of cancerous events. The detection of biomolecules implicated in cancer with a serum-based triage system would be well-suited to the clinical environment. As serum tests are already utilised in clinical practice – for example, the prostate-specific antigen (PSA) liquid biopsy for prostate cancer – it would not significantly interrupt current practices, potentially enabling a smooth transition into diagnostic pathways [135].

Attenuated total reflection (ATR) – Fourier transform infrared (FTIR) spectroscopy has proven to be a promising screening tool for detecting ovarian cancer from human blood, where both serum and plasma were used to discriminate ovarian cancer patients from healthy controls with a success rate of ~95% and ~97%, respectively [136]. Backhaus *et al.* used serum spectroscopy to differentiate between patients in good health and those with breast cancer, reporting sensitivities and specificities of >92% for both [137]. Another pilot study found that the serum biosignature for cirrhotic patients, with and without hepatocellular carcinoma (HCC), could be successfully separated using support vector machine (SVM) classification and leave-

one-out cross validation [138]. Furthermore, patients with extensive fibrosis in the liver have been separated from those without fibrosis by using their FTIR serum spectra, which is a common disorder in the early developmental stages of HCC. Ollesch *et al.* introduced automated sampling for the first time, robotically spotting serum for high throughput FTIR measurements, in their quest to identify and validate spectroscopic biomarker candidates for urinary bladder cancer [139]. In a proof-of-concept study, Hands *et al.* were able to differentiate the serum spectra of brain tumour patients and healthy controls by using as little as 1 μL of blood serum for ATR-FTIR analysis, highlighting the great potential for the detection of brain tumours [140]. Paraskevaidi *et al.* demonstrated that ATR combined with chemometrics was capable of differentiating patients with various neurodegenerative diseases. Alzheimer's disease (AD) was identified with a sensitivity and specificity of 70%, and the AD patients were further segregated from those with dementia with 90% accuracy [141].

1.4.1 Clinical Translation

The high volume of research in the field of biomedical vibrational spectroscopy has indicated the potential utility of the technique in a clinical environment. Numerous diagnostic and disease monitoring studies have reported extremely promising results, in some cases achieving sensitivity and specificity values greater than 90% [142]. The major hurdle to successful translation is arguably acceptance by health technology regulatory agencies, who determine which technologies are made available for public health. Criteria for successful acceptance require statistically verified clinical trials to prove clinical utility, but also clear understanding of the

current clinical pathway in order to determine the economic and clinical impact of new technologies.

Current advances in technology may also facilitate the uptake of vibrational spectroscopy into standard clinical practice in the near future. Automated or high-throughput instrumentation would be best suited to clinical settings so as to minimise pressure on personnel resource. High-throughput technologies are available in IR transmission (or transflection) systems, largely attributed to the development of multichannel detectors and IR sources for discrete frequency spectroscopy, as well as the use of sample substrates which can be batch processed. This could have specific impacts on the translation of tissue imaging applications which have the potential to complement histopathology [143]. On the other hand, ATR-FTIR spectroscopy is inherently limited to a single point of analysis, the internal reflection element (IRE). The fixed IRE restricts the overall sample throughput, particularly when taking into account cleaning the crystal between measurements as well as background subtraction. However, the development of low cost IREs may provide a disposable substrate for ATR-FTIR spectroscopy, similarly enabling batch processing of samples and high-throughput spectral acquisition alongside the development of novel instrumentation [144].

ATR is preferred over other sampling modes for biofluids analysis, but the strong absorbance of water is still evident in biological spectra, which can obscure protein absorbance in liquid samples. Hence, the analysis of biofluids has been predominantly performed on air dried samples, which can lead to chemical and

physical inhomogeneity. The complex patterns that arise from dried biofluid drops have been of great interest over that past few decades, and various models have been published in an attempt to explain the complicated drying behaviour [145].

In analysing dried droplets using single-point transmission FTIR, Hughes *et al.* found the absorbance of the Amide I/II protein region to be highly variable across a small drop of blood serum. Spectra obtained from random locations across the dried serum spot, showed evidence of differences in sample thickness and heterogeneity. IR transmission imaging verified that there were biochemical differences across the drop [146]. Furthermore, the presence of cracks throughout the sample – along with varied drop thickness – caused scattered IR light and led to the conclusion that samples need to be smooth and evenly spread for transmission measurements [147].

Deegan *et al.* proposed the coffee ring effect, whereby capillary flow forces biomolecules to move out towards a drop's edge leaving behind dense ring at the periphery [148]. This is common when drying biofluid drops, which is a concern for spectroscopists, as the centre of the drop may not be representative of the whole sample (Figure 1.12). Specifically in blood serum a process known as the Vroman effect is of interest, whereby a series of molecular displacements arise through protein exchange [149]. It is thought that when biological fluids are applied to a solid surface, low molecular weight proteins attach to the surface first, before being displaced by larger protein molecules over time. Therefore, the adsorption of proteins on to the substrate surface will be based on their differing affinities [150–152]. Gelation and cracking patterns have also been observed in dried biofluid drops, which are thought to be dependent on protein concentration [153,154].

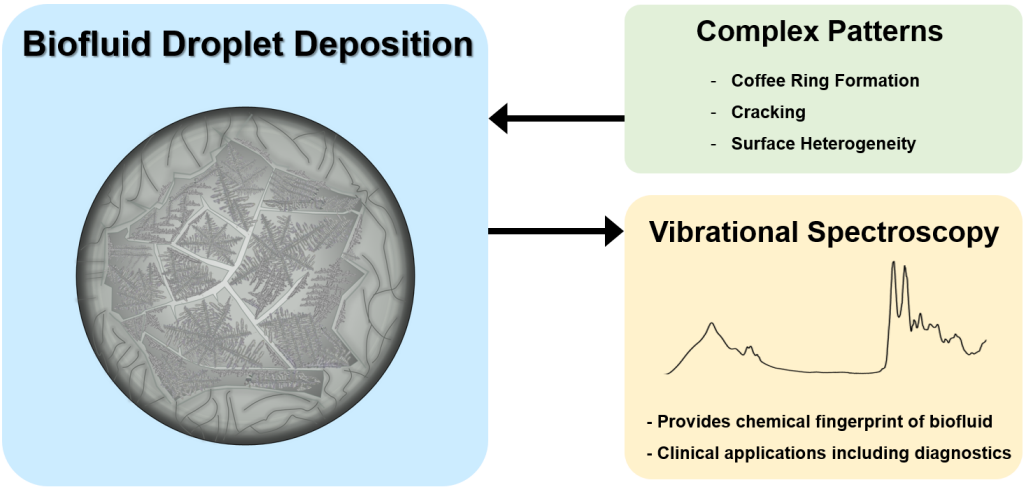

Figure 1.12 – Complex drying patterns in biofluid droplets as a potential cause of spectral variance.

These are the main limiting factors of using dried biofluids, as the surface inhomogeneity has shown to cause peak shifts and alterations in band intensities [146]. Environmental - temperature and humidity - and experimental - volume and concentration - conditions have also been shown to affect the drying patterns. However, when measured in the ATR mode the sample deposit can be completely contained within the area of the crystal, such that the evanescent wave measures the average of the entire drop, and in theory, should average out any inhomogeneities. Nonetheless, it is desirable that the drying conditions are controlled and optimal protocols are developed in order to obtain a more homogenous deposition across the sample [145,155].

While promising proof-of-principal studies have supported clinical suitability, there have been few reported clinical trials employing IR spectroscopy to confirm the utility in a prospective patient population. One of the examples closest to translation

is the analysis of whole blood for the detection of malarial infection, currently being tested in a prospective cohort in Papua New Guinea [156]. This application of ATR-FTIR spectroscopy also looks to quantify levels of parasitaemia in blood, providing clinically relevant information more rapidly than current methods [157]. The potential implementation analysis of blood serum using ATR-FTIR spectroscopy for the early detection of cancer in a primary care environment, would enable a paradigm shift in the clinical management of patients.

1.5 Aims & Objectives

The project outlined in this thesis aims to develop a rapid, label-free spectroscopic test for the detection and stratification of brain tumours. The theme of this thesis can be described by the following scenario.

Patient X is presenting with persistent headaches at their local GP surgery, but lacks any other 'common' symptoms. The GP currently has two options: (1) presume the patient is fine and send them away with pain relief medication, telling them to return if the headaches continue, or (2) send the patient for a brain scan in order to rule out a potential lesion. At present the former is the most common choice, as brain imaging is costly and many of those referred to the neurology department will not have a tumour. Yet, as already discussed, the main concern around current brain tumour pathway is the delay to diagnosis, as early detection is vital. This thesis is focused on implementing a cost-effective test which can help GPs in primary care with referral decisions, assist neurologists in secondary care with subtype differentiation, and ultimately improve patient survival and quality of life.

The main aims of this project are to see how far we can push the capabilities of IR spectroscopy. The following questions will be addressed:

- Can our spectroscopic test determine whether patient X is likely to have a brain tumour?
- Can we tell which type of brain tumour?
- Can we provide data on molecular status, which may offer prognostic information?
- Lastly, is this health technology translatable, and would the health services be interested?

Herein, the objectives undertaken to achieve the thesis aims include:

1) Rapid detection of brain cancer with ATR-FTIR serum spectroscopy using novel high-throughput technology (Chapter 3 and 4);
2) Stratification of brain tumour subtypes via serum spectroscopy for secondary care applications (Chapter 3 and 4);
3) Identification of molecular gene expression in gliomas through interrogation of *IDH1* status (Chapter 5);
4) Health economic evaluation of a serum-based blood test for brain tumour detection and stratification (Chapter 6).

1.6 References

[1] Cancer Research UK, How Cancer Starts, Accessed August 2017. (2017). http://www.cancerresearchuk.org/about-cancer/what-is-cancer/how-cancer-starts.

[2] M. Hejmadi, Introduction to cancer biology, BoonBooks.com, Frederiksberg, Denmark, 2010. http://bookboon.com/int/student/biology/introduction-to-cancer-biology (accessed August 8, 2017).

[3] A. Silverstein, V.B. Silverstein, L.S. Nunn, Cancer, Twenty-First Century Books, Minneapolis, Minn, 2006.

[4] Cancer Research UK, Cancer Cells, Accessed August 2017. (2017). http://www.cancerresearchuk.org/about-cancer/what-is-cancer/how-cancer-starts/cancer-cells.

[5] Cancer Research UK, Types of Cancer, Accessed August 2017. (2017). http://www.cancerresearchuk.org/about-cancer/what-is-cancer/how-cancer-starts/types-of-cancer.

[6] J.E. Rundhaug, S.M. Fischer, Molecular Mechanisms of Mouse Skin Tumor Promotion, Cancers. 2 (2010) 436–482. https://doi.org/10.3390/cancers2020436.

[7] B. Kaina, DNA damage-triggered apoptosis: critical role of DNA repair, double-strand breaks, cell proliferation and signaling, Biochem. Pharmacol. 66 (2003) 1547–1554.

[8] D. Hanahan, R.A. Weinberg, The Hallmarks of Cancer, Cell. 100 (2000) 57–70. https://doi.org/10.1016/S0092-8674(00)81683-9.

[9] S. Elmore, Apoptosis: A Review of Programmed Cell Death, Toxicol. Pathol. 35 (2007) 495–516. https://doi.org/10.1080/01926230701320337.

[10] K. Fernald, M. Kurokawa, Evading apoptosis in cancer, Trends Cell Biol. 23 (2013) 620–633. https://doi.org/10.1016/j.tcb.2013.07.006.

[11] N. Rivlin, R. Brosh, M. Oren, V. Rotter, Mutations in the p53 Tumor Suppressor Gene: Important Milestones at the Various Steps of Tumorigenesis, Genes Cancer. 2 (2011) 466–474. https://doi.org/10.1177/1947601911408889.

[12] H. Higashitsuji, H. Higashitsuji, T. Masuda, Y. Liu, K. Itoh, J. Fujita, Enhanced Deacetylation of p53 by the Anti-apoptotic Protein HSCO in Association with Histone Deacetylase 1, J. Biol. Chem. 282 (2007) 13716–13725. https://doi.org/10.1074/jbc.M609751200.

[13] Nature, Metastases, Accessed August 2017. (2017). https://www.nature.com/subjects/metastases.

[14] F. Arvelo, F. Sojo, C. Cotte, Tumour progression and metastasis, Ecancermedicalscience. 10 (2016). https://doi.org/10.3332/ecancer.2016.617.

[15] National Cancer Institute, Metastatic Cancer, Accessed August 2017. (2017). https://www.cancer.gov/types/metastatic-cancer.

[16] American Brain Tumour Association, Metastatic Brain Tumours, April 2018. (2018). http://www.abta.org/secure/metastatic-brain-tumor.pdf.

[17] Macmillan, What is secondary cancer, Accessed August 2017. (2017). http://www.macmillan.org.uk/information-and-support/liver-cancer-secondary/understanding-cancer/what-is-secondary-cancer-liver.html.

[18] Cancer Research UK, How can cancer spread, Accessed August 2017. (2017). http://www.cancerresearchuk.org/about-cancer/what-is-cancer/how-cancer-can-spread.
[19] National Cancer Institute, Cancer Staging, Accessed August 2017. (2017). https://www.cancer.gov/about-cancer/diagnosis-staging/staging.
[20] J. Brierley, M.K. Gospodarowicz, C. Wittekind, eds., TNM classification of malignant tumours, Eighth edition, John Wiley & Sons, Inc, Chichester, West Sussex, UK ; Hoboken, NJ, 2017.
[21] Cancer Research UK, Cancer Grading, Accessed August 2017. (2017). http://www.cancerresearchuk.org/about-cancer/what-is-cancer/cancer-grading.
[22] National Cancer Institute, Tumour Grade, Accessed August 2017. (2017). https://www.cancer.gov/about-cancer/diagnosis-staging/prognosis/tumor-grade-fact-sheet.
[23] National Cancer Institute, Cancer types, Accessed August 2017. (2017). https://www.cancer.gov/types.
[24] Cancer Research UK, Cancer statistics, Accessed August 2017. (2017). http://www.cancerresearchuk.org/health-professional/cancer-statistics.
[25] S.E. Huether, K.L. McCance, Understanding Pathophysiology., Elsevier Health Sciences, Saint Louis, 2013.
[26] Macmillan, Cancer statistics, Accessed August 2017. (2017). http://www.macmillan.org.uk/_images/cancer-statistics-factsheet_tcm9-260514.pdf.
[27] R. Hesketh, Introduction to cancer biology, Cambridge University Press, Cambridge ; New York, 2013.
[28] Cancer Research UK, Cancer incidence with age, Accessed August 2017. (2017). http://www.cancerresearchuk.org/health-professional/cancer-statistics/incidence/age.
[29] American Cancer Society, Lynch Syndrome, Accessed April 2018. (2018). https://www.cancer.org/cancer/cancer-causes/genetics/family-cancer-syndromes.html.
[30] Li-Fraumeni Syndrome Association, Li-Fraumeni Syndrome, Accessed April 2018. (2018). https://www.lfsassociation.org/what-is-lfs/.
[31] Medicine Net, Cancer causes, Accessed August 2017. (2017). http://www.medicinenet.com/cancer_causes/article.htm.
[32] Brain Tumour Research, Brain Tumour Research, Accessed Sept. 2017. (2017). https://www.braintumourresearch.org/campaigning/stark-facts?gclid=CjwKCAiAp5nyBRABEiwApTwjXkb2HvKCz7rHEiQBR4swacKw6zZK3X3d6Fj6W0p8TGOfm_Ab6VNhURoCplgQAvD_BwE.
[33] Cancer Research UK, Brain and other CNS tumours mortality rates, Accessed Sept. 2017. (2017). http://www.cancerresearchuk.org/health-professional/cancer-statistics/statistics-by-cancer-type/brain-other-cns-and-intracranial-tumours/mortality.
[34] N.G. Burnet, S.J. Jefferies, R.J. Benson, D.P. Hunt, F.P. Treasure, Years of life lost (YLL) from cancer is an important measure of population burden – and should be considered when allocating research funds, Br. J. Cancer. (2005). https://doi.org/10.1038/sj.bjc.6602321.
[35] WebMD, Picture of the Brain, Accessed Sept. 2017. (2017). http://www.webmd.com/brain/picture-of-the-brain#1.

[36] Mayfield Clinic, Brain Anatomy, Accessed Sept. 2017. (2017). https://www.mayfieldclinic.com/PE-AnatBrain.htm.
[37] Macmillan, The Brain, Accessed Sept. 2017. (2017). http://www.macmillan.org.uk/information-and-support/brain-tumours/understanding-cancer/the-brain.html#7553.
[38] World Health Organization, WHO classification of tumours of the central nervous system, Revised 4th edition, International Agency for Research on Cancer, Lyon, 2016.
[39] The Brain Tumour Charity, Types of Brain Tumour, Accessed Sept. 2017. (2017). https://www.thebraintumourcharity.org/understanding-brain-tumours/types-of-brain-tumour-adult/.
[40] J.S. Rao, Molecular mechanisms of glioma invasiveness: the role of proteases, Nat. Rev. Cancer. 3 (2003) 489–501. https://doi.org/10.1038/nrc1121.
[41] K. Urbańska, J. Sokołowska, M. Szmidt, P. Sysa, Review Glioblastoma multiforme – an overview, Współczesna Onkol. 5 (2014) 307–312. https://doi.org/10.5114/wo.2014.40559.
[42] D.N. Louis, H. Ohgaki, O.D. Wiestler, W.K. Cavenee, P.C. Burger, A. Jouvet, B.W. Scheithauer, P. Kleihues, The 2007 WHO Classification of Tumours of the Central Nervous System, Acta Neuropathol. (Berl.). 114 (2007) 97–109. https://doi.org/10.1007/s00401-007-0243-4.
[43] D.N. Louis, A. Perry, G. Reifenberger, A. von Deimling, D. Figarella-Branger, W.K. Cavenee, H. Ohgaki, O.D. Wiestler, P. Kleihues, D.W. Ellison, The 2016 World Health Organization Classification of Tumors of the Central Nervous System: a summary, Acta Neuropathol. (Berl.). 131 (2016) 803–820. https://doi.org/10.1007/s00401-016-1545-1.
[44] J.K. Myung, H. jin Cho, H. Kim, C.-K. Park, S.H. Lee, S.H. Choi, P. Park, J.M. Yoon, S.-H. Park, Prognosis of Glioblastoma With Oligodendroglioma Component is Associated With the IDH1 Mutation and MGMT Methylation Status, Transl. Oncol. 7 (2014) 712–719. https://doi.org/10.1016/j.tranon.2014.10.002.
[45] H. Yan, D.W. Parsons, G. Jin, R. McLendon, B.A. Rasheed, W. Yuan, I. Kos, I. Batinic-Haberle, S. Jones, G.J. Riggins, others, IDH1 and IDH2 mutations in gliomas, N. Engl. J. Med. 360 (2009) 765–773.
[46] N. Hu, R. Richards, R. Jensen, Role of chromosomal 1p/19q co-deletion on the prognosis of oligodendrogliomas: A systematic review and meta-analysis, Interdiscip. Neurosurg. 5 (2016) 58–63. https://doi.org/10.1016/j.inat.2016.06.008.
[47] D. Nassehi, L.P. Sørensen, H. Dyrbye, C. Thomsen, M. Juhler, H. Laursen, H. Broholm, Peritumoral brain edema in angiomatous supratentorial meningiomas: an investigation of the vascular endothelial growth factor A pathway, APMIS. 121 (2013) 1025–1036. https://doi.org/10.1111/apm.12052.
[48] A.D. Norden, J. Drappatz, P.Y. Wen, Targeted drug therapy for meningiomas, (2007). http://thejns.org/doi/full/10.3171/FOC-07/10/E12 (accessed September 5, 2017).
[49] P.A. Northcott, I. Buchhalter, A.S. Morrissy, V. Hovestadt, J. Weischenfeldt, T. Ehrenberger, S. Gröbner, M. Segura-Wang, T. Zichner, V.A. Rudneva, H.-J. Warnatz, N. Sidiropoulos, A.H. Phillips, S. Schumacher, K. Kleinheinz, S.M. Waszak, S. Erkek, D.T.W. Jones, B.C. Worst, M. Kool, M. Zapatka, N. Jäger,

L. Chavez, B. Hutter, M. Bieg, N. Paramasivam, M. Heinold, Z. Gu, N. Ishaque, C. Jäger-Schmidt, C.D. Imbusch, A. Jugold, D. Hübschmann, T. Risch, V. Amstislavskiy, F.G.R. Gonzalez, U.D. Weber, S. Wolf, G.W. Robinson, X. Zhou, G. Wu, D. Finkelstein, Y. Liu, F.M.G. Cavalli, B. Luu, V. Ramaswamy, X. Wu, J. Koster, M. Ryzhova, Y.-J. Cho, S.L. Pomeroy, C. Herold-Mende, M. Schuhmann, M. Ebinger, L.M. Liau, J. Mora, R.E. McLendon, N. Jabado, T. Kumabe, E. Chuah, Y. Ma, R.A. Moore, A.J. Mungall, K.L. Mungall, N. Thiessen, K. Tse, T. Wong, S.J.M. Jones, O. Witt, T. Milde, A. Von Deimling, D. Capper, A. Korshunov, M.-L. Yaspo, R. Kriwacki, A. Gajjar, J. Zhang, R. Beroukhim, E. Fraenkel, J.O. Korbel, B. Brors, M. Schlesner, R. Eils, M.A. Marra, S.M. Pfister, M.D. Taylor, P. Lichter, The whole-genome landscape of medulloblastoma subtypes, Nature. 547 (2017) 311–317. https://doi.org/10.1038/nature22973.

[50] N.R. Smoll, K.J. Drummond, The incidence of medulloblastomas and primitive neurectodermal tumours in adults and children, J. Clin. Neurosci. 19 (2012) 1541–1544. https://doi.org/10.1016/j.jocn.2012.04.009.

[51] Macmillan, Types of Brain Tumour, Accessed Sept. 2017. (2017). http://www.macmillan.org.uk/information-and-support/brain-tumours/understanding-cancer/types-brain-tumour.html.

[52] R.A. Patchell, The management of brain metastases, Cancer Treat. Rev. 29 (2003) 533–540. https://doi.org/10.1016/S0305-7372(03)00105-1.

[53] G. Rahmathulla, S.A. Toms, R.J. Weil, The Molecular Biology of Brain Metastasis, J. Oncol. 2012 (2012) 1–16. https://doi.org/10.1155/2012/723541.

[54] D.A. Hardesty, P. Nakaji, The Current and Future Treatment of Brain Metastases, Front. Surg. 3 (2016). https://doi.org/10.3389/fsurg.2016.00030.

[55] Brain Tumour Research, Brain Cancer Symptoms, Accessed Sept. 2017. (2017). https://www.braintumourresearch.org/info-support/symptoms.

[56] Mayfield Clinic, Brain Tumour Symptoms, Accessed Sept. 2017. (2017). http://www.mayfieldclinic.com/pe-braintumor.htm.

[57] P. Kelly, Gliomas: Survival, origin and early detection, Surg. Neurol. Int. 1 (2010) 96. https://doi.org/10.4103/2152-7806.74243.

[58] W. Hamilton, D. Kernick, Clinical features of primary brain tumours: a case–control study using electronic primary care records, Br J Gen Pr. 57 (2007) 695–699.

[59] M. Morgan, L. Jenkins, L. Ridsdale, Patient pressure for referral for headache: a qualitative study of GPs' referral behaviour, Br J Gen Pr. 57 (2007) 29–35.

[60] E. Gray, H.J. Butler, R. Board, P.M. Brennan, A.J. Chalmers, T. Dawson, J. Goodden, W. Hamilton, M.G. Hegarty, A. James, M.D. Jenkinson, D. Kernick, E. Lekka, L.J. Livermore, S.J. Mills, K. O'Neill, D.S. Palmer, B. Vaqas, M.J. Baker, Health economic evaluation of a serum-based blood test for brain tumour diagnosis: exploration of two clinical scenarios, BMJ Open. 8 (2018) e017593. https://doi.org/10.1136/bmjopen-2017-017593.

[61] Advantages and Disadvantages of MRI, in: Basics Magn. Reson. Imaging, Springer US, Boston, MA, 1988: pp. 125–138. https://doi.org/10.1007/978-1-4613-2081-4_9.

[62] S. Campos, P. Davey, A. Hird, B. Pressnail, J. Bilbao, R.I. Aviv, S. Symons, F. Pirouzmand, E. Sinclair, S. Culleton, others, Brain metastasis from an

unknown primary, or primary brain tumour? A diagnostic dilemma, Curr. Oncol. 16 (2009) 62.
[63] D.-D. Xiao, P.-F. Yan, Y.-X. Wang, M.S. Osman, H.-Y. Zhao, Glioblastoma and primary central nervous system lymphoma: Preoperative differentiation by using MRI-based 3D texture analysis, Clin. Neurol. Neurosurg. 173 (2018) 84–90. https://doi.org/10.1016/j.clineuro.2018.08.004.
[64] H.M. Sakr, M.A. Mohamed, H. Jalalod′din, Y.A. Abbas, Influence of fMRI on operative planning of brain tumors: Initial experience in a histopathologically variable subset of tumors, Egypt. J. Radiol. Nucl. Med. 42 (2011) 215–221. https://doi.org/10.1016/j.ejrnm.2011.06.001.
[65] M. Wengenroth, M. Blatow, J. Guenther, M. Akbar, V.M. Tronnier, C. Stippich, Diagnostic benefits of presurgical fMRI in patients with brain tumours in the primary sensorimotor cortex, Eur. Radiol. 21 (2011) 1517–1525. https://doi.org/10.1007/s00330-011-2067-9.
[66] S. Cha, Update on Brain Tumor Imaging: From Anatomy to Physiology, Am. J. Neuroradiol. 27 (2006) 475.
[67] E. Gray, H.J. Butler, R. Board, P. Brennan, A. Chalmers, T. Dawson, J. Goodden, W. Hamilton, M. Hegarty, A. James, M.D. Jenkinson, D. Kernick, E. Lekka, L. Livermore, S. Mills, K. O'Neill, D.S. Palmer, B. Vaqas, M.J. Baker, Health economic evaluation of a serum based blood test for brain tumour diagnosis: Exploration of two clinical scenarios., (n.d.).
[68] D.J. Brenner, E.J. Hall, Computed tomography—an increasing source of radiation exposure, N. Engl. J. Med. 357 (2007) 2277–2284.
[69] A. Trivedi, J. Thakkar, M. Jethva, I. Virda, CT & MRI Evaluation of Brain Tumour & Tumour like Conditions, Int. J. Sci. Res. 6 (2017).
[70] C.S. Muratore, Pediatric abdominal CT scans: do it correctly. Better yet, don't do it at all, J. Surg. Res. 185 (2013) 533–534. https://doi.org/10.1016/j.jss.2012.08.005.
[71] G. Gupta, R. Kaur, A. Bansal, M. Bansal, Analysis and comparison of brain tumor detection and extraction techniques from MRI images, Int. J. Adv. Res. Electr. Electron. Instrum. Eng. IJAREEIE. 3 (2014). https://pdfs.semanticscholar.org/a0f9/3a417c09da123b61025165066e3bc6a17d66.pdf (accessed September 8, 2017).
[72] K. Kobayashi, P. Bhargava, S. Raja, F. Nasseri, H.A. Al-Balas, D.D. Smith, S.P. George, M.S. Vij, Image-guided Biopsy: What the Interventional Radiologist Needs to Know about PET/CT, RadioGraphics. 32 (2012) 1483–1501. https://doi.org/10.1148/rg.325115159.
[73] L. Fass, Imaging and cancer: A review, Mol. Oncol. 2 (2008) 115–152. https://doi.org/10.1016/j.molonc.2008.04.001.
[74] M.C. Mabray, R.F. Barajas, S. Cha, Modern Brain Tumor Imaging, Brain Tumor Res. Treat. 3 (2015) 8. https://doi.org/10.14791/btrt.2015.3.1.8.
[75] Accelerate Brain Cancer Cure, Frankly Speaking About Brain Tumors, (2018). http://abc2.org/sites/default/files/Frankly%20Speaking%20About%20Cancer_Brain%20Tumors_0.pdf.
[76] Cancer.Net, Tumour grades and prognostic factors, Accessed Sept. 2017. (2017). http://www.cancer.net/cancer-types/brain-tumor/grades-and-prognostic-factors.

[77] Neurosurgery UF Health, Stereotactic Brain Biopsy, Accessed Sept. 2017. (2017). https://neurosurgery.ufl.edu/residency/about-us/clinical-specialties/stereotactic-brain-biopsy/.
[78] Healthline, Brain Biopsy, Accessed Sept. 2017. (2017). http://www.healthline.com/health/brain-biopsy#overview1.
[79] L.J. Cook, J. Freedman, Brain tumors, 1st ed, Rosen Pub, New York, 2012.
[80] A.H. Fischer, K.A. Jacobson, J. Rose, R. Zeller, Hematoxylin and Eosin Staining of Tissue and Cell Sections, Cold Spring Harb. Protoc. 2008 (2008) pdb.prot4986-pdb.prot4986. https://doi.org/10.1101/pdb.prot4986.
[81] P. Wesseling, J.M. Kros, J.W. Jeuken, The pathological diagnosis of diffuse gliomas: towards a smart synthesis of microscopic and molecular information in a multidisciplinary context, Diagn. Histopathol. 17 (2011) 486–494.
[82] Cancer Connect, Malignancy type and grade, Accessed Sept. 2017. (2017). http://news.cancerconnect.com/types-of-cancer/brain-cancer/brain-cancer-overview/the-diagnosis-brain-tumor-malignancy-type-and-grade/.
[83] A. Grin, C.J. Streutker, Histopathology in Barrett Esophagus and Barrett Esophagus-Related Dysplasia, Clin. Endosc. 47 (2014) 31. https://doi.org/10.5946/ce.2014.47.1.31.
[84] M.J. Baker, E. Gazi, M.D. Brown, J.H. Shanks, N.W. Clarke, P. Gardner, Investigating FTIR based histopathology for the diagnosis of prostate cancer, J. Biophotonics. 2 (2009) 104–113. https://doi.org/10.1002/jbio.200810062.
[85] National Cancer Institute, Biomarker Definition, Acessed Sept. 2017. (2017). https://www.cancer.gov/publications/dictionaries/cancer-terms?CdrID=45618.
[86] N.L. Henry, D.F. Hayes, Cancer biomarkers, Mol. Oncol. 6 (2012) 140–146. https://doi.org/10.1016/j.molonc.2012.01.010.
[87] E.P. Diamandis, Mass Spectrometry as a Diagnostic and a Cancer Biomarker Discovery Tool: Opportunities and Potential Limitations, Mol. Cell. Proteomics. 3 (2004) 367–378. https://doi.org/10.1074/mcp.R400007-MCP200.
[88] S. Liang, G. Shen, Biomarkers of glioma, in: Mol. Targets CNS Tumors, InTech, 2011. https://www.intechopen.com/download/pdf/19940 (accessed September 15, 2017).
[89] G.D. Dakubo, Cancer Biomarkers in Body Fluids, Springer International Publishing, Cham, 2017. https://doi.org/10.1007/978-3-319-48360-3.
[90] V.M. Lu, M.A. Alvi, K.L. McDonald, D.J. Daniels, Impact of the H3K27M mutation on survival in pediatric high-grade glioma: a systematic review and meta-analysis, J. Neurosurg. Pediatr. 23 (2019) 308–316. https://doi.org/10.3171/2018.9.PEDS18419.
[91] A.L. Cohen, S.L. Holmen, H. Colman, IDH1 and IDH2 Mutations in Gliomas, Curr. Neurol. Neurosci. Rep. 13 (2013). https://doi.org/10.1007/s11910-013-0345-4.
[92] M. Cankovic, M.N. Nikiforova, M. Snuderl, A.M. Adesina, N. Lindeman, P.Y. Wen, E.Q. Lee, The role of MGMT testing in clinical practice: a report of the association for molecular pathology, J. Mol. Diagn. 15 (2013) 539–555.
[93] Oncology Pro, 1p/19q Co-deletion in Glioma, Accessed Sept. 2017. (2017). http://oncologypro.esmo.org/Education-Library/Factsheets-on-Biomarkers/1p-19q-Co-deletion-in-Glioma#eztoc1727416_0_0_2.

[94] S. Maraka, F. Janku, BRAF alterations in primary brain tumors, Discov. Med. 26 (2018) 51–60.
[95] The Brain Tumour Charity, Biomarkers and Brain Tumours, Accessed April 2018. (2018). https://assets.thebraintumourcharity.org/live/media/filer_public/ce/7d/ce7d15fd-8e17-4c87-9410-79230ae15e89/biomarkers-brain-tumour-diagnosis-v2a-factsheet.pdf.
[96] M.E. Hegi, A.-C. Diserens, T. Gorlia, M.-F. Hamou, N. de Tribolet, M. Weller, J.M. Kros, J.A. Hainfellner, W. Mason, L. Mariani, J.E.C. Bromberg, P. Hau, R.O. Mirimanoff, J.G. Cairncross, R.C. Janzer, R. Stupp, MGMT Gene Silencing and Benefit from Temozolomide in Glioblastoma, N. Engl. J. Med. 352 (2005) 997–1003. https://doi.org/10.1056/NEJMoa043331.
[97] N. Thon, S. Kreth, F.W. Kreth, Personalized treatment strategies in glioblastoma: MGMT promoter methylation status, OncoTargets Ther. (2013) 1363. https://doi.org/10.2147/OTT.S50208.
[98] R.B. Jenkins, H. Blair, K.V. Ballman, C. Giannini, R.M. Arusell, M. Law, H. Flynn, S. Passe, S. Felten, P.D. Brown, E.G. Shaw, J.C. Buckner, A t(1;19)(q10;p10) Mediates the Combined Deletions of 1p and 19q and Predicts a Better Prognosis of Patients with Oligodendroglioma, Cancer Res. 66 (2006) 9852–9861. https://doi.org/10.1158/0008-5472.CAN-06-1796.
[99] C. Hartmann, B. Hentschel, W. Wick, D. Capper, J. Felsberg, M. Simon, M. Westphal, G. Schackert, R. Meyermann, T. Pietsch, G. Reifenberger, M. Weller, M. Loeffler, A. von Deimling, Patients with IDH1 wild type anaplastic astrocytomas exhibit worse prognosis than IDH1-mutated glioblastomas, and IDH1 mutation status accounts for the unfavorable prognostic effect of higher age: implications for classification of gliomas, Acta Neuropathol. (Berl.). 120 (2010) 707–718. https://doi.org/10.1007/s00401-010-0781-z.
[100] D. Capper, S. WeiÃŸert, J. Balss, A. Habel, J. Meyer, D. JÃ¤ger, U. Ackermann, C. Tessmer, A. Korshunov, H. Zentgraf, C. Hartmann, A. Von Deimling, Characterization of R132H Mutation-specific IDH1 Antibody Binding in Brain Tumors: IDH1R132H Mutation-specific Antibody, Brain Pathol. 20 (2010) 245–254. https://doi.org/10.1111/j.1750-3639.2009.00352.x.
[101] G. Reifenberger, H.-G. Wirsching, C.B. Knobbe-Thomsen, M. Weller, Advances in the molecular genetics of gliomas — implications for classification and therapy, Nat. Rev. Clin. Oncol. 14 (2017) 434–452. https://doi.org/10.1038/nrclinonc.2016.204.
[102] NHS England, Waiting Times for Suspected and Diagnosed Cancer Patients, 2016. https://www.england.nhs.uk/statistics/wp-content/uploads/sites/2/2017/06/Cancer-Waiting-Times-Annual-Report-201617-1.pdf.
[103] The Brain Tumour Charity, Finding a Better way?, Accessed August 2017. (2017). http://cdn.basw.co.uk/upload/basw_21512-10.pdf.
[104] L. Elliss-Brookes, S. McPhail, A. Ives, M. Greenslade, J. Shelton, S. Hiom, M. Richards, Routes to diagnosis for cancer – determining the patient journey using multiple routine data sets, Br. J. Cancer. 107 (2012) 1220–1226. https://doi.org/10.1038/bjc.2012.408.

[105] K. Herholz, K.-J. Langen, C. Schiepers, J.M. Mountz, Brain Tumors, Semin. Nucl. Med. 42 (2012) 356–370. https://doi.org/10.1053/j.semnuclmed.2012.06.001.
[106] S.S. Raab, D.M. Grzybicki, J.E. Janosky, R.J. Zarbo, F.A. Meier, C. Jensen, S.J. Geyer, Clinical impact and frequency of anatomic pathology errors in cancer diagnoses, Cancer. 104 (2005) 2205–2213. https://doi.org/10.1002/cncr.21431.
[107] D. Weller, P. Vedsted, G. Rubin, F.M. Walter, J. Emery, S. Scott, C. Campbell, R.S. Andersen, W. Hamilton, F. Olesen, P. Rose, S. Nafees, E. van Rijswijk, S. Hiom, C. Muth, M. Beyer, R.D. Neal, The Aarhus statement: improving design and reporting of studies on early cancer diagnosis, Br. J. Cancer. 106 (2012) 1262–1267. https://doi.org/10.1038/bjc.2012.68.
[108] M. Ozawa, P.M. Brennan, K. Zienius, K.M. Kurian, W. Hollingworth, D. Weller, W. Hamilton, R. Grant, Y. Ben-Shlomo, Symptoms in primary care with time to diagnosis of brain tumours, Fam. Pract. 35 (2018) 551–558. https://doi.org/10.1093/fampra/cmx139.
[109] M.J. Baker, Photonic Biofluid Diagnostics, J. Biophotonics. 7 (2014) 151–152. https://doi.org/10.1002/jbio.201400504.
[110] M. Baker, Biophotonics: Vibrational Spectroscopic Diagnostics, IOP Publishing, 2016. https://doi.org/10.1088/978-1-6817-4071-3.
[111] G. Clemens, J.R. Hands, K.M. Dorling, M.J. Baker, Vibrational spectroscopic methods for cytology and cellular research, The Analyst. 139 (2014) 4411–4444. https://doi.org/10.1039/C4AN00636D.
[112] H.J. Byrne, Vibrational Spectroscopy: Disease Diagnostics and Beyond, in: Opt. Spectrosc. Comput. Methods Biol. Med., Springer, New York, 2013.
[113] C. Hughes, G. Clemens, B. Bird, T. Dawson, K.M. Ashton, M.D. Jenkinson, A. Brodbelt, M. Weida, E. Fotheringham, M. Barre, J. Rowlette, M.J. Baker, Introducing Discrete Frequency Infrared Technology for High-Throughput Biofluid Screening, Sci. Rep. 6 (2016). https://doi.org/10.1038/srep20173.
[114] K. Spalding, R. Board, T. Dawson, M.D. Jenkinson, M.J. Baker, A review of novel analytical diagnostics for liquid biopsies: spectroscopic and spectrometric serum profiling of primary and secondary brain tumors, Brain Behav. 6 (2016) e00502. https://doi.org/10.1002/brb3.502.
[115] K. Dorling, M.J. Baker, Highlighting attenuated total reflection Fourier transform infrared spectroscopy for rapid serum analysis, Trends Biotechnol. 31 (2013) 325–327. https://doi.org/10.1016/j.tibtech.2013.03.009.
[116] K. Kong, C. Kendall, N. Stone, I. Notingher, Raman spectroscopy for medical diagnostics — From in-vitro biofluid assays to in-vivo cancer detection, Adv. Drug Deliv. Rev. 89 (2015) 121–134. https://doi.org/10.1016/j.addr.2015.03.009.
[117] O.J. Old, L.M. Fullwood, R. Scott, G.R. Lloyd, L.M. Almond, N.A. Shepherd, N. Stone, H. Barr, C. Kendall, Vibrational spectroscopy for cancer diagnostics, Anal. Methods. 6 (2014) 3901. https://doi.org/10.1039/c3ay42235f.
[118] F. Bonnier, M.J. Baker, H.J. Byrne, Vibrational spectroscopic analysis of body fluids: avoiding molecular contamination using centrifugal filtration, Anal. Methods. 6 (2014) 5155. https://doi.org/10.1039/c4ay00891j.

[119] M.J. Baker, S.R. Hussain, L. Lovergne, V. Untereiner, C. Hughes, R.A. Lukaszewski, G. Thiéfin, G.D. Sockalingum, Developing and understanding biofluid vibrational spectroscopy: a critical review, Chem. Soc. Rev. 45 (2016) 1803–1818.
[120] A. Barth, Infrared spectroscopy of proteins, Biochim. Biophys. Acta BBA - Bioenerg. 1767 (2007) 1073–1101. https://doi.org/10.1016/j.bbabio.2007.06.004.
[121] M.J. Baker, J. Trevisan, P. Bassan, R. Bhargava, H.J. Butler, K.M. Dorling, P.R. Fielden, S.W. Fogarty, N.J. Fullwood, K.A. Heys, C. Hughes, P. Lasch, P.L. Martin-Hirsch, B. Obinaju, G.D. Sockalingum, J. Sulé-Suso, R.J. Strong, M.J. Walsh, B.R. Wood, P. Gardner, F.L. Martin, Using Fourier transform IR spectroscopy to analyze biological materials, Nat. Protoc. 9 (2014) 1771–1791. https://doi.org/10.1038/nprot.2014.110.
[122] G. Bellisola, C. Sorio, Infrared spectroscopy and microscopy in cancer research and diagnosis, Am. J. Cancer Res. 2 (2012) 1.
[123] B.R. Smith, K.M. Ashton, A. Brodbelt, T. Dawson, M.D. Jenkinson, N.T. Hunt, D.S. Palmer, M.J. Baker, Combining random forest and 2D correlation analysis to identify serum spectral signatures for neuro-oncology, Analyst. 141 (2016) 3668–3678.
[124] Z. Movasaghi, S. Rehman, Dr.I. ur Rehman, Fourier Transform Infrared (FTIR) Spectroscopy of Biological Tissues, Appl. Spectrosc. Rev. 43 (2008) 134–179. https://doi.org/10.1080/05704920701829043.
[125] M.J. Walsh, S.E. Holton, A. Kajdacsy-Balla, R. Bhargava, Attenuated total reflectance Fourier-transform infrared spectroscopic imaging for breast histopathology, Vib. Spectrosc. 60 (2012) 23–28. https://doi.org/10.1016/j.vibspec.2012.01.010.
[126] B. Bird, S. Remiszewski, A. Akalin, M. Kon, M. Diem, others, Infrared spectral histopathology (SHP): a novel diagnostic tool for the accurate classification of lung cancer, Lab. Invest. 92 (2012) 1358.
[127] P. Lasch, W. Haensch, D. Naumann, M. Diem, Imaging of colorectal adenocarcinoma using FT-IR microspectroscopy and cluster analysis, Biochim. Biophys. Acta BBA - Mol. Basis Dis. 1688 (2004) 176–186. https://doi.org/10.1016/j.bbadis.2003.12.006.
[128] M.J. Baker, E. Gazi, M.D. Brown, J.H. Shanks, P. Gardner, N.W. Clarke, FTIR-based spectroscopic analysis in the identification of clinically aggressive prostate cancer, Br. J. Cancer. 99 (2008) 1859–1866. https://doi.org/10.1038/sj.bjc.6604753.
[129] E. Gazi, M. Baker, J. Dwyer, N.P. Lockyer, P. Gardner, J.H. Shanks, R.S. Reeve, C.A. Hart, N.W. Clarke, M.D. Brown, A Correlation of FTIR Spectra Derived from Prostate Cancer Biopsies with Gleason Grade and Tumour Stage, Eur. Urol. 50 (2006) 750–761. https://doi.org/10.1016/j.eururo.2006.03.031.
[130] M.J. Walsh, M.N. Singh, H.M. Pollock, L.J. Cooper, M.J. German, H.F. Stringfellow, N.J. Fullwood, E. Paraskevaidis, P.L. Martin-Hirsch, F.L. Martin, ATR microspectroscopy with multivariate analysis segregates grades of exfoliative cervical cytology, Biochem. Biophys. Res. Commun. 352 (2007) 213–219. https://doi.org/10.1016/j.bbrc.2006.11.005.

[131] M.J. Walsh, M.N. Singh, H.F. Stringfellow, H.M. Pollock, A. Hammiche, O. Grude, N.J. Fullwood, M.A. Pitt, P.L. Martin-Hirsch, F.L. Martin, FTIR microspectroscopy coupled with two-class discrimination segregates markers responsible for inter-and intra-category variance in exfoliative cervical cytology, Biomark. Insights. 3 (2008) BMI–S592.
[132] A.L. Mitchell, K.B. Gajjar, G. Theophilou, F.L. Martin, P.L. Martin-Hirsch, Vibrational spectroscopy of biofluids for disease screening or diagnosis: Translation from the laboratory to a clinical setting, J. Biophotonics. 7 (2014) 153–165. https://doi.org/10.1002/jbio.201400018.
[133] M.J. Baker, C.S. Hughes, K.A. Hollywood, Biophotonics: Vibrational Spectroscopic Diagnostics, Morgan & Claypool Publishers, 2016. https://doi.org/10.1088/978-1-6817-4071-3.
[134] R.S. Tirumalai, K.C. Chan, D.A. Prieto, H.J. Issaq, T.P. Conrads, T.D. Veenstra, Characterization of the Low Molecular Weight Human Serum Proteome, Mol. Cell. Proteomics. 2 (2003) 1096–1103. https://doi.org/10.1074/mcp.M300031-MCP200.
[135] I. Infusino, M. Panteghini, Serum albumin: Accuracy and clinical use, Clin. Chim. Acta. 419 (2013) 15–18. https://doi.org/10.1016/j.cca.2013.01.005.
[136] K. Gajjar, J. Trevisan, G. Owens, P.J. Keating, N.J. Wood, H.F. Stringfellow, P.L. Martin-Hirsch, F.L. Martin, Fourier-transform infrared spectroscopy coupled with a classification machine for the analysis of blood plasma or serum: a novel diagnostic approach for ovarian cancer, Analyst. 138 (2013) 3917–3926. https://doi.org/10.1039/C3AN36654E.
[137] J. Backhaus, R. Mueller, N. Formanski, N. Szlama, H.-G. Meerpohl, M. Eidt, P. Bugert, Diagnosis of breast cancer with infrared spectroscopy from serum samples, Vib. Spectrosc. 52 (2010) 173–177. https://doi.org/10.1016/j.vibspec.2010.01.013.
[138] X. Zhang, G. Thiéfin, C. Gobinet, V. Untereiner, I. Taleb, B. Bernard-Chabert, A. Heurgué, C. Truntzer, P. Ducoroy, P. Hillon, G.D. Sockalingum, Profiling serologic biomarkers in cirrhotic patients via high-throughput Fourier transform infrared spectroscopy: toward a new diagnostic tool of hepatocellular carcinoma, Transl. Res. 162 (2013) 279–286. https://doi.org/10.1016/j.trsl.2013.07.007.
[139] J. Ollesch, M. Heinze, H.M. Heise, T. Behrens, T. Brüning, K. Gerwert, It's in your blood: spectral biomarker candidates for urinary bladder cancer from automated FTIR spectroscopy: Spectral cancer biomarkers from high-throughput FTIR spectroscopy, J. Biophotonics. 7 (2014) 210–221. https://doi.org/10.1002/jbio.201300163.
[140] J.R. Hands, K.M. Dorling, P. Abel, K.M. Ashton, A. Brodbelt, C. Davis, T. Dawson, M.D. Jenkinson, R.W. Lea, C. Walker, M.J. Baker, Attenuated Total Reflection Fourier Transform Infrared (ATR-FTIR) spectral discrimination of brain tumour severity from serum samples: Serum spectroscopy gliomas, J. Biophotonics. 7 (2014) 189–199. https://doi.org/10.1002/jbio.201300149.
[141] M. Paraskevaidi, C.L.M. Morais, K.M.G. Lima, J.S. Snowden, J.A. Saxon, A.M.T. Richardson, M. Jones, D.M.A. Mann, D. Allsop, P.L. Martin-Hirsch, F.L. Martin, Differential diagnosis of Alzheimer's disease using spectrochemical analysis of blood, Proc. Natl. Acad. Sci. 114 (2017) E7929–E7938. https://doi.org/10.1073/pnas.1701517114.

[142] H.J. Byrne, M. Baranska, G.J. Puppels, N. Stone, B. Wood, K.M. Gough, P. Lasch, P. Heraud, J. Sulé-Suso, G.D. Sockalingum, Spectropathology for the next generation: Quo vadis?, The Analyst. 140 (2015) 2066–2073. https://doi.org/10.1039/C4AN02036G.
[143] D.C. Fernandez, R. Bhargava, S.M. Hewitt, I.W. Levin, Infrared spectroscopic imaging for histopathologic recognition, Nat. Biotechnol. 23 (2005) 469–474. https://doi.org/10.1038/nbt1080.
[144] M. Koç, E. Karabudak, History of spectroscopy and modern micromachined disposable Si ATR-IR spectroscopy, Appl. Spectrosc. Rev. 53 (2018) 420–438. https://doi.org/10.1080/05704928.2017.1366341.
[145] J.M. Cameron, H.J. Butler, D.S. Palmer, M.J. Baker, Biofluid spectroscopic disease diagnostics: A review on the processes and spectral impact of drying, J. Biophotonics. 11 (2018) e201700299. https://doi.org/10.1002/jbio.201700299.
[146] F. Bonnier, F. Petitjean, M.J. Baker, H.J. Byrne, Improved protocols for vibrational spectroscopic analysis of body fluids: Improved protocols for vibrational spectroscopic analysis of body fluids, J. Biophotonics. 7 (2014) 167–179. https://doi.org/10.1002/jbio.201300130.
[147] C. Hughes, M. Brown, G. Clemens, A. Henderson, G. Monjardez, N.W. Clarke, P. Gardner, Assessing the challenges of FTIR spectroscopic analysis of blood serum, J. Biophotonics. 7 (2014) 180–188. https://doi.org/10.1002/jbio.201300167.
[148] R.D. Deegan, Pattern formation in drying drops, Phys. Rev. E. 61 (2000) 475.
[149] S.L. Hirsh, D.R. McKenzie, N.J. Nosworthy, J.A. Denman, O.U. Sezerman, M.M.M. Bilek, The Vroman effect: Competitive protein exchange with dynamic multilayer protein aggregates, Colloids Surf. B Biointerfaces. 103 (2013) 395–404. https://doi.org/10.1016/j.colsurfb.2012.10.039.
[150] L. Vroman, A.L. Adams, G.C. Fischer, P.C. Munoz, Interaction of high molecular weight kininogen, factor XII, and fibrinogen in plasma at interfaces., Blood. 55 (1980) 156–159.
[151] A.H. Schmaier, L. Silver, Ann.L. Adams, G.C. Fischer, P.C. Munoz, L. Vroman, R.W. Colman, The effect of high molecular weight kininogen on surface-adsorbed fibrinogen, Thromb. Res. 33 (2017) 51–67. https://doi.org/10.1016/0049-3848(84)90154-3.
[152] A.L. Adams, G.C. Fischer, P.C. Munoz, L. Vroman, Convex-lens-on-slide: A simple system for the study of human plasma and blood in narrow spaces, J. Biomed. Mater. Res. 18 (1984) 643–654. https://doi.org/10.1002/jbm.820180606.
[153] C.C. Annarelli, J. Fornazero, J. Bert, J. Colombani, Crack patterns in drying protein solution drops, Eur. Phys. J. E Soft Matter Biol. Phys. 5 (2001) 599–603.
[154] L. Lovergne, G. Clemens, V. Untereiner, R.A. Lukaszweski, G.D. Sockalingum, M.J. Baker, Investigating optimum sample preparation for infrared spectroscopic serum diagnostics, Anal Methods. 7 (2015) 7140–7149. https://doi.org/10.1039/C5AY00502G.
[155] L. Lovergne, P. Bouzy, V. Untereiner, R. Garnotel, M.J. Baker, G. Thiéfin, G.D. Sockalingum, Biofluid infrared spectro-diagnostics: pre-analytical

considerations for clinical applications, Faraday Discuss. 187 (2016) 521–537. https://doi.org/10.1039/C5FD00184F.
[156] D. Perez-Guaita, K.M. Marzec, A. Hudson, C. Evans, T. Chernenko, C. Matthäus, M. Miljkovic, M. Diem, P. Heraud, J.S. Richards, D. Andrew, D.A. Anderson, C. Doerig, J. Garcia-Bustos, D. McNaughton, B.R. Wood, Parasites under the Spotlight: Applications of Vibrational Spectroscopy to Malaria Research, Chem. Rev. 118 (2018) 5330–5358. https://doi.org/10.1021/acs.chemrev.7b00661.
[157] M. Martin, D. Perez-Guaita, D.W. Andrew, J.S. Richards, B.R. Wood, P. Heraud, Detection and Quantification of Plasmodium falciparum in Aqueous Red Blood Cells by Attenuated Total Reflection Infrared Spectroscopy and Multivariate Data Analysis, J. Vis. Exp. (2018). https://doi.org/10.3791/56797.

Chapter 2

Experimental Theory and Data Analysis

2.1 Infrared Spectroscopy

2.1.1 Electromagnetic Spectrum

Spectroscopy is the study of the interaction between electromagnetic radiation and matter. Electromagnetic radiation involves photons travelling at the speed of light, producing oscillating electric and magnetic fields. The magnetic and electric vectors undulate in planes perpendicular to one another, and to the direction of the wave [1]. The oscillating waves go through cycles, as the motion of the resulting wave is repetitive (Figure 2.1).

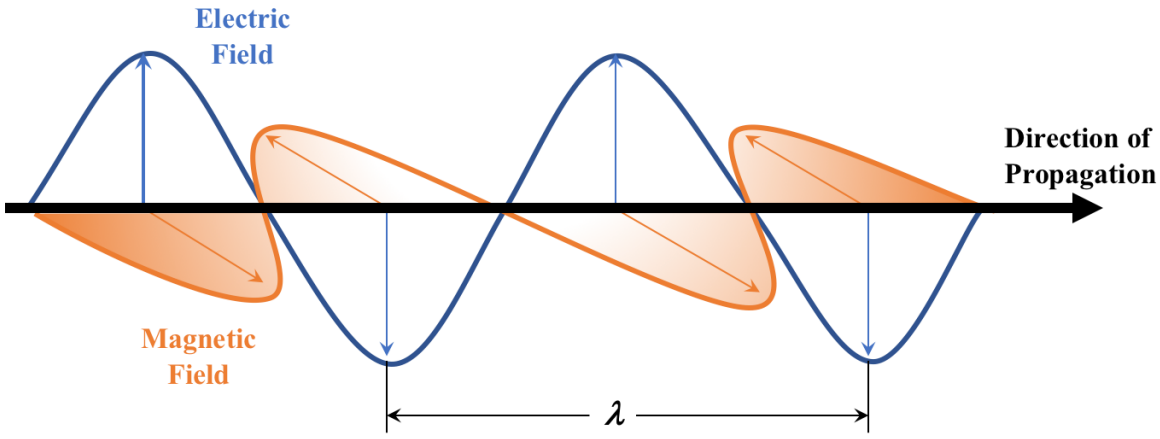

Figure 2.1 – Electromagnetic wave showing electric field oscillating perpendicular to the magnetic field, where λ represents wavelength. Adapted from ref [2].

The type of electromagnetic radiation varies depending on frequency and wavelength. The wavelength (λ) of a wave is the distance travelled during one complete cycle. For a photon moving at the speed of light c (2.998x10^8 m/s), wavelength is inversely proportional to frequency (ν), which is described as the number of cycles per unit time (Eq. 2.1) [3].

$$\nu = \frac{c}{\lambda} \tag{2.1}$$

An expansion of Planck's Law directly relates the energy of a photon E to the frequency and wavelength of the radiation (Eq. 2.2).

$$E = h\nu = \frac{hc}{\lambda} \tag{2.2}$$

where h is Planck's constant (h = 6.626 x 10^{-34} J·s).

The wavenumber ($\tilde{\nu}$) corresponds to the reciprocal wavelength (Eq. 2.3), which is defined as number of cycles per distance, with the units cm^{-1}.

$$\tilde{\nu} = \frac{1}{\lambda} \tag{2.3}$$

The electromagnetic spectrum defines the different types of radiation, ranging from low frequency radiowaves (long wavelength) to high frequency (short wavelength) cosmic rays (Figure 2.2) [4]. The area of interest for IR spectroscopy exists between the visible and microwave regions, ranging between wavelengths of ~780 nm – 1 mm, and can be broadly spilt into near- (~12820-4000 cm^{-1}), mid- (~4000-400 cm^{-1}) and far-IR (~400-33 cm^{-1}) sub-regions.

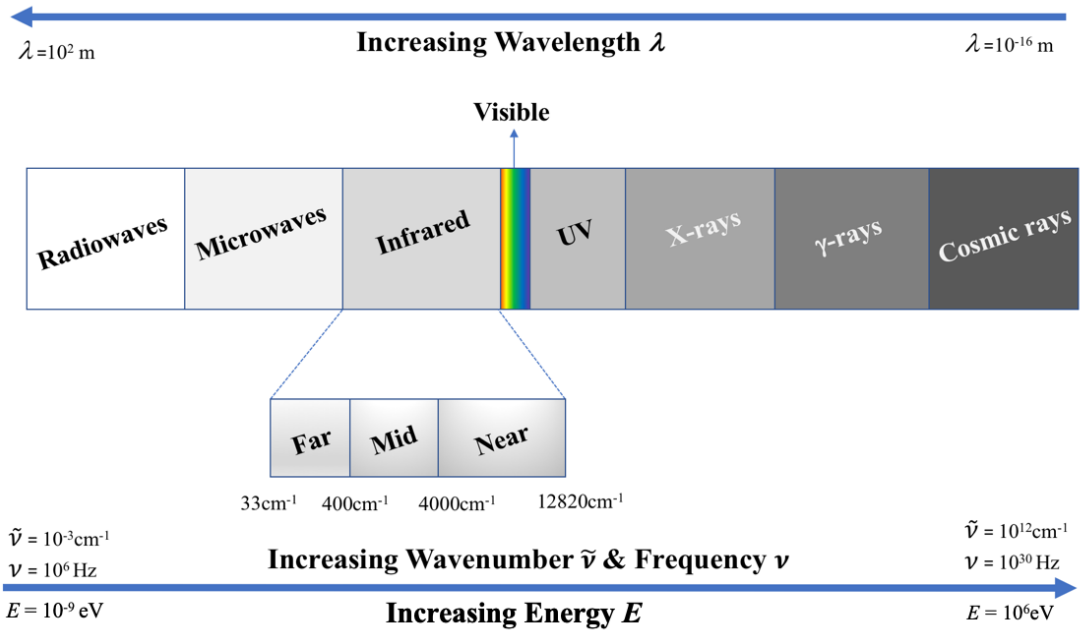

Figure 2.2 – Electromagnetic Spectrum with focus on the IR region.

IR spectroscopic methods are rapid and convenient for both qualitative and quantitative analysis [5]. Mid-IR and near-IR are the most widely used regions in IR spectroscopy, with mid-IR generally preferred for analytical investigations due to the abundance of molecules that absorb strongly within 4000-400 cm^{-1}. Determination of chemical structures is also easier in this spectral region, due to the clear absorption bands of organic functional groups and biomolecular components [6].

2.1.2 Molecular Transitions

The total energy of a molecule ΔE is described by the Born-Oppenheimer approximation as the combination of electronic ΔE_e, vibrational ΔE_v, rotational ΔE_r and translational ΔE_t energies (Eq. 2.4). The energy of electron transitions from ground state to excited state is discretely quantised. Vibrational energy relates to the specific atomic vibrations within a molecule. The molecular rotations around the axis

perpendicular to the inter-nuclear axis is related to rotational energy, and the translational energy is associated with movement of the molecule's centre of gravity [7].

$$\Delta E = \Delta E_e + \Delta E_v + \Delta E_r + \Delta E_t \qquad (2.4)$$

There are multiple rotational energy levels in within the vibrational energy states, and likewise, many vibrational energy levels within an electronic energy state. As a general rule $\Delta E_e > \Delta E_v > \Delta E_r$, therefore promoting an electron from the ground state to an excited state requires more energy than raising the vibrational state, which then requires more energy than raising a rotational energy state (Figure 2.3) [7].

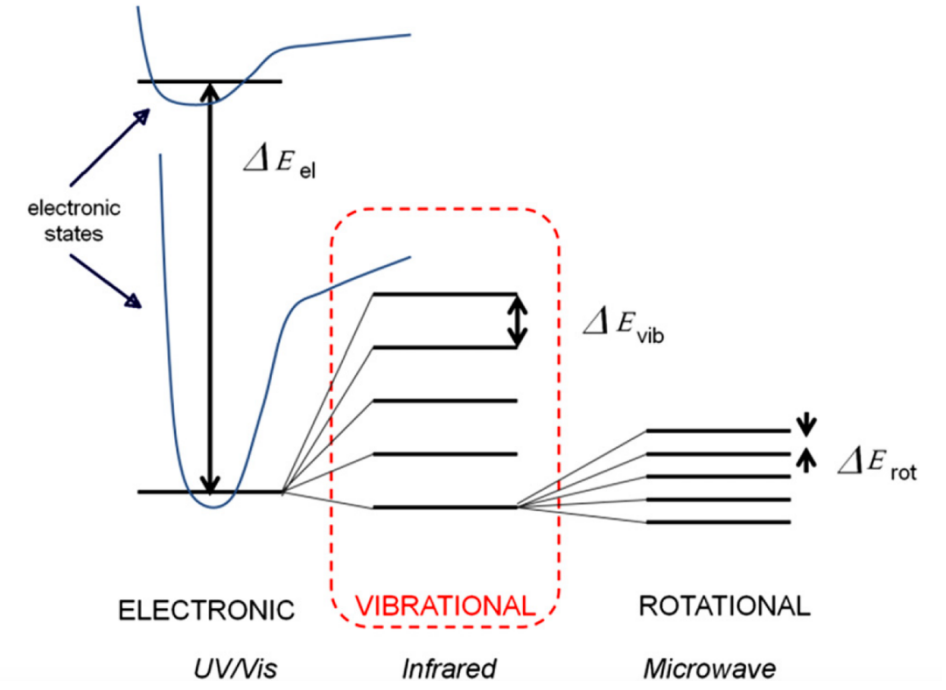

Figure 2.3 – Types of energy changes associated with molecular spectra. Duplicated from ref [7].

Ultraviolet, visible and x-ray radiation are all capable of electronic excitation, however the energy gap is too large for IR radiation. As shown in Figure 2.3, IR spectroscopy is concerned with vibrational energy levels [3]. The concept of infrared spectroscopy is based upon the vibration of chemical bonds when irradiated with polychromatic light. When molecules absorb this IR radiation, they can be promoted to an excited state, but only if there is a change in dipole moment μ during the vibration [8]. The fundamental transition is between the ground state and the first excited vibrational state ($\upsilon_0 \rightarrow 1$). Each vibrational mode involves harmonic displacements of the atoms from their equilibrium positions. When considering a simple diatomic molecule, Hooke's Law suggests the two masses are bound together by a spring. The harmonic oscillator obeys Hooke's Law (Eq. 2.5);

$$F = -kx \tag{2.5}$$

where *F* is the overall force, *k* is the force constant (stiffness of the spring) and *x* represents the displacement from equilibrium.

At any instant of oscillation, a mass m is accelerated at a rate $a = (d^2x/\,dt^2)$, and according to Newton's 2nd law of motion (force = mass x acceleration);

$$-kx = m(d^2x/\,dt^2) \tag{2.6}$$

By dividing by the mass;

$$(d^2x/\,dt^2) + \omega^2 x = 0 \tag{2.7}$$

where $\omega = \sqrt{\frac{k}{m}}$ and represents angular frequency. This is commonly related to frequency by;

$$\omega = 2\pi\nu \tag{2.8}$$

where ν is the frequency of the vibration. From this, we can determine the frequency of IR radiation required to successfully quantise a diatomic molecule, in order to promote it to a higher vibrational energy level (Eq. 2.9).

$$\nu = \frac{1}{2\pi}\sqrt{\frac{k}{\mu}} \tag{2.9}$$

where $\mu = \frac{m_1 m_2}{m_1 + m_2}$ and represents the reduced mass (m_1 and m_2 are the masses of the two atoms in the diatomic molecule).

Each molecule has a frequency that is characteristic of its atomic structure. The wavenumber position on an IR spectrum can be altered by a change to the masses of atoms and their bond strengths. As described in Eq. 2.9, molecules with smaller atoms will result in a lower reduced mass, causing vibrations at a higher frequency. Likewise, stronger bonds will mean a larger force is required to displace the atoms from equilibrium, also resulting in peaks at higher frequencies. For each mode of vibration *i*, all atoms in a given molecule will vibrate at a characteristic frequency ν_i, and Eq. 2.10 describes for those in which the atoms vibrate with simple harmonic

motion [9]. This equation is only fitting for extremely low values of v_i, and in reality, molecules vibrate with anharmonic (Morse) motion (Eq. 2.11) [7].

$$V_{iv} = h\nu_i \left(v_i + \frac{1}{2}\right) \tag{2.10}$$

where V_{iv} is the vibrational energy states, v_i is the vibrational quantum number of the *i*th mode and *h* is Planck's constant, and;

$$V_{iv} = h\nu_i \left(v_i + \frac{1}{2}\right) + h\nu_i x_i \left(v_i + \frac{1}{2}\right)^2 \tag{2.11}$$

where x_i is the anharmonicity constant.

The relationship between force and displacement for an anharmonic oscillator is non-linear and is dependent on the amplitude of the displacement and the energy levels, therefore differs to the equidistant harmonic oscillator (Figure 2.4). The harmonic energy levels are evenly spaced by *hv*, which means all transitions would occur at the same frequency. The harmonic oscillator does not predict bond dissociation, suggesting bonds would refrain from breaking no matter how much energy is introduced. The anharmonic potential includes the effects of bond breaking and accounts for the anharmonicity of real bonds. In this model, the energy level spacing decreases as the energy approaches the dissociation energy D_E , where D_0 is the true energy required for dissociation from the zero-point energy of the lowest vibrational level v_0 .

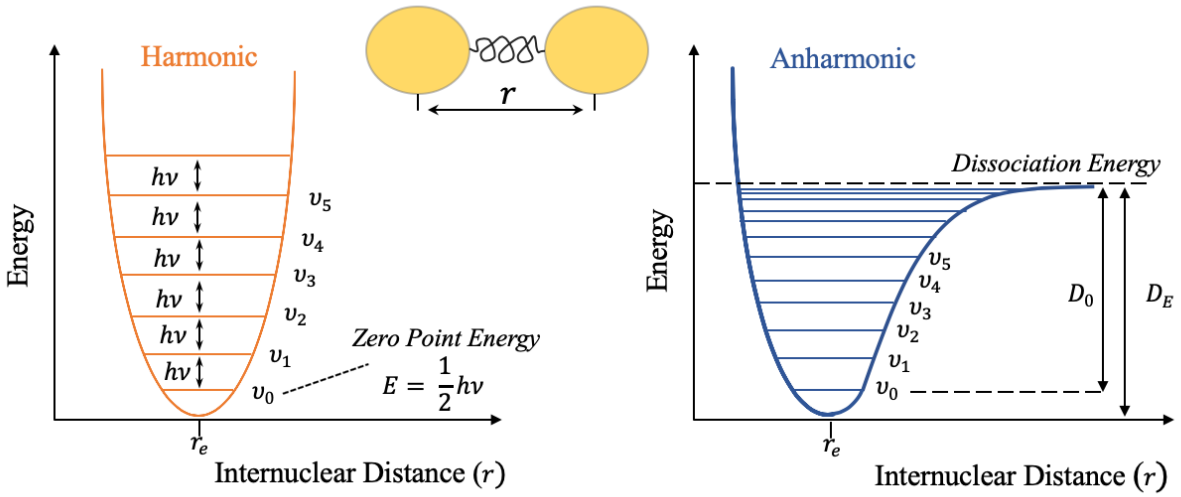

Figure 2.4 – Potential energy graphs for the harmonic (orange) and anharmonic (blue) oscillators. The horizontal lines represent the quantised vibrational energy levels.

Transitions involving $\Delta\upsilon > 1$ would not be allowed if the vibrational modes were strictly harmonic, therefore the fundamental transition would generally only be permitted, as per the selection rule $\Delta\upsilon \pm 1$. The anharmonicity relaxes this selection rule such that the promotion to higher vibrational energy levels becomes possible. This gives rise to overtone bands, which are multiples of the fundamental absorption frequency. The first overtone band ($\upsilon_0 \rightarrow \upsilon_2$) will appear at twice the wavenumber of the fundamental in the spectrum, as it would require twice the amount of excitation energy. The band intensity will become progressively weaker as the overtone number increases ($\upsilon_0 \rightarrow \upsilon_3, \upsilon_4$ ...). When two fundamental bands absorb at the same wavenumber, combination bands are often observed [8]. Hot bands have also been found where high temperatures can further excite molecules that have already been promoted to a higher energy level ($\upsilon_1 \rightarrow \upsilon_2$). In the harmonic oscillator model the hot bands are not easily distinguishable due to the equidistant energy

levels, but since the spacing in the anharmonic oscillator becomes smaller with increasing vibrational states, the hot bands occur at lower frequencies than the fundamental bands [10]. Fermi resonances can appear whenever a fundamental vibrational level lies closely to an overtone. Quantum mechanical mixing causes shifting of the intensities and energies of both the fundamental and overtone bands which results in two relatively strong bands in the form of a doublet [11].

2.1.3 Vibrational Modes

The number of vibrational modes for a given molecule will depend on its structure. For a molecule with *N* number of atoms, it will have *3N* degrees of freedom. As a general rule, non-linear molecules will exhibit *3N-6* vibrational modes, corresponding to three translational and three rotational modes around the *x, y* and *z* axes. That said, some molecules that have symmetrical elements may be IR inactive, as some vibrational modes will be degenerate, i.e. homonuclear diatomic molecules. In contrast, a linear molecule is unable to rotate upon its axis, so one of the rotational degrees of freedom is lost thus e can be described as having *3N-5* vibrational modes [12].

Bond stretching and bending are the two fundamental types of molecular vibration. There can be either symmetric or asymmetric stretching which alters the bond length, while bending vibrations consist of changing the bond angle by twisting, rocking, wagging and scissoring (Figure 2.5).

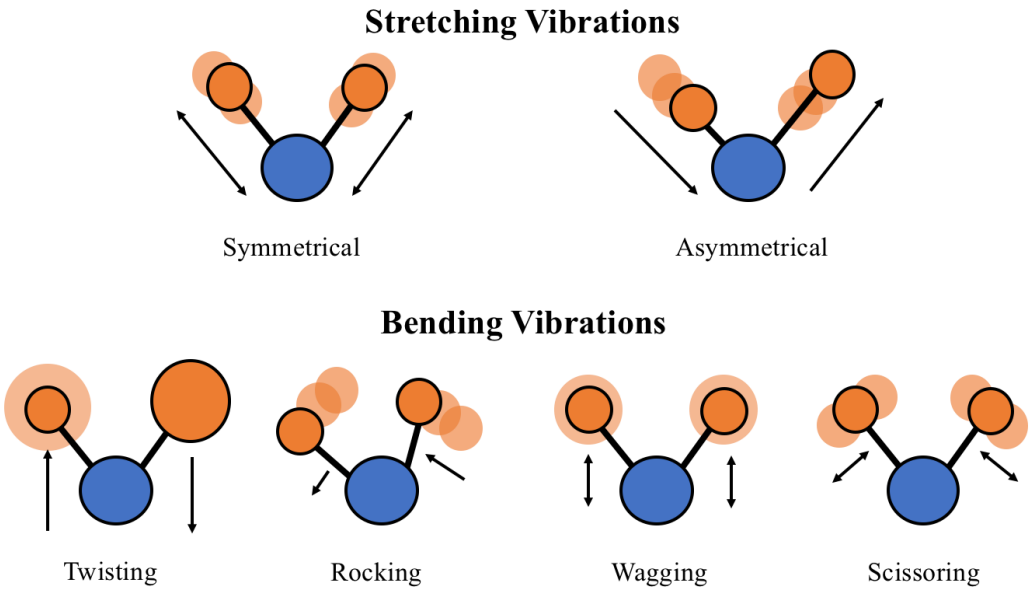

Figure 2.5 – Common vibrational modes of chemical bonds.

When these bond vibrations occur, there is a consequent alteration to the energy of the incident photon. The incident light can be transmitted, reflected, absorbed, or scattered when it comes into contact with the sample [13]. The fundamental principle of IR spectroscopy obeys the Beer-Lambert law, which relates the absorbance with the intensity of the incident radiation I_0 and the amount of light that passes through the sample I (Eq. 2.12).

$$A = \varepsilon c l = log\left(\frac{I_0}{I}\right) \tag{2.12}$$

The absorbed IR light A is also directly proportional to the concentration of a given sample c, the molar absorptivity ε and pathlength l. Hence, the concentration of biomolecules can be found by the absorbance at a single wavelength. IR spectroscopy therefore can quantify the levels of biomolecules, as the proportion of light absorbed by the sample correlates with the concentration of molecules present within that sample [9].

2.2 Fourier-Transform Infrared Spectroscopy

2.2.1 FTIR Instrumentation

Dispersive infrared instruments were traditionally used in the 1940s, although more recently Fourier-transform infrared (FTIR) spectrometers have become more commonly employed, due to their superior speed and sensitivity [5]. FTIR spectroscopy utilises a Michelson interferometer, which is based on the concept that when there is an interference of radiation between two beams, then there will be a change in pathlength producing signals that result in an interferogram [8]. The spectrum obtained is a function of time, which is then converted to the frequency domain through Fourier transformation. Standard benchtop FTIR spectrometers are comprised of a light source, a Michelson interferometer and a detector.

2.2.1.1 Light sources

The most common mid-IR light source found in traditional benchtop instruments is a resistively heated silicon carbide rod, known as a globar or thermal IR source, which behaves like a black body source where radiance is dependent on temperature [9]. More recently there has been the implementation of superior alternatives, such as quantum cascade lasers (QCL), that are capable of providing high intensity light and acquiring spectra over discrete frequencies resulting in a greater signal-to-noise ratio (SNR) [14,15]. Unlike typical inter-band semiconductor lasers – that emit electromagnetic radiation through the recombination of electron-hole pairs across the material band gap – the emission in QCLs is achieved through the use of inter-sub-band transitions [16]. QCL-based instruments provide a coherent and polarized light source that emit photons of narrow line widths, with increased spectral power

densities compared to globar sources [17]. Thus, the discrete frequency approach in QCL instruments may reduce long acquisitions times by allowing more selective sampling, particularly in FTIR imaging experiments [18].

2.2.1.2 Synchrotron at Diamond Light Source

Synchrotron light sources can further improve the spectral quality and spatial resolution. Synchrotrons are electron storage rings that use magnetic fields to bend electrons into a closed orbit, which in turn generates IR radiation up to 10^3 times brighter than conventional IR sources [19]. For globar sources the SNR is often limited due to their low intrinsic brightness, but with the superior flux of the synchrotron radiation recent studies have been able to achieve spatial resolution in the nanoscale [20,21]. Globally, there are various synchrotron facilities available for research proposals – Diamond Light Source at the Rutherford Appleton Laboratory, Oxford, is the only facility based in the UK. Figure 2.6 describes the layout of the Diamond Light Source synchrotron, which essentially acts as an electron accelerator [22].

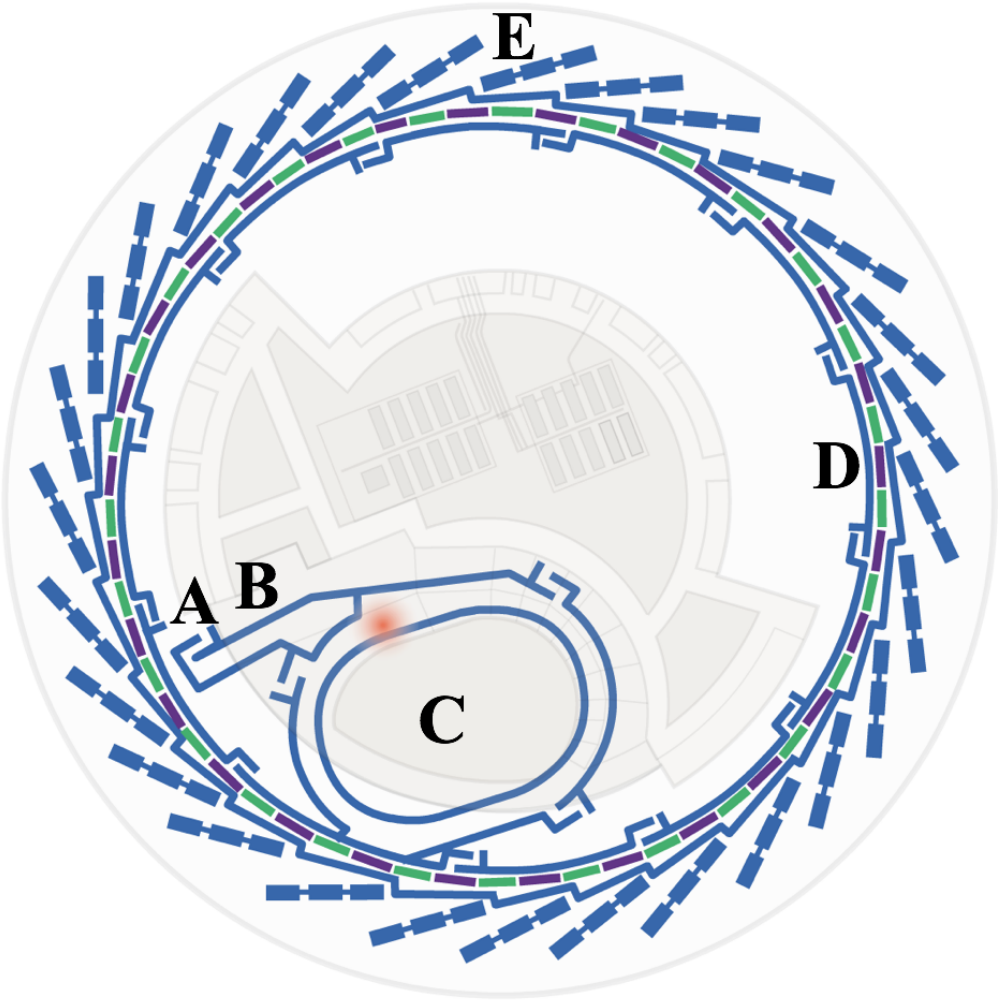

Figure 2.6 – Schematic of the Synchrotron facility at Diamond Light Source, UK. A: Electron Gun; B: Linac; C: Booster Synchrotron; D: Storage Ring; E: Beamline. Sourced from ref [22].

The electrons are generated through thermoionic emission in the electron gun (A), then fired through three particle accelerators up to extremely high speeds. Firstly, they move through a linear accelerator, or linac (B), into the booster synchrotron (C), which both work to accelerate the electrons until they are travelling at the speed of light. From there they enter the large storage ring (D), where magnetism is used to steer the electrons around the ring, causing them to lose energy in the form of light. This light in finally channelled out into the experimental stations, called beamlines

(E), and is emitted at a range of wavelengths across the electromagnetic spectrum, hence is applicable for IR studies.

2.2.1.3 Michelson Interferometer

The Michelson interferometer is a device that splits a single beam of light into two paths, and then recombines them after a path difference has been introduced. In general, the interferometers are composed of a fixed mirror, a movable mirror and a beam splitter (Figure 2.7). The purpose of the beam splitter is to reflect some of the radiation toward the fixed mirror, meanwhile partially transmitting the rest to the adjustable mirror. When the waves return to the beam splitter, they interact and are then further reflected and transmitted. The moving mirror causes the split beams to travel different pathlengths, thus have altered intensity of beams when recombined [23]. The waves can have either constructive or destructive interference. Constructive interference occurs when two waves of the same frequency line up and the amplitude of the resultant wave is the summation of the two, whereas destructive interference is when the waves are out of phase - one wave's crests will coincide with the other wave's troughs - and essentially cancel each other out resulting in an amplitude of zero [9]. The output of this relationship is the interferogram - a measurement of the intensity as a function of distance and time. Fourier-transformation of the interferogram produces a standard IR spectrum, that is a function of frequency against spectral absorbance intensity [24].

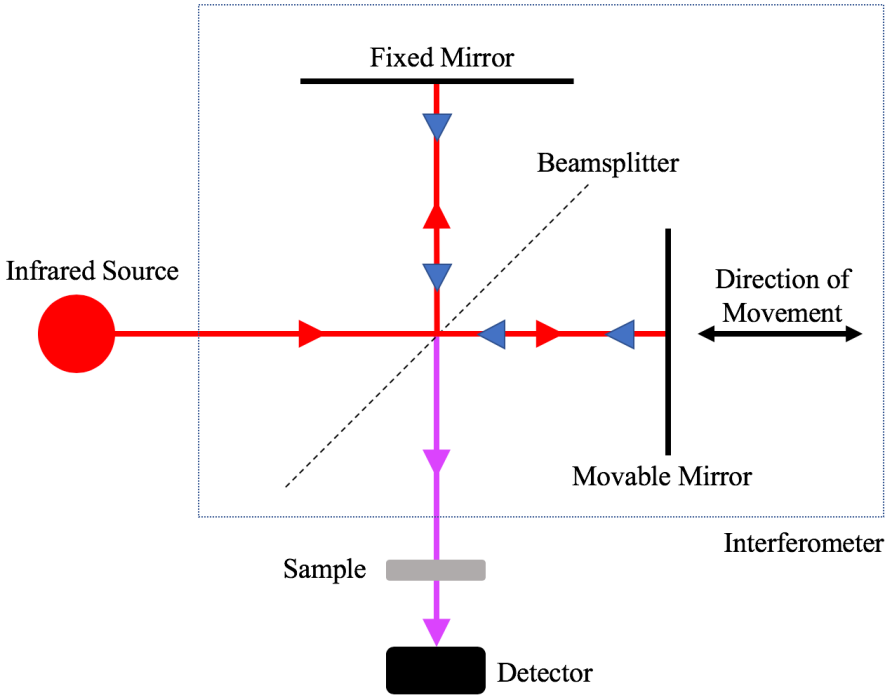

Figure 2.7 – Michelson interferometer consisting of a fixed mirror (F), movable mirror (M) and beam splitter (dashed line). Adapted from ref [9].

2.2.1.4 Detectors

There are various different detectors used in benchtop instruments, all of which will be either thermal or quantum detectors. The function of the detector is to transduce the light intensity into electrical signal [9]. Deuterated triglycine sulphate (DTGS) detectors are thermal detectors which are commonly used in laboratory benchtop spectrometers. A change in intensity of the IR radiation that strikes the detector causes a change in temperature, which in turn causes a change in dielectric constant, and hence its capacitance [25]. Quantum detectors seem to be the preferred choice for obtaining better spectral quality - mercury cadmium telluride (MCT) detectors typically have up to 50 times greater sensitivity than DTGS detectors. The MCT is a semiconductor, and the electrons present are promoted from the valence band to the

conduction band when they absorb IR light. These electrons generate electrical current proportional to the IR intensity. MCT detectors can provide spectra with much higher SNR, but they are unable to operate at room temperature and need to be cooled with liquid nitrogen [26].

Single element detectors, where individual point spectra can be obtained across a whole sample, can be practical when analysing substances like biofluids. Point spectra often have high SNR which can result in high quality spectral acquisition. Sample maps can be obtained using step-wise point spectra, but this can become rather time consuming when analysing a large sample area. The development of array detectors has allowed simultaneous measurements of spectra from defined points across a sample, which can improve acquisition times [14]. Focal plane array (FPA) and linear array detectors are commonly used for IR imaging techniques, which can provide high spatial-resolution images of the target area [27]. The multiple detector elements of the FPA detector enable the concurrent acquisition of several spectra at each spatial point of the area of the sample under investigation, allowing the examination of larger areas at reasonable experimental time periods [28]. This method can generate a ‘hypercube’ containing information in two spatial dimensions; a pseudo-image and a spectral dimension corresponding to the spectrum for each pixel of that image [27].

2.2.3 Background Spectrum

In order to correct for atmospheric conditions, it is standard procedure to collect a background spectrum before sample analysis. Absorbance sample spectra are susceptible atmospheric gases such as water vapour and carbon dioxide, thus absorptions of IR energy by the gases can result in unwanted bands, obscuring the important sample peaks in the process. Obtaining the background spectrum prior to sample analysis removes all environmental influences, allowing more accurate collection of the biological and chemical information of the sample.

2.2.4 Spectral Signals of Biomolecules

FTIR spectroscopy monitors the vibrational bending and stretching modes of molecules that are active within the infrared region. The wavelengths at which they absorb the IR radiation are measured, and as every compound has a characteristic set of absorption bands, it results in a unique spectroscopic fingerprint [29]. The frequencies of biological bond vibrations exist in the mid-IR region, meaning it is well suited for biomedical studies. In recent years, biomedical spectroscopy has become a rapidly expanding research area; the technique is quick, simple and reproducible, and only tiny quantities of sample are generally required for analysis. Lipids, proteins, nucleic acids and carbohydrates are the four biomolecular groups characteristically found in a biological spectrum (Figure 2.8). The most important spectral region in relation to disease diagnostics is the fingerprint region (1800-1000 cm^{-1}), which contains the valuable Amide I and II peaks (1700-1500 cm^{-1}) [27]. Stretching vibrations are found in the higher-wavenumber region (3500-2500 cm^{-1}),

such as CH, NH and OH stretches, whereas bending and carbon skeleton fingerprint vibrations tend to occur in the lower-wavenumber regions. The wealth of information that exists in a vibrational spectrum of a biological sample, detailed in Table 2.1, renders the technique as an interesting tool for investigating molecular systems ranging from amino acids, nucleic material, peptides and protein complexes [30–33]. Vibrational spectroscopy can enhance the understanding of protein function, as it is sensitive to changes to the protonation state of amino acid side chains and the strength of hydrogen bonding between amide bonds [34,35].

In typical biological IR spectra, most characteristic bands are associated with the CONH group, referred to as Amide A (NH stretching, ~3300 cm^{-1}), Amide B (NH stretching, ~3100 cm^{-1}) and Amide I to III (I: 1600-1700 cm^{-1}, II: 1480-1580 cm^{-1}, III: 1230-1300 cm^{-1}) as described in Figure 2.9 [36]. The Amide A band (~3300 cm^{-1}) originates from the NH stretching vibration, and often exists as a resonance doublet with the weakly absorbing Amide B (~3170 cm^{-1}), arising from a Fermi resonance between the first overtone of Amide II [36]. The Amide I, which absorbs near 1650 cm^{-1}, is primarily caused by the C=O stretching vibrations, with smaller contributions from CN stretching, deformation of CCN and NH in-plane bending vibrations. The out-of-phase combination of the NH bending and the CN stretching vibrations, as well as minor contributions from the CO in-plane bend and the CC and NC stretching vibrations, give rise to the Amide II band at ~1550 cm^{-1} [40].

Table 2.1 - Tentative peak assignments for FTIR spectral data of biological samples as described in the literature [36–39].

Approximate Wavenumbers (cm^{-1})	**Vibration**	**Biochemical Assignments**
3300	ν(N-H)	Amide A of proteins/peptides
3100	ν(N-H)	Amide B of proteins/peptides
2957	$\nu_{as}(CH_3)$	Lipids
2920	$\nu_{as}(CH_2)$	
2872	$\nu_{s}(CH_2)$	
2850	$\nu_{s}(CH_2)$	
1740	ν(C=O)	Phospholipid esters
1715-1680	ν(C=O)	Nucleic acids
1650	>75%ν(C=O), ν(C-N), δ(N-H)	Amide I of proteins
1645	γ(HOH)	Water
1550	~60% δ(N-H), ν(C-N), δ(C-O), ν(C-C)	Amide II of proteins
1453	$\gamma(CH_2)$	CH_2 Scissoring
1450	$\delta_{as}(CH_3)$	Lipid/Proteins
1395	$\delta_{s}(CH_3)$	Lipid/Proteins Carboxylate COO^-
1395	ν(C=O)	
1380	$\gamma_{s}(CH_3)$	Phospholipid/triglyceride
1350-1250	δ(N-H), ν(C-N), γ(C=O), ν(C-C),	Amide III – peptide/protein/collagen
1242	$\nu_{as}(PO_2^-)$	DNA/RNA/phospholipid
1170	ν_{as}(C-O)	Ester
1150	ν(C-O), γ(COH)	Carbohydrates
1090	$\nu_{s}(PO_2^-)$	DNA/RNA/phospholipid
1086	ν(C-O), ν(C-C), def(CHO)	Carbohydrates
1079	ν(C-C)	Glycogen
1065	ν(C-O)	DNA and RNA ribose
1050	ν(C-O)	Phosphate ester
1028	def(CHO)	Glycogen
965	$\nu(PO_3^{2-})$	DNA and RNA Ribose
710-620	def(O=C-N)	Amide IV

ν = stretching; δ = bending; γ = wagging, twisting and rocking; def = deformation; as = asymmetric; s = symmetric

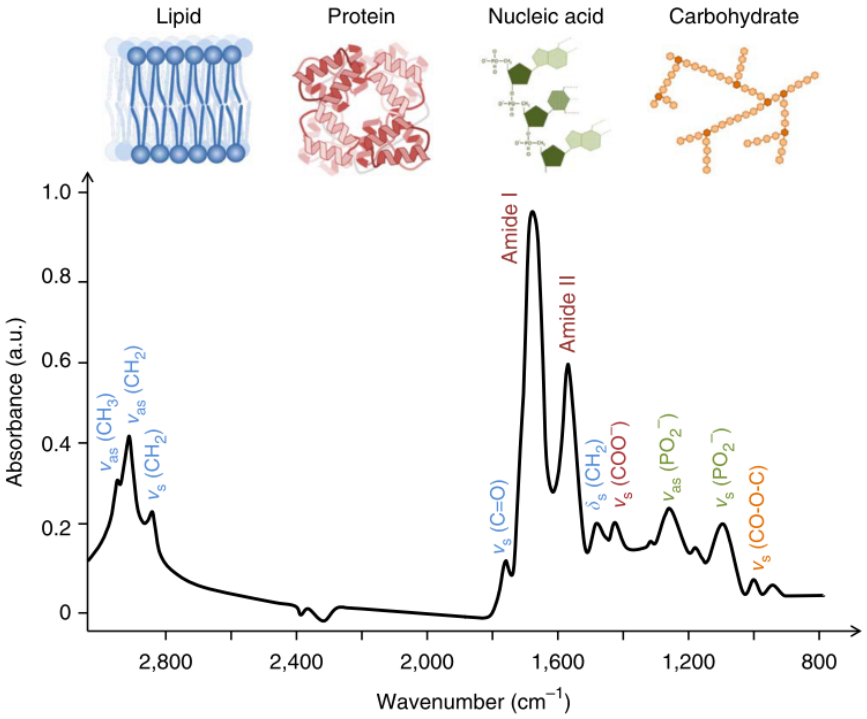

Figure 2.8 – A typical IR spectrum for a biological sample with peak assignments. Replicated from ref [27].

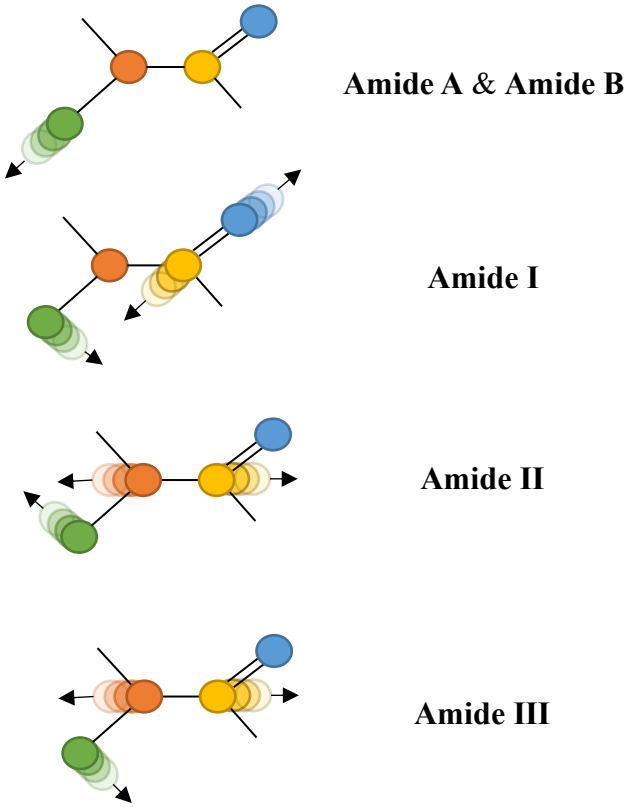

Figure 2.9 - Molecular vibrations of the Amide group - Green: Hydrogen, Orange: Nitrogen, Yellow: Carbon, Blue: Oxygen. Adapted from ref [41].

2.3 Sampling Modes

There are three main sampling modes involved in FTIR spectroscopy; transmission, transflection and attenuated total reflection (ATR). Historically FTIR instruments used transmission mode, where IR light is irradiated through samples that have been prepared on IR transparent windows, i.e. calcium fluoride (CaF_2), and is collected at a detector at the other side [27]. There are a number of flaws related to transmission mode. Sample preparation can be exhaustive, and short pathlengths (≤10 μm) are required to prevent full absorption of the IR radiation by the sample before reaching the detector. This limiting factor also affects aqueous samples, since water is highly IR active [42]. Furthermore, IR transparent substrates that are required for this technique are fragile and often rather expensive to replace [43].

In transflection mode, the incident IR beam travels through a sample initially, but differs to transmission mode in that the light is then redirected off an IR reflecting substrate back through the sample toward the detector. The substrates are generally inexpensive low emissivity (low *e*) slides, and the approximate sample thickness can usually be smaller than that required for transmission measurements (1-4 μm c.f. 2-10 μm) which can be beneficial when sample quantity is limited. On the other hand, as the pathlength is effectively doubled there is also a maximum thickness limitation. Transflection mode may also be prone to standing wave artefacts that cause spectral variance, although the implications of this effect for diagnostic applications are still being assessed [27,44,45].

In assessing the suitability of the measurement mode for analysis of biological samples which are highly physically and chemically inhomogeneous, it is important to recognise the physical processes involved. When a sample is measured in reflection, or transflection, a proportion of the light registered derives from the top surface, the reflectance of which is governed by the real component of the refractive index of the material. The transmitted light, measured in transmission or transflectance, can be reduced by the intrinsic absorptions of the constituent molecules, giving rise to the desired fingerprint of the sample. However, it can also be reduced by "Mie-like" scattering from structures (cells and cell nuclei) which have dimensions similar to the wavelength of light employed (5-20 μm). This scattering is resonantly enhanced in the neighbourhood of an absorption, and can give rise to spectral artefacts in transflection and transmission modes [46,47]. These resonant Mie effects can be ameliorated by application of specific pre-processing methods [48].

Adaptations to these standard FTIR spectroscopy methods have further developed the technique in the biomedical field. The addition of a microscope for instance has allowed the focusing of IR light on microscopic sample areas, providing high spatial resolution data [38,49]. As already mentioned, the use of alternative light sources, such as broadband radiation with high flux density from a synchrotron source or QCL that can provide rapid discrete frequency sampling, can also provide greater sensitivity when measuring biological samples [14,20]. The development of imaging technologies, largely based upon the detector capabilities in the spectrometers, have also allowed greater flexibility in spectral acquisition [19].

2.3.1 Attenuated Total Reflection

The development of attenuated total reflection-Fourier transform infrared (ATR-FTIR) spectroscopy has attracted wide interest in recent years. The technique is unique in that the incident IR beam does not physically travel through the sample. The IR light is directed through a substrate with a high refractive index – such as diamond – known as an internal reflection element (IRE). The sample must be placed in direct contact with the IRE, as when the incident radiation reflects off the internal surface of the IRE, an evanescent wave projects orthogonally into the sample, which then attenuates the IR beam before exiting the IRE to the detector (Figure 2.10) [42]. Intimate sample-IRE contact must be achieved in order to gain a high resolution spectrum, as the evanescent wave only extends a few microns (0.5-5 μm) beyond the IRE surface [50].

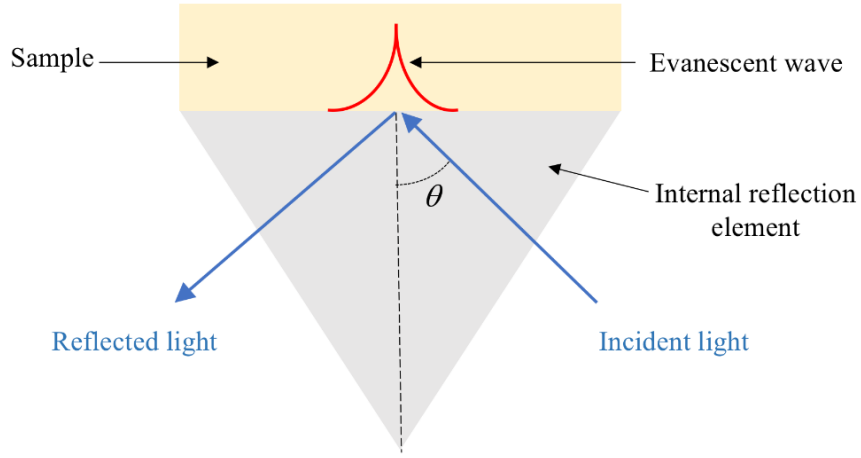

Figure 2.10 – Schematic representation of the ATR sampling mode through a traditional diamond crystal, where θ represents the angle of incidence.

The refractive index of the chosen IRE and sample govern the basic ATR phenomenon (Eq. 2.13).

$$\theta_c = \sin^{-1}\left(\frac{n_2}{n_1}\right) \quad (2.13)$$

where θ_c is the critical angle and n_1 and n_2 are the refractive indices of the IRE and sample, respectively.

The IR radiation undergoes total internal reflection when the angle of incidence at the sample-crystal interface is greater than the critical angle, hence materials with a high refractive index are commonly chosen to minimise the critical angle [8]. Another important factor is the depth of penetration d_p of the evanescent wave into the sample as it determines how much of the sample is actually analysed - d_p can be defined as the distance required for the electric field amplitude to decay into the sample by 1/e (Eq. 2.14) [9].

$$d_p = \frac{\lambda}{2\pi n_1 \sqrt{sin^2\theta - (n_2/n_1)^2}} \quad (2.14)$$

where θ is the angle of incidence.

In contrast to transmission mode, the ATR-FTIR approach negates the need for time consuming preparation as the sample can be examined directly on to the IRE, in liquid, semi-solid or solid form [50]. However, the ATR IRE must be kept clean to ensure there's no cross-contamination between samples, and traditional IREs are rather expensive, e.g. a diamond IRE crystal. Scratches on the surface of the IRE are known to affect the sample-IRE contact, and loss of sensitivity is common due to shallow penetration depths [1]. That said, the shorter pathlength makes it more

applicable for aqueous samples, as there is less IR radiation lost through water absorbance compared to transmission measurements [42]. Likewise, the lack of scattering effects and high SNR are valuable attributes [27].

Biological samples, such as human blood serum, are well suited to ATR analysis. Only tiny amounts of biofluid drops are required to dry efficiently onto the IRE. This has the advantage of ensuring intimate contact occurs between the sample and the IRE – allowing effective penetration of the evanescent wave – meanwhile curtailing the spectral interference of water [51]. ATR-FTIR has been shown to be a promising tool for disease diagnostics [52–55], but efficient clinical translation has been inhibited by issues such as long drying times and cleaning the diamond crystal between samples. However, it has recently been suggested that a high-throughput ATR accessory, comprising a multi-sample IRE could assist with translation into a clinical environment [56].

2.3.2 Silicon Internal Reflection Element

As the IRE material can impact the penetration depth of the evanescent wave, it is important to select a material that's best suited to the desired experimental protocol. The most common IREs used for ATR studies are those composed of diamond, zinc selenide (ZnSe) and germanium (Ge), each of which have different optical properties (Table 2.2) [57]. Diamond is the gold standard – it is chemically inert and extremely robust making it the ideal crystal material. However, diamond is the most expensive, so high-throughput analysis is not feasible. ZnSe is a cheaper alternative to diamond and can be preferred for liquid and gel-like analysis, but it can only be used for

materials with a pH between 5-9. Ge has the highest refractive index, hence is used for highly absorbing samples due to its low d_p.

Table 2.2 – Common internal reflection element materials and their properties [57].

Material	**Spectral Region (cm^{-1})**	**Refractive Index**	**d_p at 45°, 1000cm^{-1} (μm)**	**Hardness (Knoop)**
Diamond	45,000-10	2.40	1.66	9,000
ZnSe	20,000-500	2.43	1.54	130
Ge	5,000-600	4.01	0.65	550
Si	10,000-100	3.42	0.81	11,150

Another material with similar properties is silicon (Si), which is relatively low-cost in comparison to its competitors. Si is non-toxic, robust, chemically stable, and its transparency to IR light makes silicon (Si) an ideal material for novel low cost IREs [58]. For most IR studies, silicon IREs (SIREs) are not usually favoured due to Si lattice vibrations presenting within the biologically relevant fingerprint region, obscuring information below 1500 cm^{-1} [59]. Typical multi-reflection SIREs (Figure 2.11a) lose absorbance signal due to the long pathlength through the IRE. However, similar to the phenomena of ATR-FTIR spectroscopy overcoming water absorption, by reducing the pathlength of the IR beam through the SIRE the contributions of the Si lattice vibrations can be minimised. Microfabricated SIREs can allow single-bounce internal reflections (Figure 2.11b), which effectively minimises the IR beam pathlength (< 3 mm), meaning the IRE absorbs less IR light thus circumventing unwanted spectral contributions from Si [60].

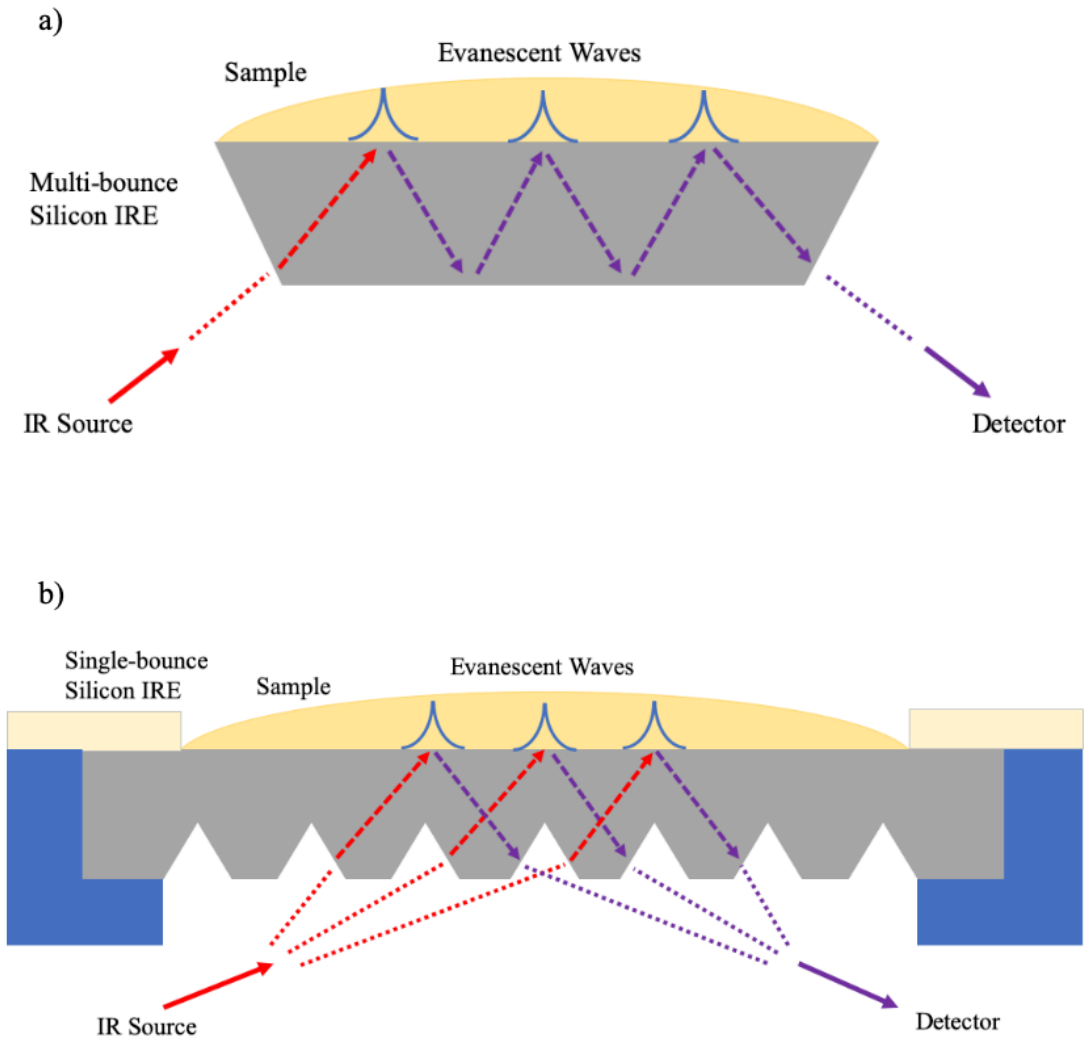

Figure 2.11 – Schematic representation of the ATR sampling mode through a) a multi-reflection silicon IRE and b) a microfabricated silicon IRE utilising v-shaped grooves for single bounce internal reflection.

Anisotropic etching of Si <100> wafers enables the production of the characteristic 'v-shaped grooves' displayed in Figure 2.11b. Following the deposition of a SiO_2 protective layer and application of a light-sensitive photoresist material, the desired design is etched into the Si. Recent developments in technology have seen ClinSpec Diagnostics Ltd. (ClinSpec Dx) introduce cheap and disposable SIRE optical sample slides that allow the rapid preparation and analysis of multiple samples, enabling

high-throughput ATR-FTIR spectroscopy optimised for clinical research. Based upon the design of a microscope slide, these optical sample slides contain four sample analysis areas; one for background measurements and three for repeat measurements of a single patient (Figure 2.12a). The SIRE is mounted on a polylactic acid (PLA) holder, and the ClinSpec Dx slide indexing unit (SIU) has been designed to allow the sample to traverse across the ATR-FTIR accessory to sit directly upon the sampling aperture (Figure 2.12b). This interfaces the slides with commercial spectrometers, as illustrated in Figure 12c, which is the typical set up of the instrument used for this project (Chapters 3 and 4): Spectrum 2 FTIR spectrometer (Perkin Elmer, USA) coupled with a Quest ATR accessory (Specac, UK).

These novel designs negate the time-consuming drying step and laborious fixed IRE cleaning, meaning patient samples can be batch processed and allow high-throughput measurements. Meanwhile, the batch processing capability permits more controlled drying conditions, guiding the complex dynamics of serum dehydration [61]. These developments have the potential to pave the way for clinical utilisation. A reliable blood test in a primary care setting would effectively prioritise patients for urgent brain imaging, ultimately reducing the time-to-diagnosis. Thus, the ATR-FTIR spectroscopy test would fit seamlessly into standard blood analysis (Figure 2.13).

a)

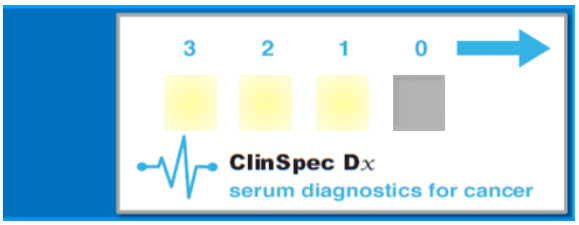

b)

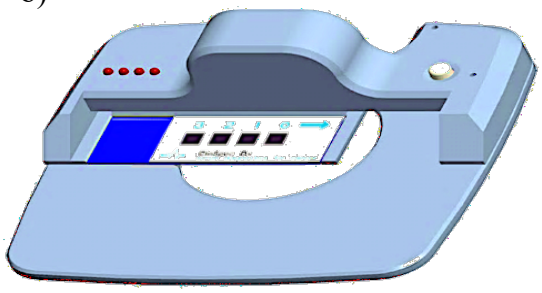

c)

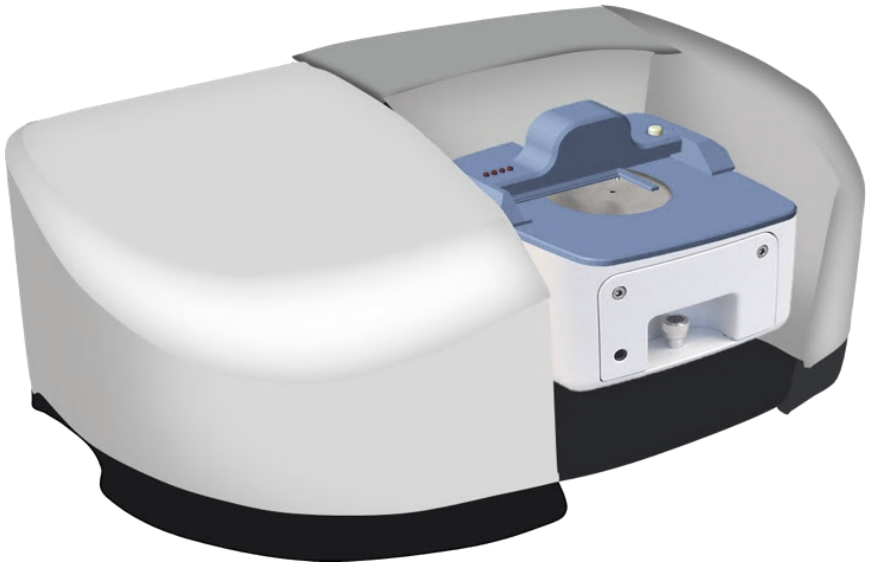

Figure 2.12 – Schematic examples of; a) a ClinSpec Dx optical sample slide with well 0 blank for background collection and 3 sample wells filled with patient serum, b) the slide indexing unit that automates the movement of the slide, and c) the typical set up of the accessory on a Perkin Elmer Spectrum 2 FTIR spectrometer.

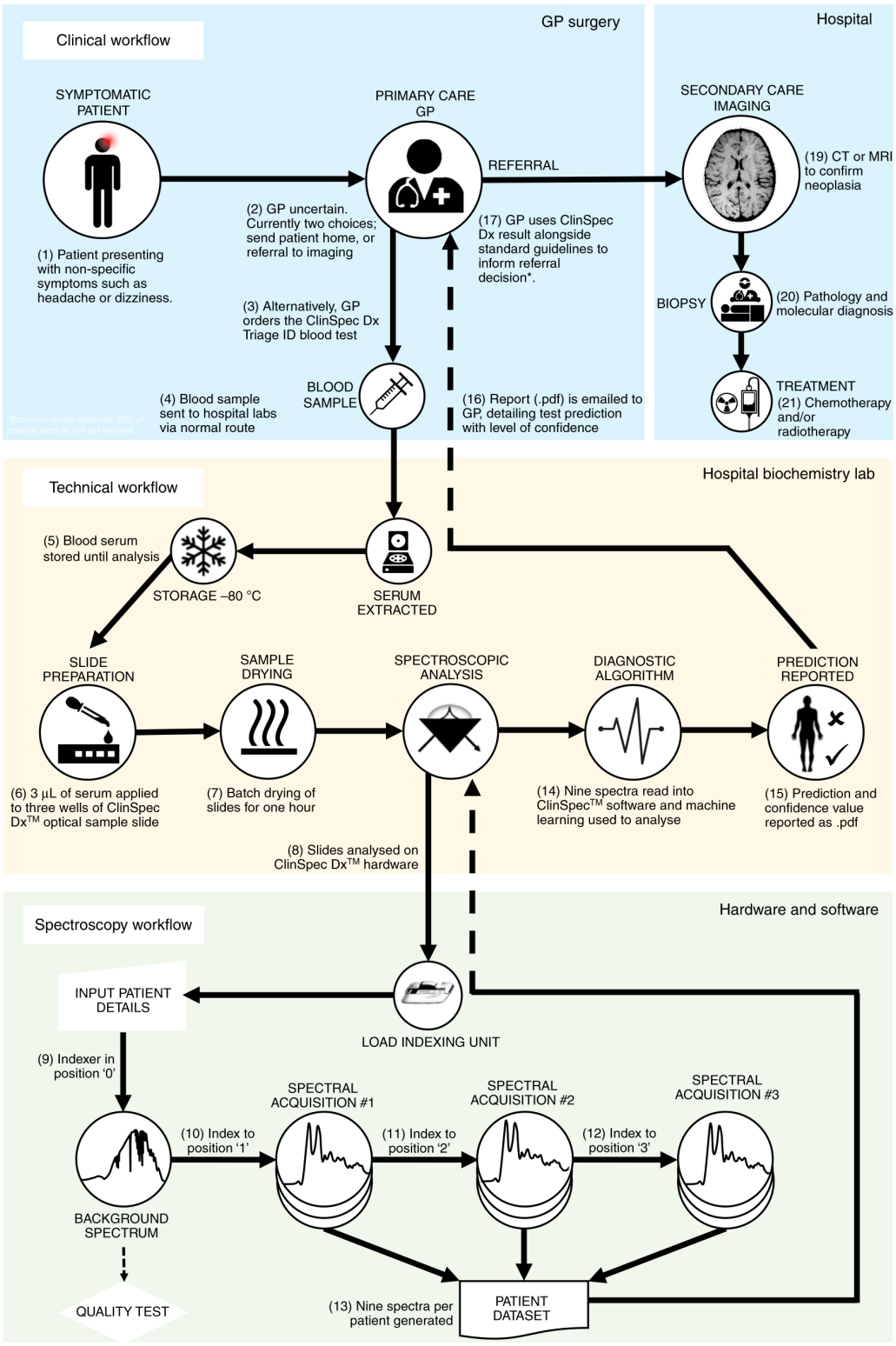

Figure 2.13 - Proposed integration of a blood test for the triage of brain cancer. Replicated from ref [62].

2.4 Spectral Pre-processing

An IR spectrum acts as a biochemical fingerprint which can allow minute differences between samples to be identified. Factors such as atmospheric background and noise can obscure the true representation of the analysed sample. Hence, it is important to try to minimise these unwanted features, and spectral pre-processing aims to ensure any information taken from the data comes purely from the sample. In short, the main goals of pre-processing are to improve the robustness and accuracy of the data, make it more easily interpretable, remove outliers and irrelevant information [63]. This section describes some of the steps required to prepare the raw data for classification.

Initially, spectral ranges can be cut to reduce variables and the size of the data set. For the analysis of biofluids, it is common to cut the spectra to the biologically relevant 'fingerprint region' which exists between 1800-1000 cm^{-1}. This region is often where the vibrations of the biomolecules of interest tend to occur and is known to be rich disease-specific information [27].

2.4.1 Baseline Correction

The incident beam of IR light can be scattered upon interaction with the sample, either at the same frequency, referred to as elastic scattering, or at a different frequency, known as inelastic scattering [64]. As IR spectroscopy is based on the absorbance of light by a sample, any scatter can impact the resulting spectrum, and can give rise to an offset or sloping baseline. This can often mean that the start and

the end point of the spectrum are at different absorption intensities, oscillating between positive and negative values. This makes it difficult to accurately compare absorbance values, as the baseline could introduce discrepancies between spectra. Likewise, the replicates of the same sample can seem different due to baseline variances, when - in theory - they should be identical.

Baseline correction tends to be the first step in spectral pre-processing. There are various correction algorithms that can be applied, but for this project the two main approaches that have been used are rubberband correction and extended multiplicative signal correction (EMSC). The rubberband correction works by dividing the spectra into *n* ranges. The lowest points in every range act as baseline points which are connected linearly. All the points in the spectrum are then 'pulled' down by the difference between the lowest point in the current range, and the lowest point on the baseline [65]. The EMSC algorithm is capable of removing oscillating baselines [66]. These are often found as a consequence of Mie scattering, which is a form of elastic scattering concerning homogeneous spherical particles that exist at the same physical dimensions as the wavelength of incident light [48].

2.4.2 Spectral Derivatives

Derivatising the spectra can eradicate baseline drifts and deconvolute the spectrum. Derivatives are obtained by differentiating the spectral intensity with respect to wavelength, and narrows the full width half maximum of bandwidths. Both first and second derivatives are used in research, with second derivatives often preferred due to easier interpretation. The first-order derivative of an absorption peak may be

observed on an IR spectrum as two bands of positive and negative amplitude positioned at frequencies that correspond to the inflection point of the zero-order band. The second derivative results in a negative band which corresponds to the frequency of the zero-order absorption maxima, as depicted in Figure 2.14.

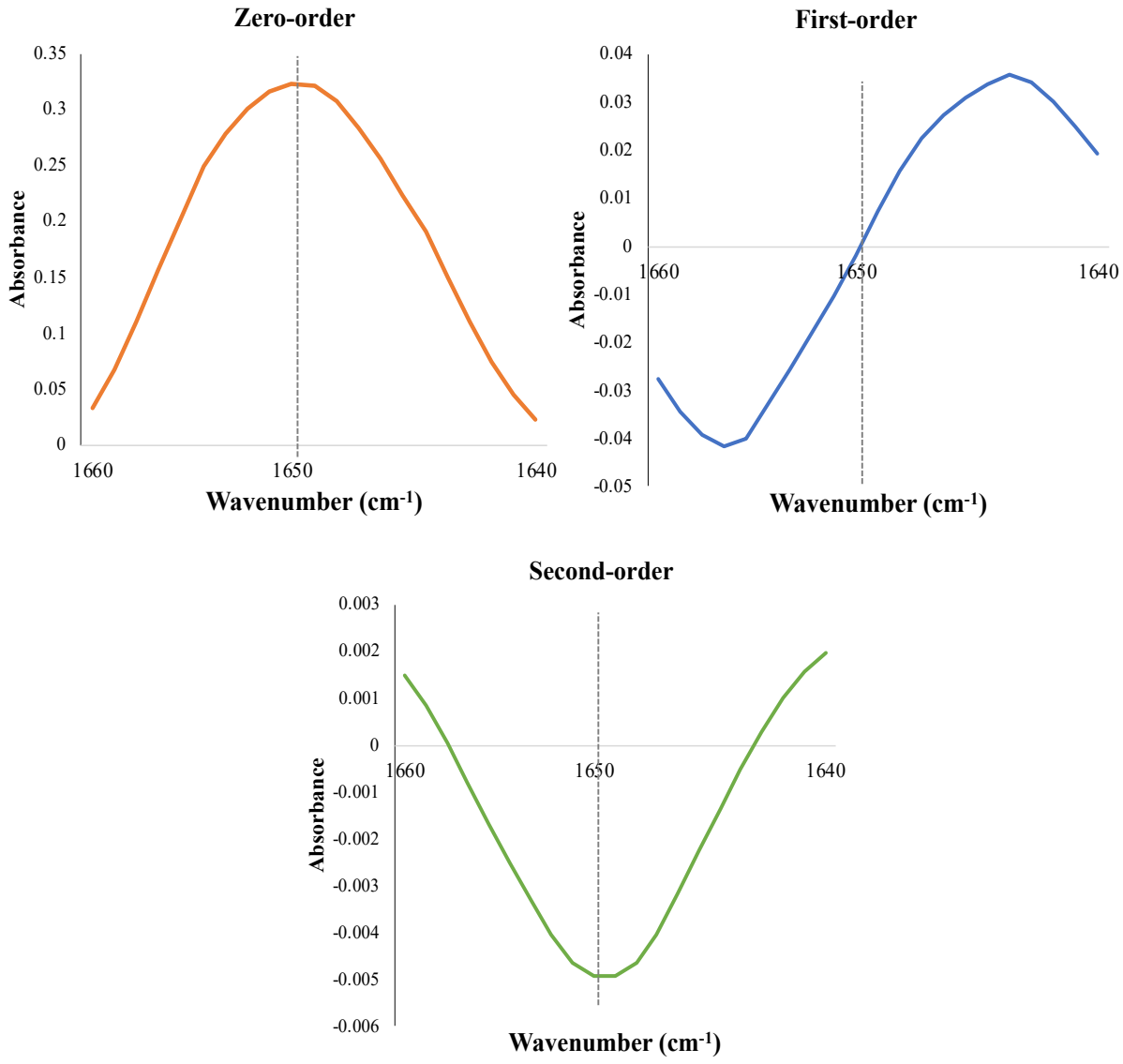

Figure 2.14 – Representation of a zero-order absorption band (orange), first-order derivative (blue) and second-order derivative (green). Processed from the peak maxima within the Amide I protein band (1660-1640 cm^{-1}).

This is of interest when there are broad absorption bands within an IR spectrum, which can be difficult to be assign. By resolving these overlapping bands, it allows subtle differences in spectra to be emphasised. For example, the broad Amide I absorption contains various hidden peaks relating to protein secondary structures, such as a-helices and b-sheets [34]. Deconvolution of the Amide band and prediction of these obscured peaks can be achieved by observing the second derivative spectrum [42,67].

2.4.3 Smoothing

Smoothing algorithms can be beneficial when there are fluctuating baselines or relatively poor SNR. These methods essentially aim to increase the SNR by reducing the amount of wavenumbers, without greatly distorting the signal [68]. The most commonly used smoothing algorithm was developed by Savitzky and Golay [69] in the 1960s, now widely known as Savitzky-Golay (SG-) filtering. SG-filters fit a polynomial to a fixed number of input data points within a moving window. The smoothed data point is determined from the fitted polynomial at each step of the algorithm. SG-filters are particularly good at removing high frequency noise from input signals, and are well established in the smoothing of biological spectra [27].

2.4.4 Normalisation

Spectral normalisation is commonly used to scale the IR spectra within a similar range. This can be helpful in accounting for discrepancies in optical pathlength and differences in sample quantity and/or thickness. The simplest method is the min-max

normalisation, where spectra are first offset-corrected by setting the minimum intensity of the spectrum to zero. The maximum absorbance is then set to equal one, resulting in scaled spectra (e.g. min = 0 and max = 1). Another frequently employed method is vector normalisation, where each wavenumber variable is initially averaged and then subtracted from the original spectrum to equal zero. Following this, each wavenumber is squared, then divided by the square root of the total sum of squared wavenumber variables, thus normalising the spectral dataset to a magnitude of one [63].

2.5 Spectral Analysis

2.5.1 Principal Component Analysis

Principal Component Analysis (PCA) is a basic linear transformation technique that is often used in spectroscopic studies. The main aim of a PCA analysis is to identify distinct patterns in complex datasets and detect a correlation between variables [70]. This type of analysis retains the majority of the information by defining the directions of maximum variance, principal components (PC), in high-dimensional data and projecting them into smaller dimensional space [71]. As described in Figure 2.15, PCA determines a new coordinate system which allows the largest variance to be described by the first PC, followed by PC2, and so on. Essentially, the goal is to reduce the dimensionality of large datasets, in order to clearly visualise the general variation, which can be achieved through scores and loadings plots.

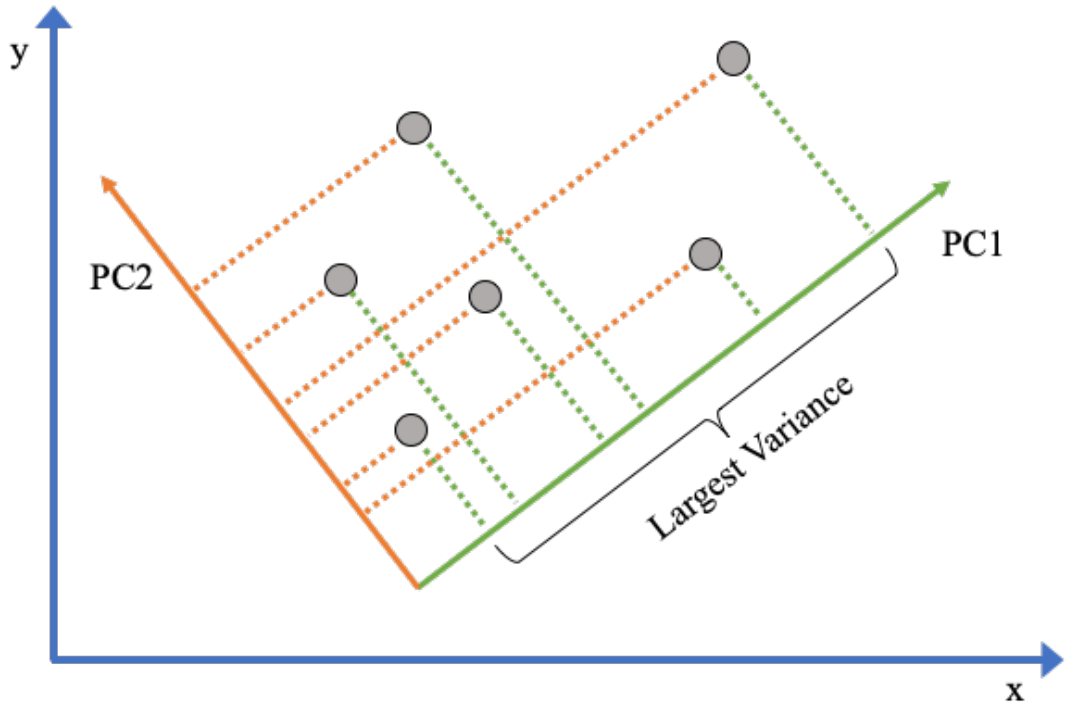

Figure 2.15 – Schematic illustration of principal component analysis. Adapted from ref [71].

2.5.2 Linear Discriminant Analysis

Linear discriminant analysis (LDA) is another dimensionality reduction technique, but it is also capable of working as a linear classifier. LDA is has similar features to PCA, but in addition to finding the component axes that maximise the variance in the data, it focuses on maximising the separability among the known categories [72]. LDA classifiers make predictions by estimating the probability that a new set of inputs belong to each category, and the class that gets the highest probability is predicted as the output class [73].

2.5.3 Partial Least Squares Discriminant Analysis

Partial Least Squares – Discriminant Analysis (PLS-DA) is supervised machine learning method that combines PLS regression (PLSR) and LDA. This technique can extract important information from complex datasets, by reducing the dimensionality to reveal hidden patterns within the data. This technique separates classes by looking for a straight line that divides the data space into two distinct regions, and can often separate classes better than PCA when known class information has been provided (Figure 2.16) [74]. The data points are projected perpendicularly to the line, which is known as the discriminator [75]. The distances from the discriminator are referred to as the discriminant scores [76]. This information is provided in the form of new variables called PLS components, similar to PCs in PCA. The PLS scores plots give an overview of the general inconsistences within large datasets, and loadings plots further explain the variance, by suggesting where the most variable regions exist e.g. which spectral regions display the highest disparity.

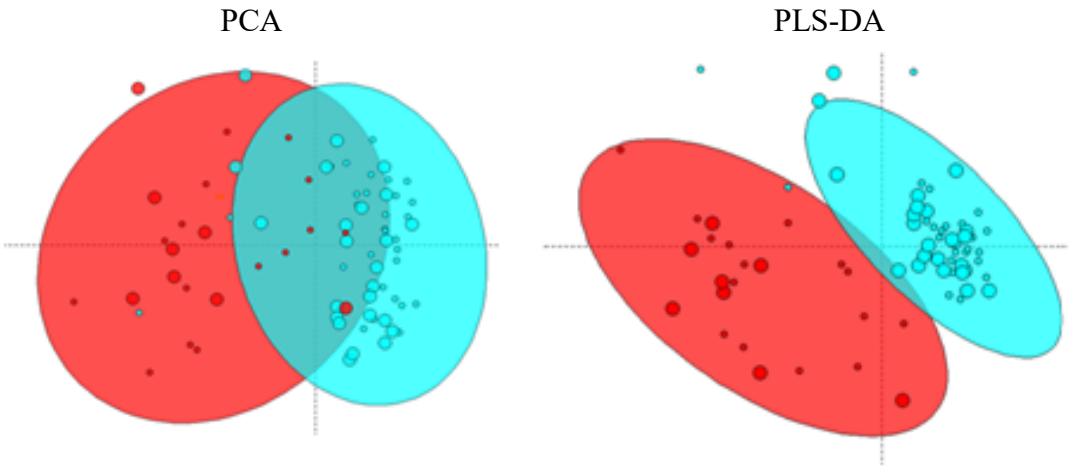

Figure 2.16 – Comparison of PCA and PLS-DA scores plots. Adapted from ref [77].

2.5.4 Random Forest

Random Forest (RF) is a robust machine learning technique that builds an ensemble of decision trees (Figure 2.17) from the training data using the Classification and Regression Trees (CART) algorithm [78].

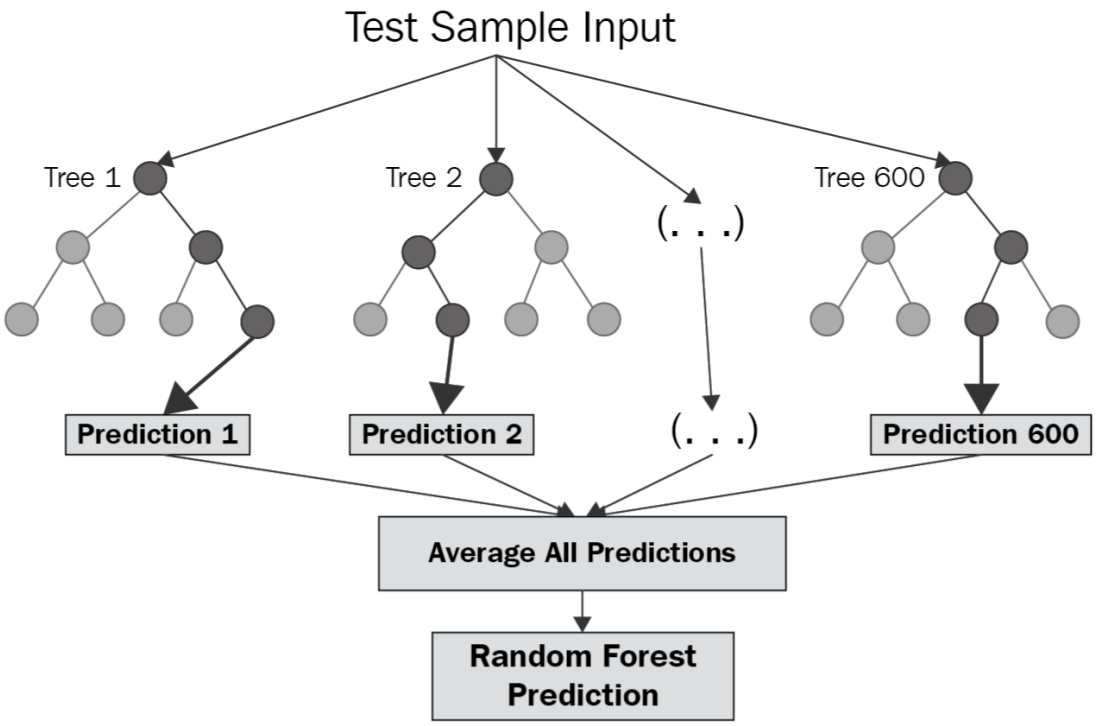

Figure 2.17 – Generic structure of a random forest ensemble model. Replicated from ref [79].

Given the training data and the input classes contained within, RF builds a 'forest' of regression trees and outputs a mean prediction which can then be used on test data. The 'trees' in the forest are a series of branching decisions. RF analysis can extract statistical values based on the number of true positives, false positives, true negatives and false negatives, determining both the accuracy and reliability of the classification. Using the Gini impurity metric, produced from the combined mean

decrease in the Gini coefficient with respect to the wavenumbers, RF can rank the spectral features in order of significance [80].

2.5.5 Support Vector Machine

A support vector machine (SVM) is a supervised algorithm, commonly employed for classification purposes [81]. From known data, SVM outputs an optimal dimension for the separation of the data, known as the hyperplane. Support vectors are the co-ordinates of the individual observation and the hyperplane can be used to categorise new samples [82]. The optimisation of SVM tuning parameters can considerably affect the classification efficiency. The penalty parameter, *cost,* is responsible for the trade-off between smooth boundaries and the ability to classify the data. The gamma parameter, γ, is responsible for the level of fit. It is important to ensure the model does not overfit the data, which can be achieved using a grid search to identify the optimal classification performance [83].

2.5.6 Sampling Methods

If there are an uneven number of samples between classes, then classification models can inaccurately overpredict the majority class. Sampling methods can be used to counteract this problem, by computationally balancing the dataset to ensure no bias is present within the model [84]. Up-sampling, down-sampling and synthetic minority over-sampling technique (SMOTE) are well-known methods that can balance uneven classes [85]. The up-sampling method consists of repeatedly sampling the minority class with replacement to increase the number of samples,

whereas down-sampling selects a subset of the majority class at random, removing the extra samples to make it the same size as the minority class. SMOTE is unique in that it artificially mixes the data to, creating ‘new’ samples to achieve a more balanced dataset.

2.6 References

[1] B.C. Smith, Fundamentals of Fourier transform infrared spectroscopy, CRC Press, Boca Raton, Fla., 2011. http://www.crcnetbase.com/isbn/9781420069303 (accessed January 31, 2018).

[2] J.L. Hollenberg, Introduction to molecular spectroscopy (Brittain, E. R. H.; George, W. O.; Wells, C. H. J.), J. Chem. Educ. 49 (1972) A98. https://doi.org/10.1021/ed049pA98.3.

[3] D.L. Pavia, G.M. Lampman, G.S. Kriz, J.R. Vyvyan, Introduction to spectroscopy, Fifth edition, Cengage Learning, Stamford, CT, 2015.

[4] L.D.S. Yadav, Organic spectroscopy, 2005. http://dx.doi.org/10.1007/978-1-4020-2575-4 (accessed January 31, 2018).

[5] T. Vo-Dinh, G. Gauglitz, eds., Handbook of spectroscopy, Wiley-VCH, Weinheim ; [Cambridge], 2003.

[6] Spectroscopyonline, NIR Versus Mid-IR: How to Choose, Accessed April 2018. (2018). http://www.spectroscopyonline.com/nir-versus-mid-ir-how-choose.

[7] M.J. Baker, C.S. Hughes, K.A. Hollywood, Biophotonics: vibrational spectroscopic diagnostics, Morgan & Claypool, San Rafael, 2016. http://iopscience.iop.org/book/978-1-6817-4071-3 (accessed February 4, 2018).

[8] B.H. Stuart, Infrared Spectroscopy: Fundamentals and Applications., John Wiley & Sons, Ltd., Hoboken, 2005. http://www.SLQ.eblib.com.au/patron/FullRecord.aspx?p=194354 (accessed February 20, 2018).

[9] P.R. Griffiths, J.A. De Haseth, Fourier transform infrared spectrometry, 2nd ed, Wiley-Interscience, Hoboken, N.J, 2007.

[10] J. Coates, Interpretation of Infrared Spectra, A Practical Approach, in: R.A. Meyers (Ed.), Encycl. Anal. Chem., John Wiley & Sons, Ltd, Chichester, UK, 2006: p. a5606. https://doi.org/10.1002/9780470027318.a5606.

[11] P. Larkin, Environmental Dependence of Vibrational Spectra, in: Infrared Raman Spectrosc., Elsevier, 2011: pp. 55–62. https://doi.org/10.1016/B978-0-12-386984-5.10004-7.

[12] N. Sheppard, The Historical Development of Experimental Techniques in Vibrational Spectroscopy, in: J.M. Chalmers, P.R. Griffiths (Eds.), Handb. Vib. Spectrosc., John Wiley & Sons, Ltd, Chichester, UK, 2006. https://doi.org/10.1002/0470027320.s0101.

[13] H. Martens, J.P. Nielsen, S.B. Engelsen, Light Scattering and Light Absorbance Separated by Extended Multiplicative Signal Correction. Application to Near-Infrared Transmission Analysis of Powder Mixtures, Anal. Chem. 75 (2003) 394–404. https://doi.org/10.1021/ac020194w.

[14] G. Clemens, B. Bird, M. Weida, J. Rowlette, M.J. Baker, Quantum cascade laser-based mid-infrared spectrochemical imaging of tissue and biofluids, Spectrosc. Eur. 26 (2014) 14–19.

[15] C. Hughes, G. Clemens, B. Bird, T. Dawson, K.M. Ashton, M.D. Jenkinson, A. Brodbelt, M. Weida, E. Fotheringham, M. Barre, J. Rowlette, M.J. Baker, Introducing Discrete Frequency Infrared Technology for High-Throughput Biofluid Screening, Sci. Rep. 6 (2016). https://doi.org/10.1038/srep20173.

[16] D.G. Revin, L.R. Wilson, J.W. Cockburn, A.B. Krysa, J.S. Roberts, R.J. Airey, Intersubband spectroscopy of quantum cascade lasers under operating conditions, Appl. Phys. Lett. 88 (2006) 131105. https://doi.org/10.1063/1.2189911.
[17] A. Schwaighofer, M. Brandstetter, B. Lendl, Quantum cascade lasers (QCLs) in biomedical spectroscopy, Chem. Soc. Rev. 46 (2017) 5903–5924. https://doi.org/10.1039/C7CS00403F.
[18] R. Mankar, M.J. Walsh, R. Bhargava, S. Prasad, D. Mayerich, Selecting optimal features from Fourier transform infrared spectroscopy for discrete-frequency imaging, The Analyst. 143 (2018) 1147–1156. https://doi.org/10.1039/C7AN01888F.
[19] L.M. Miller, R.J. Smith, Synchrotrons versus globars, point-detectors versus focal plane arrays: Selecting the best source and detector for specific infrared microspectroscopy and imaging applications, Vib. Spectrosc. 38 (2005) 237–240. https://doi.org/10.1016/j.vibspec.2005.03.010.
[20] G.L. Carr, Resolution limits for infrared microspectroscopy explored with synchrotron radiation, Rev. Sci. Instrum. 72 (2001) 1613. https://doi.org/10.1063/1.1347965.
[21] G. Cinque, C.S. Kelley, M.D. Frogley, J. Filik, K. Wehbe, A. Fitzpatrick, P.M. Donaldson, World First for Diamond in Synchrotron-Based IR Photothermal Nanospectroscopy, Synchrotron Radiat. News. 29 (2016) 37–39. https://doi.org/10.1080/08940886.2016.1198675.
[22] Diamond Light Source, How Diamond Works, Accessed July 2019. (2019). https://www.diamond.ac.uk/Public/How-Diamond-Works.html.
[23] A.A. Michelson, E.W. Morley, On the relative motion of the Earth and the luminiferous ether, Am. J. Sci. s3-34 (1887) 333–345. https://doi.org/10.2475/ajs.s3-34.203.333.
[24] M. Van de Weert, J.A. Hering, P.I. Haris, Fourier Transform Infrared Spectroscopy, in: Methods Struct. Anal. Protein Pharm., 2005: p. 131.
[25] A. Subramanian, L. Rodriguez-Saona, Fourier Transform Infrared (FTIR) Spectroscopy, in: Infrared Spectrosc. Food Qual. Anal. Control, Elsevier, 2009: pp. 145–178. https://doi.org/10.1016/B978-0-12-374136-3.00007-9.
[26] B. Stuart, Infrared Spectroscopy, in: John Wiley & Sons, Inc. (Ed.), Kirk-Othmer Encycl. Chem. Technol., John Wiley & Sons, Inc., Hoboken, NJ, USA, 2005. https://doi.org/10.1002/0471238961.0914061810151405.a01.pub2.
[27] M.J. Baker, J. Trevisan, P. Bassan, R. Bhargava, H.J. Butler, K.M. Dorling, P.R. Fielden, S.W. Fogarty, N.J. Fullwood, K.A. Heys, C. Hughes, P. Lasch, P.L. Martin-Hirsch, B. Obinaju, G.D. Sockalingum, J. Sulé-Suso, R.J. Strong, M.J. Walsh, B.R. Wood, P. Gardner, F.L. Martin, Using Fourier transform IR spectroscopy to analyze biological materials, Nat. Protoc. 9 (2014) 1771–1791. https://doi.org/10.1038/nprot.2014.110.
[28] G. Theophilou, C.L.M. Morais, D.E. Halliwell, K.M.G. Lima, J. Drury, P.L. Martin-Hirsch, H.F. Stringfellow, D.K. Hapangama, F.L. Martin, Synchrotron- and focal plane array-based Fourier-transform infrared spectroscopy differentiates the basalis and functionalis epithelial endometrial regions and identifies putative stem cell regions of human endometrial glands,

Anal. Bioanal. Chem. 410 (2018) 4541–4554. https://doi.org/10.1007/s00216-018-1111-x.
[29] Z. Movasaghi, S. Rehman, Dr.I. ur Rehman, Fourier Transform Infrared (FTIR) Spectroscopy of Biological Tissues, Appl. Spectrosc. Rev. 43 (2008) 134–179. https://doi.org/10.1080/05704920701829043.
[30] J.L.R. Arrondo, A. Muga, J. Castresana, F.M. Goñi, Quantitative studies of the structure of proteins in solution by fourier-transform infrared spectroscopy, Prog. Biophys. Mol. Biol. 59 (1993) 23–56. https://doi.org/10.1016/0079-6107(93)90006-6.
[31] J.L. Arrondo, F.M. Goñi, Structure and dynamics of membrane proteins as studied by infrared spectroscopy, Prog. Biophys. Mol. Biol. 72 (1999) 367–405.
[32] P.I. Haris, D. Chapman, Does Fourier-transform infrared spectroscopy provide useful information on protein structures?, Trends Biochem. Sci. 17 (1992) 328–333.
[33] H. Fabian, W. Mantele, Infrared Spectroscopy of Proteins, in: J.M. Chalmers, P.R. Griffiths (Eds.), Handb. Vib. Spectrosc., John Wiley & Sons, Ltd, Chichester, UK, 2006. https://doi.org/10.1002/0470027320.s8201.
[34] A. Barth, Infrared spectroscopy of proteins, Biochim. Biophys. Acta BBA - Bioenerg. 1767 (2007) 1073–1101. https://doi.org/10.1016/j.bbabio.2007.06.004.
[35] W. Gallagher, FTIR analysis of protein structure, Course Man. Chem. 455 (2009).
[36] P. Garidel, H. Schott, Fourier-Transform Midinfrared Spectroscopy for Analysis and Screening of Liquid Protein Formulations, (2006) 6.
[37] M.J. Baker, E. Gazi, M.D. Brown, J.H. Shanks, P. Gardner, N.W. Clarke, FTIR-based spectroscopic analysis in the identification of clinically aggressive prostate cancer, Br. J. Cancer. 99 (2008) 1859–1866. https://doi.org/10.1038/sj.bjc.6604753.
[38] G. Bellisola, C. Sorio, Infrared spectroscopy and microscopy in cancer research and diagnosis, Am. J. Cancer Res. 2 (2012) 1.
[39] D. Naumann, FT-INFRARED AND FT-RAMAN SPECTROSCOPY IN BIOMEDICAL RESEARCH, Appl. Spectrosc. Rev. 36 (2001) 239–298. https://doi.org/10.1081/ASR-100106157.
[40] A. Barth, C. Zscherp, What vibrations tell us about proteins, Q. Rev. Biophys. 35 (2002) 369–430. https://doi.org/10.1017/S0033583502003815.
[41] K. Spalding, Developing Spectroscopic Biofluid Diagnostics: Monitoring and Therapeutic Profiling of Melanoma Patients, University of Strathclyde, 2018.
[42] S.E. Glassford, B. Byrne, S.G. Kazarian, Recent applications of ATR FTIR spectroscopy and imaging to proteins, Biochim. Biophys. Acta BBA - Proteins Proteomics. 1834 (2013) 2849–2858. https://doi.org/10.1016/j.bbapap.2013.07.015.
[43] K. Dorling, M.J. Baker, Highlighting attenuated total reflection Fourier transform infrared spectroscopy for rapid serum analysis, Trends Biotechnol. 31 (2013) 325–327. https://doi.org/10.1016/j.tibtech.2013.03.009.
[44] J. Filik, M.D. Frogley, J.K. Pijanka, K. Wehbe, G. Cinque, Electric field standing wave artefacts in FTIR micro-spectroscopy of biological materials, The Analyst. 137 (2012) 853. https://doi.org/10.1039/c2an15995c.

[45] J. Lee, E. Gazi, J. Dwyer, M.D. Brown, N.W. Clarke, J.M. Nicholson, P. Gardner, Optical artefacts in transflection mode FTIR microspectroscopic images of single cells on a biological support: the effect of back-scattering into collection optics, The Analyst. 132 (2007) 750. https://doi.org/10.1039/b702064c.
[46] P. Bassan, H.J. Byrne, J. Lee, F. Bonnier, C. Clarke, P. Dumas, E. Gazi, M.D. Brown, N.W. Clarke, P. Gardner, Reflection contributions to the dispersion artefact in FTIR spectra of single biological cells, The Analyst. 134 (2009) 1171. https://doi.org/10.1039/b821349f.
[47] P. Bassan, H.J. Byrne, F. Bonnier, J. Lee, P. Dumas, P. Gardner, Resonant Mie scattering in infrared spectroscopy of biological materials – understanding the 'dispersion artefact,' The Analyst. 134 (2009) 1586. https://doi.org/10.1039/b904808a.
[48] P. Bassan, A. Kohler, H. Martens, J. Lee, H.J. Byrne, P. Dumas, E. Gazi, M. Brown, N. Clarke, P. Gardner, Resonant Mie Scattering (RMieS) correction of infrared spectra from highly scattering biological samples, The Analyst. 135 (2010) 268–277. https://doi.org/10.1039/B921056C.
[49] D.C. Fernandez, R. Bhargava, S.M. Hewitt, I.W. Levin, Infrared spectroscopic imaging for histopathologic recognition, Nat. Biotechnol. 23 (2005) 469–474. https://doi.org/10.1038/nbt1080.
[50] Perkin Elmer, FTIR Spectroscopy: Attenuated Total Reflectance (ATR), Accessed April 2018. (n.d.). https://shop.perkinelmer.com/content/TechnicalInfo/TCH_FTIRATR.pdf.
[51] R.A. Shaw, S. Low-Ying, A. Man, K.-Z. Liu, C. Mansfield, C.B. Rileg, M. Vijarnsorn, Infrared Spectroscopy of Biofluids in Clinical Chemistry and Medical Diagnostics, Biomed. Vib. Spectrosc. Hoboken NJ John Wiley Sons Inc. (2008) 79–103.
[52] J.R. Hands, K.M. Dorling, P. Abel, K.M. Ashton, A. Brodbelt, C. Davis, T. Dawson, M.D. Jenkinson, R.W. Lea, C. Walker, M.J. Baker, Attenuated Total Reflection Fourier Transform Infrared (ATR-FTIR) spectral discrimination of brain tumour severity from serum samples: Serum spectroscopy gliomas, J. Biophotonics. 7 (2014) 189–199. https://doi.org/10.1002/jbio.201300149.
[53] J.R. Hands, G. Clemens, R. Stables, K. Ashton, A. Brodbelt, C. Davis, T.P. Dawson, M.D. Jenkinson, R.W. Lea, C. Walker, M.J. Baker, Brain tumour differentiation: rapid stratified serum diagnostics via attenuated total reflection Fourier-transform infrared spectroscopy, J. Neurooncol. 127 (2016) 463–472. https://doi.org/10.1007/s11060-016-2060-x.
[54] K. Gajjar, J. Trevisan, G. Owens, P.J. Keating, N.J. Wood, H.F. Stringfellow, P.L. Martin-Hirsch, F.L. Martin, Fourier-transform infrared spectroscopy coupled with a classification machine for the analysis of blood plasma or serum: a novel diagnostic approach for ovarian cancer, The Analyst. 138 (2013) 3917. https://doi.org/10.1039/c3an36654e.
[55] M.J. Walsh, S.E. Holton, A. Kajdacsy-Balla, R. Bhargava, Attenuated total reflectance Fourier-transform infrared spectroscopic imaging for breast histopathology, Vib. Spectrosc. 60 (2012) 23–28. https://doi.org/10.1016/j.vibspec.2012.01.010.
[56] J.R. Hands, Investigating the use of Attenuated Total Reflection Fourier-Transform Infrared (ATR-FTIR) Spectroscopy for the Rapid Diagnosis of

Brain Tumours using Human Blood Serum, Doctor of Philosophy, University of Strathclyde, 2015.
[57] Bruker Optics, Application Note: Attenuated Total Reflection (ATR) – a versatile tool for FT-IR spectroscopy Refractive index, (2011).
[58] E. Karabudak, R. Kas, W. Ogieglo, D. Ra, S. Schlautmann, R.G.H. Lammertink, H.J.G.E. Gardeniers, G. Mul, Disposable Attenuated Total Re fl ection-Infrared Crystals from Silicon Wafer: A Versatile Approach to Surface Infrared Spectroscopy, Anal. Chem. 85 (2013) 33–38. https://doi.org/10.1021/ac302299g.
[59] M. Koç, E. Karabudak, History of spectroscopy and modern micromachined disposable Si ATR-IR spectroscopy, Appl. Spectrosc. Rev. 53 (2018) 420–438.
[60] H. Schumacher, U. Kunzelmann, B. Vasilev, K.J. Eichhorn, J.W. Bartha, Applications of microstructured silicon wafers as internal reflection elements in attenuated total reflection Fourier transform infrared spectroscopy, Appl. Spectrosc. 64 (2010) 1022–1027. https://doi.org/10.1366/000370210792434404.
[61] J.M. Cameron, H.J. Butler, D.S. Palmer, M.J. Baker, Biofluid spectroscopic disease diagnostics: A review on the processes and spectral impact of drying, J. Biophotonics. 11 (2018) e201700299. https://doi.org/10.1002/jbio.201700299.
[62] H.J. Butler, P.M. Brennan, J.M. Cameron, D. Finlayson, M.G. Hegarty, M.D. Jenkinson, D.S. Palmer, B.R. Smith, M.J. Baker, Development of high-throughput ATR-FTIR technology for rapid triage of brain cancer, Nat. Commun. 10 (2019) 4501. https://doi.org/10.1038/s41467-019-12527-5.
[63] P. Lasch, Spectral pre-processing for biomedical vibrational spectroscopy and microspectroscopic imaging, Chemom. Intell. Lab. Syst. 117 (2012) 100–114. https://doi.org/10.1016/j.chemolab.2012.03.011.
[64] P. Bassan, Light scattering during infrared spectroscopic measurements of biomedical samples, PhD Thesis, University of Manchester, 2011.
[65] M. Pirzer, J. Sawatzki, Method and device for correcting a spectrum, 7359815, n.d. http://www.freepatentsonline.com/7359815.html.
[66] A. Kohler, J. Sulé-Suso, G.D. Sockalingum, M. Tobin, F. Bahrami, Y. Yang, J. Pijanka, P. Dumas, M. Cotte, D.G. van Pittius, G. Parkes, H. Martens, Estimating and Correcting Mie Scattering in Synchrotron-Based Microscopic Fourier Transform Infrared Spectra by Extended Multiplicative Signal Correction, Appl. Spectrosc. 62 (2008) 259–266. https://doi.org/10.1366/000370208783759669.
[67] J. Kong, S. Yu, Fourier Transform Infrared Spectroscopic Analysis of Protein Secondary Structures, Acta Biochim. Biophys. Sin. 39 (2007) 549–559. https://doi.org/10.1111/j.1745-7270.2007.00320.x.
[68] B.R. Smith, M.J. Baker, D.S. Palmer, PRFFECT: A versatile tool for spectroscopists, Chemom. Intell. Lab. Syst. 172 (2018) 33–42. https://doi.org/10.1016/j.chemolab.2017.10.024.
[69] Abraham. Savitzky, M.J.E. Golay, Smoothing and Differentiation of Data by Simplified Least Squares Procedures., Anal. Chem. 36 (1964) 1627–1639. https://doi.org/10.1021/ac60214a047.

[70] H. Abdi, L.J. Williams, Principal component analysis: Principal component analysis, Wiley Interdiscip. Rev. Comput. Stat. 2 (2010) 433–459. https://doi.org/10.1002/wics.101.
[71] Z. Zhang, A. Castelló, Principal components analysis in clinical studies, Ann. Transl. Med. 5 (2017) 351–351. https://doi.org/10.21037/atm.2017.07.12.
[72] S. Raschka, Linear Discriminant Analysis - Bit by Bit, (2014). https://sebastianraschka.com/Articles/2014_python_lda.html.
[73] Linear Discriminant Analysis for Machine Learning, Mach. Learn. Mastery. (n.d.). https://machinelearningmastery.com/linear-discriminant-analysis-for-machine-learning/.
[74] D. Ballabio, V. Consonni, Classification tools in chemistry. Part 1: linear models. PLS-DA, Anal. Methods. 5 (2013) 3790. https://doi.org/10.1039/c3ay40582f.
[75] L.C. Lee, C.-Y. Liong, A.A. Jemain, Partial least squares-discriminant analysis (PLS-DA) for classification of high-dimensional (HD) data: a review of contemporary practice strategies and knowledge gaps, Analyst. 143 (2018) 3526–3539. https://doi.org/10.1039/C8AN00599K.
[76] R.G. Brereton, G.R. Lloyd, Partial least squares discriminant analysis: taking the magic away, J. Chemom. 28 (2014) 213–225. https://doi.org/10.1002/cem.2609.
[77] Creative Data Solutions, Orthogonal Signal Correction Partial Least Squares (O-PLS) in R, (2015). https://imdevsoftware.wordpress.com/2013/07/28/orthogonal-partial-least-squares-opls-in-r/.
[78] L. Breiman, Random Forests, Mach. Learn. 45 (2001) 5–32. https://doi.org/10.1023/A:1010933404324.
[79] A. Chakure, Random Forest Regression, Data Sci. (2019). https://towardsdatascience.com/random-forest-and-its-implementation-71824ced454f.
[80] B.R. Smith, K.M. Ashton, A. Brodbelt, T. Dawson, M.D. Jenkinson, N.T. Hunt, D.S. Palmer, M.J. Baker, Combining random forest and 2D correlation analysis to identify serum spectral signatures for neuro-oncology, Analyst. 141 (2016) 3668–3678.
[81] C. Cortes, V. Vapnik, Support-Vector Networks, Mach. Learn. 20 (1995) 273–297. https://doi.org/10.1023/A:1022627411411.
[82] P. de Boves Harrington, Support Vector Machine Classification Trees, Anal. Chem. 87 (2015) 11065–11071. https://doi.org/10.1021/acs.analchem.5b03113.
[83] A. Ben-Hur, J. Weston, A User's Guide to Support Vector Machines, in: O. Carugo, F. Eisenhaber (Eds.), Data Min. Tech. Life Sci., Humana Press, Totowa, NJ, 2010: pp. 223–239. https://doi.org/10.1007/978-1-60327-241-4_13.
[84] SIMAFORE, Managing unbalanced data for building machine learning models, Accessed March 2019. (2019). http://www.simafore.com/blog/handling-unbalanced-data-machine-learning-models.
[85] N.V. Chawla, K.W. Bowyer, L.O. Hall, W.P. Kegelmeyer, SMOTE: Synthetic Minority Over-sampling Technique, J. Artif. Intell. Res. 16 (2002) 321–357. https://doi.org/10.1613/jair.953.

Chapter 3

Developing Infrared Spectroscopic Detection for Stratifying Brain Tumour Patients: Glioblastoma Multiforme *vs.* Lymphoma

James M. Cameron[1], Holly J. Butler[2], Benjamin R. Smith[2], Mark G. Hegarty[2], Michael D. Jenkinson[3], Khaja Syed[4], Paul M. Brennan[5], Katherine Ashton[6], Timothy Dawson[6], David S. Palmer[2,7], Matthew J. Baker[1,2]

[1]WestCHEM, Department of Pure and Applied Chemistry, Technology and Innovation Centre, University of Strathclyde, 99 George St, Glasgow, G1 1RD, UK

[2]ClinSpec Diagnostics, University of Strathclyde, Technology and Innovation Centre, 99 George Street, Glasgow, G1 1RD, UK

[3]Institute of Translational Medicine, University of Liverpool & The Walton Centre NHS Foundation Trust, Lower Lane, Fazakerley, Liverpool, L9 7LJ, UK

[4]Walton Research Tissue Bank, Neurosciences Labs, The Walton Centre NHS Foundation Trust, Lower lane, Fazakerley, Liverpool, L9 7LJ, UK

[5]Translational Neurosurgery, Department of Clinical Neurosciences, Western General Hospital, Edinburgh, EH4 2XU, UK

[6]Neuropathology, Lancashire Teaching Hospitals NHS Trust, Royal Preston Hospital, Sharoe Green Lane North, Preston, Lancashire, PR2 9HT, UK

[7]WestCHEM, Department of Pure and Applied Chemistry, Thomas Graham Building, University of Strathclyde, 295 Cathedral Street, Glasgow, G1 1XL, UK

Published in: *Analyst,* 2019;144(22):6736-6750. doi: 10.1039/c9an01731c.

Presented at: SciX 2019 Conference, Palm Springs, CA, USA & 7th Analytical Biosciences Early Career Researcher Meeting, Glasgow, UK.

Contribution: I conducted all experimental work; produced all figures; wrote and prepared the manuscript for publication.

Abstract

Over a third of brain tumour patients visit their general practitioner more than five times prior to diagnosis in the UK, leading to 62% of patients being diagnosed as emergency presentations. Unfortunately, symptoms are non-specific to brain tumours, and the majority of these patients complain of headaches on multiple occasions before being referred to a neurologist. As there are currently no methods in place for the early detection of brain cancer, the affected patients' average life expectancy is reduced by 20 years. These statistics indicate that the current pathway is ineffective, and there is a vast need for a rapid diagnostic test.

Attenuated total reflection Fourier-transform infrared (ATR-FTIR) spectroscopy is sensitive to the hallmarks of cancer, as it analyses the full range of macromolecular classes. The combination of serum spectroscopy and advanced data analysis has previously been shown to rapidly and objectively distinguish brain tumour severity. Recently, a novel high-throughput ATR accessory has been developed, which could be cost-effective to the National Health Service in the UK, and valuable for clinical translation.

In this study, 765 blood serum samples have been collected from healthy controls and patients diagnosed with various types of brain cancer, contributing to one of the largest spectroscopic studies to date. Three robust machine learning techniques - random forest, partial least squares-discriminant analysis and support vector machine - have all provided promising results. The novel high-throughput technology has

been validated by separating brain cancer and non-cancer with balanced accuracies of 90% which is comparable to the traditional fixed diamond crystal methodology.

Furthermore, the differentiation of brain tumour type could be useful for neurologists, as some are difficult to distinguish through medical imaging alone. For example, the highly aggressive glioblastoma multiforme and primary cerebral lymphoma can appear similar on magnetic resonance imaging scans, thus are often misdiagnosed. Here, we report the ability of infrared spectroscopy to distinguish between glioblastoma and lymphoma patients, at a sensitivity and specificity of 90.1% and 86.3%, respectively. A reliable serum diagnostic test could avoid the need for surgery and speed up time to definitive chemotherapy and radiotherapy.

3.1 Introduction

Brain tumour incidence rates have been increasing since the early 1990s, rising by 34% in the UK alone [1]. Despite an improvement in patient survival, only 14% of patients survive 10 years or more after diagnosis, and the average reduction in life expectancy of 20 years is the highest of all cancers [2]. Rapid and timely diagnosis and determination of tumour type is crucial for expediting management and improving patient outcomes [3].

The symptoms most frequently associated with brain tumours are non-specific, such as headache, presenting a challenge for doctors in identifying which patients are most likely to have a brain tumour, and should have expedited brain imaging [4]. Consequently patients often visit their general practitioner (GP) multiple times before diagnosis and for nearly two thirds of patients diagnosis is in the emergency department once they deteriorate [5], [6]. Existing referral guidelines lack sensitivity and specificity. As few as 1.6% of patients referred for urgent brain imaging from primary care actually have a brain tumour, suggesting many brain scans are unnecessary [7].

Brain tumours are diagnosed on magnetic resonance imaging (MRI) or computed tomography (CT) brain imaging. There are many different types of tumours, depending on the underlying cell of origin, each with its own optimal treatment regimens. Crucially, it is not possible to identify the tumour type with certainty from imaging alone. For example, primary central nervous system lymphoma (PCNSL) and glioblastoma (GBM) can have similar appearance on MRI [8], but very different

therapy options. Patients therefore require a gold standard histological tissue diagnosis. This subjects them to surgical tumour biopsy, with attendant risks, including stroke or death, and with consequent delay to commencement of the chemotherapy and/or radiotherapy that will best impact on their disease. A rapid blood test that can identify patients with tumours amongst those with similar symptoms, and that can stratify tumour type would have a profound impact.

Analytical techniques based on vibrational spectroscopy, such as Raman and infrared (IR) spectroscopy, have emerged in the field of disease diagnostics [9]–[12]. Fourier-transform infrared spectroscopy (FTIR) in particular has become increasingly popular in medical research, because of its rapid, non-invasive analysis [13]. In FTIR spectroscopy, biological samples are irradiated with infrared light. The absorbance of this light causes molecular excitation and enables transitions between vibrational states, resulting in an IR spectrum. A typical spectrum of a biological sample represents a biochemical fingerprint, and can characterise and quantify the levels of proteins, lipids, carbohydrates and nucleic acids that are present. The imbalances in these biomolecular components can give an indication of disease states [14]. Machine learning algorithms learn the differences in IR biosignatures that are exclusive to disease and can provide a diagnostic output with a prediction on the patient's state [15].

Many spectroscopic disease diagnostic pilot studies to date have analysed human tissue, indicating the possibility to differentiate healthy and cancerous tissue, as well as benign and malignant tumours [16]. Breast, lung, colorectal and prostate lesions

have been studied, providing a platform of promising results [17]–[21]. More recently, biofluid spectroscopy has gained increased interest. Attenuated total reflection (ATR)-FTIR spectroscopy is well suited to the analysis of biofluids, as only tiny volumes are required and sample preparation is minimal [22], [23]. Blood serum contains over 20,000 different proteins and is one of the most complex biofluids [24]. Serum perfuses all body organs, gaining proteomes from surrounding tissues and cells, hence the spectroscopic biosignature of serum ideal for indicating disease states [25], [26].

There has been many biofluid-based studies looking into various cancers [27]–[30], but Hands *et al.* were the first to use blood serum and ATR-FTIR spectroscopic analysis for brain tumour detection. Comparisons have been made between glioma and non-cancer patients [31], as well as pilot studies for different brain tumour types [32]. In a further study of blood serum from 433 patients [33], the discrimination of cancer versus non-cancer of reported and sensitivity and specificity of 92.8% and 91.5%, respectively [15].

Traditional ATR-FTIR instrumentation was used in these studies, which has barred the clinical translation of the technique for a number of reasons. Conventionally, an ATR-FTIR spectrometer has a fixed point of analysis, known as the internal reflection element (IRE). IREs for ATR analysis are made from materials with high refractive indices, the most common being diamond, zinc selenide or germanium [34], to contrast with the sample that has a lower refractive index. Biofluid samples are deposited directly onto the surface of the IRE before being air dried, in order to

combat the spectral interference of water [35]. IR light is directed into the IRE and internally reflected, forming an evanescent wave at the IRE-sample interface. This evanescent wave interrogates the sample at a defined penetration depth, which is dependent upon the refractive indices of the IRE and sample, the angle of incidence and the wavelength of IR beam [36].

The traditional approach is limited in both cost and time. The IRE materials tend to be high cost, therefore would be expensive to replace. The fixed IRE needs to be cleaned between each sample, which is extremely time consuming. It takes approximately 8 minutes to adequately dry 1 μL of human serum on to a diamond crystal, and with the necessary cleaning steps, as well as the technical and biological repeats, it would take over an hour to process one patient [32]. Also, scratches on the surface of fixed IREs are known to affect the sample-IRE contact, which is essential for ATR-FTIR measurements [37]. These limitations have inhibited the progression of the technique thus far, however high-throughput ATR-FTIR could overcome these barriers for successful clinical translation. A recently published health economic study has suggested a high-throughput alternative to the traditional IRE would be cost-effective to the UK's National Health Service (NHS). Gray *et al.* highlight the clinical and economic benefits of implementing a quick diagnostic test for brain cancers into the current pathway [38]. They reported that a serum blood test at the primary care level could prioritise patients for neuroimaging, improving patient survival and quality of life, whilst also saving on the cost of unnecessary brain scans. Furthermore, since blood tests at the primary care level are already in place, an additional test at this stage would not significantly disrupt current practices.

Silicon (Si) has a high refractive index, and its relatively low cost - cf. diamond - and transparency to infrared light makes it an ideal material for Si IREs (SIREs) [39], [40]. High-throughput disposable SIREs are now commercially available, that allow single-bounce ATR-FTIR (ClinSpec Diagnostics Ltd, UK) [41]. The SIRE replaces the expensive fixed crystal, and allow multiple sampling points (Appendix 1, Figure A1.1). The design enables the slides to be batch processed, as well as having the option of repeating analysis if required, a feature that would not be possible with conventional fixed SIREs.

In this study, we further explore the largest retrospective dataset curated to date of serum samples from patients with brain tumours, with a specific focus on the spectroscopic interpretation of the variances within the brain tumour cohort. Specifically, we elucidate the ability of SIRE-based ATR-FTIR spectroscopy to successfully identify the cancerous biosignature in serum, and to differentiate between GBM and PCNSL.

3.2 Materials and Methods

3.2.1 Sample Collection and Preparation

Following a specified standard operating procedure, a total of 765 serum samples were obtained from three sources; the Walton Centre NHS Trust (Liverpool, UK), Royal Preston Hospital (Preston, UK), and the commercial source Tissue Solutions Ltd (Glasgow, UK). Ethical approval for this study was obtained (Walton Research Bank and Brain Tumour North West/WRTB 13_01/BTNW Application #1108). All patients were consented. The primary care triage study contains 724 cases - 487 brain tumour samples and 237 healthy controls. A respectable balance of male and female patients has been included, with a widespread age range – the details of which can be found in Appendix 1 (Table A1.1). A large variety of tumour types are involved in the brain cancer cohort (Table A1.2). An additional 41 serum samples were collected from patients with primary cerebral lymphoma for comparison against GBM samples (Table A1.3).

In order to be included in this study, the cancer patients must have had a pathologically confirmed primary or secondary brain tumour, and must not have been undergoing chemo- or radio-therapy at the time of collection. For control patients, obtained as above, inclusion criteria stated that they should not be undergoing any medical treatments, nor have any history of cancer. Blood samples were collected in serum collection tubes and allowed to clot for up to one hour. The tubes were centrifuged at 2200 g for 15 minutes at room temperature, then the separated serum component was subsequently aliquoted stored in an -80 °C freezer.

Prior to spectral analysis, the frozen serum samples were removed from storage and thawed at room temperature (18-25 °C) for an average time of 15-20 minutes. Using a micropipette, 3 µL of serum from one individual patient was deposited onto each of the three sample wells of the optical sample slide (wells 1, 2 and 3), whilst ensuring well '0' remained clean for background collection. The serum drops were spread across the well using the pipette tip, in order to create a thin serum film and cover the whole IRE for more uniform deposition. Prepared slides were stacked in 3D printed polylactic acid (PLA) slide holders, which were designed to enable batch drying. The stacked slides were then stored in a drying unit incubator (Thermo Fisher™ Heratherm™, GE) at 35 °C for 1 hour. Pre-analytical work prior to beginning this study showed this step to be vital, as it provides even heat and airflow for controlled drying dynamics of the serum droplet, to obtain a smooth, flat homogenous sampling surface [42]–[44].

3.2.2 Spectral Collection

For this study, a Perkin Elmer Spectrum 2 FTIR spectrometer (Perkin Elmer, UK) was used for the spectral collection. A Specac Quest ATR accessory unit was fitted with a specular reflectance puck (Specac Ltd, UK), allowing the SIRE to sit on top of the aperture and replace the traditional fixed diamond IRE. The slide indexing unit (ClinSpec Diagnostics Ltd, UK) enabled accurate and reproducible movement across the specular reflectance puck, indexing the optical slide between sample wells. With the first well acting as a background, the three sample wells provide the biological repeats. Each well was analysed in triplicate - resulting in nine spectra per patient. The spectra were acquired in the range 4000-450 cm^{-1}, at a resolution of 4 cm^{-1}, with

1 cm^{-1} data spacing and 16 co-added scans. In total 6885 spectra have been collected from all serum samples.

3.2.3 Spectral Pre-processing

Here we have used the PRFFECT toolbox within R Statistical Computing Environment software for the spectroscopic analysis [45], [46], which can be divided into two parts; spectral pre-processing and spectral classification. The pre-processing step is commonly applied in spectroscopic studies, as it reduces unwanted variance in the dataset. A combination of baseline correction, normalisation and data reduction enables the significant biological information to be emphasised and improves the classification performance [47]. The optimum pre-processing protocol was determined using a trial-and-error iterative approach. The PRFFECT toolbox offers various pre-processing methods, such as binning, smoothing, normalisation and numerical derivatives - we direct the reader towards Smith *et al.* [45] for more information on the use of this open-source program. Figure 3.1 gives an example of the data pre-processing; (a) raw spectra as the mean plot per patient, for the whole 724-patient dataset, and (b) shows the spectra cut to the fingerprint region, with baseline correction and a vector normalisation applied - greatly reducing the spectral variation.

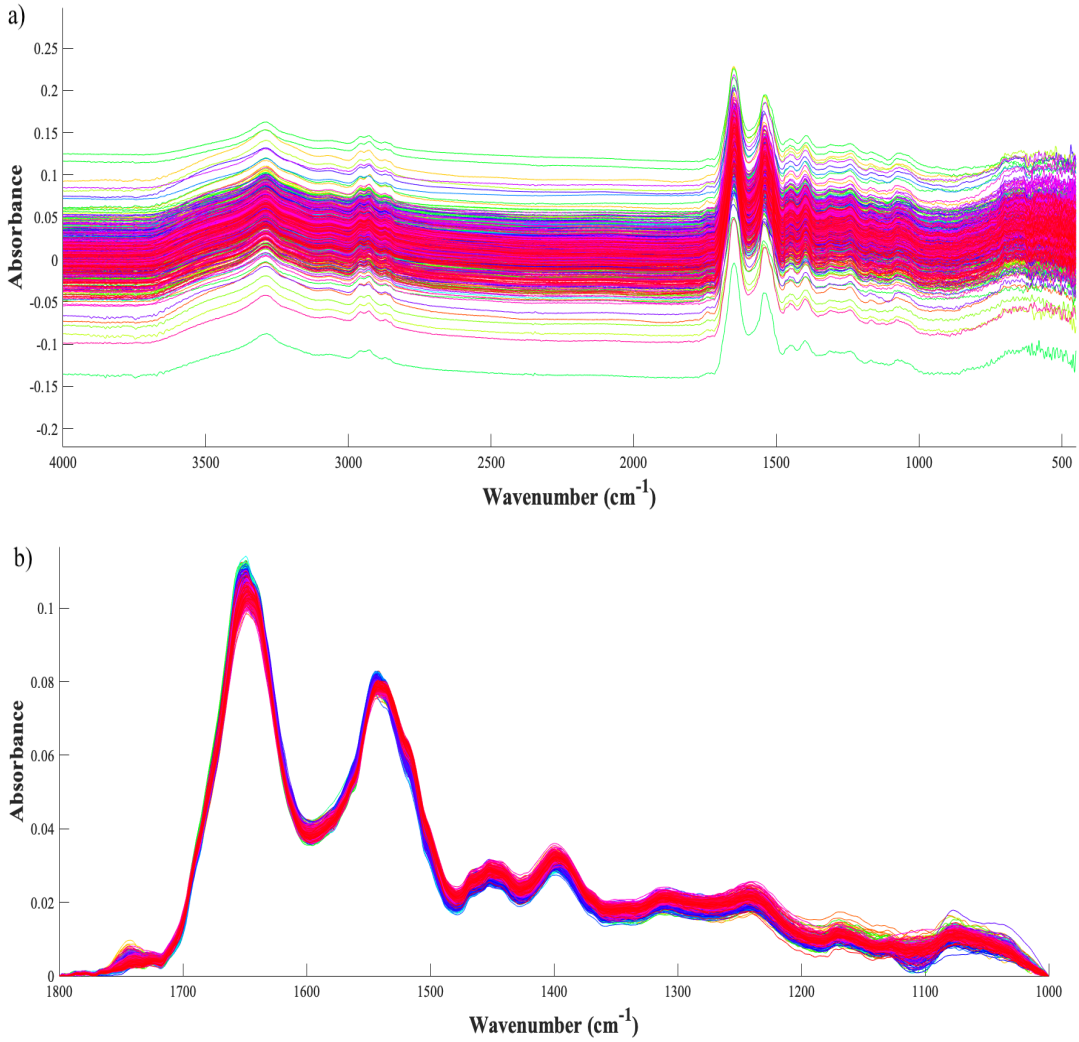

Figure 3.1 - Pre-processing example; (a) raw infrared spectra of the whole brain cancer cohort, and (b) after a spectral cut, rubberband baseline correction and vector normalisation.

Extended multiplicative signal correction (EMSC) has recently been shown to be a reliable pre-processing tool, that allows more selective correction for various types of scattering [48]. The EMSC process scales the IR spectra according to a given reference spectrum. In this case, the reference was an average spectrum of 10 background measurements of the SIRE, which was chosen to minimise the spectral

variance caused by silicon lattice vibrations. The optimal pre-processing parameters were found to be (in order); EMSC, spectral cut to the fingerprint region (1800-1000 cm^{-1}), a minmax normalisation and a binning factor of 8.

3.2.4 Spectral Analysis

Spectral analysis was carried out to identify the cancerous biosignature from a known patient cohort to develop a trained classification model, and then to use this information to predict the presence of cancer in an unknown population. Prior to running the classifications, bootstrapping analysis was carried out on the training set to search for an acceptable number of iterations. This technique resamples a dataset with replacement, to determine an optimal resample value which will maximise classification accuracy [49]. To develop the models, patients were randomly split into training and test sets, with a 70:30 split. Models were tuned on the training set (70%) and then used to make predictions for the spectra in the test set (30%). In order to ensure that the models were trained and validated correctly, spectra from a single patient's sample could only appear in one cross-validation fold, and in either the training or test set. The consensus vote amongst the nine spectra that were analysed for each patient was reported as the diagnostic outcome (cancer or non-cancer). Model performance is reported in terms of sensitivity, specificity, kappa, and balanced accuracy. For those classifications for which the class prevalence in the clinical population were known, positive and negative predictive values were also computed.

Sensitivities and specificities (Eq. 3.1 and 3.2) are based on the number of correct and incorrect predictions in the external test set. The sensitivity refers to the ability of the test to correctly identify the patients with the disease (brain cancer), and specificity is the ability to correctly pick out those without the disease (controls) [50]. True positives (TP) result from a patient with the target disease with five or more spectra out of their nine spectra correctly identified, whereas true negatives (TN) refer to the patients without the target disease who have at least five out of their nine spectra correctly identified. False positives (FP) are where a control patient has five or more spectra incorrectly identified as cancer, and a false negative (FN) is from a patient with the target disease who has five or more spectra incorrectly classified as non-cancer.

$$Sensitivity = \frac{TP}{TP+FN} = \frac{TP}{P} \tag{3.1}$$

$$Specificity = \frac{TN}{TN+FP} = \frac{TN}{N} \tag{3.2}$$

where P is the number of real positives and N is the number of real negatives.

When employing binary classifications on imbalanced datasets, the overall model performance is commonly measured using balanced accuracy (Eq. 3.3), which can be defined as the average accuracy obtained on either class [51].

$$Balanced\ Accuracy = (\frac{TP}{P} + \frac{TN}{N}) / 2 \tag{3.3}$$

In order to understand the reliability of the diagnostic model the Kappa value, κ, can give a quantitative measure of the magnitude of agreement between observers (Eq. 3.4).

$$\kappa = \frac{p_o - p_e}{1 - p_e} \tag{3.4}$$

where p_o is the relative observed agreement and p_e is hypothetical probability of the chance agreement, which can be calculated from consideration of the number of times that cancer and non-cancers occur in the real and predicted data. Values of κ range from below zero to one and equate to the level of agreement. Where in general, κ ≤0 indicates no agreement, 0.01–0.20 accounts for slight, 0.21–0.40 fair, moderate agreement is 0.41–0.60, 0.61–0.80 is substantial and lastly 0.8–1.00 is almost perfect agreement [52], [53].

Predictive values are useful to clinicians as they indicate the true likelihood of the test results. The positive predictive value (PPV) is the proportion of patients with positive test results who are correctly diagnosed, and the negative predictive value (NPV) relates to those with correctly assigned negative results [54], [55].

The predictive values are dependent upon the sensitivity, specificity and the prevalence of the disease (Eq. 3.5 and 3.6) - in this case the prevalence of brain tumours [56]. In this study the PPV and NPV have been calculated using the mean values of sensitivity and specificity from each of the resampled classification models and the prevalence is equal to that of the positive class (i.e. cancer) in the clinical environment.

$$PPV = \frac{sensitivity \times prevalence}{sensitivity \times prevalence + (1-specificity)\times(1-prevalence)} \quad (3.5)$$

$$NPV = \frac{specificity \times (1-prevalence)}{(1-sensitivity) \times prevalence + specificity \times (1-prevalence)} \quad (3.6)$$

To determine the optimum values for the tuning parameters, a 5-fold cross-validation was performed - on a patient basis - on the training data. Due to the class imbalance present when examining the difference between cancer (487 patients) vs. non-cancer (237 patients), various sampling methods were used throughout this study to ensure no bias was present within the models [57]; up-sampling, down-sampling and synthetic minority over-sampling technique (SMOTE) [58].

3.2.4.1 Random Forest

Random forest (RF) is a robust machine learning technique that for classification problems builds an ensemble of decision trees from the training data using the Classification and Regression Trees algorithm [59]. There are three main tuning parameters employed in this technique; *ntree* is the number of trees, *mtry* is the number of variables available for splitting at each tree node and *nodesize* refers to the depth of the trees. To encourage diversity amongst the forest, each of *ntree* trees is built on a bootstrap sample of the training data, and at each node in each tree the optimum feature is selected from a random subset of *mtry* available features. Each tree is grown until the terminal nodes contain no fewer than *nodesize* observations. Classification predictions are reported as the majority vote of all of the decision trees in the forest, which allows the method to benefit from the "wisdom of the crowds". Random Forest is well-known to be insensitive to the values of *ntree*, *nodesize*, and *mtry* [60]. Here, default values were adopted for *ntree* = 500 and *nodesize* = 1 and *mtry* = 30. Additionally, spectral importance results can be graphically viewed in the form of Gini plots. The Gini impurity metric accounts for how often a randomly selected component from a training set would be incorrectly labelled if it was randomly labelled according to the class distribution in a subset [61]. The mean decrease in the Gini, also known as Gini importance, is the total decrease in node impurities from splitting on the variable, averaged over all trees [62]. This is essentially a measure of how important a variable is for estimating the value of the target variable across all tress in the forest. Hence, by using this metric, RF can rank the spectral features in order of significance - for example, which wavenumbers are the most discriminating between the two classes [15].

3.2.4.2 Partial Least Squares-Discriminant Analysis

Partial least squares – discriminant analysis (PLS-DA) is supervised machine learning method that can extract important information from complex datasets, by reducing the dimensionality to reveal hidden patterns within the data [63]. PLS scores plots give an overview of the general inconsistences within large datasets, and loadings plots further explain the variance, by suggesting where the most variable regions exist e.g. which spectral regions display the highest disparity [64]. The optimal number of components, *ncomp,* is determined when tuning the classification models. The best value for *ncomp* provides the most reliable results, so that the cross-validation error is minimised. Here, *ncomp* was determined from a tuning grid with a range 1:20.

3.2.4.3 Support Vector Machine

A support vector machine (SVM) is a supervised algorithm, commonly employed for classification purposes [65]. As described in Chapter 2 (section 2.5.5), support vectors are the co-ordinates of the individual observation and the hyperplane can be used to categorise new samples [66]. Linear, radial basis function, and polynomial kernels have all been used in SVM models, but here we use the linear kernel that has previously been shown to perform well in spectral classification studies [67]. The penalty parameter *cost* has been tuned to search for optimal classification performance [68].

3.3 Results and Discussion

3.3.1 Brain Cancer *versus* Control

Each classification model was executed multiple times to ensure the variance within the dataset was fully encompassed. Bootstrapping analysis on the training set showed 51 resamples to be a reliable number of iterations, as shown in Figure 3.2, the standard error adequately converges at around 51 resamples for both (a) sensitivity and (b) specificity. A higher number of iterations reduces the variance, but also increases the time required to run the classification models. At 51 iterations, the standard error for the test set was 0.13% for sensitivity and 0.19% for specificity, which was deemed to be an acceptable level of error, with reasonable analysis time.

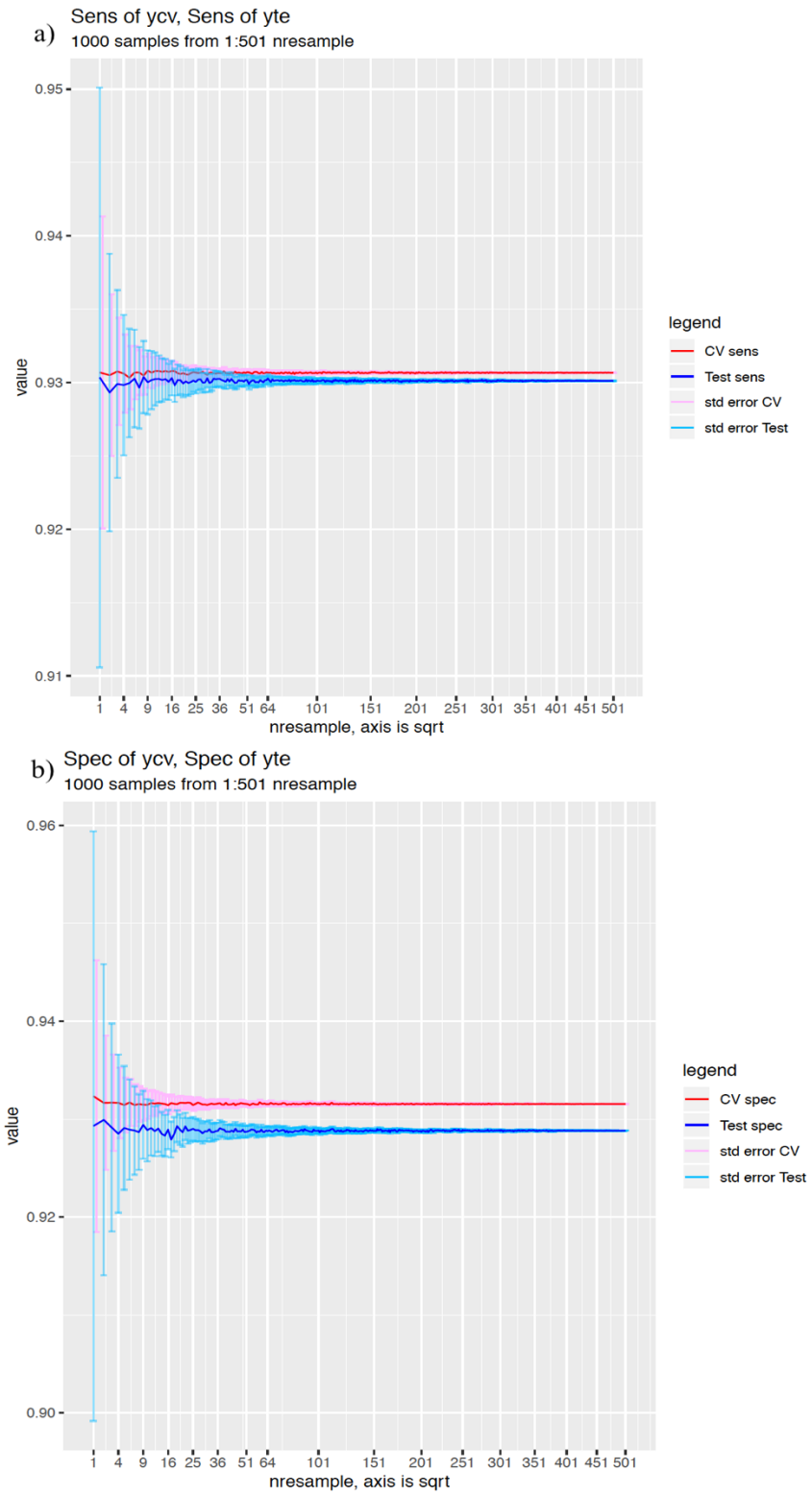

Figure 3.2 - Bootstrapping analysis to determine sufficient number of resamples required for the 724 patient dataset: (a) the sensitivity and (b) specificity.

3.3.1.1 Random Forest Results

Following optimal pre-processing, a single RF classification model was trained on the training data and used to predict the test set. The value of *mtry* was chosen to be 30, which gave sensitivity and specificity of 93.8% and 80.1% for the 5-fold cross-validation on the training data. Initial analysis of the single RF model emphasised the ability to successfully pick out the brain cancer patients from the training set, with the test set reporting a sensitivity of 92.5%. However, the specificity was much lower at 76.1%, meaning this particular model incorrectly predicted many of the control patients as having the disease. That said, the lower specificity could be attributed to the class imbalance within the dataset. As the sensitivity of a model relates to the ability to detect patients with disease, and 487 out of the 724 patient samples were cancerous, there was a bias towards the prediction of a brain cancer. The addition of statistical sampling techniques can reduce the class imbalance and improve the accuracy of the model. Table 3.1 compares classification output of the initial RF model with the three different resampling techniques. The up-sampling method was not effective in improving this model, losing 0.7% on sensitivity and only increasing specificity by 1.4%. On the other hand, down-sampling greatly improved the specificity, rising from 76.1% to 85.9%. Some studies have been critical of down-sampling, as the technique ‘ignores’ data that could provide important differences and/or similarities between the two classes [69] That being said, multiple iterations could potentially overcome this data loss, as there would be different patients down-sampled during each iteration. With SMOTE sampling technique, the minority class (controls in this case) is synthetically up-sampled in order to be more comparable

with the majority class [58]. This was found to provide the best output, with a sensitivity and specificity of 94.5% and 88.7% respectively.

Table 3.1 - Sampling comparison for single brain cancer *versus* control random forest classifications.

	RF only	**Up-sampling**	**Down-Sampling**	**SMOTE**
Sensitivity (%)	92.5	91.8	90.4	94.5
Specificity (%)	76.1	77.5	85.9	88.7

In Appendix 1, Figure A1.2 shows the confusion matrices of the (a) initial and (b) SMOTE models which describe the predictions that were made in the random forest test sets. As outlined above in Table 3.1, the specificity increased to 88.7%, predicting 63 out of 70 non-cancer patients correctly. The sensitivity remained high, only falsely predicting 8 out of 146 cancer patients as non-cancer, resulting in a sensitivity of 94.5%. As the SMOTE sampling was found to be optimal in this case, it was used for the resampled classification.

The single model results were promising, but to ensure they were reliable the RF model was resampled 51 times. The 51 independent RF models were combined to provide mean sensitivity and specificity values, as well as the standard deviations to account for the statistical variance. Table 3.2 lists the mean and standard deviation (SD) values for the sensitivity, specificity, κ and balanced accuracy relating to the 51 RF iterations. The PPV and NPV were also calculated from the mean sensitivity and specificity, as well as the prevalence of brain tumours - reported as approximately 1.6% [7]. The ability to successfully predict the brain cancer patients was high, with an average sensitivity of 93.1%. However, despite SMOTE being more beneficial for

the singular RF model, the average specificity over the 51 iterations dropped to 81.1%, ranging from 73.2% to 92.9%. This particular RF classification performed well in the detection of brain cancer, but it was incorrectly assigning more of the non-cancer patients as 'cancer' resulting in a higher number of false positives. Clearly this would not be very efficient for the clinic, as the excess brain scans would be costly to the health services, meanwhile putting healthy patients through needless stress and anxiety. However, these findings are still relatively promising, with a health economic study reporting statistics >80% would be cost-effective to the NHS [38].

Table 3.2 - Statistical results for the test set in the RF model with 51 iterations. SD, standard deviation.

	Mean	**SD**
Kappa	0.75	0.05
Sensitivity (%)	93.1	1.97
Specificity (%)	81.1	3.90
Balanced Accuracy (%)	87.1	2.35
PPV (%)	7.4	-
NPV (%)	99.9	-

The Gini impurity metric was examined to identify the most important features within the dataset. The accuracy and reliability of the model can be determined from the RF statistical value outputs, with the Gini plot highlighting wavenumbers responsible for the results for the optimal model (Figure 3.3). Table 3.3 gives an overview of the top 15 identified wavenumbers in order of importance, with their corresponding wavenumber assignments and vibrational modes. The column "∑Gini" in the table is a summation of the mean decrease in Gini for each wavenumber, over all nodes in all trees in the ensemble.

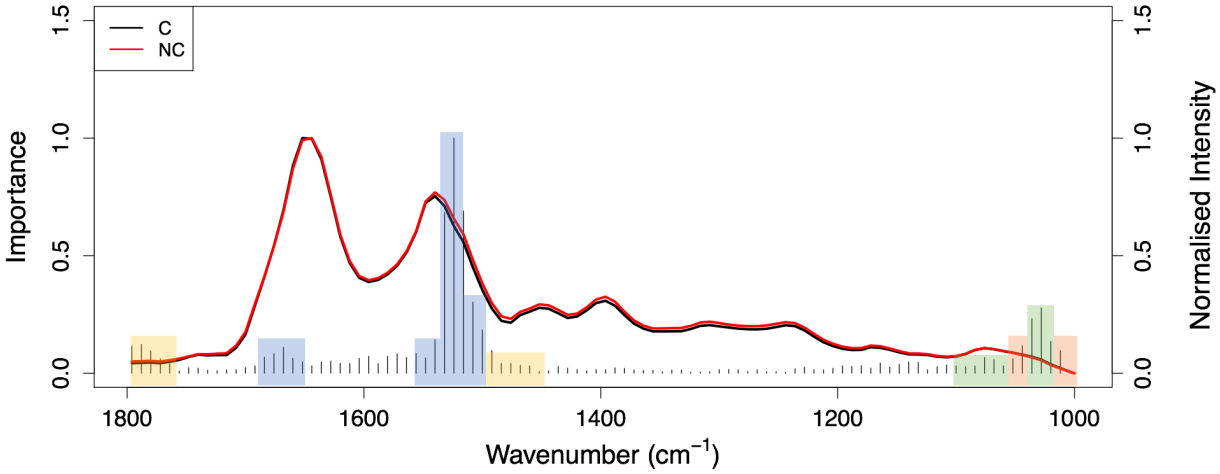

Figure 3.3 - Gini importance plot from random forest analysis showing the mean spectra from brain cancer (black) and control (red). Blue: Protein; Yellow: Lipid; Green: Nucleic acid and Orange: Carbohydrate.

Table 3.3 - Top 15 wavenumbers from RF classification of brain cancer vs non-cancer with tentative biochemical assignments [14], [16].

Wavenumbers (cm^{-1})	∑Gini	Tentative Assignments	Vibrational Modes
1524.5	619.1	Amide II of proteins	δ(N-H), ν(C-N), δ(C-O), ν(C-C)
1516.5	430.0		
1532.5	425.7		
1508.5	193.2		
1028.5	177.8	Glycogen	ν(C-O), ν(C-C), def(C-OH)
1036.5	150.0		
1500.5	120.7	Amide II of proteins	δ(N-H), ν(C-N), δ(C-O), ν(C-C)
1540.5	95.2		
1020.5	90.9	DNA/Glycogen	$\nu(PO_2^-)$/ν(C-O)
1788.5	83.2	Lipids	ν(C=O)
1044.5	79.3	Nucleic Acids	$\nu(PO_2^-)$
1796.5	79.1	Lipids	ν(C=O)
1668.5	76.1	Amide I of proteins	ν(C=O), ν(C-N), δ(N-H)
1012.5	67.2	Carbohydrate	ν(C-O)
1492.5	67.1	Amide II of proteins	δ(N-H), ν(C-N), δ(C-O), ν(C-C)

ν = stretching; δ = bending; def = deformation

The most discriminatory region is the Amide II band, making up the top 4 wavenumbers with extremely high ∑Gini values. The out-of-phase combination of the NH bending and the CN stretching vibrations, as well as minor contributions from the CO in-plane bend and the CC/NC stretching vibrations, give rise to the Amide II band [70]. Certain wavenumbers in the lower wavenumber region - relating to carbohydrates, glycogen and nucleic acids – were also shown to be highly discriminating. These areas of importance are closely followed by lipid and other protein (Amide I) contributions.

3.3.1.2 PLS-DA Results

The optimal value of *ncomp* was found to be 14, which was selected from a tuning grid with a range 1:20. This gave sensitivity of 89.4% and specificity of 88.7% for the 5-fold cross-validation on the training data. An initial PLS-DA model reported a sensitivity of 95.9% and specificity of 81.7% for the external test set. Similar to the RF analysis, the sampling techniques were used to balance the classes. All three methods greatly enhanced the specificity, each improving by 10% or greater (Table 3.4), but this was costly for the sensitivity values, each falling below 90%. It is likely that the fall in sensitivity is caused by the class imbalance, as the initial model can be biased and overpredict the majority of the patients as 'cancer', simply because there is many more within the dataset. The sampling techniques balance the classes, giving an impartial representation and hence more reliable predictions. Again, as with the RF, the best results were obtained using SMOTE sampling (Figure A1.3, Appendix 1), hence 51 iterations of the RF + SMOTE classification was employed.

Table 3.4 - Sampling comparison for single PLS-DA classifications.

	PLS-DA only	**Up-sampling**	**Down-Sampling**	**SMOTE**
Sensitivity (%)	95.9	86.3	86.3	89.7
Specificity (%)	81.7	92.9	94.3	91.6

Table 3.5 lists the results from the 51 resamples of the PLS-DA/SMOTE model. PLS-DA was not as effective at predicting the brain cancer patients correctly, reporting an average sensitivity of 90.5%, in comparison to 93.1% for the RF model. However, the average specificity was 91.1%, meaning PLS-DA was far superior in

correctly assigning the control samples as ‘non-cancer’. Out of the three classification models, PLS-DA reported the best PPV, at 14.2%, almost double that of the RF model (7.4%).

Table 3.5 - Statistical results for the test set in the PLS-DA + SMOTE model with 51 iterations. SD, standard deviation.

	Mean	**SD**
Kappa	0.71	0.10
Sensitivity (%)	90.5	2.09
Specificity (%)	91.1	3.28
Balanced Accuracy (%)	90.8	1.83
PPV (%)	14.2	-
NPV (%)	99.8	-

Figure 3.4 shows the scores plot between the first and second PLS components. There is a substantial amount of overlap between the two classes, with some separation across the 2nd PLS component (PLS2). The loadings plot for PLS2 is described in Figure 3.5, which suggests the biggest variance within the brain tumour dataset exists in the Amide II region (1500-1600 cm^{-1}), and in the lower wavenumber region (1000-1100 cm^{-1}). This agrees with the RF Gini importance values, in that the Amide II of proteins, and the bands from glycogen/carbohydrate/phosphate vibrations are most discriminatory.

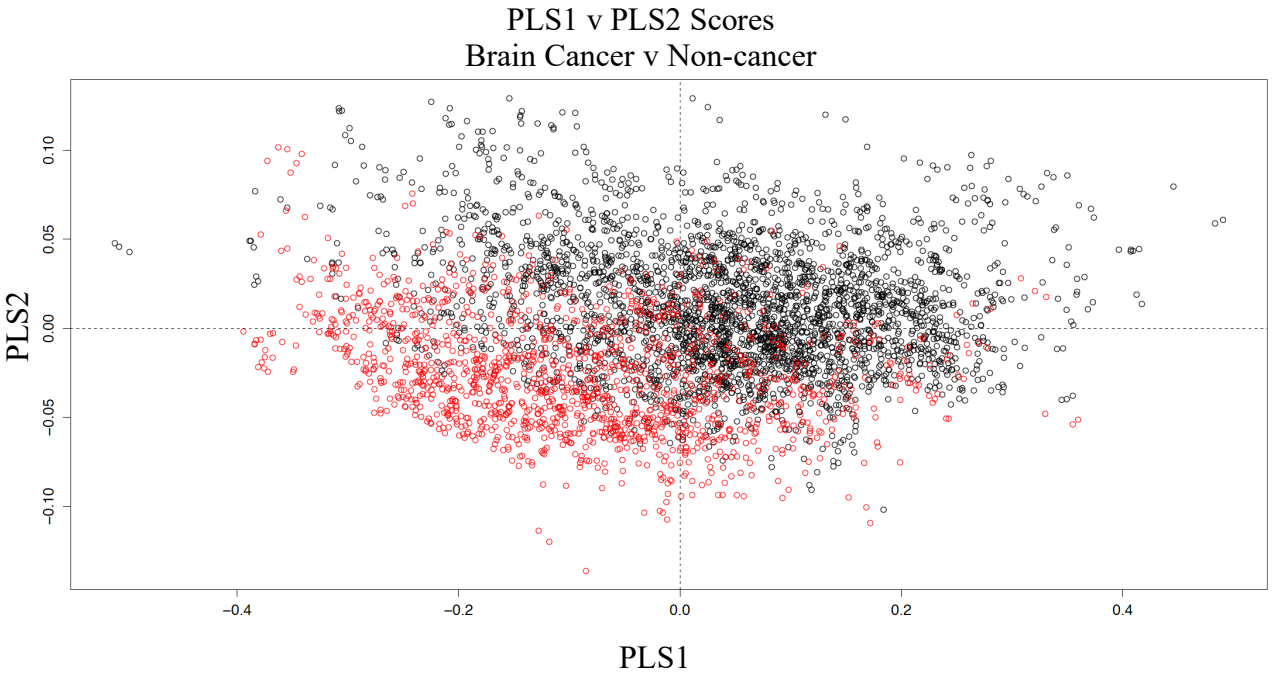

Figure 3.4 - Partial least squares-discriminant analysis; scores plot for brain cancer (black) vs control (red).

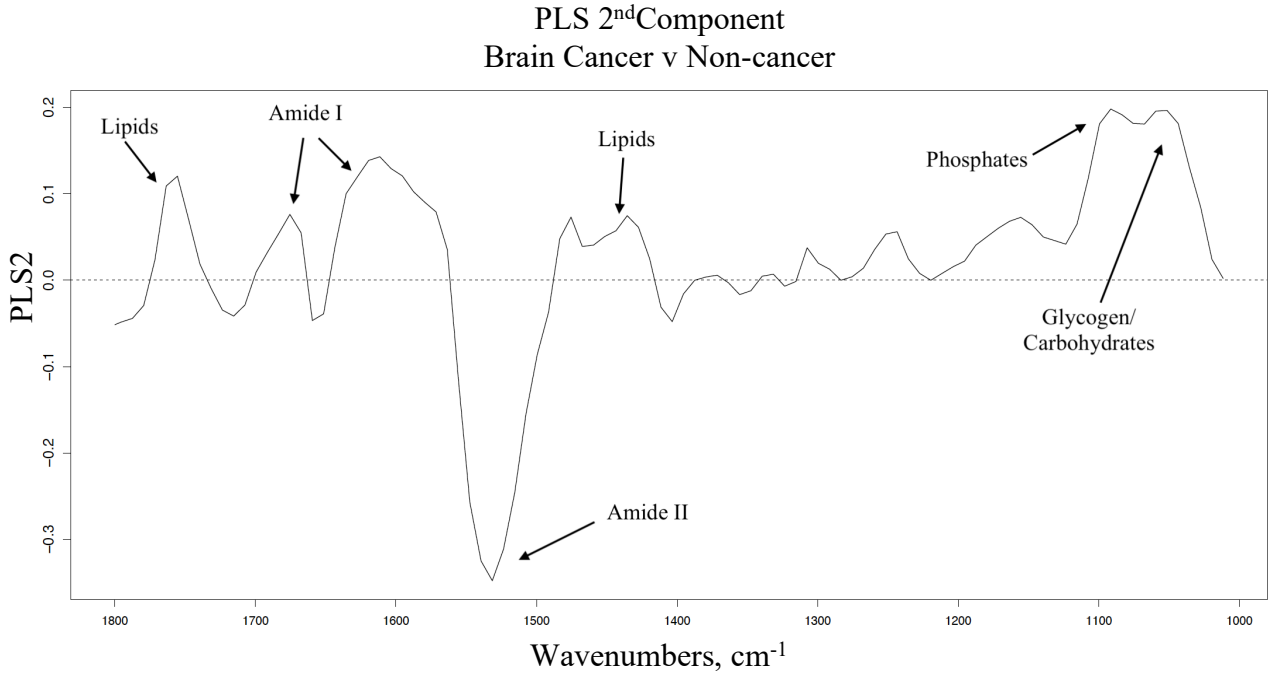

Figure 3.5 - Loadings plot for the 2nd partial least squares component with tentative biological assignments.

3.3.1.3 SVM Results

Similar analysis was carried out using an SVM-based classification (Table 3.6). The SVM model was tuned using the optimal value for *cost,* which was determined to be 0.019 by running a sequence between 0.001 and 0.3 at intervals of 0.018. Again, the use of the sample balancing techniques greatly improved the accuracy of the model, with SMOTE being the preferred method. The linear-SVM with SMOTE single model performed slightly better than RF and PLS-DA, with both sensitivity and specificity above 90%, as described in the test set confusion matrices in Appendix 2, Figure A1.4. The reported statistics in Table 3.7 are for the 51 SVM iterations using SMOTE.

Here, the average sensitivity was 92.1% but the specificity was slightly lower at 88.7%. Again, we achieve a balanced accuracy over 90%, and the PPV of 13.5% is relatively high. The SVM model produced a mean κ value of 0.8, indicating almost perfect agreement which suggests this particular model was robust and reliable.

Table 3.6 - Sampling comparison for single SVM classifications.

	SVM only	**Up-sampling**	**Down-Sampling**	**SMOTE**
Sensitivity (%)	93.2	89.7	87.7	91.7
Specificity (%)	81.7	94.4	94.4	90.1

Table 3.7 - Statistical results for the test set in the SVM model with 51 iterations. SD, standard deviation.

	Mean	**SD**
Kappa	0.80	0.03
Sensitivity (%)	92.1	2.1
Specificity (%)	88.7	3.3
Balanced Accuracy (%)	90.4	1.5
PPV (%)	13.5	-
NPV (%)	99.9	-

3.3.1.4 Receiver Operating Characteristic Curves

In addition, receiver operating characteristic (ROC) curves can illustrate the diagnostic ability of machine learning classifiers, and aid with tuning the classification model for clinical applications. The curves describe how the diagnostic ability can change when the probability threshold is varied. The area under the curve (AUC) represents the measure of separability, with the higher AUC the better the model is at distinguishing between classes [71]. The ROC graph in Figure 3.6 suggests the diagnostic performance of all three models is extremely promising. The ROC curves are all relatively symmetrical across sensitivity and specificity - the PLS-DA curve is slightly better with an AUC value of 0.948, which is regarded as excellent.

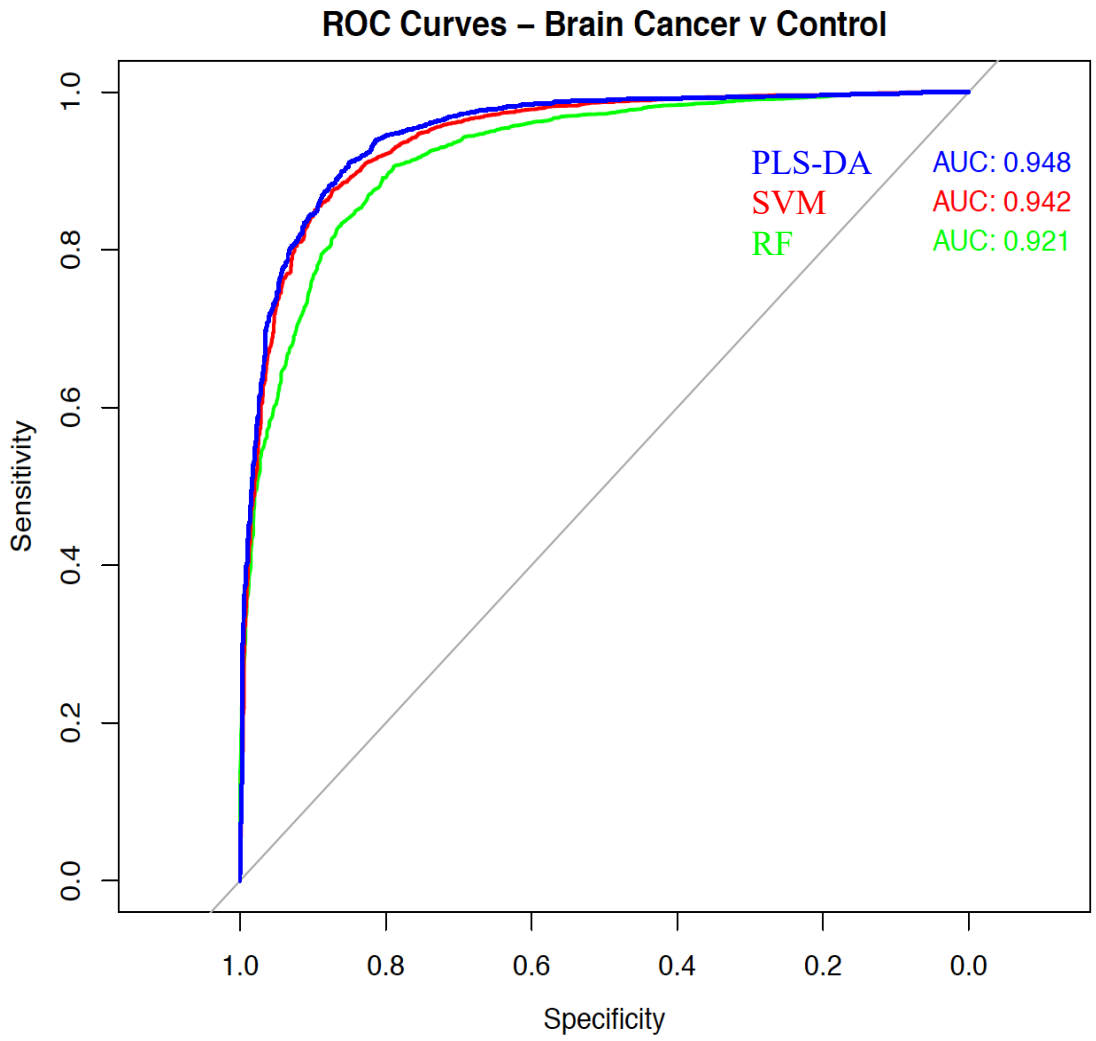

Figure 3.6 – ROC curves displaying trade-off between sensitivity and specificity of the three classification techniques for the cancer vs non-cancer patients: random forest; green, partial least squares-discriminant analysis; blue, support vector machine; red.

In general, the results from this study confirm the ability of serum spectroscopy - coupled with computational analysis - to be effective in differentiating brain lesions from healthy controls. Using basic machine learning techniques, we have successfully separated brain cancer and non-cancer with accuracies greater than 90%. Both PLS-DA and SVM performed extremely well, with the PLS-DA model reporting an average sensitivity and specificity of 90.5% and 91.1% respectively, meanwhile the linear-SVM produced 92.1% sensitivity and 88.7% specificity. These results are just slightly inferior to the 92.8% and 91.5% reported by Hands *et al*. [33]. However, there are various differences between these studies, meaning they are not entirely comparable. The patient cohorts were comprised of different patients, and this dataset contains almost 300 more serum samples. Hands *et al.* employed a radial basis function (RBF) based SVM, whereas we compare the capability of linear-SVM to basic RF and PLS-DA models, all of which provided promising results. Despite these differences, accuracies above 90% suggests that the new SIRE technology is comparable with the traditional fixed diamond IRE, indicating the high-throughput design could now be implemented into the clinical environment, to enable a quick blood test for the early detection of brain cancer.

3.3.2 Glioblastoma *versus* Primary CNS Lymphoma

Neuro-oncologists are particularly interested in the challenge of differentiating of PCNSL from GBM. It can often be difficult to distinguish between these diagnoses on brain imaging alone, such as MRI. This therefore necessitates patients to have surgical biopsy in order to identify the tumour pathology, and to determine the most appropriate regimen of surgery, chemotherapy and radiotherapy. A reliable serum diagnostic test could avoid the need for surgery and speed up time to definitive therapy.

Additional serum samples were collected from the Walton Centre and the Royal Preston hospital, to provide a total of 41 PCNSL samples. A random subset of the GBM samples from the 724 patient dataset were used for the comparisons. The patient information is summarised in Appendix 1 (Table A1.3). Similar to the 724 dataset, bootstrapping analysis was done on the GBM *versus* PCNSL training set to search for an acceptable number of iterations; 51 resamples were also found to be sufficient, with the standard error converging at this point (Figure A1.6, Appendix 1). An initial RF model provides us with the biochemical differences between the PCNSL and GBM patients. The Gini plot (Figure 3.7) suggests the Amide II region is of particular importance, closely followed by the Amide I band. Between 1150-1000 cm^{-1} there are various significant bands, relating to vibrations within nucleic material, glycogen and carbohydrates (Table 3.8).

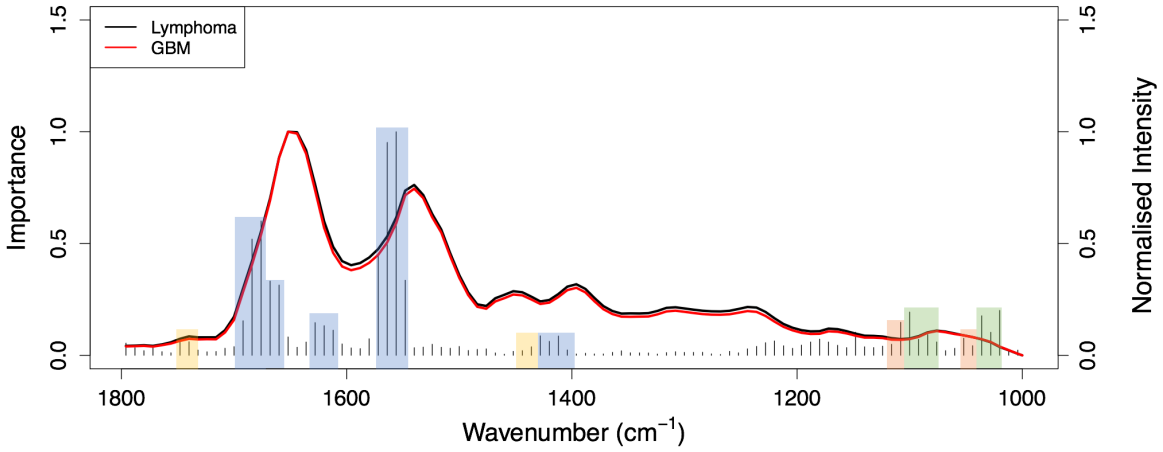

Figure 3.7 - Gini importance plot from random forest analysis showing the mean spectra from PCNS lymphoma (black) and glioblastoma (red). Blue: Protein; Yellow: Lipid; Green: Nucleic acid and Orange: Carbohydrate.

Table 3.8 - Top 15 wavenumbers from RF classification of PCNS lymphoma vs GBM with tentative biochemical assignments [14], [16].

Wavenumbers (cm^{-1})	**∑Gini**	**Tentative Assignments**	**Vibrational Modes**
1556.5	95.9	Amide II of proteins	δ(N-H), ν(C-N), δ(C-O), ν(C-C)
1564.5	91.4		
1676.5	57.9	Amide I of proteins	ν(C=O), ν(C-N), δ(N-H)
1684.5	50.1		
1572.5	42.9	Amide II of proteins	δ(N-H), ν(C-N), δ(C-O), ν(C-C)
1548.5	32.6		
1668.5	32.2	Amide I of proteins	ν(C=O), ν(C-N), δ(N-H)
1660.5	30.5		
1020.5	19.7	DNA/Glycogen	ν(PO_2^-)/ν(C-O), def(C-OH)
1100.5	19.0	Nucleic Acids	ν(PO_2^-)
1036.5	17.4	Glycogen	ν(C-O), ν(C-C)
1692.5	15.3	Amide I of proteins	ν(C=O), ν(C-N), δ(N-H)
1108.5	14.6	Carbohydrate	ν(C-O), ν(C-C)
1628.5	14.5	Amide I of proteins	ν(C=O), ν(C-N), δ(N-H)
1620.5	13.2		

ν = stretching; δ = bending; def = deformation

For the PLS-DA model, in this case the optimal value for *ncomp* was found to be 4. As with the C/NC set, the scores plot separates the PCNSL and GBM patients across the 2nd PLS component (Figure 3.8). Again, we see the highest discrimination arises from the Amide bands and the lower wavenumber region on the loadings plot (Figure 3.9). For GBM *versus* PCNSL, the Amide I region is also highly discriminatory, substantiating the RF Gini findings outlined previously in Table 3.8. The confusion matrix for a single PLS-DA model is described in Appendix 1 (Figure A1.5). SMOTE showed to be the best sampling technique for RF and PLS-DA, but up-sampling was found to be optimal for the SVM-based model (Table 3.9). The PPV and NPV are not included here, as the prevalence value for this particular classification is difficult to estimate.

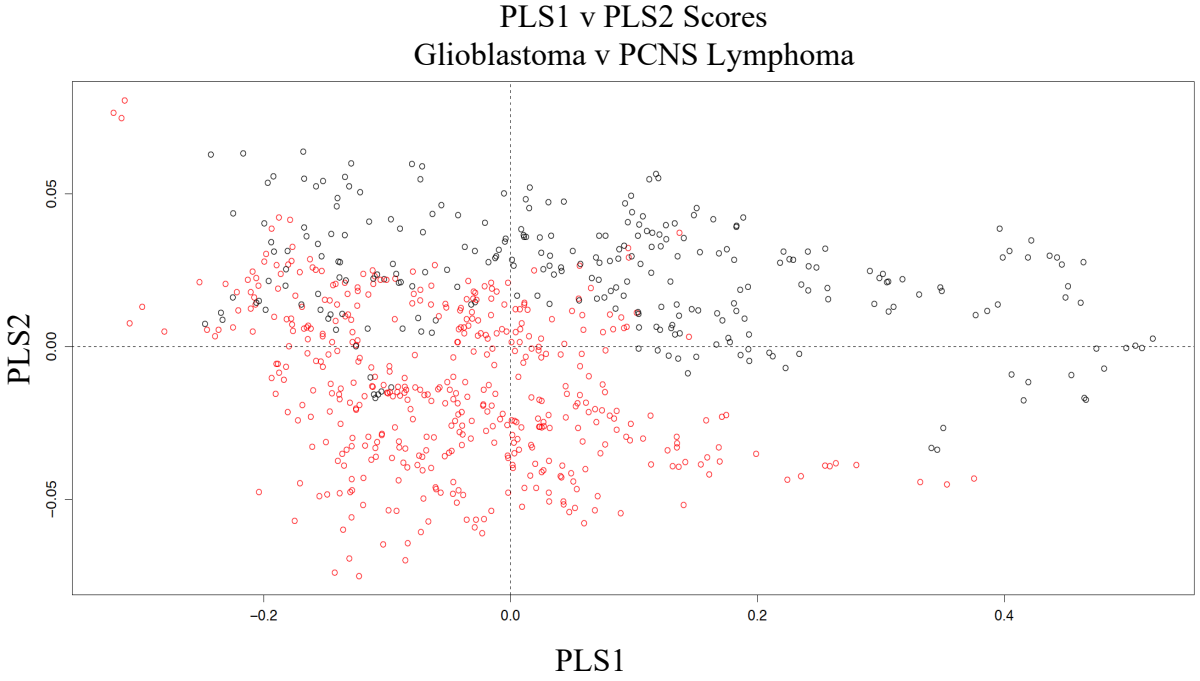

Figure 3.8 – Partial least squares-discriminant analysis; scores plot for PCNS lymphoma (black) vs glioblastoma (red).

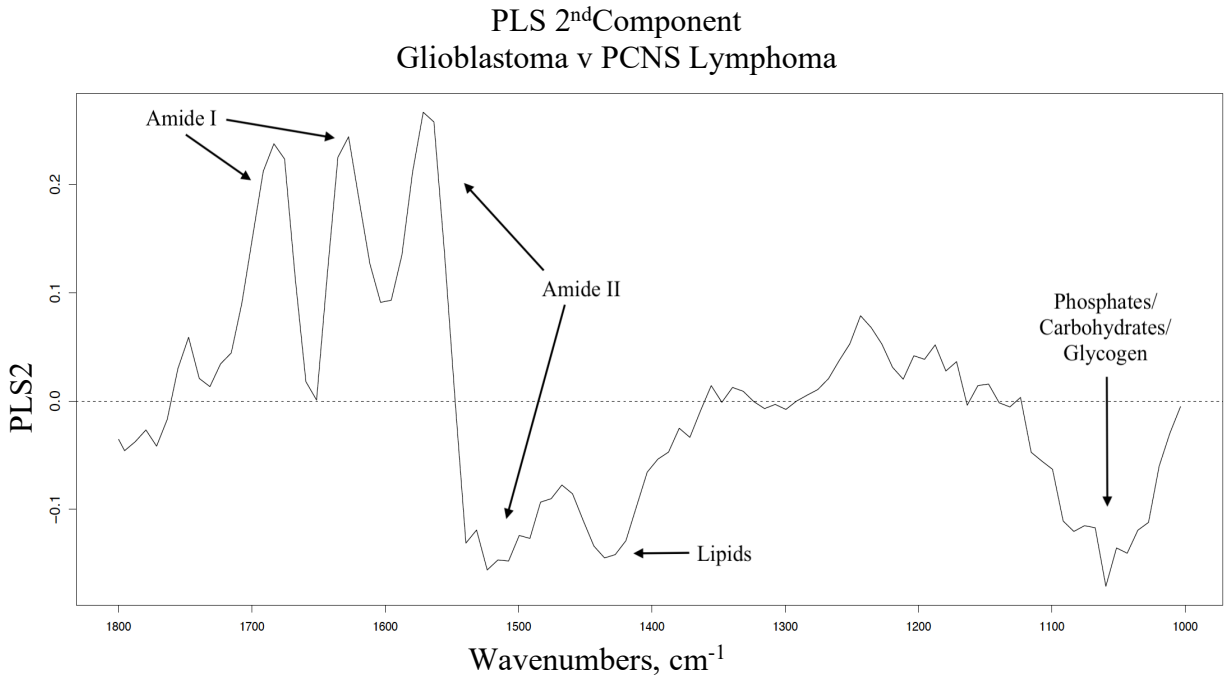

Figure 3.9 - Loadings plot for the 2nd PLS component in the PCNS lymphoma *versus* glioblastoma classification with tentative biological assignments.

For this particular dataset, the sensitivities refer to the ability to detect GBM, and the specificity relates to PCNSL. As shown in Table 3.9, the inferior model for this dataset was found to be RF – despite having a high sensitivity, the specificity was rather low at 70.8%. Although the balance between sensitivity and specificity could be tuned by optimising the probability threshold of the classifier, the fact that Kappa and balanced accuracy have significantly lower values than for the other models suggests that it would not change the rankings of the models. SVM combined with up-sampling performed well, reporting a balanced accuracy of 86.4%. The PLS-DA + SMOTE method seemed to be the optimal model, with a sensitivity of 90.1%, a specificity of 86.3%, and the highest κ value of all three models – mean $\kappa = 0.76$.

Table 3.9 - Statistical results for the GBM *versus* PCNSL test sets from the three different classification models with 51 iterations. SD, standard deviation.

	RF + SMOTE		**PLS-DA + SMOTE**		**SVM + UP**	
	Mean	**SD**	**Mean**	**SD**	**Mean**	**SD**
Kappa	0.63	0.13	0.76	0.09	0.72	0.11
Sensitivity (%)	90.9	5.8	90.1	5.7	86.6	8.5
Specificity (%)	70.8	14.9	86.3	9.4	86.3	9.5
Balanced Accuracy (%)	80.8	7.2	88.2	5.0	86.4	5.4

The sensitivities were relatively stable, but the predictions for PCNSL were more variable. For example, one of the RF resamples reported a sensitivity of 42%, which ultimately lowered the mean value. That said, the ROC curves for both the SVM-based and PLS-DA models still indicate promising diagnostic capability, with AUC values of ~0.9 (Figure 3.10). The RF ROC curve is substantially lower across sensitivity and specificity compared to the other two techniques, reporting a much lesser AUC value of 0.829, which coincides with the lower balanced accuracy from the RF classification. For this diagnostic test to be validated, it could be said that more patients would have to be introduced. However, these results indicate the potential for a serum diagnostic tool at the secondary care stage, that could aid clinicians when brain scans are inconclusive. Furthermore, it would be beneficial if this type of blood test could prevent patients undergoing unnecessary surgery.

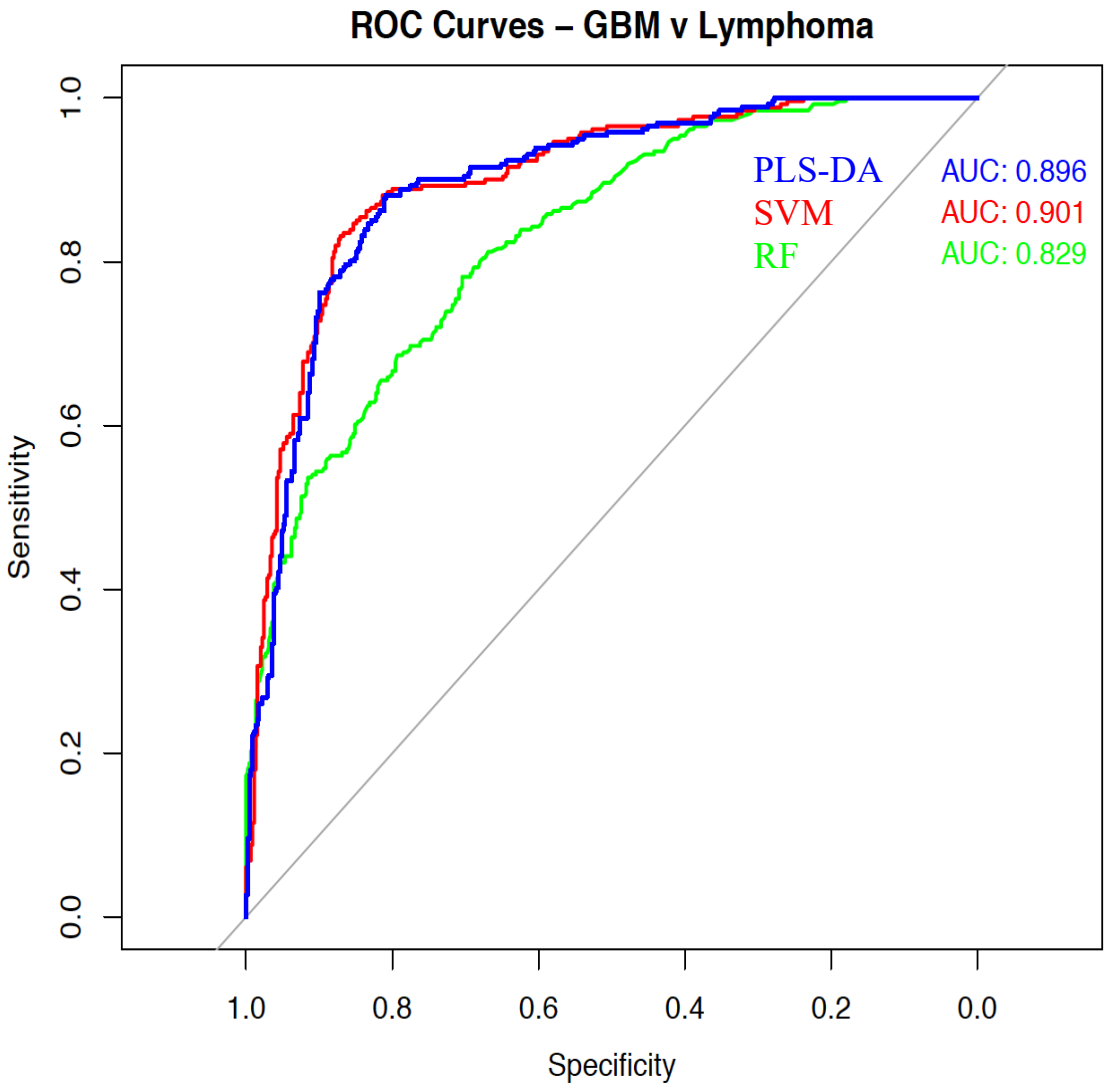

Figure 3.10 – ROC curve displaying trade-off between sensitivity and specificity of the three classification techniques for the glioblastoma vs lymphoma cohort: random forest; green, partial least squares-discriminant analysis; blue, support vector machine; red.

3.4 Conclusion

The implementation of a quick blood serum test for the early detection of brain tumours at a GP setting could have a huge impact on the quality of life and prognosis for patients. The traditional fixed diamond crystal limited the translation of the technique as the methodology was laborious, requiring long drying times and cleaning of the crystal between measurements [33]. An early health economic assessment in advance of prospective clinical data, stated the development of a high-throughput ATR accessory would be cost-effective to the UK's NHS if sensitivities and specificities >80% were achieved [38]. This study validates the capability of the novel ClinSpec Dx SIRE optical sample slides [41].

We report a sensitivity and specificity of 90.5% and 91.1% respectively when separating brain cancer patients from healthy controls, through PLS-DA. Despite the prevalence of brain tumours being extremely low (1.6%), the PLS-DA model reported a PPV of 14.2%. Three different machine learning techniques have been compared, all of which report balanced accuracies of ~90%, which would be deemed sufficient to be cost-effective to the NHS. Analysis of blood serum using this novel technique would fit ideally in the clinical pathway as a primary care triage tool for brain cancer. For the effective treatment of this disease, it is vital to identify the tumours early. A test at this stage in the diagnostic pathway would provide GPs with further information to inform their referral decision. If a positive result for cancer was reported from a spectroscopic triage test, then the 'at risk' patients would progress into secondary care quicker, whilst a negative result would provide

reassurance. The time taken to diagnose brain cancer patients could be reduced significantly, whilst also saving on NHS funds.

By training a classification algorithm on this known population, new patient samples can be predicted based upon the derivation of cancer signals from the retrospective dataset, providing an appropriate measure of the true diagnostic accuracy. The first prospective clinical study employing ATR-FTIR spectroscopy is presented in Butler *et al.* [41] which is the first initial analysis of an ongoing clinical study at the Western General Hospital, in Edinburgh.

Additionally, we present the ability of this technique to differentiate between brain tumour types. Notably, the separation of PCNSL and GBM through ATR-FTIR spectroscopy would be particularly attractive for neurologists in a secondary care setting, when imaging results are not clear. This proof-of-principle study involved 112 patients, providing a sensitivity of 90.1% and a specificity of 86.3%. These statistics are hugely promising, and a κ value of 0.76 indicates the technique is reliable. Further analysis with a larger cohort of patients would be valuable, in order to make the diagnostic model more robust.

Analysis of the ROC curves and consideration of the prevalence of the diseases to be diagnosed suggests that in some cases the models presented here could be optimised for clinical applications by modifying the probability threshold that each classifier uses to discriminate between positive and negative classes. For example, to identify brain tumours, which have low prevalence of ~1.6% in the clinical population [7],

the balance between sensitivity and specificity is important, since the probability that a positive test result is truly indicative of a brain tumour (i.e. PPV) increases rapidly with specificity. Nonetheless, we believe this kind of optimisation can be done more accurately once more is understood about the clinical population, which for the PCNSL *versus* GBM test in particular is not yet fully known. Therefore, the classifiers presented here all correspond to a default probability threshold of 0.5 used to discriminate between positive and negative classes, which is sufficient to demonstrate their efficacy.

The potential for high-throughput spectroscopy in the clinical environment goes further than purely brain tumour detection. With more research, this platform technology could address the clinical need for various malignancies and other diseases. There are also gaps for this technology in secondary care scenarios, for patient disease progression, treatment monitoring, and potentially aiding oncologists when MRI scans are inconclusive, as discussed in this study. The ultimate goal is to make the diagnostic pathways more efficient, cost effective and allow patients to obtain early treatment for optimal outcome.

3.5 References

[1] Cancer Research UK, 'Brain, other CNS and intracranial tumours statistics', *Accessed May 2019*, May 2019. https://www.cancerresearchuk.org/health-professional/cancer-statistics/statistics-by-cancer-type/brain-other-cns-and-intracranial-tumours/survival.

[2] N. G. Burnet, S. J. Jefferies, R. J. Benson, D. P. Hunt, and F. P. Treasure, 'Years of life lost (YLL) from cancer is an important measure of population burden — and should be considered when allocating research funds', *British Journal of Cancer*, vol. 92, no. 2, pp. 241–245, Jan. 2005, doi: 10.1038/sj.bjc.6602321.

[3] K. Spalding, R. Board, T. Dawson, M. D. Jenkinson, and M. J. Baker, 'A review of novel analytical diagnostics for liquid biopsies: spectroscopic and spectrometric serum profiling of primary and secondary brain tumors', *Brain and Behavior*, vol. 6, no. 9, p. e00502, Sep. 2016, doi: 10.1002/brb3.502.

[4] R. Latinovic, 'Headache and migraine in primary care: consultation, prescription, and referral rates in a large population', *Journal of Neurology, Neurosurgery & Psychiatry*, vol. 77, no. 3, pp. 385–387, Jul. 2005, doi: 10.1136/jnnp.2005.073221.

[5] The Brain Tumour Charity, 'Defeating Brain Tumours', *Accessed August 2017*, Aug. 2017. https://www.thebraintumourcharity.org/media/filer_public/49/b5/49b5e1d3-6cff-4399-9d7e-9fabbb5c76a3/the-strategy-publication-rgb-v3.pdf.

[6] The Brain Tumour Charity, 'Finding a Better way?', *Accessed August 2017*, Aug. 2017. http://cdn.basw.co.uk/upload/basw_21512-10.pdf.

[7] K. Zienius, R. Grant, and P. Brennan, 'Impact of Open access CT (OACT) for headache suspected of brain cancer in Lothian', *Neuro-Oncology*, vol. 20, no. suppl_1, pp. i8–i8, Jan. 2018, doi: 10.1093/neuonc/nox237.035.

[8] C.-H. Toh *et al.*, 'Primary Cerebral Lymphoma and Glioblastoma Multiforme: Differences in Diffusion Characteristics Evaluated with Diffusion Tensor Imaging', *AJNR Am J Neuroradiol*, vol. 29, no. 3, pp. 471–475, Mar. 2008, doi: 10.3174/ajnr.A0872.

[9] M. J. Baker *et al.*, 'Clinical applications of infrared and Raman spectroscopy: state of play and future challenges', *The Analyst*, vol. 143, no. 8, pp. 1735–1757, 2018, doi: 10.1039/C7AN01871A.

[10] H. J. Byrne *et al.*, 'Spectropathology for the next generation: Quo vadis?', *The Analyst*, vol. 140, no. 7, pp. 2066–2073, 2015, doi: 10.1039/C4AN02036G.

[11] K. Kong, C. Kendall, N. Stone, and I. Notingher, 'Raman spectroscopy for medical diagnostics — From in-vitro biofluid assays to in-vivo cancer detection', *Advanced Drug Delivery Reviews*, vol. 89, pp. 121–134, Jul. 2015, doi: 10.1016/j.addr.2015.03.009.

[12] W. Petrich, 'MID-INFRARED AND RAMAN SPECTROSCOPY FOR MEDICAL DIAGNOSTICS', *Applied Spectroscopy Reviews*, vol. 36, no. 2–3, pp. 181–237, Jun. 2001, doi: 10.1081/ASR-100106156.

[13] Perkin Elmer, 'FTIR Spectroscopy: Attenuated Total Reflectance (ATR)', *Accessed April 2018*. https://shop.perkinelmer.com/content/TechnicalInfo/TCH_FTIRATR.pdf.

[14] M. J. Baker *et al.*, 'Using Fourier transform IR spectroscopy to analyze biological materials', *Nature Protocols*, vol. 9, no. 8, pp. 1771–1791, Jul. 2014, doi: 10.1038/nprot.2014.110.
[15] B. R. Smith *et al.*, 'Combining random forest and 2D correlation analysis to identify serum spectral signatures for neuro-oncology', *Analyst*, vol. 141, no. 12, pp. 3668–3678, 2016.
[16] Z. Movasaghi, S. Rehman, and Dr. I. ur Rehman, 'Fourier Transform Infrared (FTIR) Spectroscopy of Biological Tissues', *Applied Spectroscopy Reviews*, vol. 43, no. 2, pp. 134–179, Feb. 2008, doi: 10.1080/05704920701829043.
[17] M. J. Walsh, S. E. Holton, A. Kajdacsy-Balla, and R. Bhargava, 'Attenuated total reflectance Fourier-transform infrared spectroscopic imaging for breast histopathology', *Vibrational Spectroscopy*, vol. 60, pp. 23–28, May 2012, doi: 10.1016/j.vibspec.2012.01.010.
[18] B. Bird, S. Remiszewski, A. Akalin, M. Kon, M. Diem, and others, 'Infrared spectral histopathology (SHP): a novel diagnostic tool for the accurate classification of lung cancer', *Laboratory investigation*, 92, 9, 1358, 2012.
[19] P. Lasch, W. Haensch, D. Naumann, and M. Diem, 'Imaging of colorectal adenocarcinoma using FT-IR microspectroscopy and cluster analysis', *Biochimica et Biophysica Acta (BBA) - Molecular Basis of Disease*, vol. 1688, no. 2, pp. 176–186, Mar. 2004, doi: 10.1016/j.bbadis.2003.12.006.
[20] M. J. Baker, E. Gazi, M. D. Brown, J. H. Shanks, P. Gardner, and N. W. Clarke, 'FTIR-based spectroscopic analysis in the identification of clinically aggressive prostate cancer', *British Journal of Cancer*, vol. 99, no. 11, pp. 1859–1866, Dec. 2008, doi: 10.1038/sj.bjc.6604753.
[21] E. Gazi *et al.*, 'A Correlation of FTIR Spectra Derived from Prostate Cancer Biopsies with Gleason Grade and Tumour Stage', *European Urology*, vol. 50, no. 4, pp. 750–761, Oct. 2006, doi: 10.1016/j.eururo.2006.03.031.
[22] F. Bonnier *et al.*, 'Screening the low molecular weight fraction of human serum using ATR-IR spectroscopy', *Journal of Biophotonics*, vol. 9, no. 10, pp. 1085–1097, Oct. 2016, doi: 10.1002/jbio.201600015.
[23] R. S. Tirumalai, K. C. Chan, D. A. Prieto, H. J. Issaq, T. P. Conrads, and T. D. Veenstra, 'Characterization of the Low Molecular Weight Human Serum Proteome', *Molecular & Cellular Proteomics*, vol. 2, no. 10, pp. 1096–1103, Oct. 2003, doi: 10.1074/mcp.M300031-MCP200.
[24] E. F. Petricoin, C. Belluco, R. P. Araujo, and L. A. Liotta, 'The blood peptidome: a higher dimension of information content for cancer biomarker discovery', *Nat. Rev. Cancer*, vol. 6, no. 12, pp. 961–967, 2006, doi: 10.1038/nrc2011.
[25] M. J. Baker *et al.*, 'Developing and understanding biofluid vibrational spectroscopy: a critical review', *Chemical Society Reviews*, vol. 45, no. 7, pp. 1803–1818, 2016.
[26] K. Dorling and M. J. Baker, 'Highlighting attenuated total reflection Fourier transform infrared spectroscopy for rapid serum analysis', *Trends in Biotechnology*, vol. 31, no. 6, pp. 325–327, Jun. 2013, doi: 10.1016/j.tibtech.2013.03.009.
[27] J. Backhaus *et al.*, 'Diagnosis of breast cancer with infrared spectroscopy from serum samples', *Vibrational Spectroscopy*, vol. 52, no. 2, pp. 173–177, Mar. 2010, doi: 10.1016/j.vibspec.2010.01.013.

[28] J. Ollesch, M. Heinze, H. M. Heise, T. Behrens, T. Brüning, and K. Gerwert, 'It's in your blood: spectral biomarker candidates for urinary bladder cancer from automated FTIR spectroscopy: Spectral cancer biomarkers from high-throughput FTIR spectroscopy', *Journal of Biophotonics*, vol. 7, no. 3–4, pp. 210–221, Apr. 2014, doi: 10.1002/jbio.201300163.
[29] K. Gajjar *et al.*, 'Fourier-transform infrared spectroscopy coupled with a classification machine for the analysis of blood plasma or serum: a novel diagnostic approach for ovarian cancer', *Analyst*, vol. 138, no. 14, pp. 3917–3926, 2013, doi: 10.1039/C3AN36654E.
[30] X. Zhang *et al.*, 'Profiling serologic biomarkers in cirrhotic patients via high-throughput Fourier transform infrared spectroscopy: toward a new diagnostic tool of hepatocellular carcinoma', *Translational Research*, vol. 162, no. 5, pp. 279–286, Nov. 2013, doi: 10.1016/j.trsl.2013.07.007.
[31] J. R. Hands *et al.*, 'Investigating the rapid diagnosis of gliomas from serum samples using infrared spectroscopy and cytokine and angiogenesis factors', *Analytical and Bioanalytical Chemistry*, vol. 405, no. 23, pp. 7347–7355, Sep. 2013, doi: 10.1007/s00216-013-7163-z.
[32] J. R. Hands *et al.*, 'Attenuated Total Reflection Fourier Transform Infrared (ATR-FTIR) spectral discrimination of brain tumour severity from serum samples: Serum spectroscopy gliomas', *Journal of Biophotonics*, vol. 7, no. 3–4, pp. 189–199, Apr. 2014, doi: 10.1002/jbio.201300149.
[33] J. R. Hands *et al.*, 'Brain tumour differentiation: rapid stratified serum diagnostics via attenuated total reflection Fourier-transform infrared spectroscopy', *Journal of Neuro-Oncology*, vol. 127, no. 3, pp. 463–472, May 2016, doi: 10.1007/s11060-016-2060-x.
[34] N. Ferrer, 'Forensic Science, Applications of IR Spectroscopy', in *Encyclopedia of Spectroscopy and Spectrometry*, Elsevier, 1999, pp. 603–615.
[35] F. Bonnier, F. Petitjean, M. J. Baker, and H. J. Byrne, 'Improved protocols for vibrational spectroscopic analysis of body fluids: Improved protocols for vibrational spectroscopic analysis of body fluids', *Journal of Biophotonics*, vol. 7, no. 3–4, pp. 167–179, Apr. 2014, doi: 10.1002/jbio.201300130.
[36] B. Stuart, 'Infrared Spectroscopy', in *Kirk-Othmer Encyclopedia of Chemical Technology*, John Wiley & Sons, Inc., Ed. Hoboken, NJ, USA: John Wiley & Sons, Inc., 2005.
[37] B. C. Smith, *Fundamentals of Fourier transform infrared spectroscopy*. Boca Raton, Fla.: CRC Press, 2011.
[38] E. Gray *et al.*, 'Health economic evaluation of a serum-based blood test for brain tumour diagnosis: exploration of two clinical scenarios', *BMJ Open*, vol. 8, no. 5, p. e017593, May 2018, doi: 10.1136/bmjopen-2017-017593.
[39] E. Karabudak *et al.*, 'Disposable Attenuated Total Reflection-Infrared Crystals from Silicon Wafer: A Versatile Approach to Surface Infrared Spectroscopy', *Analytical Chemistry*, vol. 85, no. 1, pp. 33–38, Jan. 2013, doi: 10.1021/ac302299g.
[40] M. Koç and E. Karabudak, 'History of spectroscopy and modern micromachined disposable Si ATR-IR spectroscopy', *Applied Spectroscopy Reviews*, vol. 53, no. 5, pp. 420–438, May 2018, doi: 10.1080/05704928.2017.1366341.

[41] H. J. Butler *et al.*, ‘A triage blood test for brain cancer: Development of high-throughput ATR-FTIR technology for rapid spectroscopic serum diagnostics’, *Accepted in Nature Communications*, Sep. 2019, doi: 10.1038/s41467-019-12527-5.
[42] L. Lovergne, G. Clemens, V. Untereiner, R. A. Lukaszweski, G. D. Sockalingum, and M. J. Baker, ‘Investigating optimum sample preparation for infrared spectroscopic serum diagnostics’, *Anal. Methods*, vol. 7, no. 17, pp. 7140–7149, 2015, doi: 10.1039/C5AY00502G.
[43] L. Lovergne *et al.*, ‘Biofluid infrared spectro-diagnostics: pre-analytical considerations for clinical applications’, *Faraday Discuss.*, vol. 187, pp. 521–537, 2016, doi: 10.1039/C5FD00184F.
[44] J. M. Cameron, H. J. Butler, D. S. Palmer, and M. J. Baker, ‘Biofluid spectroscopic disease diagnostics: A review on the processes and spectral impact of drying’, *Journal of biophotonics*, vol. 11, no. 4, p. e201700299, 2018.
[45] B. R. Smith, M. J. Baker, and D. S. Palmer, ‘PRFFECT: A versatile tool for spectroscopists’, *Chemometrics and Intelligent Laboratory Systems*, vol. 172, pp. 33–42, Jan. 2018, doi: 10.1016/j.chemolab.2017.10.024.
[46] RStudio Team, *RStudio: Integrated Development for R.* Boston, MA: RStudio Inc., 2015.
[47] H. J. Butler, B. R. Smith, R. Fritzsch, P. Radhakrishnan, D. S. Palmer, and M. J. Baker, ‘Optimised spectral pre-processing for discrimination of biofluids via ATR-FTIR spectroscopy’, *Analyst*, vol. 143, no. 24, pp. 6121–6134, 2018, doi: 10.1039/C8AN01384E.
[48] N. K. Afseth and A. Kohler, ‘Extended multiplicative signal correction in vibrational spectroscopy, a tutorial’, *Chemometrics and Intelligent Laboratory Systems*, vol. 117, pp. 92–99, Aug. 2012, doi: 10.1016/j.chemolab.2012.03.004.
[49] Bradley. Efron and R. J. Tibshirani, *An introduction to the bootstrap*. New York, N.Y.; London: Chapman & Hall, 1993.
[50] A. G. Lalkhen and A. McCluskey, ‘Clinical tests: sensitivity and specificity’, *Continuing Education in Anaesthesia Critical Care & Pain*, vol. 8, no. 6, pp. 221–223, Dec. 2008, doi: 10.1093/bjaceaccp/mkn041.
[51] K. H. Brodersen, C. S. Ong, K. E. Stephan, and J. M. Buhmann, ‘The Balanced Accuracy and Its Posterior Distribution’, in *2010 20th International Conference on Pattern Recognition*, Istanbul, Turkey, Aug. 2010, pp. 3121–3124, doi: 10.1109/ICPR.2010.764.
[52] A. J. Viera and J. M. Garrett, ‘Understanding Interobserver Agreement: The Kappa Statistic’, *Family Medicine*, p. 4.
[53] M. L. McHugh, ‘Interrater reliability: the kappa statistic’, *Biochem Med (Zagreb)*, vol. 22, no. 3, pp. 276–282, 2012.
[54] D. G. Altman and J. M. Bland, ‘Diagnostic tests 2: Predictive values’, *BMJ*, vol. 309, no. 6947, p. 102, Jul. 1994.
[55] A. M. Molinaro, ‘Diagnostic tests: how to estimate the positive predictive value’, *Neuro-Oncology Practice*, vol. 2, no. 4, pp. 162–166, Dec. 2015, doi: 10.1093/nop/npv030.
[56] S. K. Talluri, ‘Positive predictive value’, *BMJ*, vol. 339, no. sep23 1, pp. b3835–b3835, Sep. 2009, doi: 10.1136/bmj.b3835.

[57] SIMAFORE, ‘Managing unbalanced data for building machine learning models’, *Accessed March 2019*, Mar. 2019. http://www.simafore.com/blog/handling-unbalanced-data-machine-learning-models.
[58] N. V. Chawla, K. W. Bowyer, L. O. Hall, and W. P. Kegelmeyer, ‘SMOTE: Synthetic Minority Over-sampling Technique’, *Journal of Artificial Intelligence Research*, vol. 16, pp. 321–357, Jun. 2002, doi: 10.1613/jair.953.
[59] L. Breiman, ‘Random Forests’, *Machine Learning*, vol. 45, no. 1, pp. 5–32, Oct. 2001, doi: 10.1023/A:1010933404324.
[60] D. S. Palmer, N. M. O’Boyle, R. C. Glen, and J. B. O. Mitchell, ‘Random Forest Models To Predict Aqueous Solubility’, *J. Chem. Inf. Model.*, vol. 47, no. 1, pp. 150–158, Jan. 2007, doi: 10.1021/ci060164k.
[61] G. Louppe, ‘Understanding Random Forests; From Theory to Practice’, University of Liege, Liege, Belgium, 2014.
[62] Hong Han, Xiaoling Guo, and Hua Yu, ‘Variable selection using Mean Decrease Accuracy and Mean Decrease Gini based on Random Forest’, in *2016 7th IEEE International Conference on Software Engineering and Service Science (ICSESS)*, Beijing, China, Aug. 2016, pp. 219–224, doi: 10.1109/ICSESS.2016.7883053.
[63] L. C. Lee, C.-Y. Liong, and A. A. Jemain, ‘Partial least squares-discriminant analysis (PLS-DA) for classification of high-dimensional (HD) data: a review of contemporary practice strategies and knowledge gaps’, *Analyst*, vol. 143, no. 15, pp. 3526–3539, 2018, doi: 10.1039/C8AN00599K.
[64] R. G. Brereton and G. R. Lloyd, ‘Partial least squares discriminant analysis: taking the magic away’, *Journal of Chemometrics*, vol. 28, no. 4, pp. 213–225, Apr. 2014, doi: 10.1002/cem.2609.
[65] C. Cortes and V. Vapnik, ‘Support-Vector Networks’, *Machine Learning*, vol. 20, no. 3, pp. 273–297, Sep. 1995, doi: 10.1023/A:1022627411411.
[66] P. de Boves Harrington, ‘Support Vector Machine Classification Trees’, *Anal. Chem.*, vol. 87, no. 21, pp. 11065–11071, Nov. 2015, doi: 10.1021/acs.analchem.5b03113.
[67] S. Huang, N. Cai, P. P. Pacheco, S. Narrandes, Y. Wang, and W. Xu, ‘Applications of Support Vector Machine (SVM) Learning in Cancer Genomics’, *Cancer Genomics Proteomics*, vol. 15, no. 1, pp. 41–51, Feb. 2018, doi: 10.21873/cgp.20063.
[68] A. Ben-Hur and J. Weston, ‘A User’s Guide to Support Vector Machines’, in *Data Mining Techniques for the Life Sciences*, vol. 609, O. Carugo and F. Eisenhaber, Eds. Totowa, NJ: Humana Press, 2010, pp. 223–239.
[69] Towards Data Science, ‘Dealing with Imbalanced Classes in Machine Learning’, *Accessed March 2019*, Mar. 2019. https://towardsdatascience.com/dealing-with-imbalanced-classes-in-machine-learning-d43d6fa19d2.
[70] A. Barth and C. Zscherp, ‘What vibrations tell us about proteins’, *Quarterly Reviews of Biophysics*, vol. 35, no. 4, pp. 369–430, Nov. 2002, doi: 10.1017/S0033583502003815.
[71] K. Hajian-Tilaki, ‘Receiver Operating Characteristic (ROC) Curve Analysis for Medical Diagnostic Test Evaluation’, *Caspian J Intern Med*, vol. 4, no. 2, pp. 627–635, 2013.

Chapter 4

Stratifying Brain Tumour Histological Sub-types: The Application of ATR-FTIR Serum Spectroscopy in Secondary Care

James M. Cameron[1], Christopher Rinaldi[1], Holly J. Butler[2], Paul M. Brennan[3], Michael D. Jenkinson[4], Khaja Syed[5], Katherine Ashton[6], Timothy P. Dawson[6], David S. Palmer[2,7], Matthew J. Baker[1,2]

[1]WestCHEM, Department of Pure and Applied Chemistry, Technology and Innovation Centre, University of Strathclyde, 99 George St, Glasgow, G1 1RD, UK

[2]ClinSpec Diagnostics, University of Strathclyde, Technology and Innovation Centre, 99 George Street, Glasgow, G1 1RD, UK

[3]Translational Neurosurgery, Department of Clinical Neurosciences, Western General Hospital, Edinburgh, EH4 2XU, UK

[4]Institute of Translational Medicine, University of Liverpool & The Walton Centre NHS Foundation Trust, Lower Lane, Fazakerley, Liverpool, L9 7LJ, UK

[5]Walton Research Tissue Bank, Neurosciences Labs, The Walton Centre NHS Foundation Trust, Lower lane, Fazakerley, Liverpool, L9 7LJ, UK

[6]Neuropathology, Lancashire Teaching Hospitals NHS Trust, Royal Preston Hospital, Sharoe Green Lane North, Preston, Lancashire, PR2 9HT, UK

[7]WestCHEM, Department of Pure and Applied Chemistry, Thomas Graham Building, University of Strathclyde, 295 Cathedral Street, Glasgow, G1 1XL, UK

Published in: *Cancers,* 12 (7), (2020) 1710; doi: 10.3390/cancers12071710

Contribution: I conducted all experimental work; produced all figures; wrote and prepared the manuscript for publication.

Abstract

Patients living with brain tumours have the highest average years of life lost of any cancer, ultimately reducing average life expectancy by 20 years. Diagnosis depends on brain imaging and most often confirmatory tissue biopsy for histology. The majority of patients experience non-specific symptoms, such as headache, and may be reviewed in primary care on multiple occasions before diagnosis is made. Sixty-two per cent of patients are diagnosed on brain imaging performed when they deteriorate and present to the emergency department. Histological diagnosis from invasive surgical biopsy is necessary, prior to definitive treatment, because imaging techniques alone have difficulty in distinguishing between several types of brain cancer. However, surgery itself does not necessarily impact on tumour growth, and risks morbidity for the patient. Non-invasive tests that support stratification of tumour subtype would enhance early personalisation of treatment selection and prognostication, reducing the delay and risks associated with surgery for many patients.

Techniques involving vibrational spectroscopy, such as attenuated total reflection Fourier transform infrared (ATR-FTIR) spectroscopy, have previously demonstrated analytical capabilities for cancer diagnostics. In this study, infrared spectra from 641 blood serum samples obtained from brain cancer and control patients have been collected. Firstly, we highlight the capability of ATR-FTIR to distinguish between healthy controls and brain cancer at sensitivities and specificities above 90%, before defining subtle differences in protein secondary structures between patient groups through Amide I deconvolution. We successfully differentiate several

types of brain lesions (glioblastoma, meningioma, primary central nervous system lymphoma and metastasis) with balanced accuracies >80%. A reliable blood serum test capable of stratifying brain tumours would be of great value in secondary care applications.

4.1 Introduction

Brain cancer reduces a patient's average life expectancy by 20 years on average, the highest reduction of all cancers [1]. Although brain tumours are uncommon the annual incidence appears to be rising, with an increase of 19% in the United Kingdom (UK) between 2002 and 2014 [2]. Globally, around 330,000 people are diagnosed with a central nervous system (CNS) cancer per year, which equates to ~900 diagnoses every single day [3]. Fewer than 20% of patients survive beyond five years [4], which is considerably lower than other cancer types.

The current gold standard investigation for patients with a suspected brain tumour is MRI, however determining the exact brain tumour type is not possible from imaging alone [5], [6]. Some brain tumours pose particular imaging challenges, e.g. differentiating between glioma and primary CNS lymphoma (PCNSL). Consequently, oncological treatments (radiotherapy and chemotherapy) can only be initiated after histopathological diagnosis are obtained. This necessitates surgery (either resection or biopsy), and although surgery is the primary treatment option for most brain tumours, it is not always clinically indicated or appropriate. This includes patients with borderline performance status who might not benefit from treatment [7]. In patients where a biopsy is only required for histological diagnosis, the time taken to schedule and recover from surgery delays the instigation of definitive treatment.

The detection of brain cancer with a serum-based triage system would be well suited to the clinical environment. Serum analysis is already used in clinics, and a new test

could be readily integrated into the current clinical pathway [8]. A rapid blood test that can stratify brain tumour histological subtype would positively impact on the diagnosis and personalisation of patient treatment. Strategies for non-invasive assessment of tumour type, so-called liquid biopsy, have to date largely relied upon identification of cell-free tumour DNA (ctDNA) in circulating blood. This approach has met with significant technical challenges, as well as being expensive.

An alternative strategy uses vibrational spectroscopy, in particular Attenuated total reflection Fourier transform infrared (ATR-FTIR) spectroscopy, for serum analysis. ATR-FTIR is rapid, cheap and non-invasive, instruments are easy to operate, and the technique generates biochemical fingerprints from minute volumes of biological fluids. In FTIR spectroscopy, a sample is irradiated with infrared light which causes atomic displacements and molecular vibrations. The absorption of this light excites vibrational transitions of molecules, producing IR spectra that contain a vast amount of chemical and biological information [9]. Specifically, it provides qualitative interrogation of all infrared active macromolecular constituents of blood serum. It has been shown that biomolecular imbalances in biofluids can give an indication of disease states [10]. When coupled with complex data analysis systems, the technique has been shown to successfully detect various cancers [11]. Recently, we have employed this technology in a clinical study utilising a novel high-throughput approach, supporting the possibility of earlier detection of brain tumours by identifying which patients with non-specific symptoms of a possible brain tumour are most likely to actually have a tumour, demonstrating high sensitivity and specificity [12].

We have used this same FTIR and data analysis strategy to successfully differentiate between two types of brain tumours, glioblastoma (GBM) and PCNSL, which pose a dilemma in radiological diagnosis [13]. If we can differentiate likely tumour type across a broader range of tumour types when an intracranial abnormality is identified radiologically, this would enhance clinical decision and may reduce the need for some diagnostic investigations, such as full-body CT in patients with primary brain disease [14].

A simple and reliable blood test that is able to differentiate a range of primary brain tumours from brain metastases would be invaluable to neurologists in the secondary care setting. Thus, in this study we further expand our previous work by assessing various brain tumour subtypes – including meningioma, GBM and PCNSL – and for the first time we elucidate the capability of high-throughput ATR-FTIR to differentiate between GBM and brain metastases. The ability to predict the likely diagnosis through a combination of serum spectroscopy and brain imaging would have a major impact on the patient pathway, and would facilitate more timely treatment.

4.2 Materials and Methods

The methods used in this chapter are similar to those outlined in Chapter 3, section 3.2. Below is a brief summary of the experimental for this study.

4.2.1 Sample Collection and Preparation

A total of 641 retrospective serum samples were obtained from two biobanks; the Walton Centre NHS Trust (Liverpool, UK) and Royal Preston Hospital (Preston, UK). Ethical approval for this study was obtained (Walton Research Bank and BTNW/WRTB 13_01/ BTNW Application #1108). Figure 4.1 outlines the number of samples within the patient cohort for each category. A respectable balance of male and female patients has been included, with a widespread age range (Table A2.1, Appendix 2). Initially, individual brain tumour types were compared to healthy controls. The larger groups of brain tumour patients were analysed, followed by a breakdown of tumour types. The 'glioma' set was comprised of the tumours originating from glial cells; GBM, astrocytomas and oligodendrogliomas. The gliomas were contrasted to the meningioma samples, and then these two groups were then combined to form the 'primary' set, which was tested against the brain metastases. Some of the more abundant individual tumour types were then chosen for further analysis.

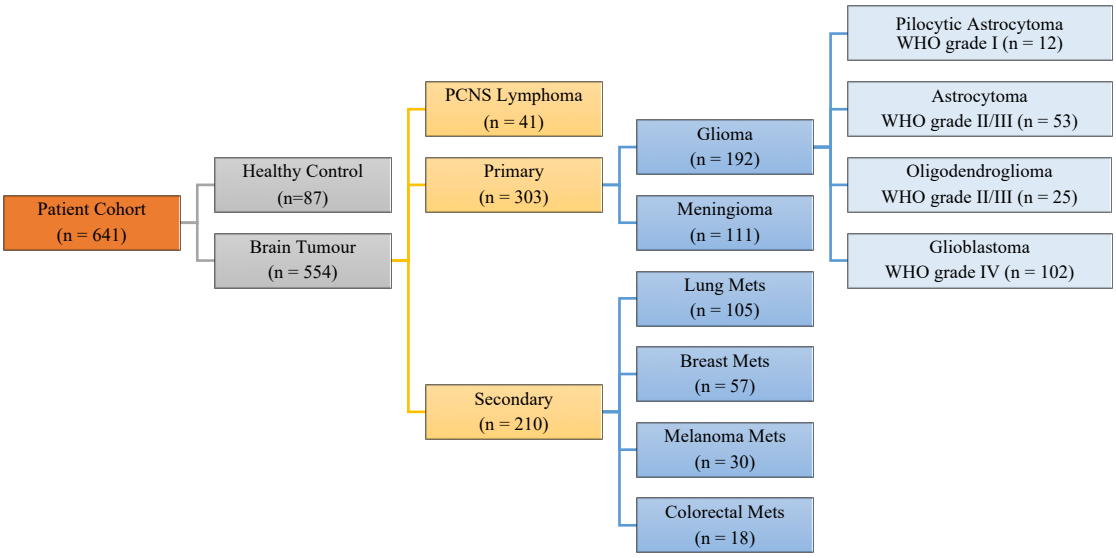

Figure 4.1 - Breakdown of the large brain cancer cohort with the number of patient samples used for the classifications.

Control patients were healthy individuals who had no history of cancer. Blood samples were collected in serum collection tubes and allowed to clot for up to one hour. The tubes were centrifuged for 15 minutes at 2200 *g*. The serum component was subsequently aliquoted then stored in a –80 °C freezer until the time of analysis. The cancer patients had a histopathologically confirmed brain tumour, but had not yet commenced chemo- or radiotherapy at the time of blood sample collection. The serum samples were removed from storage and thawed at room temperature (18-25 °C) for approximately 20 minutes prior to spectral analysis. 3 µL of serum from one individual patient was pipetted onto each of the three sample wells on a ClinSpecDx optical sample slide (ClinSpec Diagnostics Ltd., UK) [12]. The first well remained clean for background collection to subtract atmospheric conditions from the IR spectra. The serum drops were spread across the well in order to create thin homogeneous serum films. Prepared slides were stored in a drying unit incubator

(Thermo Fisher™ Heratherm™, GE) at 35 °C for 1 hour to control the drying process [15].

4.2.2 Spectral Collection

A Perkin Elmer Spectrum 2 FTIR spectrometer (Perkin Elmer, UK) was used for the spectral collection. A Specac Quest ATR accessory unit was fitted with a specular reflectance puck (Specac Ltd, UK). A slide indexing unit (ClinSpec Diagnostics Ltd., UK) automated the movement of the slides across the specular reflectance puck. With the first well acting as a background, the three sample wells provide the biological repeats. Each well was analysed in triplicate - resulting in nine spectra per patient. The spectra were acquired in the range 4000-450 cm^{-1}, at a resolution of 4 cm^{-1}, with 1 cm^{-1} data spacing and 16 co-added scans. In total 5769 spectra have been collected from all serum samples.

4.2.3 Spectral Analysis

Matlab has been used for the principal component analysis (PCA), and the PRFFECT toolbox within R Statistical Computing Environment software was utilised for the pre-processing and classifications [16]. Correcting for variation in baselines and using appropriate data reduction methods, such as binning and smoothing, can emphasise valuable biological information - such an approach is known as ‘pre-processing’ [17]. For the PCA, the spectral datasets were cut to the biologically relevant fingerprint region (1800-900 cm^{-1}), followed by a rubber band baseline correction and a vector normalisation. PCA is a relatively basic linear

transformation technique that is often used in spectroscopic studies. The main aim of a PCA analysis is to identify distinct patterns in complex data and detect a correlation between variables [18]. Ultimately, the dimensionality of large datasets is reduced, to clearly visualise the general variation achieved through scores and loadings plots.

Curve fitting analysis was carried out on MagicPlot (Magicplot Systems LLC) in order to unveil the hidden protein secondary structure bands concealed within the broad Amide I region. The mean absorbance and second derivative spectra of the control, GBM, PCNSL, metastasis and meningioma patient groups were processed using PRFFECT toolbox. A Savitzky-Golay filter was applied to reduce the noise, with the number of smoothing points set to 7. The curve-fitting procedure is based on the sum of Lorentzian functions, which exist at the location of overlapping peaks [19]. Thus, the positions of the minima observed in the second derivative spectra were used to calculate the position and intensity of the Lorentzian curves, which could then be tentatively assigned as various types of protein secondary structures.

Classifications were undertaken to recognise biological signatures from cohorts of patients with known tumour types, then predictions from 'unknown' tumour types were made using this information. Firstly, the spectra were suitably pre-processed. Using a trial-and-error approach, the optimal parameters for the classifications were established. An extended multiplicative signal correction (EMSC) was employed using a human pooled serum reference, followed by a spectral cut to 1800-1000 cm^{-1}. A min-max normalisation between 0 and 1, and a binning factor of 8 were applied.

To develop the models, patients were randomly split into training sets, consisting of 70% of the data, and test sets – the remaining 30%. Model hyperparameters were tuned to optimise the value of Cohen's Kappa coefficient (κ) for 5-fold cross-validation on the training sets. The optimised model was then used to make predictions for the spectra in the test sets. The majority vote amongst the nine spectra for each patient was reported as the diagnostic outcome. The classification models were retrained and tested on 100 different randomly selected training and test set partitions to provide a reliable measure of predictive accuracy with a low standard error. Due to the imbalances present when examining the different classes, up-sampling, down-sampling and synthetic minority over-sampling technique (SMOTE) were employed in the spectral analysis to reduce the bias in the classification models. Similar to the classification analysis reported in Chapter 3, random forest (RF), partial least squares – discriminant analysis (PLS-DA), and support vector machine (SVM) were employed in this study.

4.3 Results

4.3.1 Brain Tumour *versus* Healthy Control

4.3.1.1 Principal Component Analysis

PCA was first undertaken in order to explore the general variation between the controls and the individual brain tumour groups. The data was cut to the fingerprint region where biomolecules are known to vibrate (1800-900 cm^{-1}), before a rubberband baseline correction and vector normalisation were applied. Firstly, the GBM patients were compared to the healthy individuals (Figure 4.2). PC1 accounts for 52.3% of the general variation in the dataset, mainly from Amide I and II contributions, as shown in Figure 4.2b. Despite some slight overlap, the two groups separate across the 2nd principal component. The PC2 loadings also suggest this arises from the Amide I (CO and CN stretch, NH bending) and Amide II (NH bending, CN stretch) bands between 1500-1700 cm^{-1}. There were also contributions from the lower wavenumber region which represents the CO, CC and CH stretching modes from carbohydrates and glycogen, and the symmetric PO_2^- stretching vibrations within nucleic acids (1100-1000 cm^{-1}).

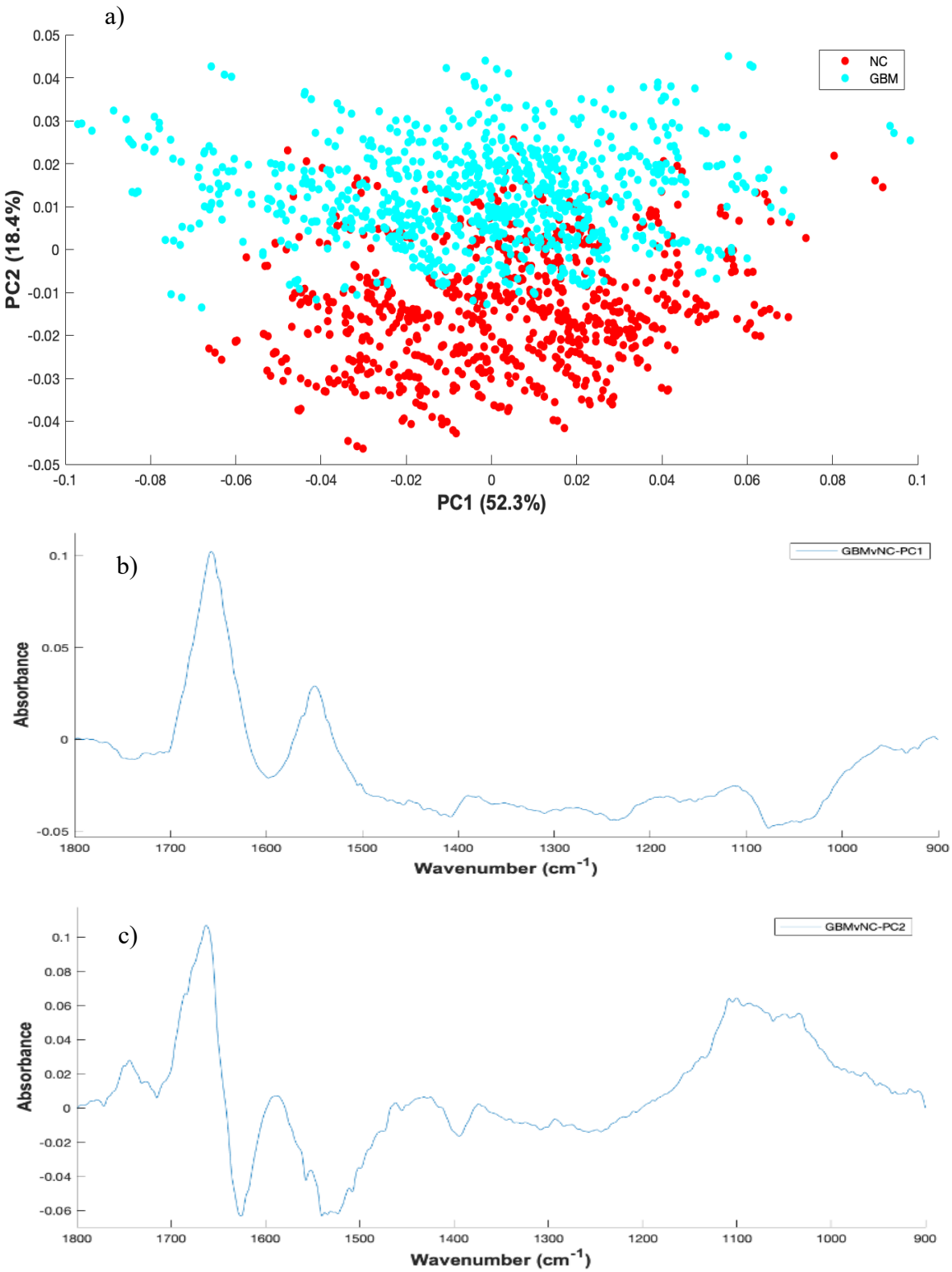

Figure 4.2 - Principal component analysis a) scores plot of PC1 and PC2 displaying the variance between GBM (blue) and healthy control (red); b) PC1 loadings and c) PC2 loadings describe which wavenumbers account for the most discrimination.

Meningioma, PCNSL and metastatic patient cohorts were also assessed individually against the control group. Figure A2.1 (Appendix 2) displays the PCA results for each of the comparisons. The scores plots and loadings presented are those that illustrate the most discrimination between classes. Similar to GBM, with the meningioma and PCNSL analysis we found that the PC2 suggested the most variance arose at the Amide I and II bands and at the phosphate, glycogen and carbohydrate region. The ~1030 cm^{-1} band is associated with the CO stretching and bending vibrations of glycogen and carbohydrates. Interestingly, the region around 1080-1000 cm^{-1} was shown to exhibit the highest discrepancies in the metastasis *versus* control set. This is consistent with a previous study, where this region was found to be distinctive when analysing normal and metastatic brain tumour tissue through FTIR imaging and linear discriminant analysis [23].

4.3.1.2 Amide I Deconvolution

The PCA analysis highlighted variances in Amide I absorbance between brain tumour groups, thus deconvolution analysis was undertaken to further explore these differences. A series of overlapping components that represent different structural elements are hidden within the broad Amide I band [24], [25]. For example, β-sheets involve two or more segments of a polypeptide chain lining up next to each other and form a sheet-like structure, as the C=O of one amino acid binds to the N-H of another through hydrogen bonding, whereas α-helices are assembled when the polypeptide chain twist into a spiral [26]. For the four brain tumour subtype groups and the control set, the mean Amide I absorbance spectra were subjected to a second derivative deconvolution in an attempt to better understand the nature of the

identified spectral differences. Figure 4.3 describes the second derivative spectra in the region between 1720-1590 cm^{-1} for each patient set, which suggests there are minute discrepancies at several points across the Amide I band, namely at ~1650 cm^{-1} and ~1638 cm^{-1}.

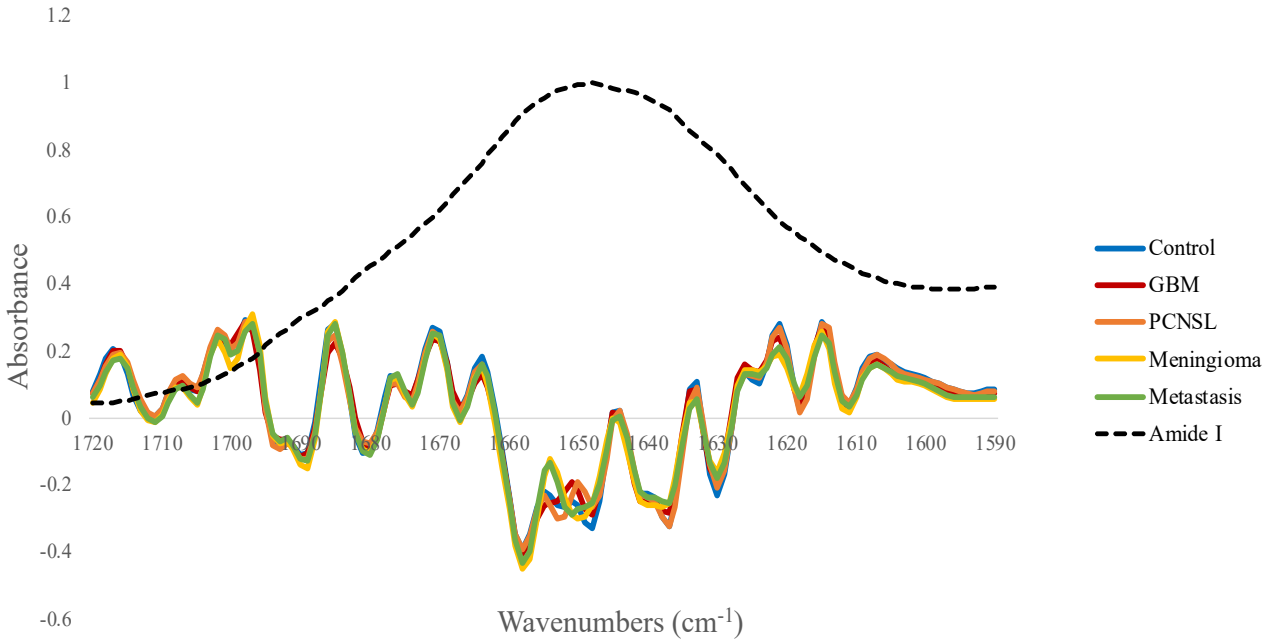

Figure 4.3 - The mean infrared absorbance and the second derivative spectra in the Amide I band (1720-1590 cm^{-1}) for the control, glioblastoma (GBM), PCNS lymphoma, meningioma and metastasis patient groups.

The position and intensity of the minima across the second derivative spectra represent those of the underlying protein bands, so it is possible to predict secondary structures using curve fitting. The deconvoluted Amide I profile for each of the patient groups are distinctly dissimilar, in terms of the number of bands and their relative positions and intensities. The curve fitting analysis is outlined in Figure 4.4, where the overlapping protein bands have been tentatively assigned as either α-helices, β-sheets, turns or random disordered structures with reference to the literature [25], [27].

Initially it seems all of the deconvoluted Amide peaks follow a similar trend. From left to right, β-sheets exist around 1700-1680 cm^{-1}; followed by turns ~1670 cm^{-1}; then the elevated α-helix bands and disordered structures between 1665 and 1645 cm^{-1}; and finally, additional β-sheet components from 1640 to 1600 cm^{-1}. On closer inspection it is clear that the profiles are rather disparate. Despite all patient groups consistently encompassing α-helix maxima, they all exist at fluctuating heights and positions. Interestingly, this region exhibited discrepancies in the second derivative spectra in Figure 4.3, corroborating the differences observed in the curve fitting analysis.

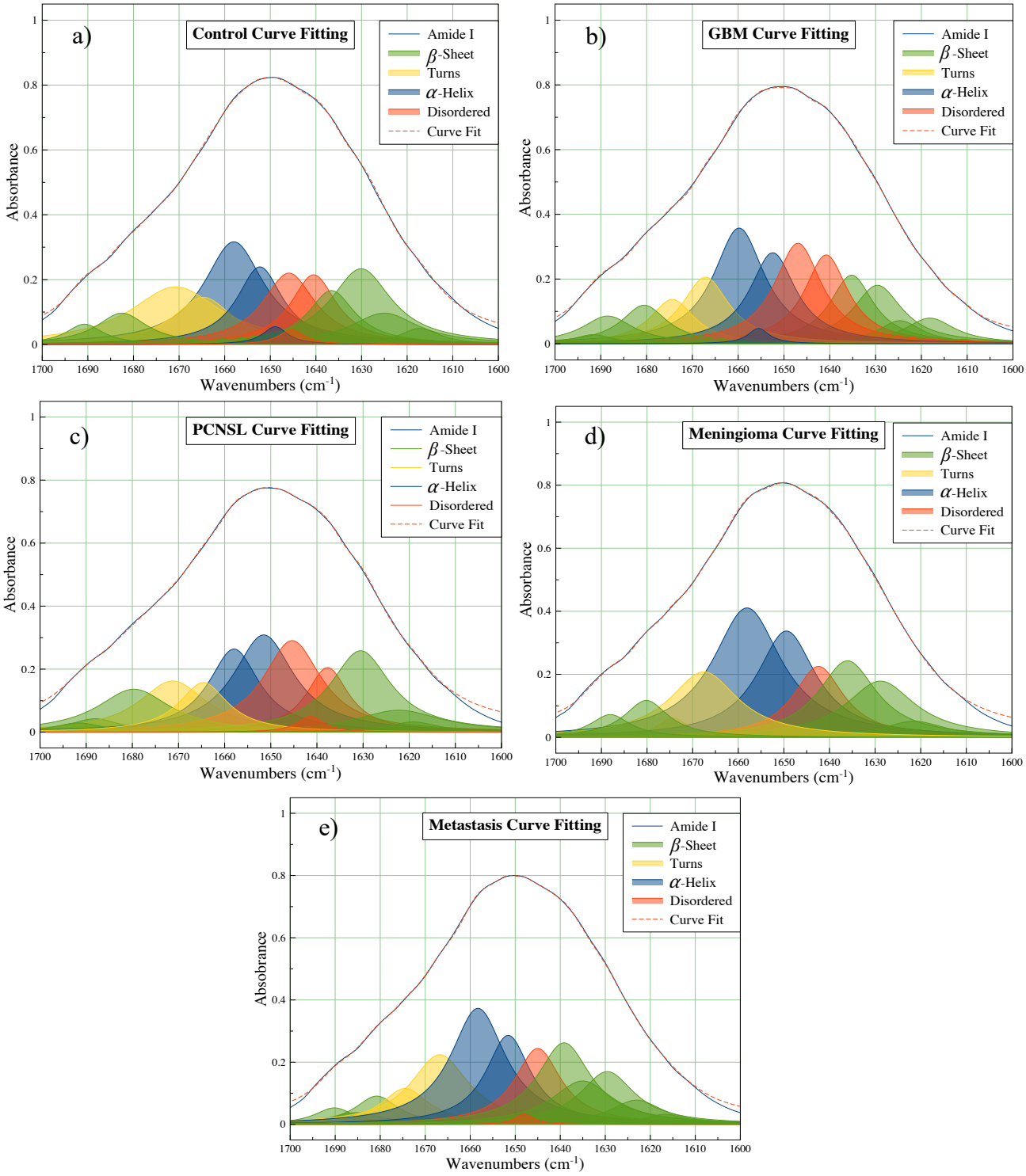

Figure 4.4 - Amide I curve fitting showing the summation of resolved second derivative bands relative to the absorption profile for the: a) control; b) GBM; c) PCNSL; d) meningioma and e) metastasis patient groups.

4.3.1.3 Partial Least Squares Discriminant Analysis

Based on our previous work [13], we used PLS-DA to classify each dataset and test the diagnostic performance. Initially each model was tested with no additional sampling, before using up, down and SMOTE sampling techniques to ensure there was no bias present within the classifications, which could be introduced by the imbalanced classes. The optimal value of *ncomp* for each model was determined from a tuning grid with a range of 1:20. The sampling method that produced the best results with 5 iterations was then chosen for 100 resamples, to generate the most accurate and reliable outcome. Table 4.1 outlines the PLS-DA results for each tumour type *versus* control dataset.

Table 4.1: Summary of PLS-DA results for brain tumours against controls. Sensitivity, specificity and balanced accuracy are reported as means and standard deviations (SD) calculated over 100 resamples.

Tumour type against healthy control (n=87)	**No. of patients**	**Sampling**	**Sensitivity (%)**		**Specificity (%)**		**Balanced accuracy (%)**	
			Mean	**SD**	**Mean**	**SD**	**Mean**	**SD**
GBM	96	No	95.5	4.3	94.9	4.2	95.2	2.9
PCNSL	41	Up	92.2	6.9	96.7	3.5	94.4	3.9
Meningioma	111	Up	94.7	3.7	98.4	2.2	96.6	2.0
Metastasis	210	Up	95.9	2.6	95.0	4.2	95.4	2.3

The analysed GBM *versus* control set contained 96 GBM patients and 87 controls, hence the sampling techniques – for equalising imbalanced patient groups – did not significantly improve the classification results. After 100 iterations, the PLS-DA model reported 95.5% and 94.9% for sensitivity and specificity, respectively. The SDs were minimal for both sensitivity and specificity (~4%), suggesting the model is robust and reproducible. Likewise, the ability to successfully pick out the PCNSL,

meningioma and metastatic patients from their respective training sets was also evident. The number of patients in these groups were not well matched, thus additional up sampling seemed to improve the performance of the models. The sensitivities after 100 resamples were 92.2% for PCNSL, 94.7% for meningioma and 95.9% for metastasis. The tests were also highly specific, with each model accurately predicting the healthy controls as non-cancer at specificities ≥ 95%.

The PLS scores plots were very similar to the PCA results, but they provided slightly better separation of the classes. Figure 4.5 shows the PLS scores plot between PLS1 and PLS2, and the loadings for the 1st PLS component based on the GBM *versus* control dataset. The PLS1 loadings in Figure 4.5b generally agree with the PCA loadings (Figure 4.2). The most discriminating regions in each of the four brain tumour subtypes *versus* control datasets were generally found between 1000-1100 cm^{-1} and 1500-1700 cm^{-1}, along with some minor lipidic contributions. The wavenumbers that were mainly responsible for all four classifications are outlined in Table 4.2 with their corresponding biological assignments and vibrational modes.

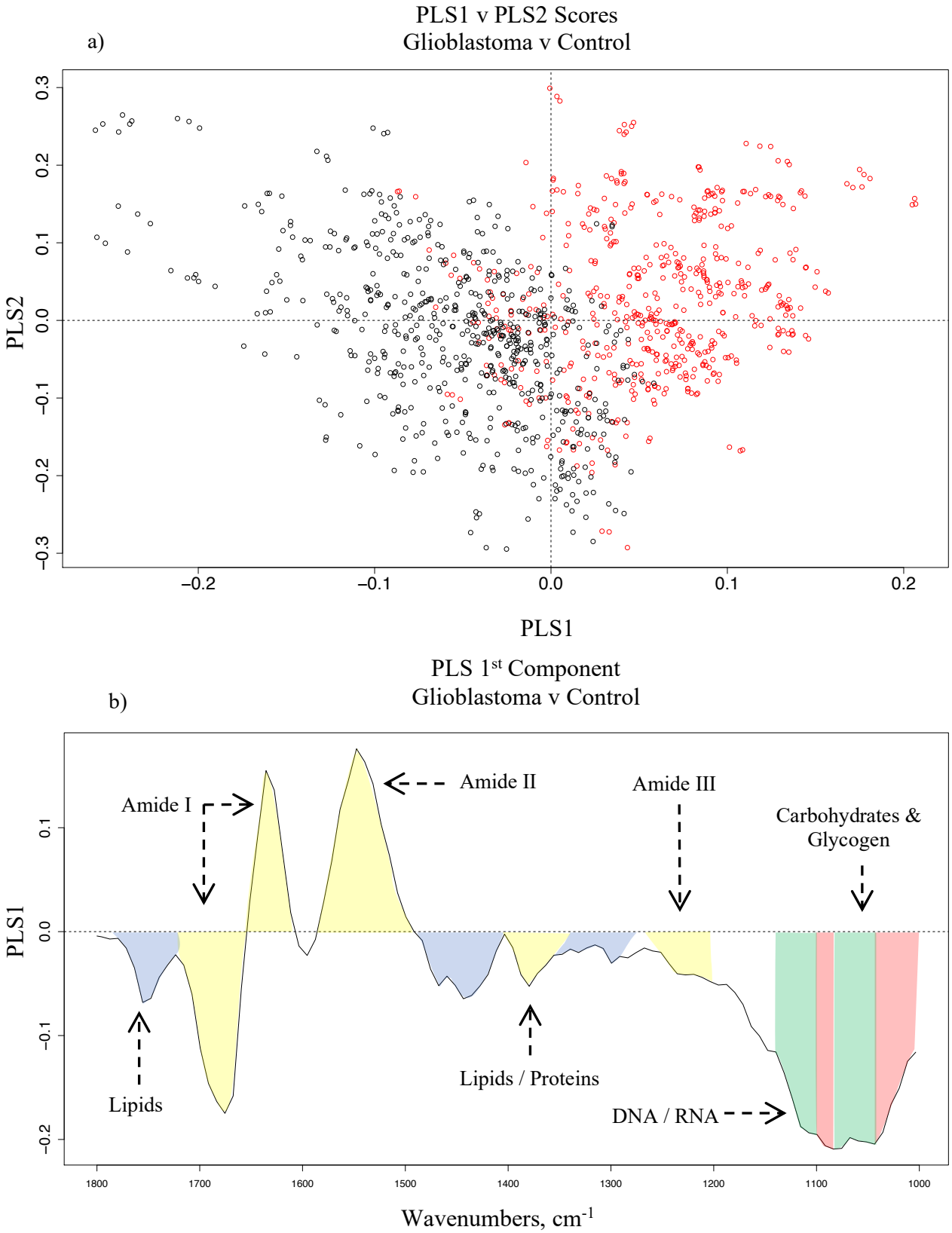

Figure 4.5 - a) the PLS scores plot between PLS1 and PLS2 for the glioblastoma (black) and control (red) dataset, and b) the loadings for the 1st PLS component with tentative biological assignments: lipids (blue), proteins (yellow), phosphates (green) and carbohydrates (red).

Table 4.2 - The main wavenumbers involved in each of the four brain tumour subtypes *versus* control classifications, with tentative biological assignments.

Approximate wavenumbers (cm^{-1})	***Tentative biological assignments***	***Vibrational modes***
1012	Carbohydrate	C-O stretch
1030	Glycogen	C-O and C-C stretch, C-OH deformation
1045	DNA and RNA	Symmetric PO_2^- stretch
1050	Carbohydrate/Glycogen	C-O-C stretching and bending
1050-1100	DNA and RNA	Symmetric PO_2^- stretch
1240-1310	Amide III of Proteins	N-H in plane bend, C-N stretch
1245	Phosphodiesters	Asymmetric PO_2^- stretch
1340	Phospholipids	CH_2 wagging
1400	Lipids/Proteins	CH_3 bending
1470	Lipids	CH_2 scissoring
1500-1600	Amide II of Proteins	N-H bending, C-N stretching
1600-1700	Amide I of Proteins	C=O and C-N stretch, N-H bending
1750	Lipids	C=O stretching

Overall, the classification results highlight the ability of ATR-FTIR to successfully differentiate individual brain tumour types from control serum samples with extremely high accuracies. A recent health economic assessment of current diagnostic practices suggested a serum-based test for the detection of brain tumours could be cost-effective to the NHS [28]. Thus, the results from this retrospective analysis indicate that this platform technology may be well suited to the clinical environment. Moreover, the Amide I deconvolution analysis has highlighted concealed differences in the proteinaceous structures of the different brain tumour types, suggesting that using similar classification techniques, it may also be possible to discriminate between brain lesions as well as brain tumour *versus* control.

4.3.2 Brain Tumour Differentiation

We next examined the ability of ATR-FTIR spectroscopy to distinguish the various brain tumour subtypes from each other, rather than individual brain tumour subtypes from controls. We built on our previously reported method to differentiate GBM and PCNSL [13], where RF, PLS-DA and linear SVM were utilised and compared. The SMOTE, up and down sampling techniques were initially tested with 5 resamples to combat the imbalanced classes, and the best model for each classification (Table A2.2, Appendix 2) was iterated 100 times for more reliable results. The optimum model is reported for each combination, in terms of sensitivity, specificity and balanced accuracy, with their corresponding standard deviations (Table 4.3).

Table 4.3 - The results from the optimal model for each brain tumour differentiation. Sensitivity, specificity and balanced accuracy are reported as means and standard deviations calculated over 100 resamples.

Classification (positive class v negative class)	**No. of patients**	**Model + Sampling**	**Sensitivity (%)**		**Specificity (%)**		**Balanced accuracy (%)**	
			Mean	**SD**	**Mean**	**SD**	**Mean**	**SD**
Primary v Metastasis	303 / 210	RF + up	90.9	3.1	66.4	5.5	78.8	2.8
Glioma v Meningioma	192 / 111	SVM + down	70.9	5.5	81.8	6.2	76.3	4.4
GBM v Meningioma	96 / 111	RF + no	94.4	5.1	83.4	5.6	88.9	3.0
Metastasis v GBM	210 / 96	SVM + down	84.3	3.8	96.2	3.4	90.3	2.6
Metastasis v PCNSL	210 / 41	PLS-DA + smote	91.5	3.1	91.1	9.2	91.3	4.6
Metastasis v Meningioma	210 / 111	PLS-DA + up	71.3	6.2	86.1	5.5	78.7	3.6

In each instance, the sensitivity refers to the positive class and the specificity refers to the negative class. For example, in the glioma *versus* meningioma classifier, the

sensitivity relates to glioma and the specificity is based on the meningioma predictions. The classification with the largest number of patients was the primary brain tumour (n = 303) *versus* brain metastasis (n = 210). The best model that was chosen for 100 resamples was the RF with additional up sampling, which provided a sensitivity of 90.9%. This model was evidently very capable of detecting the primary brain tumours within the test set, and on average only missed ~9 out of 90 patients in the resampled test sets. On the other hand, the RF model struggled to detect the metastatic brain tumours in this patient cohort, reporting a rather low mean specificity of 66.4%.

The Gini impurity metric was examined to identify the most important features within each dataset. The accuracy and reliability of the model can be determined from the RF statistical value outputs, with the Gini plot highlighting the main wavenumbers responsible for the results (Figure 4.6). Table 4.4 gives an overview of the top 15 identified wavenumbers in order of importance, with their corresponding wavenumber assignments and vibrational modes. As with the brain metastasis *versus* control results, the top two Gini values come from the lower wavenumber region around ~1050 cm^{-1}, which was found to show the most discrimination between the metastatic and primary tumour samples. The phosphate and CO stretching vibrations from nucleic material and phospholipids give rise to the bands in this region. Stretching of the carbonyl groups in proteins and lipids make up the rest of the top five wavenumbers. These areas of importance are closely followed by Amide I/II/III and lipidic vibrations, as well as contributions from glycogen and carbohydrates.

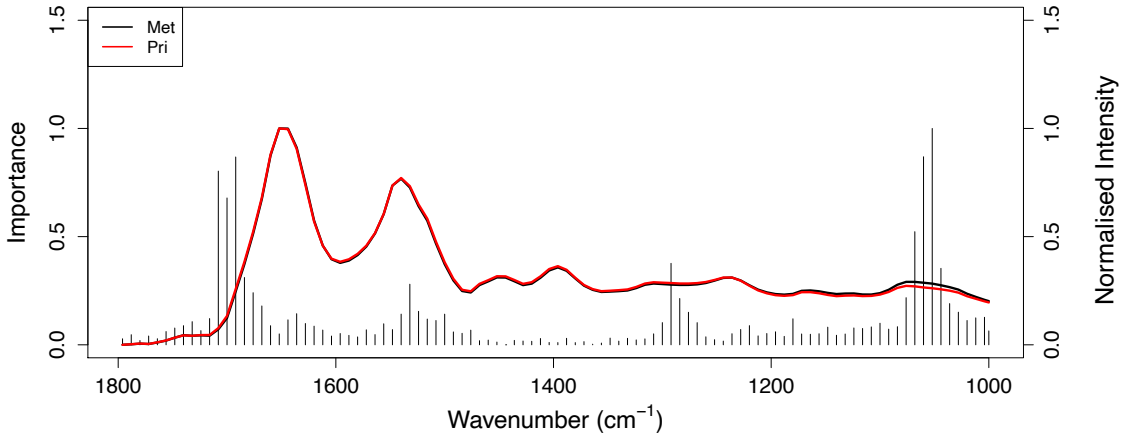

Figure – 4.6 - Gini plot outlining the most important features for the random forest classification between primary (Pri) and metastasis (Met).

Table 4.4 - The top 15 wavenumbers from the random forest classification between primary and metastasis with tentative biochemical assignments. The column "ΣGini" is a summation of the mean decrease in Gini for each wavenumber, over all nodes in all trees in the random forest ensemble, which suggests the regions of highest importance.

Wavenumbers (cm^{-1})	***ΣGini***	***Tentative biological Assignments***	***Vibrational Modes***
1052.5	123.47	DNA and RNA	Symmetric PO_2^- stretch
1060.5	107.86	Deoxyribose	C-O stretch
1692.5	107.74	Amide I of Proteins	C=O and C-N stretch, N-H bending
1708.5	99.96	Lipids/Fatty acid esters	C=O stretch
1700.5	85.15	Guanine/Thymine	C=O stretch
1068.5	66.56	Ribose/Nucleic acids	C-O stretch
1292.5	49.11	Amide III of Proteins	N-H in plane bend, C-N stretch
1044.5	46.36	Carbohydrate	C-O-C stretch and bending
1684.5	41.31	Amide I of Proteins	C=O and C-N stretch, N-H bending
1532.5	37.61	Amide II of Proteins	N-H bending, C-N stretching
1676.5	32.92	Amide I of Proteins	C=O and C-N stretch, N-H bending
1076.5	30.19	DNA and RNA	Symmetric PO_2^- stretch
1284.5	29.73	Phosphodiesters	Asymmetric PO_2^- stretch
1036.5	26.92	Carbohydrate/Glycogen	C-O and C-C stretch, C-OH deformation
1668.5	25.63	Amide I of Proteins	C=O and C-N stretch, N-H bending

The optimal results for glioma (n = 191) *versus* meningioma (n=111) were produced from a linear SVM with down sampling, where random selections of the glioma set were removed from the resampled training sets to have more evenly balanced classes. Down sampling has been criticised in the field for 'ignoring' potentially important information, but we overcome this by resampling the data as different random subsets of patients are removed in each iteration. Using this particular method, the SVM model was better at predicting the meningioma patients than picking out the gliomas, reporting a mean sensitivity of 70.2% and a mean specificity of 81.7%. A range of tumour grades are comprised within the glioma group, with lower grade tumours including grade I pilocytic astrocytoma, grade II astrocytomas and oligodendrogliomas, and the higher-grade gliomas dominated by GBMs (grade IV). On average ~16 of the 57 glioma samples in the test sets were misdiagnosed as meningioma, equivalent to a sensitivity of 70%. When the pilocytic astrocytomas, grade II astrocytomas and oligodendrogliomas were removed in order to focus on only GBM *versus* meningioma, the classification performance was greatly improved, with the sensitivity increasing to 94.4%.

One of the classifications that is of particular interest to clinicians is metastasis *versus* GBM. Tumours that transpire to be primary GBMs on histopathology can be confused radiologically with brain metastases [14]. For the resampled SVM model, the sensitivity (metastasis) was 84.3%, and the ability to detect GBM (specificity in this case) was 96.2%. Likewise, using PLS-DA, metastatic patients were separated from PCNSL and meningioma patients with mean balanced accuracies of 91.3% and 78.7%, respectively. Intriguingly, the lesser performance of the metastasis *versus*

meningioma model was not wholly unexpected. From the second derivative spectra and curve fitting analysis (Figures 4.3 and 4.4), it was noticed that their spectral signatures were relatively similar, hence a difficult classification was anticipated.

The receiver operating characteristic (ROC) curves each of the brain tumour differentiation models are outlined in Figure 4.7. The six models have varying diagnostic ability. The GBM *versus* meningioma, and the metastasis *versus* PCNSL PLS-DA models produce excellent ROC curves, achieving area under the curve (AUC) values >0.9. The metastasis *versus* GBM linear-SVM model is also highly promising, reporting an AUC of 0.896. Furthermore, the large cohort of primary *versus* metastasis and the metastasis *versus* meningioma have AUC values ~0.85. The glioma *versus* meningioma group yielded the poorest diagnostic capability, with the lowest AUC of 0.77. The AUC values coincide with the classification results in Table 4.3. Analysis of the ROC curves suggests that some of the presented models could be optimised for clinical applications. A default probability threshold value of 0.5 was used here to distinguish between brain tumour types. However, by varying the probability threshold that each classifier uses to discriminate between positive and negative classes, each model can be fine-tuned to obtain the greatest balance between sensitivity and specificity.

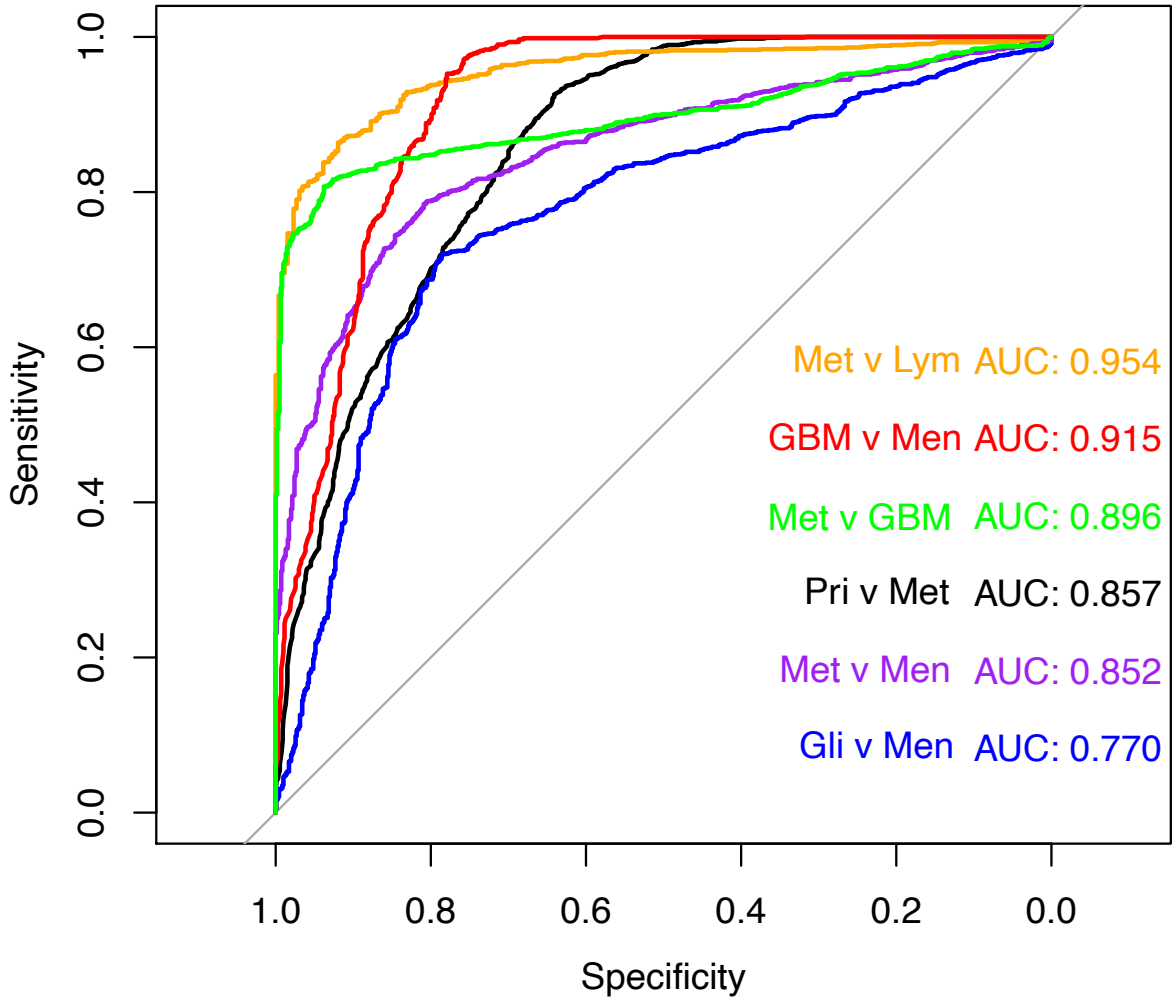

Figure 4.7 - Receiver operator curves displaying the trade-off between sensitivity and specificity for the best model of each of the six brain tumour classifiers: primary (Pri) *versus* metastasis (Met); black, glioma (Gli) *versus* meningioma (Men); blue, GBM *versus* meningioma; red, metastasis *versus* GBM; green, metastasis *versus* lymphoma (Lym); orange, metastasis *versus* meningioma; purple.

4.4 Discussion

The PCA results described differences between each patient group in the Amide region, which can be attributed to alterations in the levels of proteins. Many proteins exist as circulating markers of inflammation and angiogenesis. For example, C-reactive protein (CRP) and vascular endothelial growth factor (VEGF) were previously reported to be elevated in the plasma of GBM patients [29]. Likewise, various studies have highlighted serum YKL-40 as a potential blood-based biomarker for gliomas, with levels significantly higher in GBM patients in several cases [30], [31]. However, there are currently no protein-based biomarkers used for brain tumour differentiation and a signature approach as described here enables a full protein assay to be performed. Separation in PCA scores plots was less marked for the other tumour groups than the GBM *versus* control analysis. The chemokines, cytokines and other biomarkers that are associated with cancer exist in pg/mL concentrations in serum, and are obscured by larger protein molecules that are present in high concentration in both cancer and control patients [32], [33]. More robust supervised classification techniques are typically required to identify the most salient features within such complex datasets. That being said, PCA offers an unsupervised platform which can indicate specific regions of interest.

Through deconvolution of the Amide I bands, differences in the assignment of certain structures were observed between patient groups. The levels of β-sheets are higher in the PCNSL group when compared to the controls, as well as exhibiting a minor drop-off in α-helices. This is consistent with a previous study, that discriminated lymphoma and normal serum from mouse models [34]. In contrast,

there is a decrease in the β-sheet band (~1630 cm^{-1}) in the GBM patient group compared to the controls, plus a minor increase in α-helix intensity (~1660 cm^{-1}). Interestingly, the PLS1 loadings corroborate these differences (Figure 4.5b); which defines the variation between the two classes where the GBM patients are the negative cluster and the controls are the positive group, as shown in the scores plot between PLS1 and PLS2 (Figure 4.5a). When considering the control set, the higher level of β-sheets is described by the intense positive loading at ~1630 cm^{-1}, whilst the minor increase in GBM α-helix intensity is observed in the large negative loading around 1660 cm^{-1}. Similar findings have been observed recently in a study that utilised synchrotron-based IR micro-spectroscopy to analyse human gliomas, and which demonstrated a rise in the α-helix content while the content of β-sheets decreased with increasing malignancy grade [35]. For the meningioma and metastasis groups, the second derivative spectra were somewhat overlaid (blue and green lines in Figure 4.3), and their deconvoluted bands also seemed to exhibit some noticeable similarities – the intensities of the four largest bands followed the same pattern: two high intensity α-helices at ~1658 and ~1650 cm^{-1}, the disordered structure at ~1645 cm^{-1} and a β-sheet at ~1637 cm^{-1} with a similar intensity of ~0.25 on the absorbance scale (Figure 4.4d and 4.4e).

The alterations in protein secondary structures between the mean spectra of respective patient cohorts reflect major biochemical differences in serum content associated with each tumour group. However, blood serum is a complex medium which naturally fluctuates between individuals [36]. Hence, the assumption that protein content is irrefutably consistent within patient groups is a slight

generalisation. Nevertheless, the technique offers a further insight into the potential variances between the patient groups that have been highlighted through the loadings from PCA and PLS analysis. Furthermore, deconvolution analysis is sensitive to the pre-processing and second derivative parameters that are applied, and indeed these were consistent for this analysis and there are well-defined differences between tumour types.

It is well recognised the systemic response of cancer impacts patients' spectral signatures, which is evident in IR spectroscopy [37], [38]. In the case of primary brain tumour *versus* metastasis (Figure 4.6), it may be that the blood composition of the metastasis patients differs slightly from those with brain primaries. One plausible theory is that the levels of cell-free circulating tumour DNA and RNA (ctRNA), and circulating microRNAs (miRNA) are elevated in the bloodstream as a result of the systemic cancer, which could account for the increase in nucleic acid-related absorbance in their spectral serum profile [39]–[43]. This particular test is of great interest, as if it was possible to tell at an early stage whether a suspected brain tumour was more likely to be a brain primary or a metastatic secondary lesion, it would be both cost- and time-effective for NHS, with primary brain tumour patients not requiring further diagnostic body imaging. There are variety of metastatic brain tumours arising from different primary cancers (e.g. breast, lung, etc.) within this population. It could be that certain types of lesions have more spectral similarities than others, thus breaking the cohort down into subgroups may benefit classification performance. That said, a balanced accuracy of 78.8% is respectable, and with more thorough tuning of the classification models and by modifying the probability

threshold, the sensitivity and specificity could potentially balance out. Moreover, the accuracy could potentially improve with a larger population of metastatic patients.

Likewise, it is unclear exactly why the other glioma types were assigned to the meningioma class, though it could potentially be due to them having a lower growth potential and mitotic activity. This may be reflected by the systemic response to tumour grade, which could influence the respective spectral profiles. As many of the oligodendrogliomas, astrocytomas and meningiomas range between grade I-III, their spectroscopic signature may be more alike than the more aggressive grade IV lesion of GBM.

4.5 Conclusion

In this study, we have assessed serum from patients with various brain tumours, by comparing and contrasting their spectral signatures against each other, as well as against healthy controls. GBM, PCNSL, meningioma and brain metastases have been successfully separated from control patients through PLS-DA, all with sensitivities and specificities greater than 92%. Deconvolution of their respective mean Amide I bands highlighted subtle variations in the levels of various protein secondary structures within each tumour type. Hence, further classifications between the lesion classes were fulfilled, presenting some very encouraging results. Despite a relatively low specificity, the primary *versus* metastasis cohort showed some initial promise, with the RF model being able to pick out 90.9% of the 'primary' brain tumour samples within the resampled test sets. Most other classifiers performed remarkably well for the brain tumour differentiations, achieving balanced accuracies around 80%. Notably, the metastasis *versus* GBM linear-SVM classifier reported an 84.3% sensitivity, a 96.2% specificity and a ROC curve with an AUC value of ~0.9, suggesting that the model has high diagnostic capability. Due to their similar features on MRI scans, implementing serum spectroscopy alongside imaging protocols could help differentiate brain metastases from GBM, as well as other tumours with similar radiological appearances, e.g. PCNSL [13], [14], [44].

A simple and reliable blood test that is able to differentiate a range of primary brain tumour types from brain metastases, would lead to a paradigm shift in the clinical management of brain tumour patients. Our findings suggest this is feasible, and by using basic serum spectroscopic analysis - despite the fact that some of our sample

sets had relatively low numbers of patients - all of the presented models achieve balanced accuracies greater than 75% (Appendix 2, Figure A2.2). The ability to provide the likely diagnosis based on a blood test, and when combined with radiological assessment, would have a major impact on the patient pathway and would facilitate more timely treatment in the hospital care setting.

For these proof-of-concept tests to be validated, the models must be used to predict tumour type in prospective patients already within the current diagnostic pathway, although these results indicate the potential for a serum diagnostic tool at both the primary and hospital care stage. This would initially fast-track patients who are in urgent need of referral and brain imaging, whilst reassuring those who have a negative test result and reduce the number of patients who would normally be sent for unnecessary brain scans. Likewise, stratification of brain tumour type through serum spectroscopy would assist clinicians when brain scans are inconclusive and the primary tumour type is uncertain, and furthermore would prevent patients undergoing avoidable surgical biopsy and/or further MRI and CT imaging. The results of our study show great potential to improve the diagnostic pathway for patients with brain tumours.

References

[1] N. G. Burnet, S. J. Jefferies, R. J. Benson, D. P. Hunt, and F. P. Treasure, 'Years of life lost (YLL) from cancer is an important measure of population burden — and should be considered when allocating research funds', *British Journal of Cancer*, vol. 92, no. 2, pp. 241–245, Jan. 2005, doi: 10.1038/sj.bjc.6602321.

[2] Brain Tumour Research, 'Report on National Research Funding', 2016.

[3] A. P. Patel *et al.*, 'Global, regional, and national burden of brain and other CNS cancer, 1990–2016: a systematic analysis for the Global Burden of Disease Study 2016', *The Lancet Neurology*, vol. 18, no. 4, pp. 376–393, Apr. 2019, doi: 10.1016/S1474-4422(18)30468-X.

[4] Brain Tumour Research, 'Brain Tumour Research', *Accessed September 2017*, Sep-2017. [Online]. Available: https://www.braintumourresearch.org/campaigning/stark-facts?gclid=CjwKCAiAp5nyBRABEiwApTwjXkb2HvKCz7rHEiQBR4swacKw6zZK3X3d6Fj6W0p8TGOfm_Ab6VNhURoCplgQAvD_BwE.

[5] P.-F. Yan *et al.*, 'Accuracy of conventional MRI for preoperative diagnosis of intracranial tumors: A retrospective cohort study of 762 cases', *International Journal of Surgery*, vol. 36, pp. 109–117, Dec. 2016, doi: 10.1016/j.ijsu.2016.10.023.

[6] W. B. Pope and G. Brandal, 'Conventional and advanced magnetic resonance imaging in patients with high-grade glioma', *Q J Nucl Med Mol Imaging*, vol. 62, no. 3, Sep. 2018, doi: 10.23736/S1824-4785.18.03086-8.

[7] C. Giannini, A. Dogan, and D. R. Salomão, 'CNS Lymphoma: A Practical Diagnostic Approach', *J Neuropathol Exp Neurol*, vol. 73, no. 6, pp. 478–494, Jun. 2014, doi: 10.1097/NEN.0000000000000076.

[8] I. Infusino and M. Panteghini, 'Serum albumin: Accuracy and clinical use', *Clinica Chimica Acta*, vol. 419, pp. 15–18, Apr. 2013, doi: 10.1016/j.cca.2013.01.005.

[9] B. Stuart, *Biological applications of infrared spectroscopy*. Chichester ; New York: John Wiley & Sons, 1997.

[10] M. J. Baker *et al.*, 'Using Fourier transform IR spectroscopy to analyze biological materials', *Nature Protocols*, vol. 9, no. 8, pp. 1771–1791, Jul. 2014, doi: 10.1038/nprot.2014.110.

[11] G. Bellisola and C. Sorio, 'Infrared spectroscopy and microscopy in cancer research and diagnosis', *American journal of cancer research*, vol. 2, no. 1, p. 1, 2012.

[12] H. J. Butler *et al.*, 'Development of high-throughput ATR-FTIR technology for rapid triage of brain cancer', *Nature Communications*, vol. 10, no. 1, p. 4501, Oct. 2019, doi: 10.1038/s41467-019-12527-5.

[13] J. M. Cameron *et al.*, 'Developing infrared spectroscopic detection for stratifying brain tumour patients: glioblastoma multiforme *vs.* lymphoma', *Analyst*, vol. 144, no. 22, pp. 6736–6750, 2019, doi: 10.1039/C9AN01731C.

[14] S. Campos *et al.*, 'Brain metastasis from an unknown primary, or primary brain tumour? A diagnostic dilemma', *Current Oncology*, vol. 16, no. 1, p. 62, 2009.

[15] J. M. Cameron, H. J. Butler, D. S. Palmer, and M. J. Baker, 'Biofluid spectroscopic disease diagnostics: A review on the processes and spectral

impact of drying', *Journal of Biophotonics*, vol. 11, no. 4, p. e201700299, Apr. 2018, doi: 10.1002/jbio.201700299.
[16] B. R. Smith, M. J. Baker, and D. S. Palmer, 'PRFFECT: A versatile tool for spectroscopists', *Chemometrics and Intelligent Laboratory Systems*, vol. 172, pp. 33–42, Jan. 2018, doi: 10.1016/j.chemolab.2017.10.024.
[17] H. J. Butler, B. R. Smith, R. Fritzsch, P. Radhakrishnan, D. S. Palmer, and M. J. Baker, 'Optimised spectral pre-processing for discrimination of biofluids via ATR-FTIR spectroscopy', *Analyst*, vol. 143, no. 24, pp. 6121–6134, 2018, doi: 10.1039/C8AN01384E.
[18] H. Abdi and L. J. Williams, 'Principal component analysis: Principal component analysis', *WIREs Comp Stat*, vol. 2, no. 4, pp. 433–459, Jul. 2010, doi: 10.1002/wics.101.
[19] S. Karthikeyan and R. Easwaran, 'Analysis of a curve fitting model in the amide region applied to the muscle tissues of an edible fish: Labeo rohita fingerlings', *JBPC*, vol. 13, no. 4, pp. 125–130, Dec. 2013, doi: 10.4024/13KA13A.jbpc.13.04.
[20] L. Breiman, 'Random Forests', *Machine Learning*, vol. 45, no. 1, pp. 5–32, Oct. 2001, doi: 10.1023/A:1010933404324.
[21] D. Ballabio and V. Consonni, 'Classification tools in chemistry. Part 1: linear models. PLS-DA', *Analytical Methods*, vol. 5, no. 16, p. 3790, 2013, doi: 10.1039/c3ay40582f.
[22] S. Huang, N. Cai, P. P. Pacheco, S. Narrandes, Y. Wang, and W. Xu, 'Applications of Support Vector Machine (SVM) Learning in Cancer Genomics', *Cancer Genomics Proteomics*, vol. 15, no. 1, pp. 41–51, Feb. 2018, doi: 10.21873/cgp.20063.
[23] C. Krafft, L. Shapoval, S. B. Sobottka, G. Schackert, and R. Salzer, 'Identification of Primary Tumors of Brain Metastases by Infrared Spectroscopic Imaging and Linear Discriminant Analysis', *Technology in Cancer Research & Treatment*, vol. 5, no. 3, pp. 291–298, Jun. 2006, doi: 10.1177/153303460600500311.
[24] S. E. Glassford, B. Byrne, and S. G. Kazarian, 'Recent applications of ATR FTIR spectroscopy and imaging to proteins', *Biochimica et Biophysica Acta (BBA) - Proteins and Proteomics*, vol. 1834, no. 12, pp. 2849–2858, Dec. 2013, doi: 10.1016/j.bbapap.2013.07.015.
[25] J. Kong and S. Yu, 'Fourier Transform Infrared Spectroscopic Analysis of Protein Secondary Structures', *Acta Biochimica et Biophysica Sinica*, vol. 39, no. 8, pp. 549–559, Aug. 2007, doi: 10.1111/j.1745-7270.2007.00320.x.
[26] J. M. Berg, J. L. Tymoczko, and L. Stryer, 'Secondary Structure: Polypeptide Chains Can Fold Into Regular Structures Such as the Alpha Helix, the Beta Sheet, and Turns and Loops', in *Biochemistry*, 5th ed., New York: W.H. Freeman, 2002.
[27] A. Barth, 'Infrared spectroscopy of proteins', *Biochimica et Biophysica Acta (BBA) - Bioenergetics*, vol. 1767, no. 9, pp. 1073–1101, Sep. 2007, doi: 10.1016/j.bbabio.2007.06.004.
[28] E. Gray *et al.*, 'Health economic evaluation of a serum-based blood test for brain tumour diagnosis: exploration of two clinical scenarios', *BMJ Open*, vol. 8, no. 5, p. e017593, May 2018, doi: 10.1136/bmjopen-2017-017593.

[29] G. Reynés *et al.*, 'Circulating markers of angiogenesis, inflammation, and coagulation in patients with glioblastoma', *J Neurooncol*, vol. 102, no. 1, pp. 35–41, Mar. 2011, doi: 10.1007/s11060-010-0290-x.
[30] A. Hormigo *et al.*, 'YKL-40 and Matrix Metalloproteinase-9 as Potential Serum Biomarkers for Patients with High-Grade Gliomas', *Clinical Cancer Research*, vol. 12, no. 19, pp. 5698–5704, Oct. 2006, doi: 10.1158/1078-0432.CCR-06-0181.
[31] F. M. Iwamoto *et al.*, 'Serum YKL-40 is a marker of prognosis and disease status in high-grade gliomas', *Neuro-Oncology*, vol. 13, no. 11, pp. 1244–1251, Nov. 2011, doi: 10.1093/neuonc/nor117.
[32] R. Albulescu *et al.*, 'Cytokine Patterns in Brain Tumour Progression', *Mediators of Inflammation*, vol. 2013, pp. 1–7, 2013, doi: 10.1155/2013/979748.
[33] B. E. Lippitz and R. A. Harris, 'Cytokine patterns in cancer patients: A review of the correlation between interleukin 6 and prognosis', *OncoImmunology*, vol. 5, no. 5, p. e1093722, May 2016, doi: 10.1080/2162402X.2015.1093722.
[34] H. Ghimire, M. Venkataramani, Z. Bian, Y. Liu, and A. G. U. Perera, 'ATR-FTIR spectral discrimination between normal and tumorous mouse models of lymphoma and melanoma from serum samples', *Sci Rep*, vol. 7, no. 1, p. 16993, Dec. 2017, doi: 10.1038/s41598-017-17027-4.
[35] A. D. Surowka, D. Adamek, and M. Szczerbowska-Boruchowska, 'The combination of artificial neural networks and synchrotron radiation-based infrared micro-spectroscopy for a study on the protein composition of human glial tumors', *Analyst*, vol. 140, no. 7, pp. 2428–2438, 2015, doi: 10.1039/C4AN01867B.
[36] E. F. Petricoin, C. Belluco, R. P. Araujo, and L. A. Liotta, 'The blood peptidome: a higher dimension of information content for cancer biomarker discovery', *Nat. Rev. Cancer*, vol. 6, no. 12, pp. 961–967, 2006, doi: 10.1038/nrc2011.
[37] W. Petrich, 'mid-infrared and raman spectroscopy for medical diagnostics', *Applied Spectroscopy Reviews*, vol. 36, no. 2–3, pp. 181–237, Jun. 2001, doi: 10.1081/ASR-100106156.
[38] H. J. Byrne, 'Vibrational Spectroscopy: Disease Diagnostics and Beyond', in *Optical spectroscopy and computational methods in biology and medicine*, New York: Springer, 2013.
[39] D. A. Haber and V. E. Velculescu, 'Blood-Based Analyses of Cancer: Circulating Tumor Cells and Circulating Tumor DNA', *Cancer Discovery*, vol. 4, no. 6, pp. 650–661, Jun. 2014, doi: 10.1158/2159-8290.CD-13-1014.
[40] L. Zhang *et al.*, 'The interplay of circulating tumor DNA and chromatin modification, therapeutic resistance, and metastasis', *Mol Cancer*, vol. 18, no. 1, p. 36, Dec. 2019, doi: 10.1186/s12943-019-0989-z.
[41] J. Müller Bark, A. Kulasinghe, B. Chua, B. W. Day, and C. Punyadeera, 'Circulating biomarkers in patients with glioblastoma', *Br J Cancer*, vol. 122, no. 3, pp. 295–305, Feb. 2020, doi: 10.1038/s41416-019-0603-6.
[42] A. Boire *et al.*, 'Liquid biopsy in central nervous system metastases: a RANO review and proposals for clinical applications', *Neuro-Oncology*, vol. 21, no. 5, pp. 571–584, May 2019, doi: 10.1093/neuonc/noz012.

[43] P. D. Mariner, A. Korst, A. Karimpour-Fard, B. L. Stauffer, S. D. Miyamoto, and C. C. Sucharov, 'Improved Detection of Circulating miRNAs in Serum and Plasma Following Rapid Heat/Freeze Cycling', *MIRNA*, vol. 7, no. 2, pp. 138–147, Jun. 2018, doi: 10.2174/2211536607666180416152112.
[44] D.-D. Xiao, P.-F. Yan, Y.-X. Wang, M. S. Osman, and H.-Y. Zhao, 'Glioblastoma and primary central nervous system lymphoma: Preoperative differentiation by using MRI-based 3D texture analysis', *Clinical Neurology and Neurosurgery*, vol. 173, pp. 84–90, Oct. 2018, doi: 10.1016/j.clineuro.2018.08.004.

Chapter 5

Interrogation of *IDH1* status in gliomas by Fourier transform infrared spectroscopy

James M. Cameron[1], Justin J.A. Conn[2], Christopher Rinaldi[1], Alexandra Sala[1], Paul M. Brennan[3], Michael D. Jenkinson[4], Gianfelice Cinque[5], Khaja Syed[6], Holly J. Butler[2], Mark G. Hegarty[2], David S. Palmer[2,7], Matthew J. Baker[1,2]

[1]WestCHEM, Department of Pure and Applied Chemistry, Technology and Innovation Centre, University of Strathclyde, 99 George St, Glasgow, G1 1RD, UK

[2]ClinSpec Diagnostics, University of Strathclyde, Technology and Innovation Centre, 99 George Street, Glasgow, G1 1RD, UK

[3]Translational Neurosurgery, Department of Clinical Neurosciences, Western General Hospital, Edinburgh, EH4 2XU, UK

[4]Institute of Translational Medicine, University of Liverpool & The Walton Centre NHS Foundation Trust, Lower Lane, Fazakerley, Liverpool, L9 7LJ, UK

[5]Diamond Light Source, Hardwell Science and Innovation Campus, Chilton, Oxfordshire, OX11 0DE, UK

[6]Walton Research Tissue Bank, Neurosciences Labs, The Walton Centre NHS Foundation Trust, Lower lane, Fazakerley, Liverpool, L9 7LJ, UK

[7]WestCHEM, Department of Pure and Applied Chemistry, Thomas Graham Building, University of Strathclyde, 295 Cathedral Street, Glasgow, G1 1XL, UK

In draft for submission to: *Analyst* (2020)

Contribution: I conducted all experimental work; produced all figures; wrote and prepared the manuscript.

Abstract

At present, current brain cancer diagnostics are based on the World Health Organisation (WHO) classification system that is composed of classical histopathology and molecular biomarkers, namely the *IDH1*, *ATRX* and *1p/19q* status. The tumour grade and marker status are used to determine treatment, as they are indicative of response to chemotherapy. Techniques involving vibrational spectroscopy, such as Fourier transform infrared (FTIR) spectroscopy, have previously demonstrated analytical capabilities for cancer detection, and have the potential to become a more powerful tool in the diagnostics field. For example, rapid determination of a glioma patient's *IDH1* status facilitates vital neurosurgical decisions, such as pursuing with resection or opting for alternative therapeutics. Thus, implementation of FTIR spectroscopy during surgical procedures could present a fast, label-free method for the molecular genetic classification of gliomas. In this study, we utilise synchrotron-based infrared light to probe brain tumour tissue microarrays and distinguish between *IDH1*-mutated and *IDH1*-wildtype glioma, at a sensitivity and specificity of 82.4% and 83.4%, respectively. Additionally, the sensitivity of attenuated total reflection (ATR)-FTIR has been examined with the aim of detecting biomolecular events and the global epigenetic and metabolic changes associated with mutations in the *IDH1* enzyme, via centrifugal filtration of patient serum. The ability to provide this information prior to resection would enable patients to receive personalised chemo- and/or radiotherapy treatment to reduce tumour volume, allow a more efficient resection, signifying a shift in the clinical management of brain tumour patients.

5.1 Introduction

Somatic mutations in the human cytosolic isocitrate dehydrogenase 1 (*IDH1*) gene is a frequent feature observed in malignant gliomas. The *IDH1* mutation tends to occur in the early stages of gliomagenesis, thus are regularly found in low-grade diffuse astrocytoma and oligodendrogliomas [1]. The mutation rate varies in glioblastoma (GBM) cases [2]. The *IDH1* mutation is rare in primary GBM – aggressive lesions that arise *de novo* without neural precursor cells, accounting for the vast majority of GBM [3]. In contrast, secondary GBM develops from previously diagnosed diffuse or anaplastic astrocytoma, and often exhibit the *IDH1* mutation. Whilst >80% of astrocytomas, oligodendrogliomas and secondary GBM carry *IDH1* mutations, the genetic alteration is only observed in <10% of primary GBM patients [4,5]. Consequently, the *IDH1* mutation serves as a valuable diagnostic marker (Table 5.1), especially in distinguishing the epigenetic nature of primary and secondary GBM lesions that are often indistinguishable through histopathological analysis [5].

Table 5.1 - Common genetic and chromosomal aberrations associated with the major glioma subtypes [6].

Glioma entity	**WHO grade**	***IDH1* mutation**	**Additional associated mutations**
Pilocytic astrocytoma	I	Extremely rare	*BRAF, KRAS, NF1, FGFR1*
Diffuse astrocytoma	II	Common	*IDH2, TP53, ATRX, LOH 17p*
Anaplastic astrocytoma	III	Common	*IDH2, TP53, ATRX, LOH 17p*
Oligodendroglioma	II	Majority of cases	*IDH2, TP53, ATRX, 1p/19q codeletion*
Anaplastic oligodendroglioma	III	Majority of cases	*IDH2, TP53, ATRX, 1p/19q codeletion*
Glioblastoma (primary)	IV	Rare	*TERT, PTEN, TP53, MGMT, EGFR*
Glioblastoma (secondary)	IV	Extremely Common	*IDH2, TP53, ATRX, LOH 17p*

NF1, neurofibromatosis type 1; FGFR1, fibroblast growth receptor 1; IDH2, isocitrate dehydrogenase 2 ; TP53, tumour suppressor protein 53; ATRX, alpha thalassemia/mental retardation syndrome X-linked mutation; LOH 17p, loss of heterozygosity on chromosome 17; TERT, telomerase reverse transcriptase; PTEN, phosphatase and tensin homolog; MGMT, O(6)-methlyguanine-DNA-methyltransferase; EGFR, epidermal growth factor receptor.

The normal function of the *IDH1* enzyme is to convert isocitrate to a-ketoglutarate (aKG). Cancer-associated mutations in *IDH1* inactivate this standard enzymatic activity, but enables a neomorphic conversion of aKG to the oncometabolite 2-hydroxyglutarate (2HG) [7,8]. This results in an accumulation of 2HG in glioma cells, which drives oncogenic activity and tumorigenesis [9]. The vast majority (~90%) of *IDH1* mutations involve transitions in codon 132, where the arginine residue is replaced by histidine (R132H-*IDH1*) [2]. It is now well established that glioma patients who have this *IDH1* mutation have significantly better prognosis compared to those with *IDH1*-wildtype lesions of the same histologic grade [10]. One study reported a median survival of 65 months for anaplastic astrocytoma patients that expressed the *IDH1*-mutation, compared to only 20 months for those classed as *IDH1*-wildtype [11]. Another study suggested that *IDH*-mutated GBM

patients were projected to have a better prognosis than those with a lower grade *IDH*-wildtype astrocytoma [4]. R132H-*IDH1* alterations represent an ideal diagnostic and prognostic tool. Consequently, testing for *IDH1* mutations is now considered standard by international guidelines for the management of gliomas patients [12]. The presence of R132H-*IDH1* can be established through immunohistochemistry (IHC) by applying the *mIDH1R132H* antibody to resected glioma tissue [13]. Despite being fairly sensitive and specific to the R132H-*IDH1* mutation, there are a few limitations with the procedure. Successful IHC relies on invasive biopsies, meaning patients will always require a surgical procedure prior to a definitive diagnosis. Occasionally, the R132H-*IDH1* expression is only present in a fraction of tumour cells in some diffuse gliomas, thus several sections of brain tissue are generally removed during biopsy to increase the chances of a reliable result. False positives have been observed due to non-specific background staining, and regional heterogeneity of R132H-*IDH1* expression can cause doubt in the diagnosis which necessitates confirmatory genetic analysis [14]. In general there are several problems associated with IHC analysis, including the experience of the histopathologist, differences in clinical opinion and issues with tissue sampling [15,16].

The development of a simple, rapid and label-free diagnostic tool for *IDH1* detection could be revolutionary for neuropathology. Analytical techniques involving vibrational spectroscopy have great potential for diagnosing disease states, namely infrared and Raman spectroscopy [17,18]. In particular, Fourier transform infrared spectroscopy (FTIR) has been shown to be valuable for the detection of various cancers, as it can probe the biochemical composition of normal and pathological

tissue, and generate the fingerprint structure of several biomolecular components, such as proteins, lipids and nucleic material [19–25]. Several studies have looked into diagnosing brain lesions utilising vibrational spectroscopy, focused on Raman techniques [26–29]. Similarly, FTIR can detect and stratify brain malignancies through analysis of resected tissue sections [30–33]. These spectroscopic studies highlight the capability of the technique to become a powerful tool in the diagnostic field [34]. For example, complete surgical resection is associated with improved survival in patients with the *IDH1* mutation [35], therefore rapid determination of a glioma patient's *IDH1* status facilitates vital neurosurgical decisions, such as pursuing with resection or opting for alternative therapeutics [36]. The implementation of FTIR spectroscopy during surgery could afford a fast, label-free method for the molecular genetic classification of gliomas. Likewise, attenuated total reflection (ATR)-FTIR is suitable for biological fluids, such as blood serum. Specifically, it provides qualitative interrogation of all IR active macromolecular constituents of blood serum, and it is well established that biomolecular imbalances in biofluids can give an indication of disease states [37].

Uckermann *et al.* recently highlighted the capability of FTIR in identifying mutated *IDH1* expression in 34 cryosections of frozen brain tissue samples, and 64 fresh unfixed biopsies of human gliomas [38]. This proof-of-concept study yielded encouraging results, correctly assigning 88% of the of the frozen cryosections to the correct group when combining transmission FTIR imaging with quadratic discriminant analysis. Similarly, classification of ATR-FTIR spectra of the fresh glioma biopsies reported an accuracy of 86%. In spite of these promising results,

they found that the spectra of both the cryosections and fresh tissue biopsies showed high inter-patient variability. The variance in the fresh tissue analysis may have been accentuated by the use of ATR-FTIR, which only interrogates the region of the sample that is in contact with the IRE. Consequently, it can be difficult to ensure the biopsy area being examined is representative of the tumour. Likewise, it is well recognised that the frozen section procedure can damage the structural integrity of tissue, resulting in specimens that may be of lower quality than fresh frozen paraffin-embedded (FFPE) tissue slides, hence fixed tissue processing is generally preferred for more accurate diagnosis [37]. Uckermann *et al.* proposed that further work would be required to fully evaluate the ability of the technique in the application of detecting the *IDH1* mutation and other potential biomarkers.

Synchrotron radiation-based FTIR (SR-FTIR) spectroscopy is a technique that can extract greater detail from biological tissue samples [37]. In SR-FTIR, a synchrotron source emits a collimated light beam more intense than standard bench-top spectrometers [39]. Synchrotron radiation can be up to 10^3 times brighter than any other conventional broadband IR source, allowing smaller regions of tissue to be probed with superior signal-to-noise [40].

The implementation of this powerful biospectroscopy technique may enhance our perception of the epigenetic nature within malignant glial lesions. In this study, SR-FTIR has been used to examine human brain glioma tissue, where single-point spectra have been collected from tissue microarray (TMA) sections comprising *IDH1*-mutated and *IDH1*-wildtype glioma tissue cores, further probing the ability of

the technology to potentially assist in the clinical management of glioma patients. Furthermore, we examine the potential for earlier molecular subclassification of tumours by identifying the systemic and global changes caused by the genetic *IDH1* mutation in gliomas, through centrifugal filtration of patient serum and ATR-FTIR spectroscopy, which could be implemented prior to biopsy or resection.

5.2 Materials and Methods

5.2.1 Sample Collection and Preparation

5.2.1.1 Glioma Tissue

Ethical approval for construction of the TMA was from the Lothian NRS Bioresource (15 ES 0094). Inclusion criteria for this retrospective study were: i) patients who underwent neurosurgery (tumour biopsy or debulking) ii) patients with histologically confirmed glioma, as diagnosed by a consultant neuropathologist. 137 patients were selected for inclusion in the TMA, representing a range of tumour grades and recurrent tumours in the microarray. Clinical information was retrospectively collected for these patients. FFPE tumour biopsies were available in tumour blocks for all 137 patients. Tissue cores in 0.6 mm diameter were removed from the donor block and inserted into a recipient block using a manual tissue arrayer. 10 μm sections of the TMA block were sliced with a microtome and floated onto 76 x 26 x 1 mm calcium fluoride (CaF_2) substrates in a heated water bath (~40 °C). The CaF_2 slides were then placed into an automated Leica ST5010 Autostainer XL (Leica, Germany) for a dewaxing protocol, designed to remove paraffin wax before spectroscopic analysis: immersion in xylene (3 x 5 min); ethanol wash (2 x 2 min 100%, 1 x 2 min 80%, 1 x 2 min 50%); rinse in distilled water (2 x 2 min). The dewaxed slides were then placed in an oven at 60 °C for 3 hours to dry the tissue samples efficiently onto the CaF_2 substrates. Once dehydrated, the slides were stored in petri dishes at room temperature until the time of IR interrogation. Subsequent microtoming of the TMA enabled IHC staining of the tissue cores with the *mIDH1R132H* antibody. Reference microscope images were collected, allowing the

determination of the *IDH1*-status for each sample - a positive result is observed by a strong brown colour in the glioma cells (Figure 5.1).

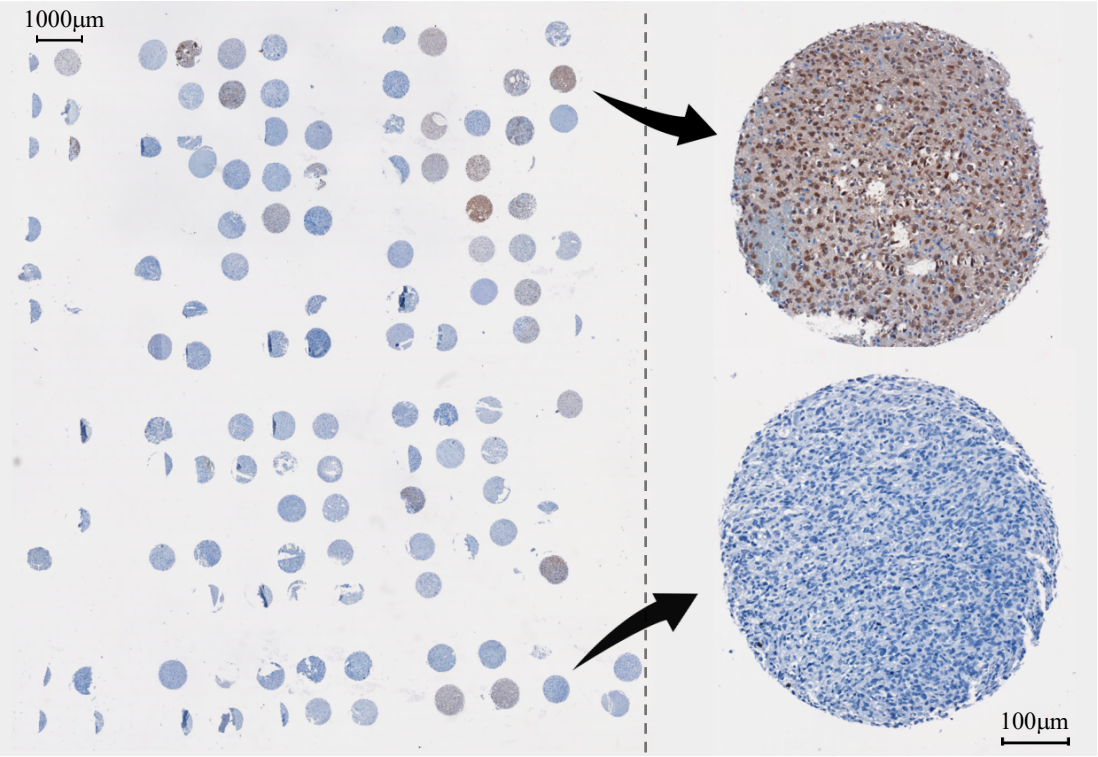

Figure 5.1 – Overview of the tissue microarray with *IDH1* staining, with focus on a mutated core (brown) and wildtype core (blue).

5.2.1.2 Patient Serum

A total of 72 retrospective serum samples were obtained the Walton Centre NHS Trust biobank (Liverpool, UK). Ethical approval was obtained prior to investigation (Walton Research Bank and BTNW/WRTB 13_01/ BTNW Application #1108). Blood samples were gathered in serum collection tubes and allowed to clot for up to one hour. The tubes were centrifuged for 15 minutes at 2200 *g*. The serum component was subsequently aliquoted then stored in an –80 °C freezer until the time of analysis. The serum samples were removed from storage and thawed at room temperature for approximately 20 minutes prior to spectral analysis. 3 µL of serum

from one individual patient was pipetted onto each of the three sample wells on a ClinSpec Dx optical sample slide (ClinSpec Diagnostics Ltd., UK) [41]. The first well remained clean for background collection to subtract atmospheric conditions from the IR spectra. The serum drops were spread across the well in order to create thin homogeneous serum films [42]. Prepared slides were dried at 35 °C for 1 hour to dehydrate the serum drops [43,44].

5.2.1.2.1 Centrifugal Filtration

To examine the potential of ATR-FTIR spectroscopy to detect *IDH1* mutation, centrifugal filtration was undertaken to enable analysis of the low molecular weight (LMW) fraction of the serum samples. The whole serum samples from the 72 brain cancer patients (Appendix 3, Table A3.2) were filtered to remove the more abundant high molecular weight (HMW) biomolecules. Commercially available Amicon Ultra-0.5 mL centrifugal filtering devices (Millipore-Merck, Germany) with cut-off points at 3kDa were used to fractionate the serum samples. The serum was split into two fractions; the 'filtrate' and the 'concentrate'. The filtrate accounts for the biomolecular components below the 3kDa cut-off point, and the concentrate represents the higher MW serum constituents. Serum from each patient (0.3 mL) was placed in the centrifugal filters, and the filtration tubes were centrifuged for 30 minutes at a speed of 14000 *g*. The filtrates passed through the membranes into the collection vials. The filters were then inverted and centrifuged for 2 minutes at 1000 *g* to collect the HMW concentrates. The filtrates and concentrates were stored in a –80 °C freezer until the time of analysis.

5.2.2 Spectral Collection and Data Analysis

5.2.2.1 Synchrotron Radiation-based FTIR Microspectroscopy

Experiments were carried out at the Diamond Light Source synchrotron facility, UK, namely the MIRIAM B22 beamline [45]. FTIR microspectra were acquired in transmission mode via a Hyperion 3000 microscope system with a 36x magnification (NA=0.5) Cassegrain objective/condenser optics coupled to a Bruker Vertex 80v FTIR spectrometer (Bruker Optics, Germany). A high sensitivity liquid nitrogen cooled mercury cadmium telluride (MCT) single element detector with a 50 mm pitch size was used to collect data between 4000-600 cm^{-1}, at a spectral resolution of 4 cm^{-1}. Background spectra were recorded from clean sections on the CaF_2 substrates. The aperture size was set to have a projected detection area of 10 x 10 μm at the sample plane, with FTIR spectral acquisition performed by co-addition of 256 background scans and 128 sample scans at FTIR nominal scanner rate of 80 kHz (equivalent to 10s and 20s per point, respectively). Point spectra were collected as linescans through diagonal cross-sections of the TMA cores, acquiring ~70 spectra for each TMA core across a line approximately 0.6 mm in length. In total, 8532 spectra were accumulated from 99 TMA cores (Table A3.1 in Appendix 3), comprised of tissue from 79 glioma patients. Each transmission spectrum was ratioed to the background spectrum and converted to absorbance.

An initial atmospheric compensation was performed to subtract the contribution of spectral water vapour bands in OPUS 8 software (Bruker Optics, Germany), and the resulting spectra were cut to 4000-900 cm^{-1}. The spectral data was exported for further pre-processing and analysis. Absorbance spectra collected from clean

sections of the CaF_2 substrates were subtracted from sample absorbance spectra. The PRFFECT toolbox on the R Statistical Computing Environment was utilised for the pre-processing and classifications [16]. Iterative extended multiplicative signal correction (EMSC) was applied five times with five different reference spectra to account for Mie scattering [46]. Principal component analysis (PCA) was employed on the Quasar software (Orange Data Mining [47]) for a PCA-based quality test, to remove spectra that fell outside the central cluster of PC scores. Thereafter, spectra with Amide I (1650 cm^{-1}) absorbance < 0.01 or > 2 were removed from the dataset. The synchrotron datasets were classified based on *IDH1* status using linear discriminant analysis (LDA). Firstly, a grid search was utilised to test various pre-processing parameters, then the top 10 models were further examined with a greater number of iterations – this is defined in more detail in the results section.

5.2.2.2 ATR-FTIR Spectroscopy

A Perkin Elmer Spectrum 2 FTIR spectrometer (Perkin Elmer, UK) was used for the spectral collection. A Specac Quest ATR accessory unit was fitted with a specular reflectance puck (Specac Ltd, UK). A slide indexing unit (ClinSpec Diagnostics Ltd, UK) automated the movement of the slides across ATR accessory. The spectra were acquired in the range 4000-450 cm^{-1}, at a resolution of 4 cm^{-1}, with 1 cm^{-1} data spacing and 16 co-added scans. Each sample well was analysed in triplicate, acquiring 9 spectra per patient. Thus, we gathered 648 whole serum spectra, and 648 spectra were collected from the <3kDa filtrates, resulting in 1296 spectra in total.

An EMSC was also employed for the serum data analysis. The 'whole serum' dataset used a human pooled serum reference, followed by a spectral cut to 1800-1000 cm^{-1}. To develop the models, patients were randomly split into training and test sets at a 70:30 split. Spectra from a single patient's serum could only appear in one cross-validation fold, and in either the training or test set to ensure that the models were trained and validated correctly. The majority vote amongst the nine spectra for each patient was reported as the diagnostic outcome. The classification models were retrained and tested on 100 different randomly selected training and test set partitions to provide a more reliable result. Classification results of the ATR-FTIR spectra through random forest (RF), partial least squares – discriminant analysis (PLS-DA), and support vector machine (SVM) have been compared here, as described in Chapters 3 and 4.

5.2.2.3.1 Centrifugal Filtration

For the centrifugal filtration study, the spectra were initially corrected with an EMSC using an averaged filtrate spectrum as the reference. As there were two prominent bands present between 1000-800 cm^{-1} in the filtered serum spectrum, the dataset was cut down to 800 cm^{-1} to ensure all potentially important biological information was retained. Thus, three spectral cuts were tested; 4000-800 cm^{-1}, 1800-800 cm^{-1} and 1800-1000 cm^{-1}. All other parameters were the consistent from the whole serum analysis.

5.3 Results and Discussion

5.3.1 Synchrotron Results

The data collected at the Diamond Light Source synchrotron required some initial data handling. Due to restricted beamtime, it was decided that the most efficient spectral collection method was to collect large images containing multiple tissue cores, and accumulate single-point spectra across each individual core. Of the 8532 spectra that were collected, many were not entirely representative of the tissue samples as some of the diagonal cross-sections contained blank CaF_2 – mainly at the sample's edge (Figure 5.2). Thus, the spectra of the blank substrate were removed from the dataset. As shown in Figure 5.3, the raw spectra collected from the tissue samples were highly variable. It is well established that transmission IR microscopy of tissue samples can suffer from significant baseline distortions due to scattering effects, predominantly resonant Mie scattering [48]. To combat this, an iterative EMSC approach was employed in an attempt to correct for the scatter effects at the left side of the Amide I band, as described elsewhere [46]. The resulting spectra were subjected to a PCA-quality test, described in Figure 5.4 (initial PCA plot in can be found in Appendix 3, Figure A3.1). All datapoints positioned outside of the centroid ellipse were removed from subsequent analysis. Additional quality testing was based of the intensity of the Amide I band, with only spectra falling within an acceptance window of 0.01 - 2 being retained. The resulting spectra are outlined in Figure 5.5, where the baseline variation and scattering effects have been significantly reduced.

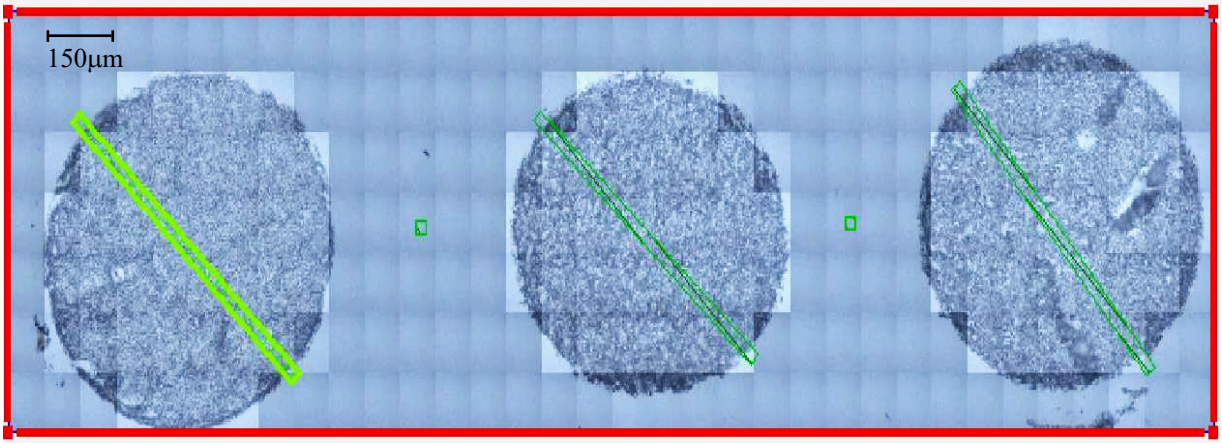

Figure 5.2 – Microscope image taken of three brain tumour tissue microarray cores prior to infrared interrogation. Green squares (10 x 10 µm) represent the points where spectra were collected.

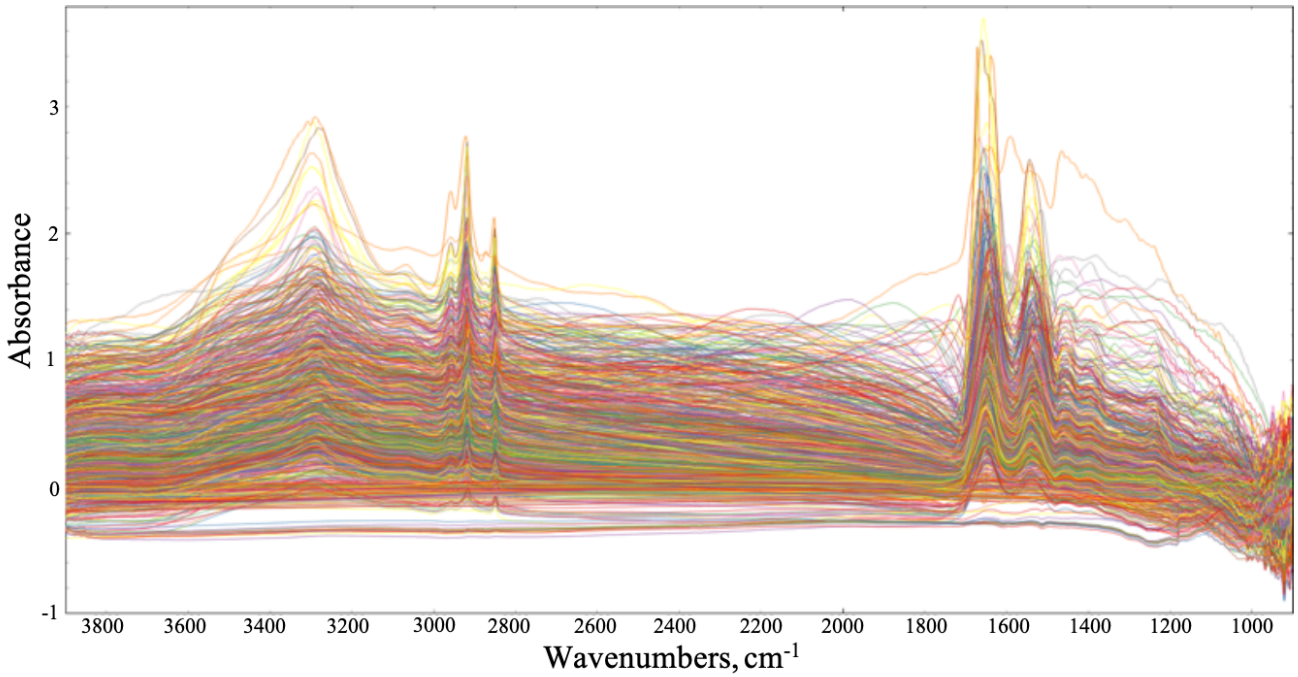

Figure 5.3 - 1000 randomly selected raw spectra from the synchrotron dataset displaying highly variable baselines and scattering effects.

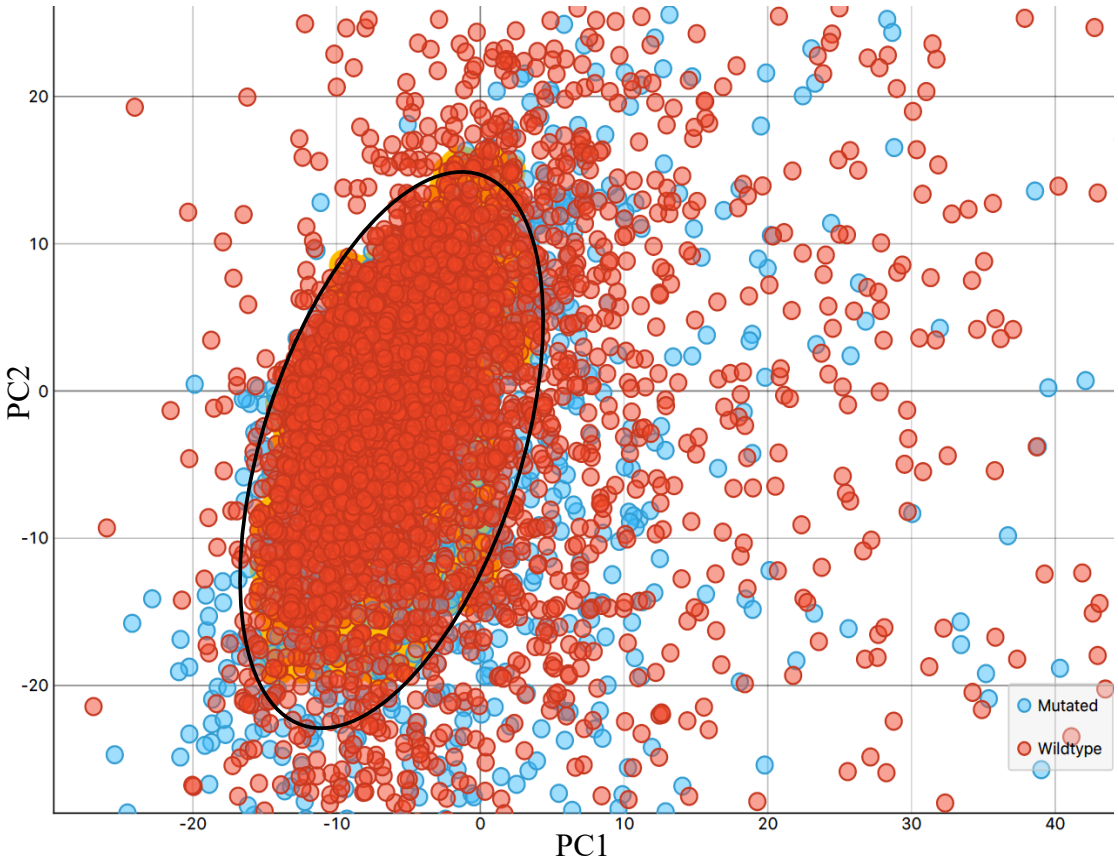

Figure 5.4 - PCA-based quality test: PCA scores plot of PC1 and PC2 with focus on centre of cluster highlighting the ellipse (black circle) containing the data that was carried forward for investigation, all spectral datapoints laying outside of the ellipse were removed from subsequent analysis.

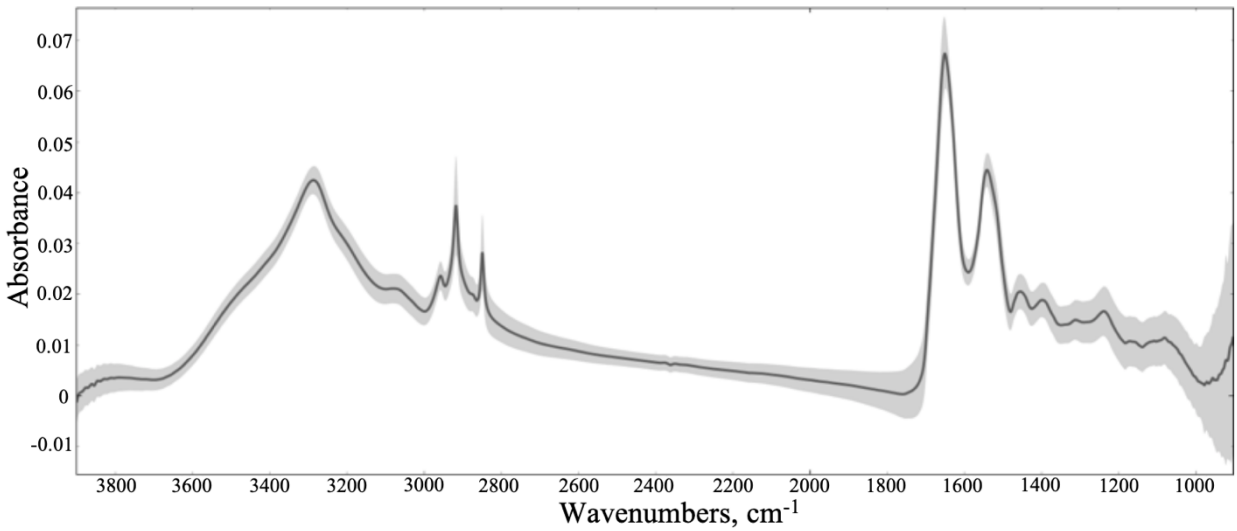

Figure 5.5 - Mean spectra of all samples combined after EMSC, PCA quality test and removal of Amide I outliers with the standard deviation shaded in grey.

Following initial data management, 4822 spectra were retained for further spectral pre-processing and classification. In order to determine the optimal pre-processing parameters for the *IDH1*-mutated versus *IDH1*-wildtype dataset, a grid search was carried out using the PRFFECT toolbox, where the values for normalisation, binning, smoothing, order of derivative, and spectral cut were altered, as outlined in Table 5.2. An unusual spectral cut of 1800-1200 cm^{-1} was included as there appeared to be a drop in absorbance <1200 cm^{-1} for many samples, which was thought to be due to the loss of IR light transmittance through the CaF_2 slides (Appendix 3, Figure A3.2). This cut-off effect for CaF_2 in the low wavenumber region is common in scanning microscopy and can be caused by the change in refractive index (RI), e.g. the RI of CaF_2 decreases from ~1.4 at 5 μm to ~1.3 at 10 μm. Also, when using a synchrotron source in scanning microscopy mode for high spatial resolution, the diffraction limit is achieved when the microscope's apertures define a spot size scaled with the longest wavelength of the spectral region of interest [49]. Here we used 10 μm slits, therefore the diffraction limit could be affecting the signal towards ~1000 cm^{-1} (λ = 10 μm $\Leftrightarrow$ 1000 cm^{-1}). Thus, the fingerprint region with the removal of wavenumbers <1200 cm^{-1} was included in the grid search, along with the typical biological fingerprint region (1800-1000 cm^{-1}) and the full spectral region. In total, 576 combinations of pre-processing parameters were tested.

Table 5.2 - Pre-processing parameters examined in machine learning grid search.

Parameter	**Variations**			
Normalisation (n)	None (0)	Min-max (1)	Vector (2)	Amide I (3)
Derivative (l)	None (0)	First (1)	Second (2)	-
Binning (b)	1	2	4	8
Smoothing with Savitzky-Golay filter (s)	None (0)	2	3	4
Spectral cut (p)	None (0)	1800-1000 cm^{-1}	1800-1200 cm^{-1}	-

The processed datasets were split 70:30 into training and testing sets. An LDA classifier was trained and predictions made on the testing set, resampled 11 times – e.g. repeated for 11 different train-test splits – and the classification probability threshold was chosen to optimise Cohen's Kappa (κ). Briefly, the values of κ range from below zero to one and measures the level of agreement between the classifier and the pathology, with higher values representing better agreement, thus signifying a more reliable diagnostic model - see Chapter 3 (section 3.2.4) for a thorough description of κ. The models predicted *IDH1* status on a 'by sample' basis, where the majority vote for each tissue core was reported as either *IDH1*-mutated or *IDH1*-wildtype. Here, the sensitivity is the ability to detect the positive class (the *IDH1* mutation), and specificity refers to *IDH1*-wildtype predictions.

The results from all 11 iterations were averaged and compiled for comparison (Table A3.3, Appendix 3). The best performing model from the grid search reported a κ value of 0.65, which demonstrates a 'substantial' level of agreement [50]. This model provided a sensitivity and specificity of 87.8% and 86.2%, respectively. The pre-processing used for this model was a min-max normalisation (scaling the spectra between 0 and 1), followed by a binning factor of 4, a Savitzky-Golay (SG)-filter

with a filter length 7 and filter order 4, and a spectral cut to between 1800-1200 cm^{-1}. The resulting mean spectra for both the *IDH1*-mutated and *IDH1*-wildtype patient groups are outlined in Figure 5.6. By plotting the difference between the mean spectra, it becomes evident that there are dissimilarities between the two *IDH1* groups (Figure 5.7). Arguably the largest difference arises in within the Amide I band, associated with the stretching of double-bonded carbonyl groups (C=O) and C-N bonds, as well as N-H bending vibrations in proteinaceous biomolecules [19]. The lower-wavenumber side of the Amide I band (1620-1600 cm^{-1}) was more intense in the *IDH1*-mutated spectra (positive regions in the difference spectrum), whereas the band intensities between 1700-1650 cm^{-1} were lower compared to the *IDH1*-wildtype tissue spectra. Interestingly, these results are consistent with Uckermann *et al.*, where *IDH1*-mutated cell lines exhibited an elevated absorbance at 1610 cm^{-1}, but lower intensity around 1690 cm^{-1} [38]. These findings are not directly comparable to the results presented here, as cell lines may not adequately represent primary cells in clinical specimens [51]. The observed differences are likely to be due to alterations in overlapping bands existing within the broad Amide I envelope, accounting for various protein secondary structures that can only be suitably predicted with deconvolution techniques (as described in Chapter 4) [52]. Nevertheless, it is thought that the large negative peak in the difference spectrum at ~1660 cm^{-1} may represent deviation in the levels of α-helical structures, and the smaller positive peak ~1615 cm^{-1} may be tentatively assigned to β-sheet components [53]. The band intensities at approximately ~1750 cm^{-1} and ~1560 cm^{-1} were lower in the mean *IDH1*-mutated spectrum, while those at ~1495 cm^{-1} and between 1450-1200 cm^{-1} displayed a higher absorbance than the *IDH1*-wildtype spectra (Figure 5.7). Several spectral differences

are similar to previous findings, namely the variances in Amide III of proteins (mainly N-H in plane bending and C-N stretch, ~1300 cm^{-1}), nucleic material such as DNA and RNA (PO_2^- asymmetric stretch, ~1230 cm^{-1}), and lipidic contributions (C=O stretch, ~1750 cm^{-1}; CH_3 bending, ~1450 cm^{-1}) [38]. The disparities in the IR spectra could potentially be attributed to the increase in 2HG in the *IDH1*-mutated glioma tissue, which is known to be elevated in tumour cells with the *IDH1* mutation [8]. With reference to an IR spectrum of pure 2HG [38], the bands around 1589, 1450, 1416, 1344, 1311, 1267, 1236 and 1203 cm^{-1} could explain some of the differences observed between *IDH1*-mutated and *IDH1*-wildtype tissue in this study, as the band intensities at these wavenumbers are all elevated in *IDH1*-mutated patients, portrayed by the difference spectrum (Figure 5.7). That being said, it may only indicate a global change in biomolecular content, reflected by the systemic response of the genetic mutation within glial tumour cells.

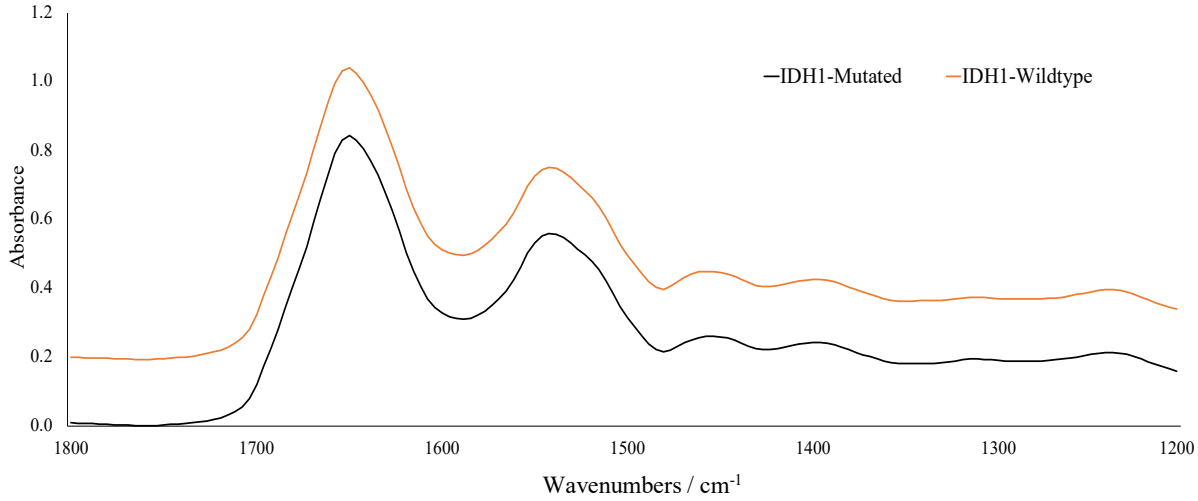

Figure 5.6 - Mean pre-processed spectra for the synchrotron-based *IDH1* dataset, cut between 1800-1200 cm^{-1}. Spectra offset for clarity; mutated (black) and wildtype (orange).

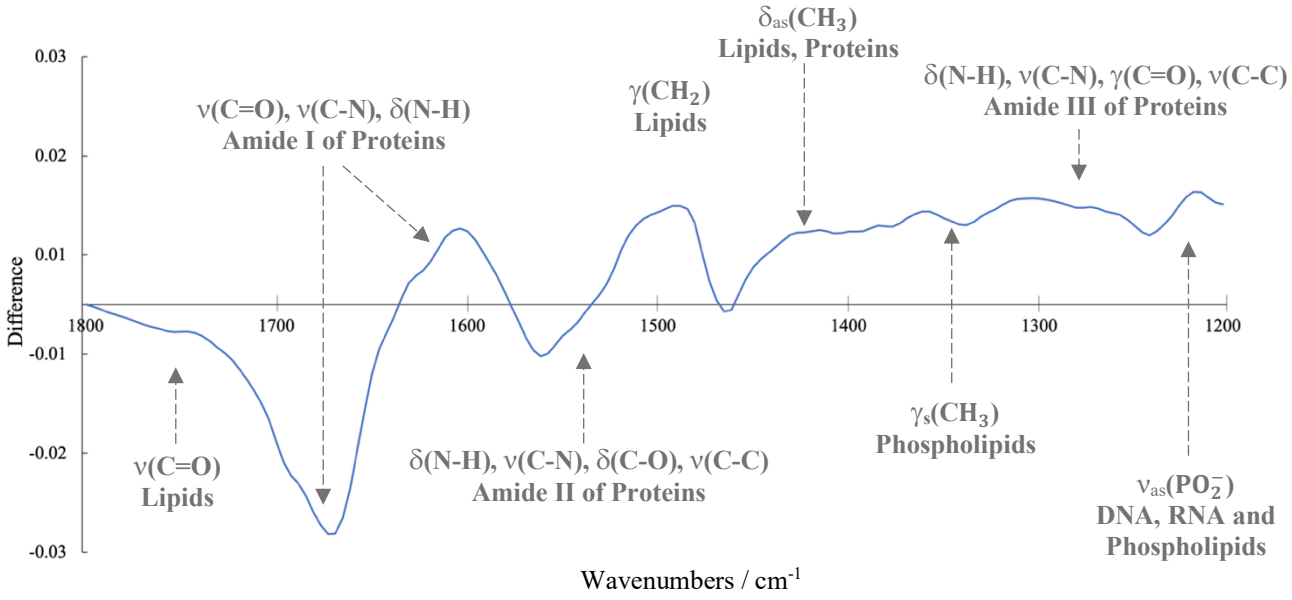

Figure 5.7 - Difference spectra of mean *IDH1*-mutated and *IDH1*-wildtype absorbance spectra for the synchrotron-based *IDH1* dataset, with tentative biological assignments and associated vibrational modes: ν = stretching; δ = bending; γ = wagging, twisting and rocking; as = asymmetric; s = symmetric.

11 resamples were employed in the grid search with different randomly selected training and test sets each time, and the model reported a substantial level of agreement ($\kappa = 0.65$). To ensure these findings were consistent, the top 10 pre-processing parameters from the grid search were further examined. Additionally, the use of sampling techniques, were utilised to ensure no bias was present within the models, due to the class imbalance between mutated and wildtype samples. Each of the retained pre-processing combinations were classified by LDA with 51 resamples, and four sampling methods were tested in each instance: no additional sampling, up- and down-sampling, and synthetic minority over-sampling technique (SMOTE) [54], as described in Chapter 3.

The optimal pre-processing parameters from the initial grid search were also found to be the best in this case, when combined with additional upsampling (Appendix 3, Table A3.4). The diagnostic ability decreased slightly, with a reported 82.4% sensitivity and 83.4% specificity (Table 5.3), highlighting the importance of resampling the data with a reasonable number of iterations in order to minimise the variance whilst maintaining a respectable analysis time. Nonetheless, the sensitivity and specificity remained well-balanced and above 80%. As shown in Table 5.3, the standard deviation is much higher for the sensitivity than the specificity, which is not entirely surprising due to the lower number of *IDH1*-mutated samples within the dataset. A 70:30 split between training and testing data meant that there were only 7 randomly selected *IDH1*-mutated samples in each of the 51 resampled test sets. Therefore, when a known mutated tissue core is misdiagnosed as *IDH1*-wildtype, it has a substantial effect on the sensitivity. As depicted by the confusion matrices in Figure 5.8, there is a drop in ~15% sensitivity when an *IDH1*-mutated sample is predicted wrongly. Conversely, there is only a ~4% difference in specificity with a misdiagnosed *IDH1*-wildtype sample, as there were 26 *IDH1*-wildtype samples in every test set. Thus, the addition of more glioma samples with the *IDH1* mutation would be beneficial for this analysis, in order to minimise the associated error. That being said, a balanced accuracy of 82.9% after 51 LDA iterations indicates synchrotron-based transmission FTIR may well be capable of detecting minute molecular alterations triggered by genetic mutations in the *IDH1* enzyme.

Table 5.3 - Classification results from 51 resamples of the optimal LDA model with additional upsampling, in terms of sensitivity, specificity and balanced accuracy. SD, standard deviation.

Statistic	**Mean**	**SD**
Sensitivity (%)	82.4	16.8
Specificity (%)	83.4	8.2
Balanced Accuracy (%)	82.9	9.6

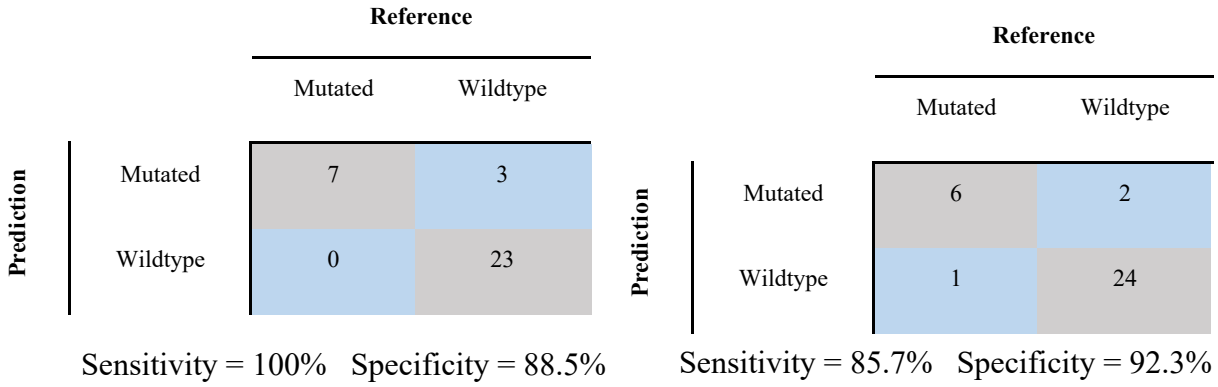

Figure 5.8 - Confusion matrices showing the predictions of two of the randomly selected test sets in from the linear discriminant analysis classification.

Receiver operating characteristic (ROC) curves can also demonstrate a model's diagnostic ability. A ROC curve is a probability curve, which can suggest how capable certain models are at distinguishing between classes. The area under the curve (AUC) represents the measure of separation, thus a valuable model will have an AUC value close to 1 and an excellent measure of separability [55]. On the other hand, an AUC <0.5 typically means the model has no class separation, and any differentiation is achieved by chance. Figure 5.9 describes a ROC curve obtained from the LDA 'by sample' classifier between *IDH1*-mutated and *IDH1*-wildtype.

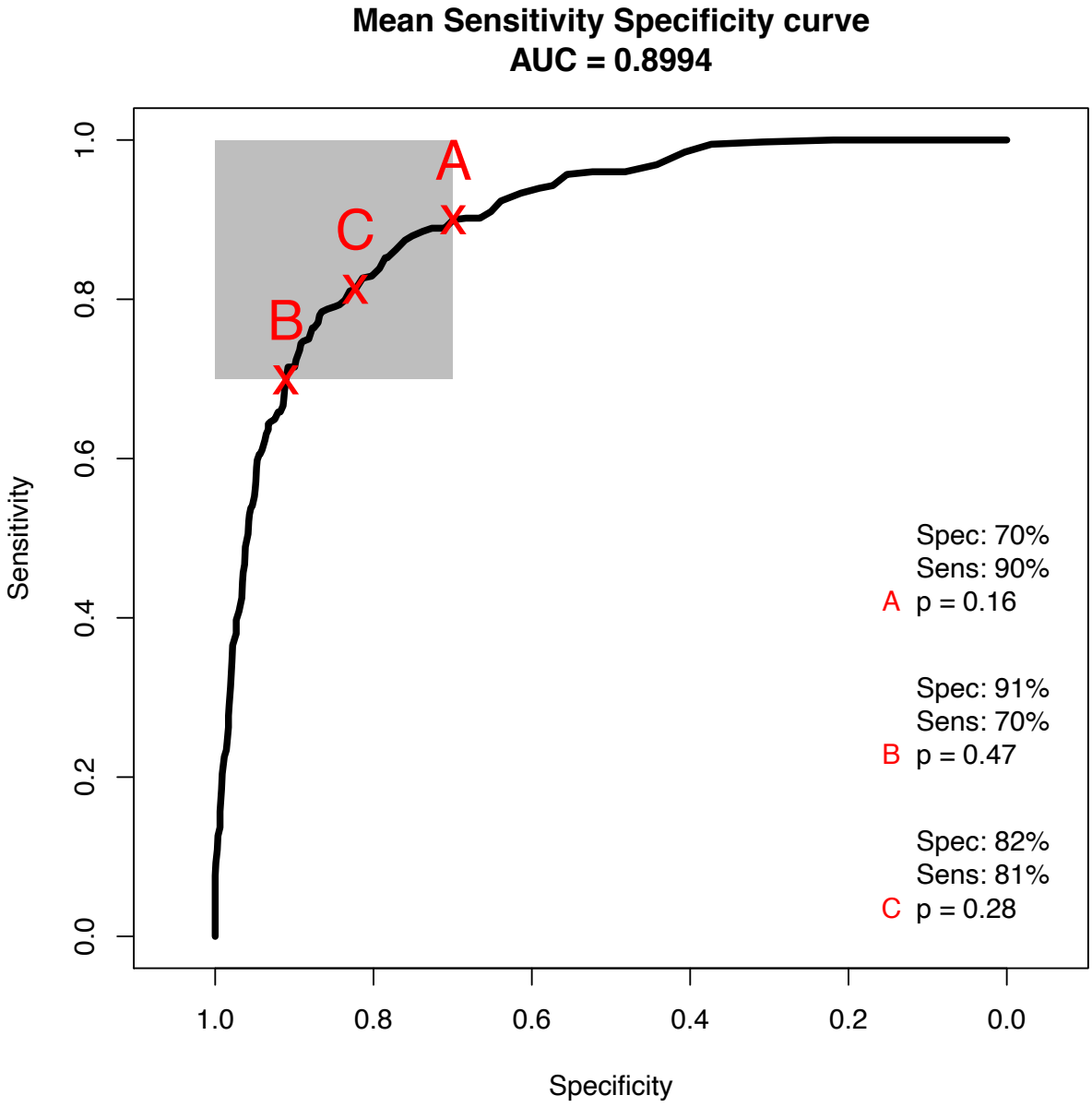

Figure 5.9 - Mean receiver operator characteristic (ROC) curve displaying the trade-off between sensitivity and specificity for the linear discriminant analysis (LDA) classifier. The grey square is a target region of at least 70% for both sensitivity and specificity. The 'x' labels are the points on the curve that maximise sensitivity (A), specificity (B) and balance the two (C) whilst remaining in the target area, and 'p' represents the probability thresholds at those points on the curve.

The curve is nicely symmetrical across sensitivity and specificity, and reports an AUC of 0.8994, which is typically considered an excellent degree of discrimination between the two classes [56]. By altering the probability threshold, denoted ‘p’ in Figure 5.9, we can maximise the sensitivity (A) or specificity (B), or obtain the greatest balance between the two (C). Point A represents the highest sensitivity (90%) whilst remaining in the 70-100% target region, whereas B denotes the maximum specificity (91%). The most balanced point on the curve reports a sensitivity and specificity of 82% and 81%, respectively, again illustrating the high diagnostic ability of the model, and signifying some real promise for the determination of *IDH1* status through SR-FTIR spectroscopy.

5.3.2 ATR-FTIR Results

In this section, brain cancer patients - with either astrocytoma, oligodendroglioma or GBM - were separated based upon their *IDH1* status using ATR-FTIR serum spectroscopy. Of the 72 patients included, there were 36 with the *IDH1* mutation, and 36 *IDH1*-wildtype. The data was classified through RF, PLS-DA and SVM with 100 resamples for each, and the findings are reported in Table 5.4 on a 'by patient' basis. For the whole serum dataset, the SVM model reported a promising sensitivity of 75.9% but had an extremely low specificity of 28%. All models seemed to be more effective at picking out the *IDH1*-mutated serum samples from the test sets, as the sensitivities were much higher than the specificities in each case. It is not clear why this may be as there were an equal number of samples in each class, meaning there should be no bias present in the models. However, the results did not appear to be reliable, and given the poor balanced accuracies (~50%) it could be assumed the correct predictions were ultimately made by chance.

Table 5.4 - Classification results for the *IDH1*-mutated versus *IDH1*-wildtype whole serum dataset, after 100 resamples. The mean sensitivity, specificity and balanced accuracy are reported with their corresponding standard deviations (SD).

Sample fraction	***Model***	***Sensitivity (%)***		***Specificity (%)***		***Balanced accuracy (%)***	
		Mean	**SD**	**Mean**	**SD**	**Mean**	**SD**
Whole Serum	RF	50.3	15.2	45.4	15.1	47.9	8.6
	PLS-DA	69.3	13.8	35.3	14.7	52.3	7.4
	SVM	75.9	17.5	28.0	14.6	51.9	7.7

Blood serum constitutes thousands of different proteins, ranging from the more abundant HMW serum albumin (50 g/L) to the LMW proteins like troponin (1 ng/L) [57]. Due to the wealth of various biomolecules that exist in a normal serum sample, it was expected to be a significant challenge to identify the subtle alterations in blood composition associated with the *IDH1* mutation. The LMW fraction of serum is believed to contain disease-specific information, making the spectroscopic signature of this fraction useful for diagnostics [58]. After the poor classification performance for the whole serum data, it was thought that discrete molecular differences could potentially be emphasised through the use of centrifugal filtration. Figure 5.10 provides an example of the IR spectra for whole serum, the >3kDa 'HMW' fraction and the <3kDa 'LMW' fraction. The HMW concentrate appears almost identical to the whole serum spectrum – notably, they have a very similar absorbance from the more abundant proteins that exist within the Amide region, such as albumin and immunoglobulins. With these large proteins and other HMW constituents removed, the filtrate spectrum looks remarkably different, with only a few distinct peaks in the fingerprint region (red spectrum). Note that the concentrate samples were not included in classification analysis, as the spectral collection was not reproducible. This was due to severe sample cracking during the dehydration process, causing the drops to lift off the substrate surface (Appendix 3, Figures A3.3 and A3.4).

As described in the Materials and Methods (section 5.2.2.3.1), three spectral regions were chosen for examination: 4000-800 cm^{-1} and 1800-800 cm^{-1} – to encompass the two distinct peaks around 950 cm^{-1} and 850 cm^{-1} – as well as the typical biological fingerprint region (1800-1000 cm^{-1}). The classification results are reported in Table

5.5. In each case, the filtrate models were superior than the whole serum models at successfully detecting the *IDH1*-wildtype patients, reporting specificity values above 60%. The improvement in diagnostic ability due to the filtration step is emphasised in Appendix 3, Figure A3.5, which displays single model ROC curves for the three whole serum classifiers and the best models for each of the three filtrate datasets. The ROC curves for the whole serum models fall on the diagonal line and the reported AUC values of ~0.5 suggests the test has essentially no diagnostic accuracy. However, the inclusion of centrifugal filtration enhanced the ability to successfully discriminate the two *IDH1* classes. The corresponding ROC curves in report AUC values >0.7, which is often deemed an 'acceptable' level of discrimination.

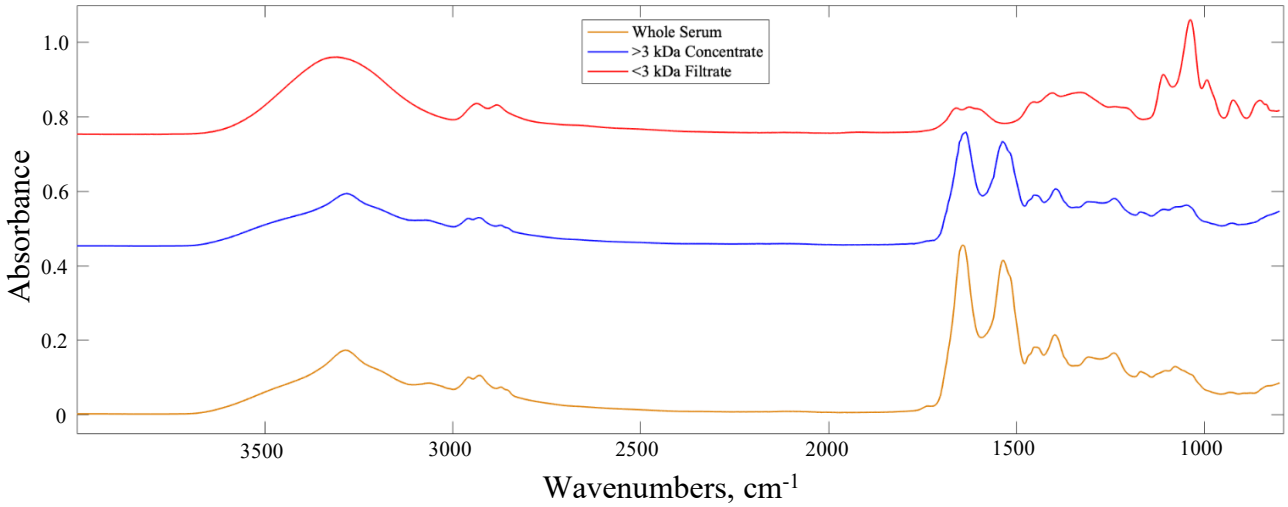

Figure 5.10 - Examples of whole serum (orange), the high molecular weight concentrate (blue) and the low molecular weight filtrate (red) spectra. Raw spectra offset for clarity.

The <3kDa filtered serum 'full spectra' dataset (4000-800 cm^{-1}) delivered the greatest balanced accuracy of 69.1% when classified by the PLS-DA model. The PLS scores plot in Figure 5.11a describes the general variation within the dataset. The major variance is generally described by the first PLS component (PLS1). The

PLS1 loadings suggest large differences ~3400 cm^{-1} and ~1650 cm^{-1} (Appendix 3, Figure A3.6), although there is no apparent class separation across PLS1 in the scores plot. Despite some overlap, it is evident that the 2nd PLS component separates the two classes better than PLS1. The PLS2 loadings also highlight significant spectral differences around ~1650 cm^{-1} (Figure 5.11b). Interestingly, this is the typical location of the large Amide I band in a normal serum spectrum, accounting for the bond vibrations within an abundance of protein molecules. Even with the HMW proteins filtered out of the sample - like albumin and immunoglobulins - it still appears to be a region of importance when examining molecules of very low molecular weights (<3kDa), signifying the smaller protein molecules still have diagnostic potential. Considerable contributions from lipids (~1450 cm^{-1}) and nucleic material (~1100 cm^{-1}) and C-O-C stretching vibrations associated with carbohydrates and glycogen were also apparent in the PLS2 loadings, as well as other proteinaceous vibrations (~1550 cm^{-1} and ~1300 cm^{-1}).

Table 5.5 - Classification results for the *IDH1*-mutated versus *IDH1*-wildtype serum datasets after 100 resamples. The mean sensitivity, specificity and balanced accuracy are reported with their corresponding standard deviations (SD).

Sample fraction	***Model***	***Sensitivity (%)***		***Specificity (%)***		***Balanced accuracy (%)***	
		Mean	**SD**	**Mean**	**SD**	**Mean**	**SD**
<3kDa Filtered Serum (4000-800 cm^{-1})	RF	68.4	16.2	67.5	15.9	68.0	11.1
	PLS-DA	75.5	12.3	62.6	15.5	69.1	9.0
	SVM	68.4	16.5	64.2	16.0	66.4	10.2
<3kDa Filtered Serum (1800-800 cm^{-1})	RF	70.6	17.8	66.4	14.5	68.5	11.2
	PLS-DA	65.0	14.6	64.6	16.5	64.8	8.7
	SVM	63.2	16.3	63.8	16.9	63.5	9.6
<3kDa Filtered Serum (1800-1000 cm^{-1})	RF	66.6	15.4	68.1	14.1	67.4	9.9
	PLS-DA	65.9	14.6	56.2	15.5	61.1	9.1
	SVM	68.1	15.6	56.8	15.6	62.5	10.1

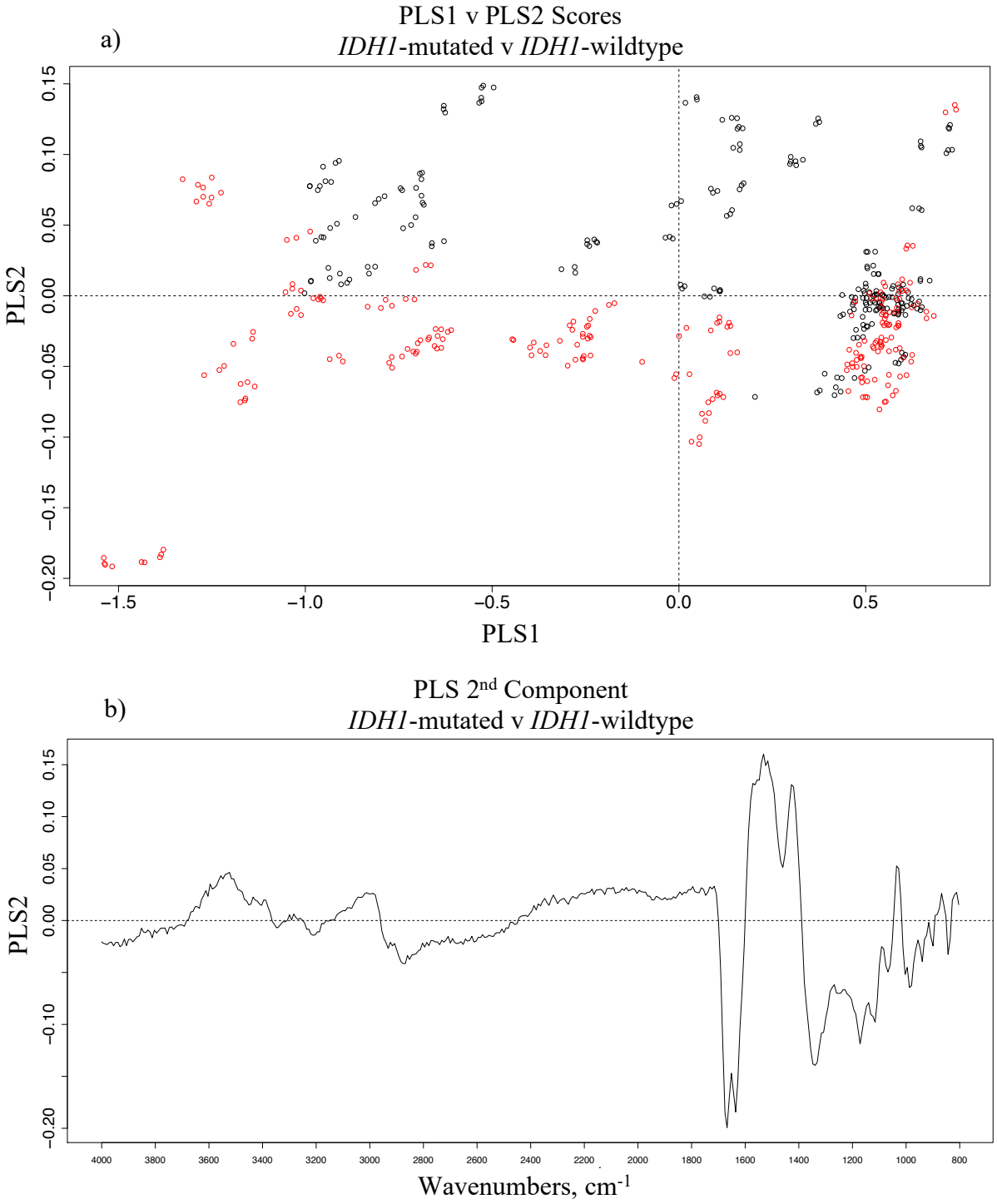

Figure 5.11 - a) the PLS scores plot between PLS1 and PLS2 for the *IDH1*-mutated (black) and *IDH1*-wildtype (red) <3kDa serum filtrate (4000-800 cm^{-1}) dataset, and b) the loadings for the 2nd PLS component.

The Gini impurity metric was also examined for the RF models, to identify the most important features within each dataset (see Chapter 3 for more details). The Gini plots highlighting the main wavenumbers responsible for the RF results can be found in Appendix 3 (Figure A3.7). The RF model for the 1800-800 cm^{-1} dataset also reported respectable results, with a sensitivity and specificity of 70.6% and 66.4%, respectively. Table 5.6 gives an overview of the top 15 identified wavenumbers in order of importance, with their corresponding wavenumber assignments and vibrational modes. The top wavenumbers mostly account for stretching vibrations of C-O, C-C and C-OH bonds, which are often associated with carbohydrates, glycogen and nucleic acids. Additionally, symmetric PO_2^- stretching vibrations from DNA and CH_2 twisting and bending vibrations associated with lipids were deemed significant in the RF classification. Likewise, wavenumbers in the Amide region were considered important here, accounting for C=O/C-N stretching and N-H bending vibrations in the amide bonds within protein molecules, similar to the PLS loadings described in Figure 5.13.

Table 5.6 - The top 15 wavenumbers from the <3kDa serum filtrate (1800-800 cm^{-1}) random forest classification between *IDH1*-mutated and *IDH1*-wildtype with associated vibrational modes [19]. The column "ΣGini" is a summation of the mean decrease in Gini for each wavenumber, over all nodes in all trees in the random forest ensemble, which suggests the regions of highest importance.

Wavenumbers (cm^{-1})	***ΣGini***	***Vibrational Modes***
1124.5	12.31	C-O stretch
1172.5	11.22	C-O, C-OH stretch
1164.5	9.07	C-C, C-O and C-OH stretch
1180.5	6.43	CH_2 twisting
1116.5	5.39	RNA; C-OH stretch
1028.5	5.01	Carbohydrate; C-O stretch
1188.5	4.46	DNA; Symmetric PO_2^- stretch
1740.5	4.19	Lipids; C=O stretch
1020.5	3.60	Glycogen; C-O stretch
1132.5	3.49	C-O and C-C stretch
1588.5	2.77	Amide I; C=O and C-N stretch, N-H bending
1548.5	2.73	Amide II; N-H bending, C-N stretching
1444.5	2.57	Lipids; CH_2 bending
1468.5	2.52	Lipids/Proteins; CH_2 bending
1612.5	2.45	Amide I; C=O and C-N stretch, N-H bending

In general, the balanced accuracies were enhanced to between 60-70% for all tested models. This is by no means perfect, but the centrifugal filtration step has produced a significant improvement on the model performance, by delivering more balanced sensitivities and specificities. Similar to the tissue-based results, these findings are based on a relatively small cohort with only 36 patients in each class, thus misdiagnosed patients have a profound effect on the sensitivity or specificity values. Additional analysis with a larger patient cohort would be beneficial in identifying the true potential of the technique for this particular clinical application. Moreover, Bonnier *et al.* have suggested that the large absorbance band observed in the filtered serum spectrum (~1030 cm^{-1}) is due to glycerine interference - introduced into the

sample from the centrifugal filters [59]. This could potentially be obscuring crucial information, therefore further analysis with an added washing step prior to centrifugation could be useful. There are also many filter sizes to choose from, hence filtration with a different cut-off point may also improve classification performance - many cytokines and chemokines exist at molecular weights greater than 3kDa, which may be indicative of disease. That being said, these findings suggest there is potential for the centrifugal filtration of serum to improve the model's diagnostic ability, specifically in detecting spectroscopic signatures that may be related to subtle molecular mutations.

5.4 Conclusion

The implementation of FTIR spectroscopy during biopsy could have the potential to offer a label-free test for molecular genetic classification of gliomas. Glioma patients who have the somatic *IDH1* mutation tend to have significantly better prognosis compared to those with *IDH1*-wildtype lesions of the same histologic grade, therefore such a test would be a useful prognostic and decision-making tool. Knowledge of a glioma patient's *IDH1* status prior to or during surgery may impact on neurosurgical decision, e.g. IDH1 mutated patients may have more complete resection, whilst IDH1-wildtype may have more limited surgery.

Initial analysis of the synchrotron-based data produced highly promising results, where the pre-processing grid search (with 11 LDA iterations) reported an optimal model with a κ value of 0.65, and a sensitivity and specificity of 87.8% and 86.2%, respectively. Further examination utilising a higher number of resamples slightly reduced the diagnostic outcome, but with 51 LDA iterations the model was more reliable and reported a balanced accuracy of 82.9%. ROC analysis produced a mean curve with an AUC of 0.8994, which also suggests a good degree of diagnostic separability. These findings demonstrate significant potential and suggest synchrotron-based transmission FTIR is capable of detecting molecular alterations likely initiated by genetic mutations in the *IDH1* enzyme.

Additionally, the ability of centrifugal filtration to improve the classification performance when exploring the ability of ATR-FTIR has been highlighted. In a cohort of 72 glioma patients, classification models were designed to distinguish

between *IDH1*-mutated and *IDH1*-wildtype in human serum. Initially, the whole serum classifiers performed disappointingly – delivering balanced accuracies of ~50% - yet with the introduction of centrifugal filtration the classification performance considerably improved. For the <3kDa filtered serum 'full spectra' dataset (4000-800 cm^{-1}), the PLS-DA model provided optimal diagnostic ability, delivering a balanced accuracy of 69.1% . Moreover, the RF model for the 1800-800 cm^{-1} dataset also reported relatively promising results, with a sensitivity and specificity of 70.6% and 66.4%, respectively. These strategies can now be validated and optimised in prospective clinical studies, and can be extended to identify other important molecular alterations, such as *ATRX* loss, *1p/19q* co-deletion and/or *MGMT* hypermethylation, with which brain cancer type can be stratified pre-operatively.

5.5 References

[1] S.H. Boots-Sprenger, A. Sijben, J. Rijntjes, B.B. Tops, A.J. Idema, A.L. Rivera, F.E. Bleeker, A.M. Gijtenbeek, K. Diefes, L. Heathcock, others, Significance of complete 1p/19q co-deletion, IDH1 mutation and MGMT promoter methylation in gliomas: use with caution, Mod. Pathol. 26 (2013) 922.

[2] C. Horbinski, What do we know about IDH1/2 mutations so far, and how do we use it?, Acta Neuropathol. (Berl.). 125 (2013) 621–636. https://doi.org/10.1007/s00401-013-1106-9.

[3] A.L. Cohen, S.L. Holmen, H. Colman, IDH1 and IDH2 Mutations in Gliomas, Curr. Neurol. Neurosci. Rep. 13 (2013). https://doi.org/10.1007/s11910-013-0345-4.

[4] C. Hartmann, B. Hentschel, W. Wick, D. Capper, J. Felsberg, M. Simon, M. Westphal, G. Schackert, R. Meyermann, T. Pietsch, G. Reifenberger, M. Weller, M. Loeffler, A. von Deimling, Patients with IDH1 wild type anaplastic astrocytomas exhibit worse prognosis than IDH1-mutated glioblastomas, and IDH1 mutation status accounts for the unfavorable prognostic effect of higher age: implications for classification of gliomas, Acta Neuropathol. (Berl.). 120 (2010) 707–718. https://doi.org/10.1007/s00401-010-0781-z.

[5] H. Ohgaki, P. Kleihues, The Definition of Primary and Secondary Glioblastoma, Clin. Cancer Res. 19 (2013) 764–772. https://doi.org/10.1158/1078-0432.CCR-12-3002.

[6] G. Reifenberger, H.-G. Wirsching, C.B. Knobbe-Thomsen, M. Weller, Advances in the molecular genetics of gliomas — implications for classification and therapy, Nat. Rev. Clin. Oncol. 14 (2017) 434–452. https://doi.org/10.1038/nrclinonc.2016.204.

[7] A.R. Rendina, B. Pietrak, A. Smallwood, H. Zhao, H. Qi, C. Quinn, N.D. Adams, N. Concha, C. Duraiswami, S.H. Thrall, S. Sweitzer, B. Schwartz, Mutant IDH1 Enhances the Production of 2-Hydroxyglutarate Due to Its Kinetic Mechanism, Biochemistry. 52 (2013) 4563–4577. https://doi.org/10.1021/bi400514k.

[8] L. Dang, D.W. White, S. Gross, B.D. Bennett, M.A. Bittinger, E.M. Driggers, V.R. Fantin, H.G. Jang, S. Jin, M.C. Keenan, K.M. Marks, R.M. Prins, P.S. Ward, K.E. Yen, L.M. Liau, J.D. Rabinowitz, L.C. Cantley, C.B. Thompson, M.G. Vander Heiden, S.M. Su, Cancer-associated IDH1 mutations produce 2-hydroxyglutarate, Nature. 462 (2009) 739–744. https://doi.org/10.1038/nature08617.

[9] S. Ohba, Y. Hirose, Association between mutant IDHs and tumorigenesis in gliomas, Med. Mol. Morphol. 51 (2018) 194–198. https://doi.org/10.1007/s00795-018-0189-8.

[10] M. Sanson, Y. Marie, S. Paris, A. Idbaih, J. Laffaire, F. Ducray, S. El Hallani, B. Boisselier, K. Mokhtari, K. Hoang-Xuan, J.-Y. Delattre, Isocitrate Dehydrogenase 1 Codon 132 Mutation Is an Important Prognostic Biomarker in Gliomas, J. Clin. Oncol. 27 (2009) 4150–4154. https://doi.org/10.1200/JCO.2009.21.9832.

[11] H. Yan, D.W. Parsons, G. Jin, R. McLendon, B.A. Rasheed, W. Yuan, I. Kos, I. Batinic-Haberle, S. Jones, G.J. Riggins, others, IDH1 and IDH2 mutations in gliomas, N. Engl. J. Med. 360 (2009) 765–773.

[12] D.P. Cahill, A.E. Sloan, B.V. Nahed, K.D. Aldape, D.N. Louis, T.C. Ryken, S.N. Kalkanis, J.J. Olson, The role of neuropathology in the management of patients with diffuse low grade glioma: A systematic review and evidence-based clinical practice guideline, J. Neurooncol. 125 (2015) 531–549. https://doi.org/10.1007/s11060-015-1909-8.
[13] D. Capper, S. WeiÃŸert, J. Balss, A. Habel, J. Meyer, D. JÃ¤ger, U. Ackermann, C. Tessmer, A. Korshunov, H. Zentgraf, C. Hartmann, A. Von Deimling, Characterization of R132H Mutation-specific IDH1 Antibody Binding in Brain Tumors: IDH1R132H Mutation-specific Antibody, Brain Pathol. 20 (2010) 245–254. https://doi.org/10.1111/j.1750-3639.2009.00352.x.
[14] M. Preusser, A. Wöhrer, S. Stary, R. Höftberger, B. Streubel, J.A. Hainfellner, Value and Limitations of Immunohistochemistry and Gene Sequencing for Detection of the *IDH1-R132H* Mutation in Diffuse Glioma Biopsy Specimens, J. Neuropathol. Exp. Neurol. 70 (2011) 715–723. https://doi.org/10.1097/NEN.0b013e31822713f0.
[15] A. Lopez-Beltran, R. Canas-Marques, L. Cheng, R. Montironi, Histopathologic challenges: The second OPINION issue, Eur. J. Surg. Oncol. 45 (2019) 12–15. https://doi.org/10.1016/j.ejso.2018.09.003.
[16] P. Wesseling, J.M. Kros, J.W. Jeuken, The pathological diagnosis of diffuse gliomas: towards a smart synthesis of microscopic and molecular information in a multidisciplinary context, Diagn. Histopathol. 17 (2011) 486–494.
[17] R. Dukor, Vibrational spectroscopy in the detection of cancer, in: Handb. Vib. Spectrosc., J. M. Chalmers and P.R. Griffths Edition, Wiley, Chichester, 2002.
[18] O.J. Old, L.M. Fullwood, R. Scott, G.R. Lloyd, L.M. Almond, N.A. Shepherd, N. Stone, H. Barr, C. Kendall, Vibrational spectroscopy for cancer diagnostics, Anal. Methods. 6 (2014) 3901. https://doi.org/10.1039/c3ay42235f.
[19] Z. Movasaghi, S. Rehman, Dr.I. ur Rehman, Fourier Transform Infrared (FTIR) Spectroscopy of Biological Tissues, Appl. Spectrosc. Rev. 43 (2008) 134–179. https://doi.org/10.1080/05704920701829043.
[20] G. Theophilou, K.M.G. Lima, P.L. Martin-Hirsch, H.F. Stringfellow, F.L. Martin, ATR-FTIR spectroscopy coupled with chemometric analysis discriminates normal, borderline and malignant ovarian tissue: classifying subtypes of human cancer, The Analyst. 141 (2016) 585–594. https://doi.org/10.1039/C5AN00939A.
[21] M.J. Walsh, S.E. Holton, A. Kajdacsy-Balla, R. Bhargava, Attenuated total reflectance Fourier-transform infrared spectroscopic imaging for breast histopathology, Vib. Spectrosc. 60 (2012) 23–28. https://doi.org/10.1016/j.vibspec.2012.01.010.
[22] M.J. Walsh, M.N. Singh, H.F. Stringfellow, H.M. Pollock, A. Hammiche, O. Grude, N.J. Fullwood, M.A. Pitt, P.L. Martin-Hirsch, F.L. Martin, FTIR microspectroscopy coupled with two-class discrimination segregates markers responsible for inter-and intra-category variance in exfoliative cervical cytology, Biomark. Insights. 3 (2008) BMI–S592.
[23] B. Bird, S. Remiszewski, A. Akalin, M. Kon, M. Diem, others, Infrared spectral histopathology (SHP): a novel diagnostic tool for the accurate classification of lung cancer, Lab. Invest. 92 (2012) 1358.

[24] B. Bird, K. Bedrossian, N. Laver, M. Miljković, M.J. Romeo, M. Diem, Detection of breast micro-metastases in axillary lymph nodes by infrared micro-spectral imaging, The Analyst. 134 (2009) 1067. https://doi.org/10.1039/b821166c.
[25] P. Lasch, W. Haensch, D. Naumann, M. Diem, Imaging of colorectal adenocarcinoma using FT-IR microspectroscopy and cluster analysis, Biochim. Biophys. Acta BBA - Mol. Basis Dis. 1688 (2004) 176–186. https://doi.org/10.1016/j.bbadis.2003.12.006.
[26] M. Jermyn, K. Mok, J. Mercier, J. Desroches, J. Pichette, K. Saint-Arnaud, L. Bernstein, M.-C. Guiot, K. Petrecca, F. Leblond, Intraoperative brain cancer detection with Raman spectroscopy in humans, Sci. Transl. Med. 7 (2015) 274ra19-274ra19. https://doi.org/10.1126/scitranslmed.aaa2384.
[27] J. Desroches, M. Jermyn, M. Pinto, F. Picot, M.-A. Tremblay, S. Obaid, E. Marple, K. Urmey, D. Trudel, G. Soulez, M.-C. Guiot, B.C. Wilson, K. Petrecca, F. Leblond, A new method using Raman spectroscopy for in vivo targeted brain cancer tissue biopsy, Sci. Rep. 8 (2018) 1792. https://doi.org/10.1038/s41598-018-20233-3.
[28] T. Hollon, S. Lewis, C.W. Freudiger, X. Sunney Xie, D.A. Orringer, Improving the accuracy of brain tumor surgery via Raman-based technology, Neurosurg. Focus. 40 (2016) E9. https://doi.org/10.3171/2015.12.FOCUS15557.
[29] B. Broadbent, J. Tseng, R. Kast, T. Noh, M. Brusatori, S.N. Kalkanis, G.W. Auner, Shining light on neurosurgery diagnostics using Raman spectroscopy, J. Neurooncol. 130 (2016) 1–9. https://doi.org/10.1007/s11060-016-2223-9.
[30] C. Beleites, G. Steiner, M.G. Sowa, R. Baumgartner, S. Sobottka, G. Schackert, R. Salzer, Classification of human gliomas by infrared imaging spectroscopy and chemometric image processing, Vib. Spectrosc. 38 (2005) 143–149. https://doi.org/10.1016/j.vibspec.2005.02.020.
[31] C. Krafft, K. Thümmler, S.B. Sobottka, G. Schackert, R. Salzer, Classification of malignant gliomas by infrared spectroscopy and linear discriminant analysis, Biopolymers. 82 (2006) 301–305. https://doi.org/10.1002/bip.20492.
[32] C. Krafft, L. Shapoval, S.B. Sobottka, G. Schackert, R. Salzer, Identification of Primary Tumors of Brain Metastases by Infrared Spectroscopic Imaging and Linear Discriminant Analysis, Technol. Cancer Res. Treat. 5 (2006) 291–298. https://doi.org/10.1177/153303460600500311.
[33] K. Gajjar, L.D. Heppenstall, W. Pang, K.M. Ashton, J. Trevisan, I.I. Patel, V. Llabjani, H.F. Stringfellow, P.L. Martin-Hirsch, T. Dawson, F.L. Martin, Diagnostic segregation of human brain tumours using Fourier-transform infrared and/or Raman spectroscopy coupled with discriminant analysis, Anal Methods. 5 (2013) 89–102. https://doi.org/10.1039/C2AY25544H.
[34] A.D. Surowka, D. Adamek, M. Szczerbowska-Boruchowska, The combination of artificial neural networks and synchrotron radiation-based infrared micro-spectroscopy for a study on the protein composition of human glial tumors, The Analyst. 140 (2015) 2428–2438. https://doi.org/10.1039/C4AN01867B.
[35] W. Szopa, T.A. Burley, G. Kramer-Marek, W. Kaspera, Diagnostic and Therapeutic Biomarkers in Glioblastoma: Current Status and Future Perspectives, BioMed Res. Int. 2017 (2017) 1–13. https://doi.org/10.1155/2017/8013575.

[36] G.M. Shankar, J.M. Francis, M.L. Rinne, S.H. Ramkissoon, F.W. Huang, A.S. Venteicher, E.H. Akama-Garren, Y.J. Kang, N. Lelic, J.C. Kim, L.E. Brown, S.K. Charbonneau, A.J. Golby, C. Sekhar Pedamallu, M.P. Hoang, R.J. Sullivan, A.D. Cherniack, L.A. Garraway, A. Stemmer-Rachamimov, D.A. Reardon, P.Y. Wen, P.K. Brastianos, W.T. Curry, F.G. Barker, W.C. Hahn, B.V. Nahed, K.L. Ligon, D.N. Louis, D.P. Cahill, M. Meyerson, Rapid Intraoperative Molecular Characterization of Glioma, JAMA Oncol. 1 (2015) 662. https://doi.org/10.1001/jamaoncol.2015.0917.

[37] M.J. Baker, J. Trevisan, P. Bassan, R. Bhargava, H.J. Butler, K.M. Dorling, P.R. Fielden, S.W. Fogarty, N.J. Fullwood, K.A. Heys, C. Hughes, P. Lasch, P.L. Martin-Hirsch, B. Obinaju, G.D. Sockalingum, J. Sulé-Suso, R.J. Strong, M.J. Walsh, B.R. Wood, P. Gardner, F.L. Martin, Using Fourier transform IR spectroscopy to analyze biological materials, Nat. Protoc. 9 (2014) 1771–1791. https://doi.org/10.1038/nprot.2014.110.

[38] O. Uckermann, T.A. Juratli, R. Galli, M. Conde, R. Wiedemuth, D. Krex, K. Geiger, A. Temme, G. Schackert, E. Koch, G. Steiner, M. Kirsch, Optical Analysis of Glioma: Fourier-Transform Infrared Spectroscopy Reveals the *IDH1* Mutation Status, Clin. Cancer Res. 24 (2018) 2530–2538. https://doi.org/10.1158/1078-0432.CCR-17-1795.

[39] G. Theophilou, C.L.M. Morais, D.E. Halliwell, K.M.G. Lima, J. Drury, P.L. Martin-Hirsch, H.F. Stringfellow, D.K. Hapangama, F.L. Martin, Synchrotron- and focal plane array-based Fourier-transform infrared spectroscopy differentiates the basalis and functionalis epithelial endometrial regions and identifies putative stem cell regions of human endometrial glands, Anal. Bioanal. Chem. 410 (2018) 4541–4554. https://doi.org/10.1007/s00216-018-1111-x.

[40] L.M. Miller, R.J. Smith, Synchrotrons versus globars, point-detectors versus focal plane arrays: Selecting the best source and detector for specific infrared microspectroscopy and imaging applications, Vib. Spectrosc. 38 (2005) 237–240. https://doi.org/10.1016/j.vibspec.2005.03.010.

[41] H.J. Butler, P.M. Brennan, J.M. Cameron, D. Finlayson, M.G. Hegarty, M.D. Jenkinson, D.S. Palmer, B.R. Smith, M.J. Baker, Development of high-throughput ATR-FTIR technology for rapid triage of brain cancer, Nat. Commun. 10 (2019) 4501. https://doi.org/10.1038/s41467-019-12527-5.

[42] J.M. Cameron, H.J. Butler, D.S. Palmer, M.J. Baker, Biofluid spectroscopic disease diagnostics: A review on the processes and spectral impact of drying, J. Biophotonics. 11 (2018) e201700299. https://doi.org/10.1002/jbio.201700299.

[43] L. Lovergne, G. Clemens, V. Untereiner, R.A. Lukaszweski, G.D. Sockalingum, M.J. Baker, Investigating optimum sample preparation for infrared spectroscopic serum diagnostics, Anal Methods. 7 (2015) 7140–7149. https://doi.org/10.1039/C5AY00502G.

[44] L. Lovergne, P. Bouzy, V. Untereiner, R. Garnotel, M.J. Baker, G. Thiéfin, G.D. Sockalingum, Biofluid infrared spectro-diagnostics: pre-analytical considerations for clinical applications, Faraday Discuss. 187 (2016) 521–537. https://doi.org/10.1039/C5FD00184F.

[45] Diamond Light Source, MIRIAM B22 Beamline, (n.d.). https://www.diamond.ac.uk/Instruments/Soft-Condensed-Matter/B22.html.

[46] P. Bassan, A. Sachdeva, A. Kohler, C. Hughes, A. Henderson, J. Boyle, J.H. Shanks, M. Brown, N.W. Clarke, P. Gardner, FTIR microscopy of biological cells and tissue: data analysis using resonant Mie scattering (RMieS) EMSC algorithm, The Analyst. 137 (2012) 1370. https://doi.org/10.1039/c2an16088a.
[47] M. Toplak, G. Birarda, S. Read, C. Sandt, S.M. Rosendahl, L. Vaccari, J. Demšar, F. Borondics, Infrared Orange: Connecting Hyperspectral Data with Machine Learning, Synchrotron Radiat. News. 30 (2017) 40–45. https://doi.org/10.1080/08940886.2017.1338424.
[48] P. Bassan, H.J. Byrne, F. Bonnier, J. Lee, P. Dumas, P. Gardner, Resonant Mie scattering in infrared spectroscopy of biological materials – understanding the 'dispersion artefact,' The Analyst. 134 (2009) 1586. https://doi.org/10.1039/b904808a.
[49] P. Dumas, L.M. Miller, M.J. Tobin, Challenges in Biology and Medicine with Synchrotron Infrared Light, Acta Phys. Pol. A. 115 (2009) 446–454. https://doi.org/10.12693/APhysPolA.115.446.
[50] M.L. McHugh, Interrater reliability: the kappa statistic, Biochem. Medica. 22 (2012) 276–282.
[51] G. Kaur, J.M. Dufour, Cell lines: Valuable tools or useless artifacts, Spermatogenesis. 2 (2012) 1–5. https://doi.org/10.4161/spmg.19885.
[52] J. Kong, S. Yu, Fourier Transform Infrared Spectroscopic Analysis of Protein Secondary Structures, Acta Biochim. Biophys. Sin. 39 (2007) 549–559. https://doi.org/10.1111/j.1745-7270.2007.00320.x.
[53] A. Barth, Infrared spectroscopy of proteins, Biochim. Biophys. Acta BBA - Bioenerg. 1767 (2007) 1073–1101. https://doi.org/10.1016/j.bbabio.2007.06.004.
[54] J.M. Cameron, H.J. Butler, B.R. Smith, M.G. Hegarty, M.D. Jenkinson, K. Syed, P.M. Brennan, K. Ashton, T. Dawson, D.S. Palmer, M.J. Baker, Developing infrared spectroscopic detection for stratifying brain tumour patients: glioblastoma multiforme *vs.* lymphoma, The Analyst. 144 (2019) 6736–6750. https://doi.org/10.1039/C9AN01731C.
[55] K. Hajian-Tilaki, Receiver Operating Characteristic (ROC) Curve Analysis for Medical Diagnostic Test Evaluation, Casp. J. Intern. Med. 4 (2013) 627–635.
[56] J.N. Mandrekar, Receiver Operating Characteristic Curve in Diagnostic Test Assessment, J. Thorac. Oncol. 5 (2010) 1315–1316. https://doi.org/10.1097/JTO.0b013e3181ec173d.
[57] F. Bonnier, M.J. Baker, H.J. Byrne, Vibrational spectroscopic analysis of body fluids: avoiding molecular contamination using centrifugal filtration, Anal. Methods. 6 (2014) 5155. https://doi.org/10.1039/c4ay00891j.
[58] E.F. Petricoin, C. Belluco, R.P. Araujo, L.A. Liotta, The blood peptidome: a higher dimension of information content for cancer biomarker discovery, Nat. Rev. Cancer. 6 (2006) 961–967. https://doi.org/10.1038/nrc2011.
[59] F. Bonnier, F. Petitjean, M.J. Baker, H.J. Byrne, Improved protocols for vibrational spectroscopic analysis of body fluids: Improved protocols for vibrational spectroscopic analysis of body fluids, J. Biophotonics. 7 (2014) 167–179. https://doi.org/10.1002/jbio.201300130.

Chapter 6

Health economic evaluation of a serum-based blood test for brain tumour diagnosis: cost-effectiveness analysis of prospective clinical study and extension to brain cancer subtype classification

This chapter has led to the submission of a collaborative peer-reviewed publication; *Early economic evaluation to guide development of a spectroscopic liquid biopsy for the detection of brain cancer,* **Submitted to:** International Journal of Technology Assessment in Health Care (2020), by E. Gray, J.M. Cameron, H.J. Butler, M.D. Jenkinson, M.G. Hegarty, D.S. Palmer, P.M. Brennan, M.J. Baker.

Contribution: I conducted a literature review; performed the health economic assessment; wrote and prepared this manuscript.

Abstract

Over the years there have been many proof-of-concept studies highlighting the medical utility of vibrational spectroscopy. It is evident that many researchers do not fully understand the requirements to translate into the clinic, thus many promising studies seem to stall following initial publication. Arguably for successful translation of such techniques, it is essential to examine the existing competition, define where in the current pathway the new intervention would be suited, and undertake an economic evaluation to establish the potential cost and health benefits for the health services. Previous work outlined a pre-trial health economic assessment for the introduction of a serum-based spectroscopic blood test into the clinic, which highlighted the test could be cost-effective to the National Health Service.

Here we explore the results from the prospective clinical data gathered from the first 385 patients in our ongoing feasibility study, through cost-effectiveness analysis and one-way sensitivity analysis. For both primary and secondary care scenarios - based on the prospective clinical data - test costs up to £100 would likely be considered cost-effective in health technology assessment agency decision making processes. Moreover, it is expected that primary care tests set at £75 would be cost-saving to the health services.

Additionally, an extension of the economic evaluation has been developed to assess the efficiency of the spectroscopic serum test being employed in secondary care for the differentiation of brain tumour types, namely, glioblastoma multiforme (GBM), primary central nervous system lymphoma (PCNSL) and metastatic brain lesions,

through a cost-consequence analysis. When comparing the costs ‘with’ and ‘without’ the additional subtype test, the cost-consequence analysis reported an estimated saving of ~£138,075 per 10,000 patients, equating to a potential saving of ~£568 per individual cancer case. Furthermore, this could prevent up to 8 unnecessary surgeries, per 100 patients. Thus, a capable diagnostic test that can stratify brain tumour type would have a profound impact for patients as well as the health services.

6.1 Introduction

There has been an abundance of diagnostic studies in the field of biomedical vibrational spectroscopy in the last few decades signifying its potential clinical utility [1–8]. Thus, it is surprising that there is yet to be a successful transition from laboratory benchtop into regular clinical practice. The absence of translation can be attributed to various reasons. Firstly, there is often a lack of concrete understanding of what the unmet clinical needs are, and the limitations of the current gold standard techniques [9]. Secondly, many proof-of-concept studies involve relatively small patient cohorts, which can over-estimate the significance of the results as they are not entirely representative of larger populations [10]. Likewise, the majority are based on retrospective samples, but these studies can be susceptible to bias as the disease states of the patients are already known. Hence, when progressing on to a prospective study, it is common to observe a lesser diagnostic performance [11]. These effects are commonly described as 'spectrum bias', which accounts for the variation in test performance for prediction, screening and disease diagnostics among different population subgroups. For example, a test that has been developed in a population with higher disease prevalence, will normally have a lower sensitivity and higher specificity when applied in a population with lower prevalence of disease [12]. Likewise, symptomatic patients who do not have the disease become more prevalent in prospective studies, thus can be more difficult to successfully detect the disease in these cohorts. Currently, the standardisation of sample preparation and measurement protocols is inadequate, and with a wide array of data pre-processing and analysis techniques to choose from, the lack of consistency in the vibrational spectroscopy field could be detrimental for potential funding and inhibit progress.

There is a vast quantity of research projects being halted at the proof-of-principle stage, meaning very few spectroscopic studies have advanced towards the scale of a clinical trial [8]. Two major hurdles are placed in the path to successful translation; 1) approval from regulatory agencies for marketing and 2) the acceptance from health technology assessment (HTA) agencies who determine which technologies are made available in the public health system. Regulatory agencies are responsible for ensuring new medicines and medical devices are safe, such as the Food and Drug Administration (FDA) in the USA, and Medicines and Healthcare products Regulatory Agency (MHRA) in the UK. These agencies ensure the manufacturer of new interventions follow the appropriate conformity assessment procedure, which is essential for products to attain CE marking and comply with relevant health, safety and environmental requirements [13]. Criteria for successful acceptance require statistically verified clinical trials to prove medical utility, but also clear understanding of the current diagnostic pathways in order to determine the economic and clinical impact of new technologies. For successful translation of such techniques, it is vital to examine the existing competition, define where in the current pathway the proposed 'diagnostic test' would be best suited, and undertake an economic evaluation to establish the potential cost and health benefits for the health services.

Health economics concerns how the health services allocates its resources. The desire of obtaining value for money is evident within this discipline, by promoting both *efficiency* and *equity* – maximising the benefits meanwhile ensuring a fair distribution of available resources. However, due to the scarcity of resources, the

health services are faced with tough decisions regarding new and innovative health care technologies [14]. They must also consider *opportunity costs* which is the loss of other alternatives when one alterative is chosen; where additional costs in one area mean a reduction in what is offered in another area, resulting in a loss of some type of health benefit [15]. Thus, health economists will commonly undertake an *economic evaluation,* which analyses alternative courses of action - in terms of both their *costs* and *consequences* – often in comparison to current practices [16,17]. Simply put, this exercise offers a framework for measuring, valuing and comparing the costs (negative consequences) and benefits (positive consequences) of different health care interventions [16].

How the costs and the benefits are defined will vary according to the desired analyses, hence there are a number of health economic models that could be useful; *cost-minimisation analysis*, *cost-benefit analysis* and *cost-utility analysis*, to name a few [18]. One of the more commonly employed models is *cost-effectiveness analysis* (CEA), which is a comparison of costs in monetary units with outcomes in quantitative non-monetary terms [19]. As described by the World Health Organisation (WHO), CEA can quantify "the gains, or setbacks, in population health as a result of a particular policy or intervention" [20]. This type of analysis compares the costs and outcomes for a new intervention with the best currently available alternative treatment, strategy or intervention [21]. The benefits of an intervention can be portrayed by variety of different outcomes. For example, the differences in quality adjusted life years (QALY) incorporates the impact on both the quantity and quality of life of a proposed intervention [22]. In the UK, the National Institute for

Health and Care Excellence (NICE) make decisions regarding whether a new technology will be funded within the NHS, and this is informed by the evidence of cost-effectiveness. When a new intervention is deemed to be more effective than current practice, but is also more costly, then NICE would have to weigh up the additional costs against the additional QALYs, often expressed as the incremental cost-effectiveness ratio (ICER), which corresponds to the difference in costs between two strategies, to the difference in effectiveness [23]. In general, NICE are willing to pay around £20,000-30,000 per QALY gained by new intervention [24].

Economic evaluation and CEA have been progressively employed in the last few decades to examine the feasibility of novel pharmaceuticals, drugs, biomarkers and medical devices [25]. Notably, the first health economic assessment (HEA) of a new technology relating to vibrational spectroscopy was issued recently in BMJ Open. In 2018, Gray *et al.* published a pre-trial HEA for the introduction of a serum-based spectroscopic blood test into the clinic [26]. The proposed test was for the diagnosis of brain tumours, which utilises attenuated total reflection-Fourier transform infrared (ATR-FTIR) spectroscopy to detect the biosignature of the disease from a patient's blood serum. Based on a retrospective cohort of 433 patients, ATR-FTIR combined with machine learning analysis could successfully identify brain tumour patients at a sensitivity and specificity of 92.3% and 91.5%, respectively [27,28]. As brain tumour symptoms are non-specific, patients often visit their general practitioner (GP) up to five times complaining of headaches or migraines before receiving a referral to secondary care, leading to 62% of lesions being diagnosed as emergency presentations [29]. Brain tumours reduce average life expectancy by 20 years - the

highest of all cancers – highlighting that early detection is imperative for improved patient survival and prognosis [30]. The current pathway for brain tumour diagnosis consists of magnetic resonance imaging (MRI) or computed tomography (CT) imaging followed by surgical biopsy and histopathology. MRI and CT imaging are considerably expensive: a single patient costs the NHS around ~£300 for imaging alone [26]. This means GPs are faced with a difficult decision when a patient complains of persistent headaches. The prevalence of brain tumours in this symptomatic population is minimal (~1%), and considering the financial burden of medical imaging on the health services, it is not entirely surprising that the GPs decide not to refer the patients after their first, or even second, visit. Moreover, patients may be unnecessarily exposed to radiation (CT scans) [31], and incidental findings - unexpected brain abnormalities - are not uncommon in brain scans, which understandably result in anxiety as the vast majority are of no real consequence to the patient [32]. A reliable blood serum test at the primary care setting could fast track these patients into the diagnostic pathway much quicker. Another benefit of such approach would be the reduction in unnecessary brain scans, saving the health services on avoidable spending. A patient with a positive result from the triage test would progress for an urgent brain scan, enhancing the likelihood of survival and improving their prognosis. Likewise, a negative result would allow their GP to explore other options, provide reassurance to patients and prevent the needless anxiety and stress involved with attending imaging appointments. In addition to primary care, the HEA from Gray *et al.* also looked at the potential implementation of the serum triage test into secondary care. In this scenario, the patients are already in the diagnostic pathway for a suspected brain tumour.

Based on retrospective studies, the early economic evaluation from Gray *et al.* reported highly promising results [26]. Their findings indicated that a blood-based spectroscopic test in both a primary and secondary setting, had the potential to be cost-effective if the prospective trial replicated the initial success. This research was based on traditional ATR-FTIR spectroscopy, which used a fixed diamond crystal for the internal reflection element (IRE). Clinical translation has been delayed with this approach as the fixed IREs are expensive, and the requirement to clean the crystal between samples has inhibited throughput. To combat this, technological developments have seen ClinSpec Dx manufacture disposable optical sample slides, that are made from microfabricated silicon and have been designed to replace the traditional fixed crystal. These commercially available slides allow high-throughput spectral analysis, making them ideal for use in a clinical environment. A larger retrospective brain tumour cohort, containing 724 patients, has now been analysed using the novel accessories. We published this work recently, reporting sensitivities and specificities of 93.2% and 92.%, respectively, when differentiating brain cancer and control patients [33]. Furthermore, preliminary data from the first prospective clinical validation study was presented. From 104 patients that had been referred for brain imaging, only 12 were observed to have a brain tumour, yet the test achieved 83.3% sensitivity and 87% specificity.

Since there is scope to differentiate between tumour types using ATR-FTIR serum spectroscopy [34], this approach could reduce the number of chest or full-body scans if it is suggested that there is no metastatic brain lesion present. This could also be beneficial at this stage in the pathway when brain scans are inconclusive. For

example, the aggressive grade IV glioma, glioblastoma multiforme (GBM), is often confused with primary central nervous system lymphoma (PCNSL) and brain metastases, but all have very different treatment pathways [35–37]. Thus, surgical biopsies are always required in order to ascertain the tumour pathology, and to define the most appropriate course of treatment. A blood serum test for such cases could potentially avoid surgery and speed up the time to definitive therapy [38]. Benefits of such a test, with accuracy on subclassification, come from avoidance of unnecessary tumour debulking or resection – a type of surgery that carries substantial risks. The test could indicate if initial biopsy or additional full body imaging would be required prior to surgery. We recently highlighted the potential of the high-throughput technique to assist neurologists in secondary care, by successfully predicting 90.1% of GBM patients and 86.3% of PCNSL cases in our retrospective cohort of 112 patients (Chapter 3) [38]. Additionally, by employing a similar approach, we found that a linear-SVM binary classifier could differentiate GBM from brain metastases with a balanced accuracy of ~90% (Chapter 4) [39].

In this study, we explore the results from the clinical data gathered from the first 385 patients in the ongoing prospective trial. From these findings, CEA and sensitivity analysis will be carried out based on the updated QALY and ICER values. Furthermore, an additional HEA will be developed to assess the efficiency of the spectroscopic serum test being employed in secondary care for the differentiation of brain tumour types, namely GBM, PCNSL and metastatic brain lesions.

6.2 Materials and Methods

6.2.1 Prospective Clinical Data

6.2.1.1 Cost-effectiveness Analysis

We direct the reader to the previously published HEA for a more thorough explanation of the methods used [26]. Briefly, a CEA was conducted to calculate the effects on health outcomes and costs to the health services on the implementation of spectroscopic testing in both primary and secondary care settings, where the health outcomes were considered in life-years and QALYs. Separate models were considered for primary and secondary care, based on the initial decision tree (Figure 6.1) where the comparator was imaging alone for all scenarios. The time horizon of this model is 2 years due to the short duration of survival for this patient group: median survival is approximately 1 year for high-grade gliomas. The primary care scenario explored a population of patients with a clinical presentation that warrants further investigation of a potential brain tumour. For example, patients with consistent headaches and/or neurological deficits. The estimated brain tumour prevalence for the primary care model was ~1%. The secondary care model was based on the population of patients who were already referred for imaging studies in neurology clinics. Understandably, this patient group has the highest positive predictive value (PPV), yet even in this high-risk population the odds of a brain tumour diagnosis is approximately 1:33 [40–42]. Thus, an estimated prevalence value of 3% was employed for the secondary care model.

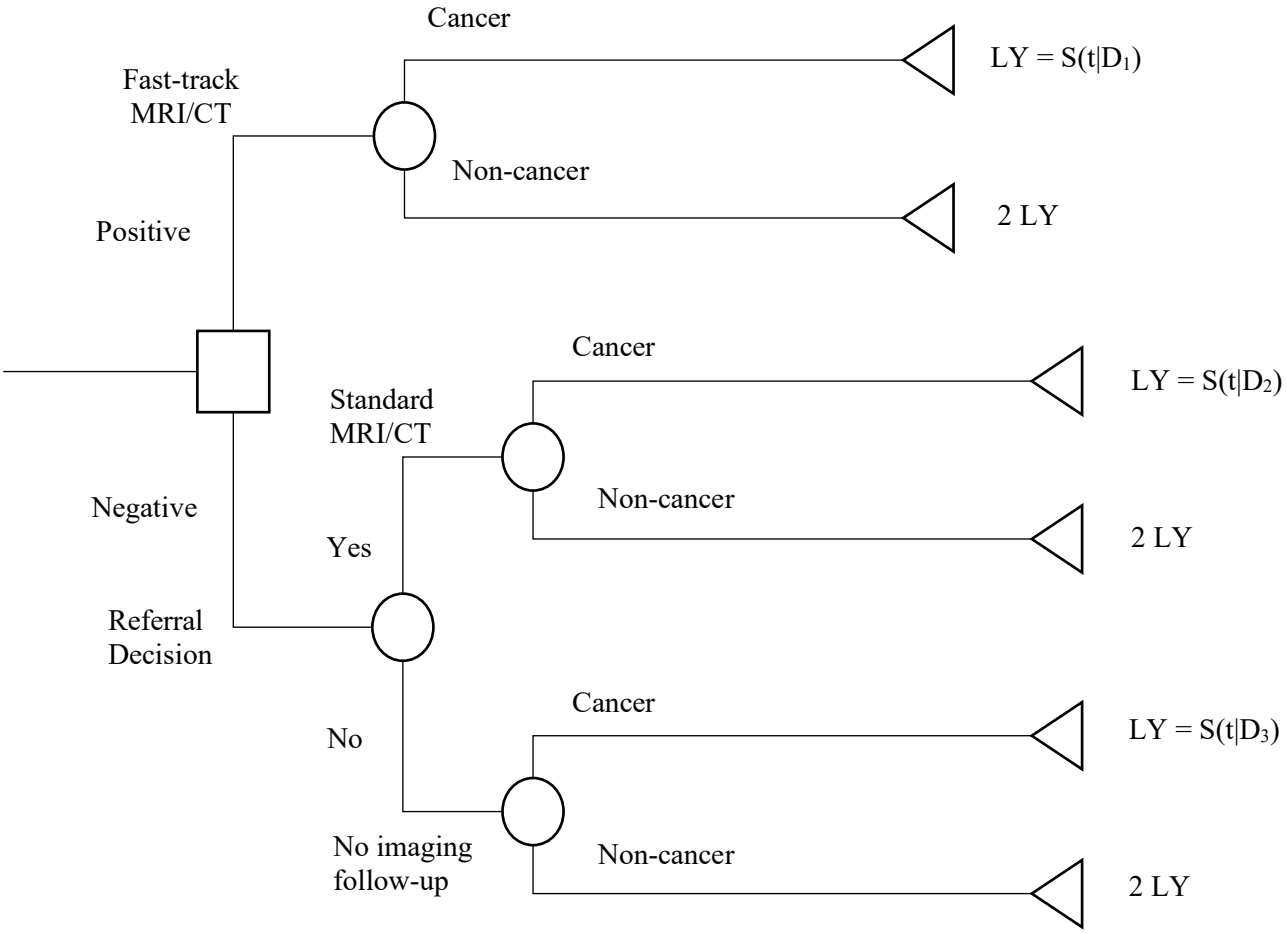

Figure 6.1 – Decision tree model describing the addition of a spectroscopic serum test in the current diagnostic pathway and the effect on imaging for suspected brain tumour. D1, 1 week; D2, 4 weeks; D3, 8 weeks; LY, life-year; S(t|D), survival time in days conditional on 'delay'. Adapted from ref [26].

6.2.1.2 Resource Use and Costs

Resource use includes the application of a spectroscopic serum test to all patients prior to imaging, the imaging studies used in the diagnostic process, outpatient neurology clinic visits and GP visits. Unit costs for imaging studies are taken from the latest UK NHS reference costs available at the time of analysis (2017/2018), and clinic and GP visits from the Personal Social Services Research Unit (PSSRU) costs schedule (Table 6.1).

Table 6.1 - Unit costs for the current brain tumour pathway.

Parameter	**Cost per unit (£)**	**Source**
CT imaging study (CT of head without contrast)	90	NHS reference costs 2017-2018, IMAGOP
MRI imaging study (MRI of brain with post-contrast)	165	NHS reference costs 2017-2018, IMAGOP
Neurology outpatient appointment	35	PSSRU (2016)
GP visit	47.25	PSSRU (2016)
Disease monitoring	116	Ref. [43]
Serum spectroscopy test	25, 50, 75, 100	Examined prices

6.2.1.3 Base Case and Sensitivity Analysis

Firstly, ICERs were calculated for both the primary and secondary care scenarios (Eq. 6.1). The ICER can be defined as the comparative cost-effectiveness of spectroscopic testing compared to no testing:

$$ICER = \frac{C_s - C_n}{H_s - H_n} \quad (6.1)$$

where C_s is the total costs with the implementation of the serum spectroscopy test, and C_n is without testing. Likewise, H_s and H_n refer to the total QALYs with and without the new intervention, and the ICER value is equivalent to the additional cost per QALY gained. The base case analysis was carried out for both scenarios using the parameters outlined in Table 6.1. Additional one-way sensitivity analysis (OWSA) was conducted, where the brain tumour prevalence and survival benefits parameters were systematically varied.

6.2.1.4 Patient Recruitment

Two related cohorts of patients were eligible for inclusion, encompassing different points on the cancer referral and diagnosis pathway. Cohort 1 comprised the symptomatic population, who were referred for direct access computed tomography (DACT) brain imaging for exclusion of significant intracranial pathology. The brain cancer population is encompassed in cohort 2 – those with a recent diagnosis of a primary or recurrent brain tumour. Data interpretation was blinded to a brain imaging and histological diagnosis; DACT imaging outcomes were recorded from the formal radiological report and histological tumour diagnosis was available for patients that underwent surgery (Table 6.2).

Table 6.2 - Patient breakdown per disease classification in eligible population.

Diagnosis	**No. of Patients**
No tumour	319
Astrocytoma – anaplastic grade III	3
Astrocytoma – diffuse grade II	1
Ependymoma	1
Glioblastoma	34
Medulloblastoma	1
Meningioma	5
Metastasis	16
Oligodendroglioma – anaplastic grade III	2
Oligodendroglioma – grade II	1
Pituitary Adenoma	1
Schwannoma	1
Subependymoma	1
TOTAL	**385**

6.2.1.5 Diagnostic Performance

The diagnostic performance was determined by comparison of the blinded test prediction against the report of the brain imaging performed (Table 6.2). In total, 385 patients were enrolled in this study, of which 66 had a confirmed brain tumour. A large proportion of brain tumour cases were diagnosed as GBM which is considered the most common primary brain cancer presentation. Brain metastases are also prominent in this dataset, of which 75% have an unknown primary origin. During the analysis a range of diagnostic algorithms were compared in order to identify the optimum approach. All algorithms were performed in an analyst blind fashion. The top performing algorithm reported 81% sensitivity and 80% specificity for the 385 population (Figure 6.2) [44].

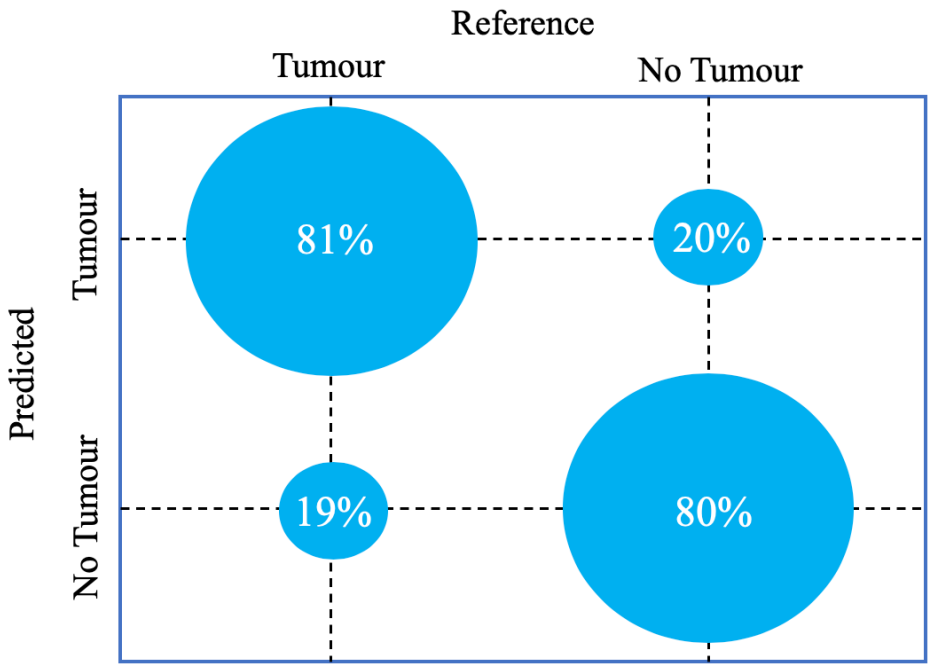

Figure 6.2 - Confusion ball visualisation of sensitivity and specificity for the brain tumour predictions from the 385 patient prospective clinical study.

6.2.2 Economic Analysis of Subtype Classification

Diagnostic subclassifications for which a pre-biopsy diagnostic test would add value, additional to initial imaging, are GBM *versus* PCNSL *versus* brain metastases with unidentified primary site. This judgement was made by iterative process of consultation with clinical experts and a comprehensive review of medical literature. In the selected subclassifications, information about the most likely tumour type can influence clinical decision making around surgery, biopsy and additional testing. Generally, those thought to have GBM would be expedited to surgery, whereas metastatic patients tend to be referred for further imaging [45,46]. Conversely, it is more common for patients with PCNSL to be treated with steroids in the first instance, in order to shrink the tumour before attempting resection [47].

6.2.2.1 Review of the Literature

Occasionally, GBM may be misclassified as PCNSL or brain metastases [48,49]. Although atypical, a small number will occur regularly in all major surgical centres. In both of these instances, surgical resection would usually not be required if the cancer was not GBM. PCNSL is rare – approximately 5% of all primary brain tumours [50] – hence there was a lack of data specific to the misdiagnosis of PCNSL observed in the literature. Thus, it was difficult to estimate the proportion of cases with mistaken diagnosis from imaging alone. It has been estimated that ~1-4% of presumed GBM may be actually be PCNSL. Moreover, the probability of PCNSL being misclassified as GBM - even following biopsy and histopathology - is thought to range between 0.125-1% of cases. Brain metastases are more common, affecting 20-40% of cancer patients [37]. Approximately ~15% of brain metastases present with an unknown primary diagnosis [51]. Regarding the confusion between GBM and brain metastases, many patients will receive full body CT scans in order to rule out metastatic disease. This ultimately delays surgery in cases that are almost certainly GBM. Figure 6.3 outlines the strategic approach for the addition of serum spectroscopy for subtype classification. Without the addition of subtype classification, cases where the patient has a presumed/uncertain GBM diagnosis they would likely be fast-tracked directly to surgery or be subjected to an invasive open biopsy for confirmation. With the addition of subtype classification, a suspected GBM case would be expedited to surgery for tumour resection. On the other hand, presumed PCNSL would be treated with steroid therapy, and metastatic patients would be referred for further imaging to locate the primary tumour origin, thus

avoiding unnecessary surgical procedures. This would not only prevent needless NHS spending, but provide the patient with the most appropriate course of treatment and the best possible prognosis.

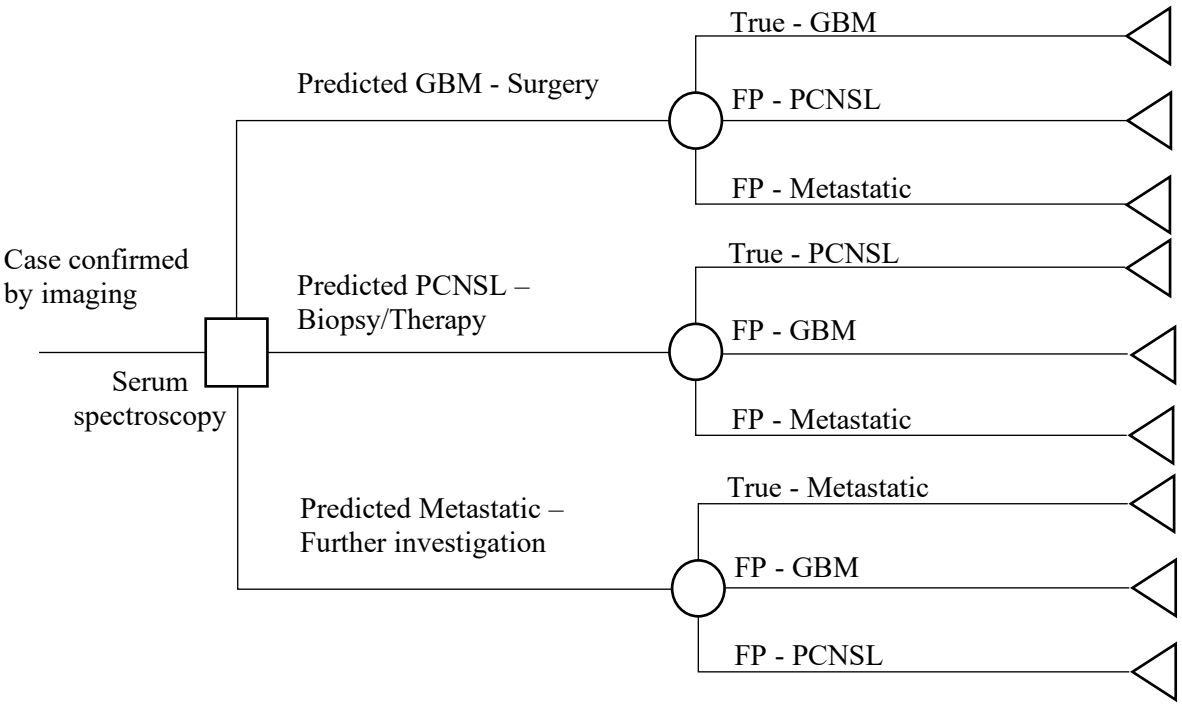

Figure 6.3 – Extension of decision tree with the inclusion of the serum spectroscopy subtype classification. FP: false positive.

Reducing unnecessary surgeries is undoubtedly most beneficial for the patients. The invasive craniotomy is the most commonly employed procedure, where a section of bone is sliced and removed from the skull in order to access the brain. As with many surgical operations, there are a number of risks associated with these procedures (Table 6.3); neurological deficit, infection and post-operative seizures, for example. Thus, decreasing the number of patients going through these invasive procedures when they are not required would enable the most appropriate treatment regime to be

employed, hopefully improve their quality of life and increase their chances of long-term survival.

Table 6.3 - Complications associated with craniotomy surgical procedures [52,53]

Complication	**Risk**
Neurological deficit (short-term or permanent)	1-4%
Post-operative seizure	1-7.5%
Infection – wound, meningitis	3%
'Systemic complications', cardiovascular disease and/or respiratory disease	4-8%
30-day mortality	1.7-3.3%
Readmission within 30 days	11.5%

6.2.2.2 Resource Use and Costs

Further to the costs highlighted in Table 6.1 for the CEA, additional parameters were required for the economic analysis of the subtype classification in secondary care (Table 6.4). The unit costs for surgery, biopsy and imaging were taken from the NHS reference costs (2017/2018). The probability values have been estimated based on discussions with clinical experts and from reviewing the literature. The analysis assumes prevalence of GBM-like PCNSL of 3% and GBM-like brain metastases as 7% of true positive test cases.

Table 6.4 - Additional parameters employed for the subtype analysis.

Parameters		**Value**	**Source**
Costs	Surgical excision/debulking	£7931	NHS reference costs 2017/18, average all AA52 and AA53
	Open biopsy	£1888	NHS reference costs 2017/18, AA54C
	CT imaging study (full body)	£139	NHS reference costs 2017/18, IMAGOP
Prevalence of each subtype among TP cases	GBM	0.9	Test data and assumption
	PCNSL	0.03	
	Metastasis	0.07	
Other	Probability PCNSL case will have primary surgery	0	Ref. [54]
	Probability metastatic disease will have primary surgery	0.1	Estimation [55,56]
	Probability a TP case will have biopsy for possible PCNSL in current practice	0.02	Estimation based on discussions with clinical experts

6.2.2.3 Diagnostic Performance

Our previous work has reported promising subclassification results based on our large retrospective brain tumour cohort. Initially, we highlighted the capability to differentiate between GBM and PCNSL at a sensitivity of 90.1% and specificity of 86.3% using serum spectroscopy [38]. Moreover, we further explored the ability to distinguish between several brain tumour subtypes using binary classifications, successfully separating metastatic brain lesions from GBM (84.3% sensitivity and 96.2% specificity) and PCNSL (91.5% sensitivity and 91.1% specificity) [39]. Three machine learning techniques were utilised as described in Chapter 3 – random forest (RF), partial least squares discriminant analysis (PLS-DA) and support vector

machine (SVM). For the purpose of this economic evaluation, additional multi-class classifiers were employed to achieve three-way classification results, which has slightly reduced the model performance. The results from the ternary classifications outlined in Table 6.5, displaying the mean sensitivities and specificities from 51 resamples of the RF, SVM and PLS-DA classification models.

Table 6.5 - Classification results for the ternary classifier between brain metastases, GBM and PCNSL. Mean sensitivities and specificities from 51 iterations are reported for random forest, support vector machine and partial least squares discriminant analysis.

Model (51 iterations)	**Sensitivity / Specificity (%)**		
	Metastasis	GBM	PCNSL
RF	83.6 / 94.2	86.2 / 84.3	74.0 / 96.4
SVM	82.7 / 94.4	78.5 / 86.4	85.7 / 93.1
PLS-DA	81.6 / 95.2	73.0 / 87.7	89.7 / 89.9

The superior technique in successfully diagnosing GBM and brain metastases appeared to be RF, with mean sensitivities of 83.6%, 86.2% and 74.0% for metastasis, GBM and PCNSL, respectively. The metastasis sensitivity was relatively consistent between the three machine learning techniques (RF: 83.6%; SVM: 82.7%; PLS-DA: 81.6%). Conversely, a higher sensitivity for PCNSL than GBM was reported in both the SVM and PLS-DA models. The results in Table 6.5 were compared to evaluate how clinical benefits and costs vary with the level of diagnostic accuracy.

6.3 Results and Discussion

Similar to the original HEA, the initial triage test scenarios are reported as ICER of cost per QALY. The subtype analysis is a cost analysis plus estimate of reduction in surgeries, and the benefits of that in terms of surgical complications. The literature review highlighted a scarcity of data related to diagnostic uncertainty and clinical outcomes for the scenarios of either GBM *versus* PCNSL or GBM *versus* brain metastases. The literature is limited to case studies involving few patients, or cohort studies of broad patient populations. Thus, a full CEA with QALY was considered infeasible, and a more limited cost-consequence analysis was carried out.

6.3.1 Prospective Clinical Data

6.3.1.1 Cost-effectiveness Assessment

New health care interventions are considered *cost-effective* where their ICER is below the threshold range of £20,000-30,000 per QALY gained [57]. Moreover, they may be deemed *cost-saving* where the new intervention has lower total costs (the ICER values are consequently negative). If the new intervention is cost-saving and also generates more QALYs then it is strictly better and called *dominant*. Base case results for both the primary and secondary care scenarios are presented in Table 6.6, constructed from the results reported in the prospective clinical study. The estimated brain tumour prevalence for primary care was 1%, whereas a 3% prevalence was used for the secondary care analysis.

Table 6.6 - Incremental QALYs, costs and ICERs for primary and secondary care based on the reported 81% sensitivity and 80% specificity.

Test cost (£)	**Primary Care (1% prev.)**			**Secondary Care (3% prev.)**		
	ΔQALY	ΔCost	ICER	ΔQALY	ΔCost	ICER
25	15.38	-545780	-35487	46.14	274130	5941
50	15.38	-295780	-19232	46.14	524130	11360
75	15.38	-45780	-2977	46.14	774130	16778
100	15.38	204220	13279	46.14	1024130	22197

ΔQALY, ΔCost: difference in QALYs/costs (with serum spectroscopy test – without test), 10, 000 patients. ICER, incremental cost-effectiveness ratio; QALY, quality adjusted life year, prev., prevalence.

The base case results show that as a triage tool in primary care, the serum spectroscopy test could improve health outcomes and reduce overall costs. Where the spectroscopic test would cost £75 at the primary care setting, the technology would be *dominant* and cost-saving to the health services, with a reported saving of £45,780 per 10,000 patients. Even at higher test costs up to £100, the test would be considered cost-effective as the ICERs exist below the lower limit of the standard threshold of £20,000 per QALY gained. In the secondary care setting additional costs are applicable, but the implementation of the serum test would also produce sizable health benefits. At test costs up to ~£90, the technology would be likely to be considered as a cost-effective use of resources in HTA agency decision processes. It could be argued that, based on a sensitivity and specificity of 81% and 80% respectively, an increase in the cost of the diagnostic test to £120 may still be considered cost-effective to the NHS. Despite not being included in base analysis, Figure 6.4 projects the potential ICER for an £120 test in primary and secondary care, both of which appear less than the upper limit of the £30,000 per QALY threshold.

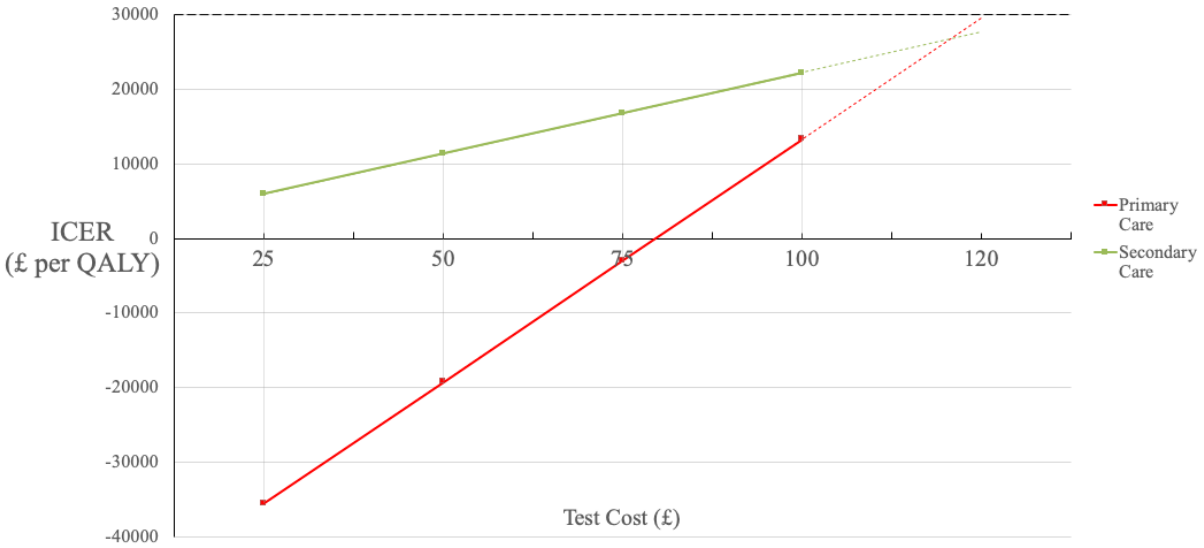

Figure 6.4 - Incremental cost-effectiveness ratios (ICER) at varying test costs for both primary (red) and secondary (green) care. Linear projection described by red and green dashed lines for primary and secondary care, respectively. The £30,000 ICER upper threshold limit is displayed as the dashed black horizontal line.

6.3.1.2 Sensitivity Analysis

The performance of the test with regard to varying levels of brain tumour prevalence is addressed using OWSA. The prevalence estimates for primary and secondary care were 1% and 3%, respectively, therefore a range of percentages less than and higher than those values were selected for the analysis. Table 6.7 outlines the chosen prevalence values for a) primary care and b) secondary care, with the resulting QALYs, costs and ICERs.

Table 6.7 - Sensitivity analysis results from varying brain tumour prevalence in a) primary care and b) secondary care, at test costs of £75 and £100.

a) Primary Care

Prevalence (%)	**£75 Test**			**£100 Test**		
	ΔQALY	ΔCost	ICER	ΔQALY	ΔCost	ICER
0.25	3.84	-56445.07	-14680.46	3.84	193554.93	50340.54
0.5	7.69	-52890.15	-6877.94	7.69	197109.85	25632.56
0.75	11.53	-49335.22	-4277.10	11.53	200664.78	17396.57
1	15.38	-45780.29	-2976.68	15.38	204219.71	13278.57
1.25	19.22	-42225.36	-2196.43	19.22	207774.64	10807.77
1.5	23.07	-38670.44	-1676.26	23.07	211329.56	9160.57
1.75	26.91	-35115.51	-1304.71	26.91	214884.49	7984.00
2	30.76	-31560.58	-1026.05	30.76	218439.42	7101.57

b) Secondary Care

Prevalence (%)	**£75 Test**			**£100 Test**		
	ΔQALY	ΔCost	ICER	ΔQALY	ΔCost	ICER
2.5	38.45	770108.65	20029.29	38.45	1020108.65	26531.39
2.75	42.29	772119.51	18255.99	42.29	1022119.51	24166.99
3	46.14	774130.37	16778.24	46.14	1024130.37	22196.66
3.25	49.98	776141.24	15527.84	49.98	1026141.24	20529.46
3.5	53.83	778152.10	14456.07	53.83	1028152.10	19100.42
3.75	57.67	780162.97	13527.19	57.67	1030162.97	17861.93
4	61.52	782173.83	12714.43	61.52	1032173.83	16778.24
4.25	65.36	784184.70	11997.29	65.36	1034184.70	15822.05

At costs of £75, a spectroscopic diagnostic test would be deemed cost-saving across the full range of tested primary care prevalence values, with negative ICERs reported in each instance. At primary care test costs of £100, it would likely be considered cost-effective in populations with a brain tumour prevalence of 0.5% and above (Figure 6.5a). Likewise, all tested secondary care prevalence values remained below the £30,000 per QALY gained threshold, thus could potentially be deemed to be a cost-effective use of NHS resources (Figure 6.5b)

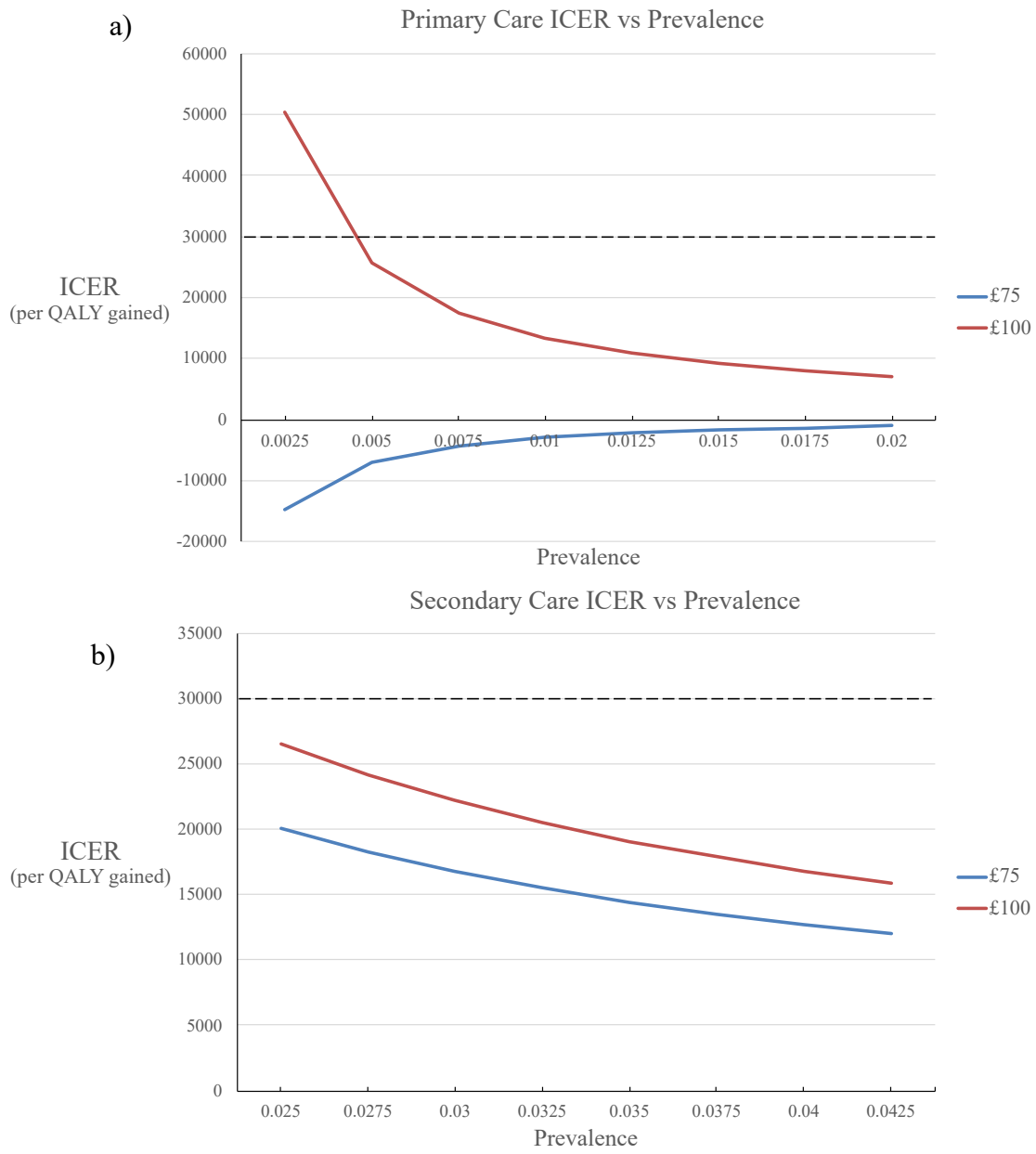

Figure 6.5 - Incremental cost-effectiveness ratios (ICER) at various brain tumour prevalence values in a) primary care and b) secondary care, for test costs of £75 (blue) and £100 (red). The £30,000 ICER threshold is displayed as the dashed black horizontal line.

Additional analysis was conducted to observe changes in ICERs and the effect of predicted survival benefits of early diagnosis by altering the hazard ratio (HR). The HR is a measure of the effect of an intervention – in this case the number of weeks

earlier diagnosis – on an outcome (death) over time - and is one of the most uncertain in the model. It is based on observational data, some assumptions about tumour growth rates and the relationship between tumour size and mortality. Slight changes to this parameter were implemented to assess the stability of our results. The original HR was 1.015 – estimated from a regression analysis which assumed an exponential distribution to survival, conditional on weeks of delay – therefore HRs between 1 and 1.03 in increments of 0.005 were examined. Regarding the effect on median survival, this evaluation uses estimates of the delays in diagnosis, and potential improvements in the speed of diagnosis, from a consecutive patient case series [58], and assumes decrements in median survival is fixed after 4 weeks delay. Table 6.8 describes the difference in median survival over time with varying hazard ratios.

Table 6.8 – Sensitivity analysis results; varying the hazard ratio parameter to determine effect on median survival.

		Hazard Ratio						
		1	1.005	1.01	1.015	1.02	1.025	1.03
Weeks delay	Decrements in median survival (weeks)	Median survival						
0	0	46	46	46	46	46	46	46
1	3.1	46	44.42	42.91	41.45	40.05	38.70	37.40
2	5.1	46	42.90	40.02	37.35	34.86	32.56	30.41
3	6.3	46	41.43	37.33	33.65	30.35	27.39	24.73
4	6.4	46	40.00	34.81	30.32	26.42	23.04	20.11
5	6.4	46	40.00	34.81	30.32	26.42	23.04	20.11
6	6.4	46	40.00	34.81	30.32	26.42	23.04	20.11
7	6.4	46	40.00	34.81	30.32	26.42	23.04	20.11
8	6.4	46	40.00	34.81	30.32	26.42	23.04	20.11
Difference in median survival with and without spectroscopic test per 10K cases (weeks)		0	357.80	673.95	901.42	1134.92	1268.28	1440.81

The median survival represents the length of survival time for the average GBM patient. After week 4, the window for maximum impact has passed, signifying the importance of early detection. Therefore, an accurate estimation of the HR is important as it has a large impact on survival within the first 4 weeks. For every 10,000 patients, the difference in total weeks survival can be estimated for each hazard ratio (Figure 6.6). An increase in HR results in a larger difference in weeks survival, with an almost linear trend for the tested values. Again, this highlights the importance of the HR parameter for reliable health economic evaluation, as altering the value can have a substantial effect on the outcome.

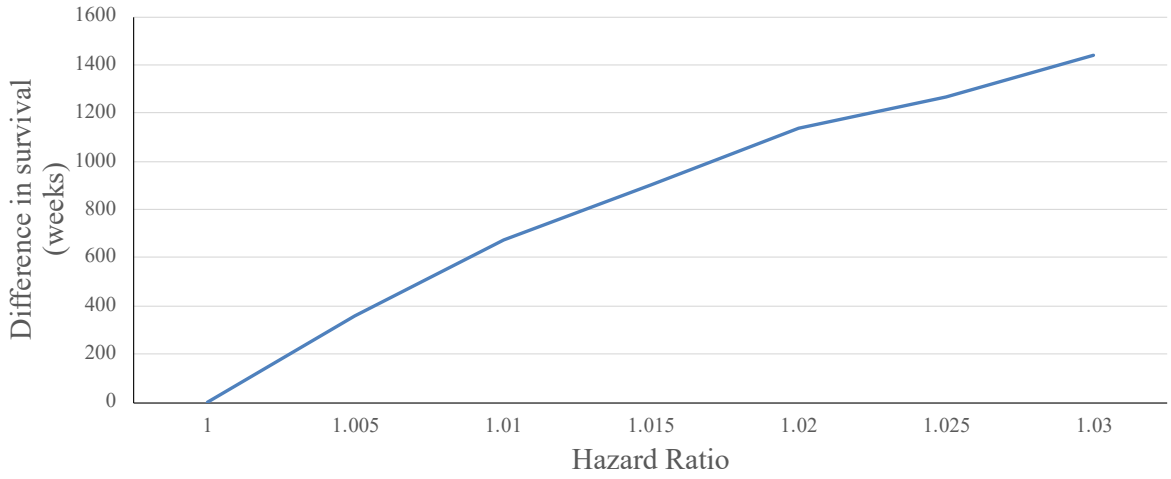

Figure 6.6 - Difference in total weeks survival per 10,000 patients against varying hazard ratio.

Figure 6.7 describes scatter plots of the incremental costs and QALYs associated with the addition of a spectroscopic test in primary and secondary care. As expected, increasing HR values instigate a rise in incremental QALYs per 10K patients, in both scenarios. Likewise, there is a slight increase in incremental costs per 10K patients when looking at potential test costs of £75 and £100. In the primary care scenario, all tested HR values – except 1.005 for £100 tests – reported datapoints that remain below the reference ICER threshold of £30,000 per QALY gained. On the other hand, in the secondary care setting, datapoints for an HR of 1.005 for £75 and £100 test costs, as well as 1.01 for £100 tests, exist above the £30,000 ICER threshold. That said, the rest of tested HRs remained below the reference line in this instance. In other words, the effect of early diagnosis on survival could be slightly smaller than in the base case analysis (e.g. lower HR), and it can still be cost-effective. Likewise, if it were significantly larger, then it could be cost-effective even at higher prices.

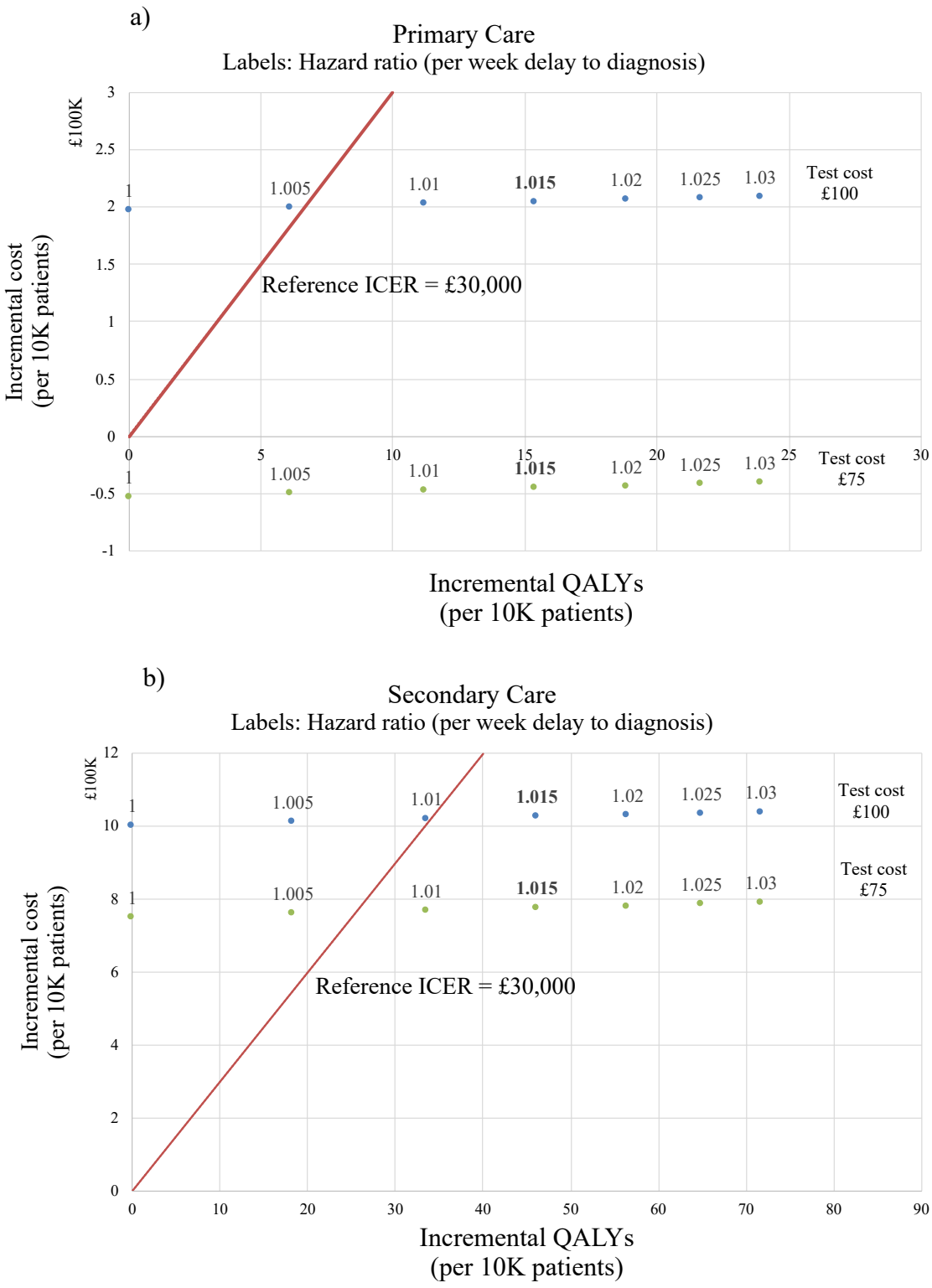

Figure 6.7 - Scatter plot of incremental cost per 10,000 patients against incremental QALYs, for the implementation of a spectroscopic blood test in a) primary care and b) secondary care. Datapoints represent varying hazard ratio estimates for £75 test costs (green) and £100 test costs (blue).

6.3.2 Brain Tumour Subtype Analysis

6.3.2.1 Cost-consequence Analysis

Table 6.9 summarises the main differences in total costs for the inclusion of the subtype extension into secondary care. The results presented are based on a scenario where the subtype has been predicted by the serum test, then confirmed by imaging techniques. When looking at the RF-based results, from the reduction in surgical procedures alone, the NHS could save £144,288. Therefore, with the higher number of biopsies and the additional full body CT scans required for the metastatic patients – accounting for around £12,219 – the health services could potentially save ~£132,069 per 10,000 patients with the implementation of the serum spectroscopy subtype test into secondary care (Table 6.10). This would result in an overall saving of ~£54k, meanwhile avoiding ~7-8 needless surgeries per 100 cancer cases.

Table 6.9 - Summary of total costs for additional clinical procedures with and without the subtype classification.

Cost category	**Cost without subtype test (£)**	**Cost with subtype prediction (£)**		
		RF	SVM	PLS-DA
Surgery	1,927,233	1,782,945	1,777,273	1,776,296
Biopsy	9,176	19,030	19,319	19,673
Full body CT (additional)	0	2,364	2,365	2,364
Total	**1,936,409**	**1,804,339**	**1,798,957**	**1,798,333**

Table 6.10 - The difference in estimated number of surgeries and total cost savings with the implementation of the subtype test.

Model	**Difference in number of surgeries**	**Difference in total costs (-£)**		
	Reduction per 100 cancer cases	per 10K patients with subtype test in secondary care	per detected cancer case (TP)	per 100 cancer cases
RF	7.49	132,069	543.49	54,349.39
SVM	7.78	137,451	565.65	56,564.54
PLS-DA	7.83	138,075	568.21	56,821.26

Despite the RF model successfully predicting more of the GBM patients correctly, it actually reported the lowest cost-saving of the three techniques. The higher PCNSL sensitivity observed in the PLS-DA model resulted in the biggest difference in total costs. With an estimated saving of ~£138,075 per 10,000 patients, the PLS-DA model would potentially save ~£568 per individual cancer case. That being said, the SVM classifier is perhaps the most consistent model, as it reported more balanced sensitivities for all three classes. Nevertheless, all three techniques have highlighted the potential for a cost-saving spectroscopic test in predicting brain tumour subtype.

6.3.2.2 Sensitivity Analysis

The estimated prevalence values for the population of patients that this test would be applicable were based on discussions with clinical experts, which were 0.9, 0.03 and 0.07 for GBM, PCNSL and metastasis, respectively. This is based on the presumption that for every 100 cases of this type of diagnostic dilemma, the vast majority will be true GBM. However, as shown in the analysis of the prospective cohort (Figure 6.5), altering prevalence may have a considerable effect on cost-effectiveness. Therefore, various probability values were chosen for each subtype in order to observe the influence on the cost-consequence analysis. Using the classification results from the PLS-DA model, the differences in the total cost savings per 100 cases are outlined in Figure 6.8.

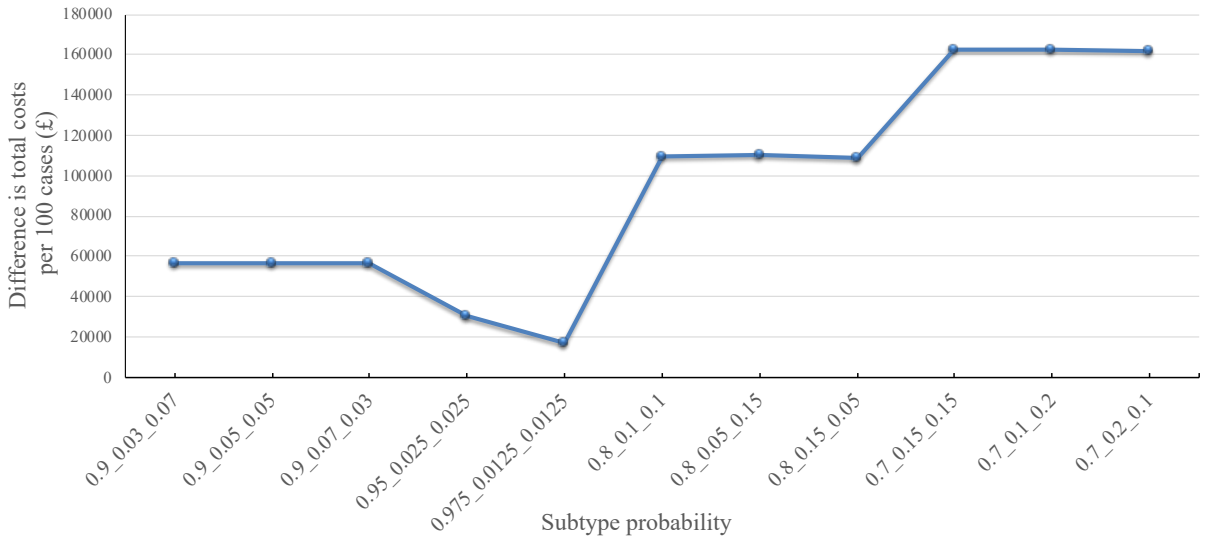

Figure 6.8 - Difference in costs with the addition of a subtype test into secondary care at varying subtype probabilities (GBM_PCNSL_Metastasis). Results presented refer total costs per 100 cancer cases.

These results show that varying the probability of PCNSL and metastasis does not significantly change the overall difference in costs, per 100 cases. Conversely, altering the GBM probability has a substantial effect on the cost savings. The health services would save considerably more in secondary care populations with lower 'true GBM' prevalence – e.g. higher PCNSL and/or metastasis prevalence. As shown in Figure 6.8, when the GBM probability was lowered to 0.8 the total difference in costs per 100 cases was around £109,000. Furthermore, the health services could potentially save ~£160,000 in populations with the true GBM prevalence around 0.7. This analysis is limited in that it is based on various assumptions, but even when utilising harsher probabilities - like 0.975 for GBM - meaning only ~2.5% of cases would be either GBM-like PCNSL or GBM-like brain metastases, the technology has the potential to save approximately £17k of the health service's funds.

6.4 Conclusion

This economic evaluation has highlighted the potential cost and health benefits of the implementation of a serum-based spectroscopic test for the early detection of brain tumours. The CEA results presented here are based on the first 385 patients from a prospective clinical study in Edinburgh, which is currently reporting a sensitivity and specificity of 81% and 80%, respectively. For both primary and secondary care scenarios, test costs up to £100 would likely be considered cost-effective in HTA agency decision making processes, reporting ICER values below the £30,000 per QALY threshold. Furthermore, it is expected that primary care test costs set at £75 would be cost-saving to the health services, with an estimated difference in costs of £45,780 per 10,000 patients, and a negative ICER value of -2977 per QALY gained.

To identify any potential limitations with the economic model that could influence the decision, OWSA looked at the effect of varying the estimated prevalence in each scenario. All tested secondary care prevalence values (2.5 - 4.25%) remained below the £30,000 per QALY gained threshold. Moreover, a spectroscopic diagnostic test could be deemed cost-saving across the full range of tested primary care prevalence values (0.25 - 2%). £100 tests in primary care would likely be deemed cost-effective in populations with a brain tumour prevalence 0.5%. Thus, the change in brain tumour prevalence down to this level did not significantly alter the economic findings. The HR sensitivity analysis highlighted that the effect of early diagnosis on survival is necessary for the intervention to be cost-effective in secondary care. It was shown that this effect could be lesser than in the base case, yet the intervention

can still be cost-effective. Furthermore, if it were significantly larger then it would still be cost-effective even at higher prices.

An extension of the HEA looked at the addition of a brain tumour subtype test, specifically to assist with the differentiation of GBM, PCNSL and brain metastases, as they can appear similar on MRI scans. When comparing the costs 'with' and 'without' the additional subtype test, the PLS-DA model resulted in the biggest difference in total costs, reporting an estimated saving of ~£138,075 per 10,000 patients. This equates to a potential saving of ~£568 per individual cancer case. The results also suggest that this test could prevent up to 8 unnecessary surgeries, per 100 patients. Where it is found that brain tumour patients do not require surgery, the avoidance of craniotomy procedures would certainly be a positive impact. The addition of the subtype test would be beneficial for both the patients and the health services, even in patient populations where MRI confusion is minimal.

The scarcity of related data in the literature meant a comprehensive CEA for the implementation of a subtype spectroscopic test was not feasible. However, by compiling additional costs and through estimation of various subtype parameters, the cost-consequence analysis suggests the test would provide additional economic benefits for health services. The accumulation of more relevant publications in the field that may highlight factors associated with GBM, PCNSL or metastatic brain tumour patients would enable a more robust health economic model to be developed – such as peri/post-operative mortality and/or quality of life after biopsy and debulking procedures. Additionally, the results from the binary classifiers in our

previous work would imply similar multi-class classifiers should have the same performance, but the three-way classifiers tested in this study exhibited slightly lower diagnostic ability. There are some issues in determining the best way to approach binary classification results to fit into a multi-class economic model, yet this may benefit from further research. Moreover, serum samples collected from our retrospective cohort have been utilised here. Thus, progression into a prospective study would aid our understanding of the true diagnostic ability and the true benefits and consequences of the translation of a brain tumour subtype spectroscopic test.

6.5 References

[1] R. Dukor, Vibrational spectroscopy in the detection of cancer, in: Handbook of Vibrational Spectroscopy, J. M. Chalmers and P.R. Griffths Edition, Wiley, Chichester, 2002.

[2] R.A. Shaw, S. Low-Ying, A. Man, K.-Z. Liu, C. Mansfield, C.B. Rileg, M. Vijarnsorn, Infrared Spectroscopy of Biofluids in Clinical Chemistry and Medical Diagnostics, Biomedical Vibrational Spectroscopy. Hoboken, NJ: John Wiley and Sons, Inc. (2008) 79–103.

[3] G. Bellisola, C. Sorio, Infrared spectroscopy and microscopy in cancer research and diagnosis, American Journal of Cancer Research. 2 (2012) 1.

[4] H.J. Byrne, Vibrational Spectroscopy: Disease Diagnostics and Beyond, in: Optical Spectroscopy and Computational Methods in Biology and Medicine, Springer, New York, 2013.

[5] A.L. Mitchell, K.B. Gajjar, G. Theophilou, F.L. Martin, P.L. Martin-Hirsch, Vibrational spectroscopy of biofluids for disease screening or diagnosis: translation from the laboratory to a clinical setting: Vibrational spectroscopy of biofluids: laboratory to clinical setting, Journal of Biophotonics. 7 (2014) 153–165. https://doi.org/10.1002/jbio.201400018.

[6] K. Kong, C. Kendall, N. Stone, I. Notingher, Raman spectroscopy for medical diagnostics — From in-vitro biofluid assays to in-vivo cancer detection, Advanced Drug Delivery Reviews. 89 (2015) 121–134. https://doi.org/10.1016/j.addr.2015.03.009.

[7] M.J. Baker, C.S. Hughes, K.A. Hollywood, Biophotonics: vibrational spectroscopic diagnostics, Morgan & Claypool, San Rafael, 2016. http://iopscience.iop.org/book/978-1-6817-4071-3 (accessed February 4, 2018).

[8] M.J. Baker, H.J. Byrne, J. Chalmers, P. Gardner, R. Goodacre, A. Henderson, S.G. Kazarian, F.L. Martin, J. Moger, N. Stone, J. Sulé-Suso, Clinical applications of infrared and Raman spectroscopy: state of play and future challenges, The Analyst. 143 (2018) 1735–1757. https://doi.org/10.1039/C7AN01871A.

[9] H.J. Byrne, M. Baranska, G.J. Puppels, N. Stone, B. Wood, K.M. Gough, P. Lasch, P. Heraud, J. Sulé-Suso, G.D. Sockalingum, Spectropathology for the next generation: Quo vadis?, The Analyst. 140 (2015) 2066–2073. https://doi.org/10.1039/C4AN02036G.

[10] A. Hackshaw, Small studies: strengths and limitations, European Respiratory Journal. 32 (2008) 1141–1143. https://doi.org/10.1183/09031936.00136408.

[11] J.W. Song, K.C. Chung, Observational Studies: Cohort and Case-Control Studies:, Plastic and Reconstructive Surgery. 126 (2010) 2234–2242. https://doi.org/10.1097/PRS.0b013e3181f44abc.

[12] J.A. Usher-Smith, S.J. Sharp,, S.J. Griffin, The spectrum effect in tests for risk prediction, screening, and diagnosis, BMJ. (2016) i3139. https://doi.org/10.1136/bmj.i3139.

[13] Medicines and Healthcare Products Regulatory Agency, Guidance of the In Vitro Diagonstic Medical Devices Directive 98/79/EC, (n.d.). https://assets.publishing.service.gov.uk/government/uploads/system/uploads/at

tachment_data/file/404335/In_vitro_diagnostic_medical_devices_-_guidance_on_legislation.pdf.
[14] A. Shiell, Health economic evaluation, Journal of Epidemiology & Community Health. 56 (2002) 85–88. https://doi.org/10.1136/jech.56.2.85.
[15] L.B. Russell, Opportunity Costs In Modern Medicine, Health Affairs. 11 (1992) 162–169. https://doi.org/10.1377/hlthaff.11.2.162.
[16] D.P. Kernick, Introduction to health economics for the medical practitioner, Postgraduate Medical Journal. 79 (2003) 147–150. https://doi.org/10.1136/pmj.79.929.147.
[17] M. Drummond, M.J. Sculpher, K. Claxton, G.L. Stoddart, G.W. Torrance, Methods for the Economic Evaluation of Health Care Programmes:, Oup Oxford, 2015. https://www.dawsonera.com:443/abstract/9780191643583.
[18] R. Robinson, Economic evaluation and health care. What does it mean?, BMJ. 307 (1993) 670–673. https://doi.org/10.1136/bmj.307.6905.670.
[19] S. Palmer, S. Byford, J. Raftery, Types of economic evaluation, BMJ. 318 (1999) 1349.1-1349. https://doi.org/10.1136/bmj.318.7194.1349-a.
[20] World Health Organization, Cost-effectiveness analysis for health interventions, Accessed October 2019. (2019). https://www.who.int/heli/economics/costeffanalysis/en/.
[21] S.R. Hill, Cost-effectiveness analysis for clinicians, BMC Medicine. 10 (2012) 10. https://doi.org/10.1186/1741-7015-10-10.
[22] S.J. Whitehead, S. Ali, Health outcomes in economic evaluation: the QALY and utilities, British Medical Bulletin. 96 (2010) 5–21. https://doi.org/10.1093/bmb/ldq033.
[23] H. Bang, H. Zhao, Median-Based Incremental Cost-Effectiveness Ratio (ICER), Journal of Statistical Theory and Practice. 6 (2012) 428–442. https://doi.org/10.1080/15598608.2012.695571.
[24] National Institute for Health and Care Excellence, Assessing cost effectiveness, Accessed October 2019. (2019). https://www.nice.org.uk/process/pmg6/chapter/assessing-cost-effectiveness.
[25] B. Pham, H.A.T. Tu, D. Han, P. Pechlivanoglou, F. Miller, V. Rac, W. Chin, A.C. Tricco, M. Paulden, J. Bielecki, M. Krahn, Early economic evaluation of emerging health technologies: protocol of a systematic review, Syst Rev. 3 (2014) 81. https://doi.org/10.1186/2046-4053-3-81.
[26] E. Gray, H.J. Butler, R. Board, P.M. Brennan, A.J. Chalmers, T. Dawson, J. Goodden, W. Hamilton, M.G. Hegarty, A. James, M.D. Jenkinson, D. Kernick, E. Lekka, L.J. Livermore, S.J. Mills, K. O'Neill, D.S. Palmer, B. Vaqas, M.J. Baker, Health economic evaluation of a serum-based blood test for brain tumour diagnosis: exploration of two clinical scenarios, BMJ Open. 8 (2018) e017593. https://doi.org/10.1136/bmjopen-2017-017593.
[27] J.R. Hands, Investigating the use of Attenuated Total Reflection Fourier-Transform Infrared (ATR-FTIR) Spectroscopy for the Rapid Diagnosis of Brain Tumours using Human Blood Serum, Doctor of Philosophy, University of Strathclyde, 2015.
[28] B.R. Smith, K.M. Ashton, A. Brodbelt, T. Dawson, M.D. Jenkinson, N.T. Hunt, D.S. Palmer, M.J. Baker, Combining random forest and 2D correlation analysis to identify serum spectral signatures for neuro-oncology, The Analyst. 141 (2016) 3668–3678. https://doi.org/10.1039/C5AN02452H.

[29] The Brain Tumour Charity, Finding a Better way?, Accessed August 2017. (2017). http://cdn.basw.co.uk/upload/basw_21512-10.pdf.
[30] The Brain Tumour Charity, Defeating Brain Tumours, Accessed August 2017. (2017). https://www.thebraintumourcharity.org/media/filer_public/49/b5/49b5e1d3-6cff-4399-9d7e-9fabbb5c76a3/the-strategy-publication-rgb-v3.pdf.
[31] R. Smith-Bindman, Y. Wang, P. Chu, R. Chung, A.J. Einstein, J. Balcombe, M. Cocker, M. Das, B.N. Delman, M. Flynn, R. Gould, R.K. Lee, T. Yellen-Nelson, S. Schindera, A. Seibert, J. Starkey, S. Suntharalingam, A. Wetter, J.E. Wildberger, D.L. Miglioretti, International variation in radiation dose for computed tomography examinations: prospective cohort study, BMJ. 364 (2019) k4931. https://doi.org/10.1136/bmj.k4931.
[32] Migraine Trust, Incidental findings on MRI brain scans, (2018). https://www.migrainetrust.org/wp-content/uploads/2018/09/Patient-information-sheet-Incidental-findings-on-brain-scans-3-2.pdf.
[33] H.J. Butler, P.M. Brennan, J.M. Cameron, D. Finlayson, M.G. Hegarty, M.D. Jenkinson, D.S. Palmer, B.R. Smith, M.J. Baker, Development of high-throughput ATR-FTIR technology for rapid triage of brain cancer, Nature Communications. 10 (2019) 4501. https://doi.org/10.1038/s41467-019-12527-5.
[34] J.R. Hands, G. Clemens, R. Stables, K. Ashton, A. Brodbelt, C. Davis, T.P. Dawson, M.D. Jenkinson, R.W. Lea, C. Walker, M.J. Baker, Brain tumour differentiation: rapid stratified serum diagnostics via attenuated total reflection Fourier-transform infrared spectroscopy, Journal of Neuro-Oncology. 127 (2016) 463–472. https://doi.org/10.1007/s11060-016-2060-x.
[35] C.-H. Toh, M. Castillo, A.M.-C. Wong, K.-C. Wei, H.-F. Wong, S.-H. Ng, Y.-L. Wan, Primary Cerebral Lymphoma and Glioblastoma Multiforme: Differences in Diffusion Characteristics Evaluated with Diffusion Tensor Imaging, AJNR Am J Neuroradiol. 29 (2008) 471–475. https://doi.org/10.3174/ajnr.A0872.
[36] D.-D. Xiao, P.-F. Yan, Y.-X. Wang, M.S. Osman, H.-Y. Zhao, Glioblastoma and primary central nervous system lymphoma: Preoperative differentiation by using MRI-based 3D texture analysis, Clinical Neurology and Neurosurgery. 173 (2018) 84–90. https://doi.org/10.1016/j.clineuro.2018.08.004.
[37] S. Campos, P. Davey, A. Hird, B. Pressnail, J. Bilbao, R.I. Aviv, S. Symons, F. Pirouzmand, E. Sinclair, S. Culleton, others, Brain metastasis from an unknown primary, or primary brain tumour? A diagnostic dilemma, Current Oncology. 16 (2009) 62.
[38] J.M. Cameron, H.J. Butler, B.R. Smith, M.G. Hegarty, M.D. Jenkinson, K. Syed, P.M. Brennan, K. Ashton, T. Dawson, D.S. Palmer, M.J. Baker, Developing infrared spectroscopic detection for stratifying brain tumour patients: glioblastoma multiforme *vs.* lymphoma, Analyst. 144 (2019) 6736–6750. https://doi.org/10.1039/C9AN01731C.
[39] J.M. Cameron, C. Rinaldi, H.J. Butler, M.G. Hegarty, P.M. Brennan, M.D. Jenkinson, K. Syed, K.M. Ashton, T.P. Dawson, D.S. Palmer, M.J. Baker, Stratifying brain tumour histological sub-types: the application of ATR-FTIR serum spectroscopy in secondary care, Accepted Article in Cancers. (2020).

[40] H.Z. Wang, T.M. Simonson, W.R. Greco, W.T.C. Yuh, Brain MR Imaging in the Evaluation of Chronic Headache in Patients without Other Neurologic Symptoms, Academic Radiology. 8 (2001) 405–408. https://doi.org/10.1016/S1076-6332(03)80548-2.
[41] A. Sempere, J. Porta-Etessam, V. Medrano, I. Garcia-Morales, L. Concepción, A. Ramos, I. Florencio, F. Bermejo, C. Botella, Neuroimaging in the Evaluation of Patients with Non-Acute Headache, Cephalalgia. 25 (2005) 30–35. https://doi.org/10.1111/j.1468-2982.2004.00798.x.
[42] C.E. Clarke, J. Edwards, D.J. Nicholl, A. Sivaguru, Imaging results in a consecutive series of 530 new patients in the Birmingham Headache Service, J Neurol. 257 (2010) 1274–1278. https://doi.org/10.1007/s00415-010-5506-7.
[43] R. Garside, M. Pitt, R. Anderson, G. Rogers, M. Dyer, S. Mealing, M. Somerville, A. Price, K. Stein, The effectiveness and cost-effectiveness of carmustine implants and temozolomide for the treatment of newly diagnosed high-grade glioma: a systematic review and economic evaluation, Health Technol Assess. 11 (2007). https://doi.org/10.3310/hta11450.
[44] P.M. Brennan, H.J. Butler, L. Christie, M.G. Hegarty, M.D. Jenkinson, C. Keerie, J. Norrie, R. O'Brien, D.S. Palmer, B.R. Smith, M.J. Baker, Early detection of brain tumours using a novel spectroscopic liquid biopsy, Submitted to Brain. (2020).
[45] C. Fernandes, A. Costa, L. Osório, R.C. Lago, P. Linhares, B. Carvalho, C. Caeiro, Current Standards of Care in Glioblastoma Therapy, in: S. De Vleeschouwer (Ed.), Glioblastoma, Codon Publications, Brisbane (AU), 2017. http://www.ncbi.nlm.nih.gov/books/NBK469987/ (accessed March 20, 2020).
[46] D.A. Hardesty, P. Nakaji, The Current and Future Treatment of Brain Metastases, Frontiers in Surgery. 3 (2016). https://doi.org/10.3389/fsurg.2016.00030.
[47] C. Giannini, A. Dogan, D.R. Salomão, CNS Lymphoma: A Practical Diagnostic Approach, J Neuropathol Exp Neurol. 73 (2014) 478–494. https://doi.org/10.1097/NEN.0000000000000076.
[48] Bhatt, Near Misdiagnosis of Glioblastoma as Primary Central Nervous System Lymphoma, J Clin Med Res. (2014). https://doi.org/10.14740/jocmr1846w.
[49] S. Cha, J.M. Lupo, M.-H. Chen, K.R. Lamborn, M.W. McDermott, M.S. Berger, S.J. Nelson, W.P. Dillon, Differentiation of Glioblastoma Multiforme and Single Brain Metastasis by Peak Height and Percentage of Signal Intensity Recovery Derived from Dynamic Susceptibility-Weighted Contrast-Enhanced Perfusion MR Imaging, American Journal of Neuroradiology. 28 (2007) 1078–1084. https://doi.org/10.3174/ajnr.A0484.
[50] J.E. Olson, C.A. Janney, R.D. Rao, J.R. Cerhan, P.J. Kurtin, D. Schiff, R.S. Kaplan, B.P. O'Neill, The continuing increase in the incidence of primary central nervous system non-Hodgkin lymphoma: A Surveillance, Epidemiology, and End Results analysis, Cancer. 95 (2002) 1504–1510. https://doi.org/10.1002/cncr.10851.
[51] H.J. Han, W.S. Chang, H.H. Jung, Y.G. Park, H.Y. Kim, J.H. Chang, Optimal Treatment Decision for Brain Metastases of Unknown Primary Origin: The Role and Timing of Radiosurgery, Brain Tumor Res Treat. 4 (2016) 107. https://doi.org/10.14791/btrt.2016.4.2.107.

[52] C. Jackson, M. Westphal, A. Quiñones-Hinojosa, Complications of glioma surgery, in: Handbook of Clinical Neurology, Elsevier, 2016: pp. 201–218. https://doi.org/10.1016/B978-0-12-802997-8.00012-8.
[53] J.T. Senders, I.S. Muskens, D.J. Cote, N.H. Goldhaber, H.Y. Dawood, W.B. Gormley, M.L.D. Broekman, T.R. Smith, Thirty-Day Outcomes After Craniotomy for Primary Malignant Brain Tumors: A National Surgical Quality Improvement Program Analysis, Neurosurgery. 83 (2018) 1249–1259. https://doi.org/10.1093/neuros/nyy001.
[54] I.S. Haldorsen, J.H. Aarseth, A. Hollender, J.L. Larsen, A. Espeland, O. Mella, Incidence, clinical features, treatment and outcome of primary central nervous system lymphoma in Norway A ten-year national survey, Acta Oncologica. 43 (2004) 520–529. https://doi.org/10.1080/02841860410015640.
[55] K. Yaeger, Mn. Nair, Surgery for brain metastases, Surg Neurol Int. 4 (2013) 203. https://doi.org/10.4103/2152-7806.111297.
[56] M.A. Hatiboglu, D.M. Wildrick, R. Sawaya, The role of surgical resection in patients with brain metastases, Ecancermedicalscience. 7 (2013) 308. https://doi.org/10.3332/ecancer.2013.308.
[57] C. McCabe, K. Claxton, A.J. Culyer, The NICE Cost-Effectiveness Threshold: What it is and What that Means, PharmacoEconomics. 26 (2008) 733–744. https://doi.org/10.2165/00019053-200826090-00004.
[58] A. Aggarwal, N. Herz, P. Campbell, L. Arkush, S. Short, J. Rees, Diagnostic delay and survival in high-grade gliomas – evidence of the 'waiting time paradox'?, British Journal of Neurosurgery. 29 (2015) 520–523. https://doi.org/10.3109/02688697.2015.1012050.

Chapter 7

Project Conclusions

The need for earlier diagnosis of cancer is a crucial evolving strategy for healthcare services in order to improve patient prognosis and streamline clinical pathways. To this extent, brain cancer is in dire need of low-cost approaches for earlier detection to supplement the primary care setting, which would reduce diagnostic delays, better inform clinical referrals and remove financial and practical constraints placed on current imaging modalities. Consequently, earlier diagnosis translates to improved patient outcomes and is a pressing need for healthcare services.

The implementation of a quick blood test for the early detection of brain tumours in primary care could have a huge impact on the quality of life and prognosis for patients. Blood serum was elected for this project as it represents a convenient, highly accessible, minimally invasive sample medium well suited for integration into current clinical workflows. Similarly, ATR-FTIR spectroscopy was used for its ability to assess the entire biochemical signature of serum, providing access to vast quantities of biochemical information relevant to clinical decision making. Until now, the traditional fixed diamond crystal limited the translation of ATR-FTIR spectroscopy, as the methodology required long drying times and cleaning of the crystal between measurements. The study in Chapter 3 validated the capability of the recently developed high-throughput ClinSpec Dx SIRE optical sample slides. When separating brain cancer patients from healthy controls in the large 724 patient cohort, a 90.5% sensitivity and 91.1% specificity was reported. Despite the estimated

prevalence of brain tumours being extremely low (1.6%), the optimal model reported a PPV of 14.2%. A spectroscopic triage test in primary care would assist GPs with referral decisions, where a patient with a positive result for brain cancer would be fast-tracked into secondary care quicker, whilst a negative result would provide reassurance. Thus, the time taken to diagnose brain cancer patients could be reduced significantly, whilst also saving on funds for the health services.

The ability of ATR-FTIR serum spectroscopy to differentiate between brain tumour types has also been presented. This would be particularly attractive for neurologists in secondary care scenarios where brain scans are inconclusive or the primary tumour type is uncertain. Moreover, this would prevent patients undergoing avoidable surgical biopsy and/or further MRI and CT imaging. Initially, the separation of GBM and PCNSL was illustrated in a proof-of-principle study involving 112 patients. The PLS-DA classifier reported a sensitivity of 90.1% and a specificity of 86.3%, indicating some real potential for tumour stratification. Later analysis expanded to additional subtypes of brain lesions. GBM, PCNSL, meningioma and brain metastases were successfully separated from healthy control patients through PLS-DA classifications, all with sensitivities and specificities greater than 92%. Subtle variations in the levels of various protein secondary structures within each patient group were assigned by Amide I deconvolution analysis. The levels of β-sheets were higher, and the α-helix bands had a lower intensity in the PCNSL group when compared to the control set. In contrast, there was a decrease in the β-sheet band (~1630 cm^{-1}) in the GBM patient group compared to the controls, plus a small increase in α-helix intensity (~1660 cm^{-1}). The intensities

of the four largest bands were similar for the meningioma and metastasis groups: two high intensity α-helices at ~1658 and ~1650 cm^{-1}, the disordered structure at ~1645 cm^{-1} and a β-sheet at ~1637 cm^{-1}. Consequently, most of the binary subtype classifications delivered encouraging results. The primary *versus* metastasis cohort showed some early promise, with the RF model able to pick out 90.9% of the 'primary' brain tumour samples within the resampled test sets. The majority of the models performed very well for the brain tumour differentiations, achieving balanced accuracies ~80%. Notably, the metastasis *versus* GBM linear-SVM classifier reported an 84.3% sensitivity and a 96.2% specificity. This could be of great value in instances of radiological confusion as it would limit the volume of unnecessary full-body CT scans, performed simply to rule out metastatic cancer. The ROC curve analysis also suggested high diagnostic capability, with metastasis *versus* PCNSL, GBM *versus* meningioma, and metastasis *versus* GBM models all reported AUC values of ~0.9, which is regarded as an excellent degree of separability. When combined with brain imaging, a spectroscopic diagnosis would have a major impact on the patient pathway and would facilitate more timely treatment in the hospital care setting.

Awareness of a glioma patient's *IDH1* status during surgery would assist vital decision making. In Chapter 5, analysis of data collected through SR-FTIR produced some promising results, where an LDA classifier with 51 iterations reported a sensitivity and specificity of 82.4% and 83.4%, respectively, when differentiating between *IDH1*-mutated and *IDH1*-wildtype glioma tissue. Due to a relatively low number of samples, the standard deviations were 16.8% (sensitivity) and 8.2%

(specificity), thus further analysis with more samples would be valuable. Additionally, ROC analysis produced a mean curve with an AUC of 0.8994, which also suggests a good degree of diagnostic separability. This demonstrates significant potential and suggests FTIR spectroscopy is capable of detecting molecular alterations initiated by genetic mutations in the *IDH1* enzyme. Furthermore, knowledge of the molecular status prior to biopsy would enable personalised therapy for patients, thus facilitating a more efficient resection. In a cohort of 72 glioma patients, classification models were designed to distinguish between *IDH1*-mutated and *IDH1*-wildtype using clinical patient serum. Initially, the whole serum classifier performed inadequately, reporting a balanced accuracy of 52.3%. After the addition of centrifugal filtration, the PLS-DA model provided a balanced accuracy of 69.1%, and the best RF model enhanced the sensitivity (70.6%) and specificity (66.4%). Thus, there may be potential for the filtration step to improve the detection of spectroscopic signatures that could be related to subtle molecular mutations.

Lastly, an economic evaluation in Chapter 6 highlighted the conceivable cost and health benefits of the implementation of a serum spectroscopy-based brain tumour diagnostic test into the clinical setting. For both primary and secondary care scenarios, test costs up to £100 could be judged as cost-effective in HTA agency decision making processes. Moreover, it was predicted that primary care tests set at £75 would actually be cost-saving to the health services. Sensitivity analysis examined the effect of varying the estimated prevalence in each scenario. The £75 test could be deemed cost-saving across the full range of tested primary care prevalence values (0.25 - 2%). Likewise, all tested secondary care prevalence values

(2.5 - 4.25%) remained below the £30,000 per QALY gained threshold. An extension of the HEA explored the addition of a brain tumour subtype test to support the diagnosis of GBM, PCNSL and brain metastases. The cost-consequence analysis reported an estimated saving of ~£138,075 per 10,000 patients, equating to a potential saving of ~£568 per individual cancer case. Furthermore, it was predicted that this could prevent multiple avoidable craniotomies, hence the addition of a subtype test would be favourable for both the patients and the health services, even in populations where MRI confusion is minimal.

Chapter 8

Future Work

This thesis has demonstrated significant potential for earlier brain cancer diagnostics through recognition of biomolecular alterations in patient serum with ATR-FTIR spectroscopy. The development of more high-throughput ATR accessories over the past few years has enabled the first prospective clinical feasibility study to commence in the Western General Hospital, Edinburgh. As described in Chapter 6, the study is ongoing with continuous patient recruitment, with the expectation of expanding out for multi-centre enrolment in the near future. At present, the prospective study is mainly focusing on early brain cancer detection at the primary care setting. However, the work in this thesis has illustrated the potential of the technique to be employed in secondary care as a stratification tool for brain tumour subtypes. Some of the patient groups described here were represented by a limited number of samples due to the rarity of certain tumours. For example, it is more difficult to source the same number of PCNSL samples as the more abundant brain tumour types, like GBM. Continuation of the analysis outlined in this thesis with additional patient samples would be inevitably be worthwhile, in order to make the diagnostic models more robust. Similarly, as with many studies the datasets are built upon retrospective blood serum samples where the disease state of the patients is already known. For these proof-of-concept tests to be validated, these models must now be used to predict tumour type in prospective patients already within the current diagnostic pathway.

The prospects for high-throughput spectroscopy in the clinical environment goes further than purely brain tumour detection. With more research, this platform technology could address the clinical need for various malignancies and other diseases. There has been an abundance of proof-of-principle studies in the clinical spectroscopy field illustrating the diagnostic potentiality for many cancers, thus future work should aim to progress these findings, firstly by determining the needs of other cancer diagnostic pathways. There is also potential for this technology to be employed for patient disease progression and treatment monitoring, which still needs to be examined in greater detail.

The proposed spectroscopic platform has also demonstrated substantial promise of stratifying glioma patients based on *IDH1* molecular status. Regarding the glioma tissue analysis in Chapter 5, the main drawback is the time required to collect and process the data. Synchrotron instruments are admirable for high spatial resolution but can be subject to lengthy analysis times. Sample preparation is also far more complex and laborious than serum analysis. Many steps require suitable equipment and well-trained operators, such as microtoming FFPE tissue blocks, using rather expensive substrates, and paraffin dewaxing protocols prior to IR interrogation. Furthermore, future studies could consider probing fresh tissue biopsies rather than FFPE tissue microarrays, which would be better suited to the idea of determining a patient's *IDH1* status mid-surgery. It is critical that more efficient methods are developed for this application before clinical translation can be realised.

The sample population for the serum study in Chapter 5 was also relatively small, as immunohistochemistry *IDH1* information was not available for many of the patients within the brain cancer cohort. Again, an enlargement of the patient database would be beneficial in identifying the true potential of ATR-FTIR spectroscopy for *IDH1* detection. It was also thought that there may have been some glycerine interference introduced into the samples from the centrifugal filters, which could possibly be obscuring important biological information. Hence, further work with an added washing step prior to centrifugation may be useful. Equally, filtration with a different size of filter may also improve classification performance, as many disease-related biomolecules exist at molecular weights greater than 3kDa.

From a clinical perspective, it is currently uncertain whether R132H-*IDH1* protein molecules are present at sufficient levels in blood serum for diagnostic purposes. Therefore, future studies could consider other proteomic techniques, such as mass spectrometry, to confirm and validate the presence of *IDH1* molecules in clinical blood serum samples. This may also elucidate the differences that have been observed in this project. Additional research into the capability of FTIR spectroscopy to detect other biomarkers may benefit secondary care decision making, such as *ATRX* mutation, *MGMT* hypermethylation and *1p/19q* co-deletion. Furthermore, the detection of other biomarkers alongside currently clinically recognised biomarkers may also provide additional diagnostic information. A research grant by Cancer Research UK was recently awarded to the research group to explore clinical biomarkers for glioma through spectroscopic detection techniques, thus significant work in this area is expected to be conducted in the immediate future.

Appendix 1 – Supplementary Information for Chapter 3

Table A1.1 – Retrospective 724 patient cohort information.

	Brain Cancer	***Non-Cancer***
Total	487	237
Sex (M/F)	280/207	149/84
Age Range	21-96	19-69
Average Age	61	35

Table A1.2 - Retrospective 724 patient cohort breakdown.

	Tumour Type	**WHO Grade**	**Total**
Cancer	Glioblastoma multiforme	IV	260
	Gliosarcoma	IV	4
	Oligodendroglioma	II	11
	Diffuse astrocytoma	II	23
	Anaplastic astrocytoma	III	10
	Oligoastrocytoma	II	3
	Glioma	I	7
	Pilocytic astrocytoma	I	9
	Pleomorphic xanthoastrocytoma	II	1
	Schwannoma	I	14
	Ependymoma	II	6
	Hemangiopericytoma	II/III	2
	Haemanglioblastoma	I	1
	Ganglioglioma	I	1
	Medulloblastoma	IV	1
	PPTID	II/III	1
	Meningioma	I	46
	Pituitary adenoma		29
	Lymphoma		2
	Metastasis		56
Control			237
		Total	724

Table A1.3 - GBM versus PCNSL patient cohort information.

	GBM	***PCNSL***
Total	71	41
Sex (M/F)	48/23	27/14
Age Range	30-85	27-86
Average Age	61	60

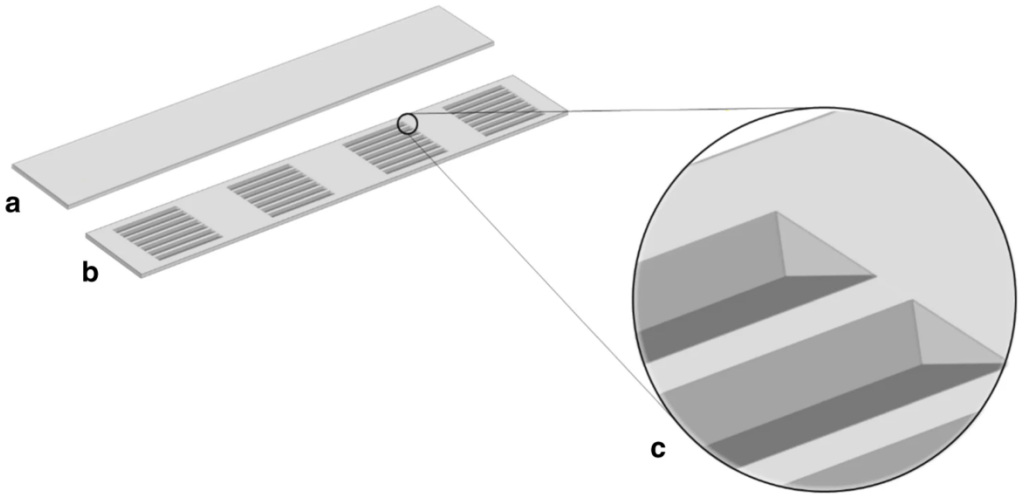

Figure A1.1 - Schematic representation of silicon internal reflection element for clinical spectroscopy. a, Sample-side; b, IR facing side; c, v-groove detailing (not to scale). From: Butler, H.J., Brennan, P.M., Cameron, J.M. et al. Development of high-throughput ATR-FTIR technology for rapid triage of brain cancer. Nat Commun 10, 4501 (2019). https://doi.org/10.1038/s41467-019-12527-5.

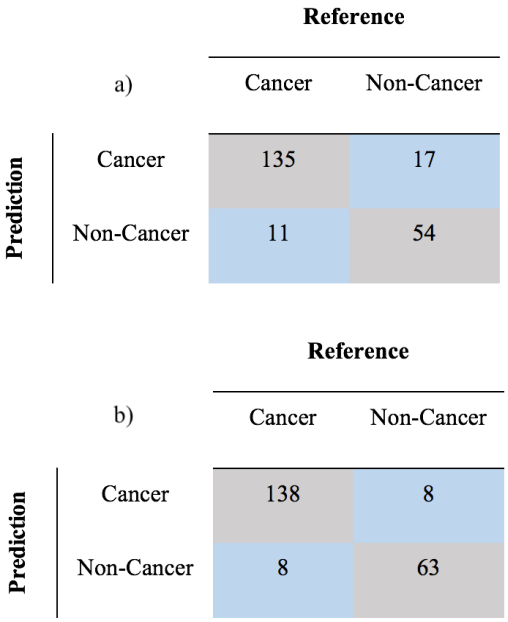

Figure A1.2 - Confusion matrices for the test set of the 724 dataset (a) initial random forest (RF) model, and (b) RF with SMOTE. Grey represents correct predictions, and blue represents incorrect predictions.

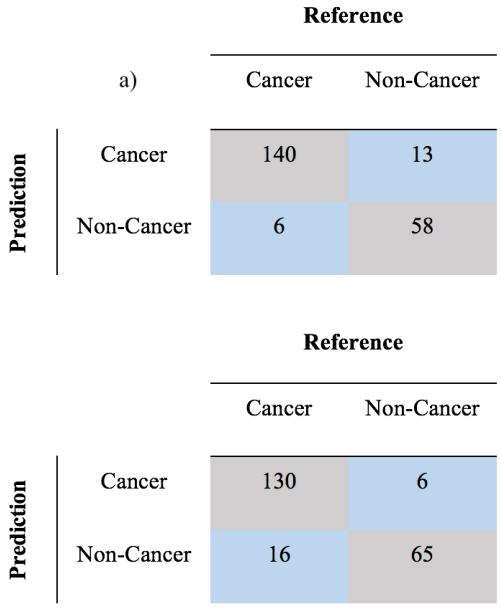

Figure A1.3 - Confusion matrices for the test set of the 724 dataset (a) initial partial least squares-discriminant analysis (PLS-DA) model, and (b) PLS-DA with SMOTE. Grey represents correct predictions, and blue represents incorrect predictions.

a)

Prediction	Reference: Cancer	Reference: Non-Cancer
Cancer	136	13
Non-Cancer	10	58

b)

Prediction	Reference: Cancer	Reference: Non-Cancer
Cancer	134	7
Non-Cancer	12	64

Figure A1.4 - Confusion matrices for the test set of the 724 dataset (a) initial support vector machine (SVM) model, and (b) SVM with SMOTE. Grey represents correct predictions, and blue represents incorrect predictions.

Prediction	Reference: GBM	Reference: Lymphoma
GBM	22	2
Lymphoma	2	11

Figure A1.5 - Confusion matrices for the test set of the glioblastoma v lymphoma dataset; partial least squares-discriminant analysis model with SMOTE. Grey represents correct predictions, and blue represents incorrect predictions.

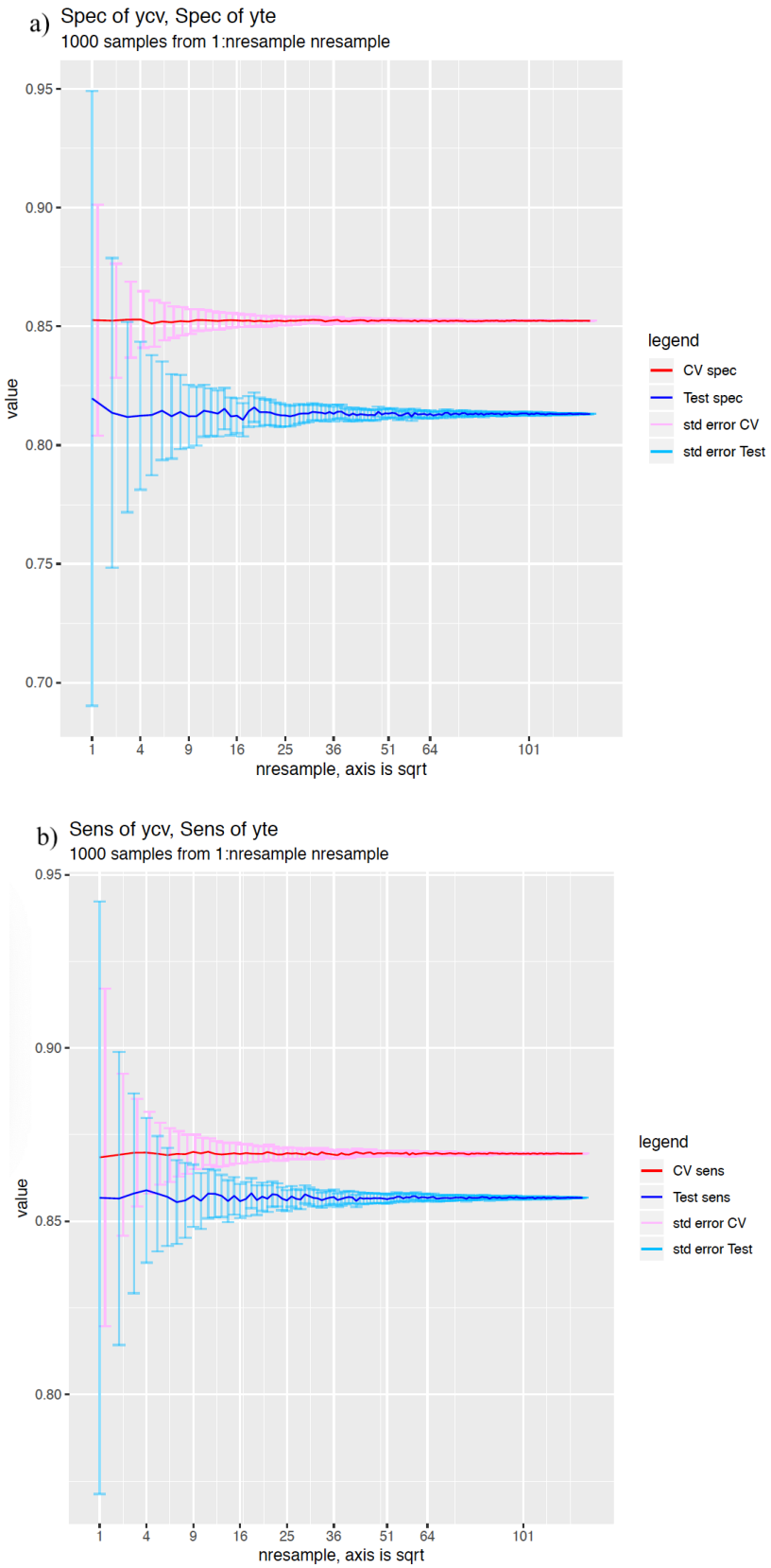

Figure A1.6 - Bootstrapping analysis to determine sufficient number of resamples required for the lymphoma vs glioblastoma patient dataset: (a) the sensitivity and (b) specificity

Appendix 2 – Supplementary Information for Chapter 4

Table A2.1 – Age and sex information for each of the tested patient groups.

	Control	***Primary***	***Glioma***	***PCNSL***	***GBM***	***Meningioma***	***Metastasis***
Total	87	303	192	41	102	111	210
Sex (M/F)	39/48	163/140	123/69	27/14	62/40	40/71	84/126
Age Range	20-64	17-85	17-85	27-86	30-85	26-81	30-86
Average Age	35	54	53	60	61	56	61

Table A2.2 – Additional information on the classification tuning parameters.

Classification (positive class v negative class)	**Tuning Parameters**	**Model + Sampling**
GBM v Control	*ncomp 10*	PLS-DA + no
PCNSL v Control	*ncomp 14*	PLS-DA + up
Meningioma v Control	*ncomp 16*	PLS-DA + up
Metastasis v Control	*ncomp 13*	PLS-DA + up
Primary v Metastasis	*ntree 500, nodesize 1, mtry 30*	RF + up
Glioma v Meningioma	*cost 0.019*	SVM + down
GBM v Meningioma	*ntree 500, nodesize 1, mtry 30*	RF + no
Metastasis v GBM	*cost 0.019*	SVM + down
Metastasis v PCNSL	*ncomp 10*	PLS-DA + smote
Metastasis v Meningioma	*ncomp 14*	PLS-DA + up

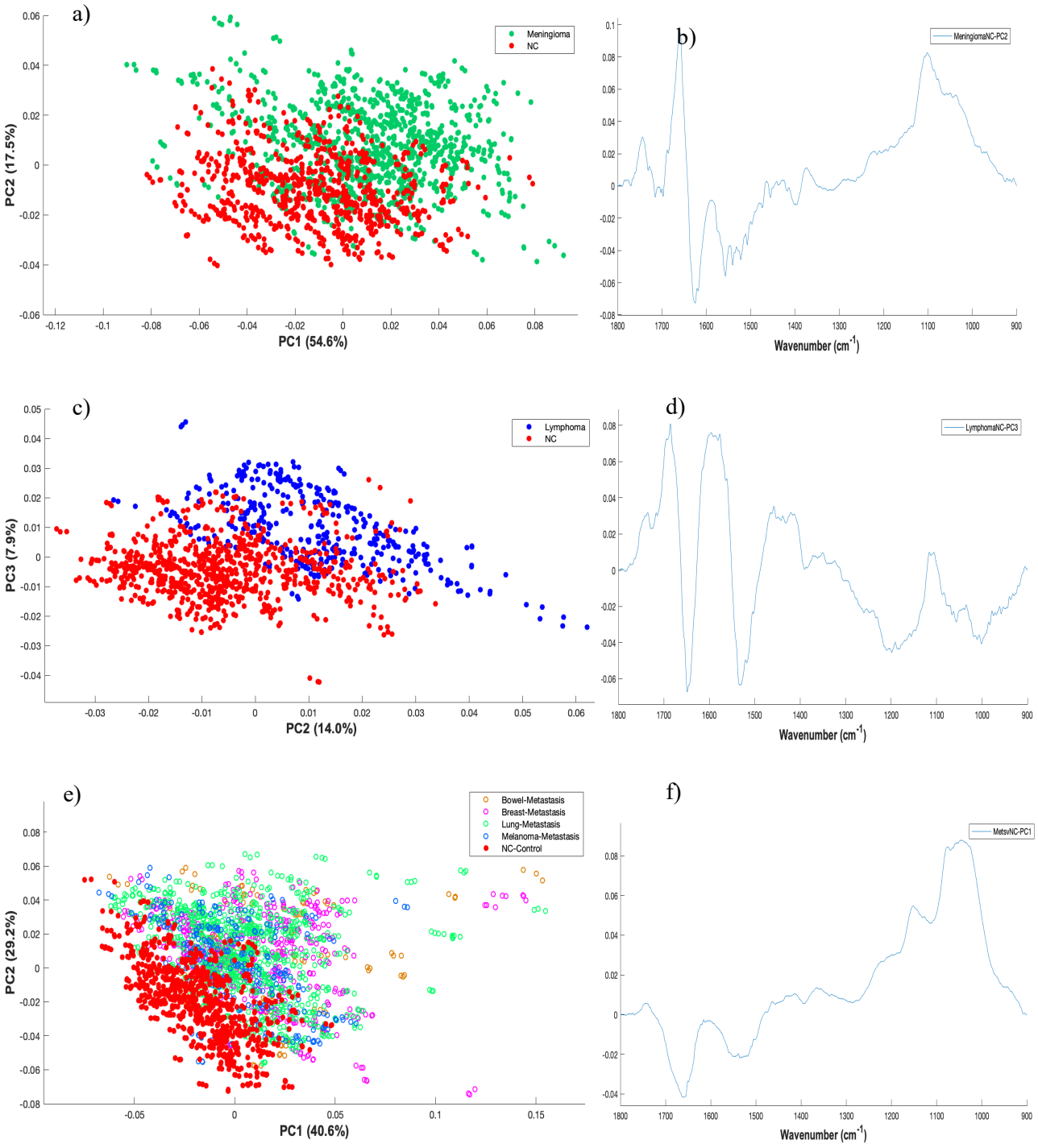

Figure A2.1 – PCA scores plots displaying the biggest separation between: healthy control (red) *versus*; a) meningioma (green), c) lymphoma (blue) and e) metastasis (bowel: orange rings, breast: pink rings, lung: green rings, melanoma: blue rings). Corresponding loadings plots for the principle component that describes which wavenumbers account for the separation of; b) meningioma, d) lymphoma and f) metastasis against control.

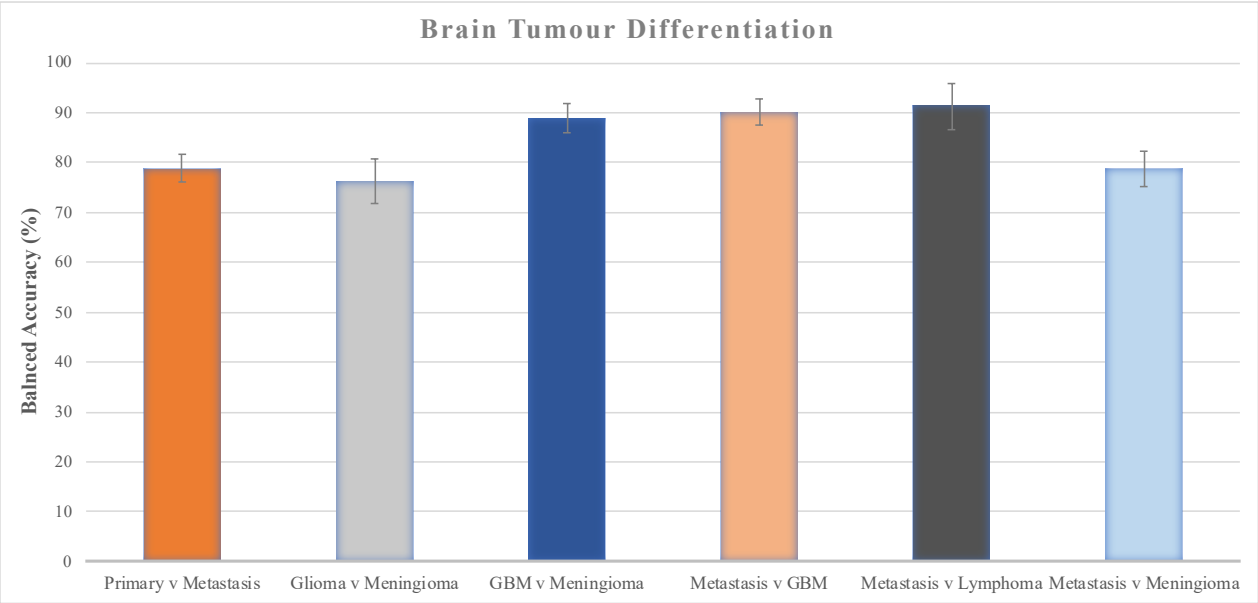

Figure A2.2 - Bar graph of balanced accuracies for the differentiation of brain tumour types with their associated standard deviations.

Appendix 3 – Supplementary Information for Chapter 5

Table A3.1 – Samples included in the synchrotron-based tissue microarray study.

	IDH1-mutated	*IDH1-wildtype*
Total	21	78
Sex (M/F)	9 / 12	48 / 30
Glioblastoma	10	67
Astrocytoma	4	4
Pilocytic Astrocytoma	0	2
Oligodendroglioma	7	5

Table A3.2 – Samples included in the centrifugal filtration of serum study.

	IDH1-mutated	*IDH1-wildtype*
Total	36	36
Sex (M/F)	21 / 15	23 / 13
Glioblastoma	0	12
Astrocytoma	24	24
Oligodendroglioma	12	0

Table A3.3 – Top 50 LDA models from pre-processing grid search, based on Kappa score.

model	Accuracy	Kappa	Sensitivity	Specificity	F1	Balanced Accuracy
n1_l0-0_b4_s1-4_p1-1200to1800	0.8652038	0.6468702	0.8787879	0.8616601	0.732303	0.870224
n2_l0-0_b2_s1-3_p1-1200to1800	0.8902821	0.6314261	0.6515152	0.9525692	0.69312	0.8020422
n0_l1-0_b4_s0-0_p1-1200to1800	0.8652038	0.6166079	0.7424242	0.8972332	0.7005675	0.8198287
n3_l2-0_b8_s1-2_p1-1000to1800	0.8777429	0.5954007	0.6363636	0.9407115	0.6674396	0.7885375
n3_l1-0_b4_s1-2_p1-1000to1800	0.8714734	0.5936348	0.6515152	0.9288538	0.6720128	0.7901845
n3_l0-0_b4_s1-2_p1-1200to1800	0.8714734	0.591284	0.6363636	0.9328063	0.6641601	0.784585
n2_l2-0_b2_s0-0_p1-1200to1800	0.8652038	0.5873832	0.6515152	0.9209486	0.6704387	0.7862319
n2_l0-0_b4_s1-3_p1-1000to1800	0.8432602	0.5841362	0.8030303	0.8537549	0.6837897	0.8283926
n1_l0-0_b4_s1-2_p1-1000to1800	0.862069	0.5782494	0.6666667	0.9130435	0.6597425	0.7898551
n2_l0-0_b4_s1-4_p1-1200to1800	0.8526646	0.5766405	0.7424242	0.8814229	0.6684959	0.8119236
n3_l2-0_b4_s1-2_p1-1200to1800	0.8369906	0.5737398	0.8181818	0.8418972	0.6777389	0.8300395
n1_l0-0_b1_s0-0_p1-1200to1800	0.8557994	0.5722462	0.6969697	0.8972332	0.66271	0.7971014
n3_l2-0_b1_s1-4_p1-1200to1800	0.8652038	0.5707929	0.6060606	0.9328063	0.6527745	0.7694335
n1_l1-0_b4_s0-0_p1-1000to1800	0.8495298	0.5705938	0.7121212	0.8853755	0.6595468	0.7987484
n3_l1-0_b4_s1-2_p1-1200to1800	0.8714734	0.5653157	0.5757576	0.9486166	0.6402981	0.7621871
n2_l1-0_b4_s1-3_p1-1200to1800	0.8683386	0.5632158	0.6060606	0.9367589	0.6385675	0.7714097
n1_l0-0_b4_s1-3_p1-1000to1800	0.8777429	0.5604897	0.530303	0.9683794	0.6263545	0.7493412
n1_l2-0_b4_s0-0_p1-1200to1800	0.8401254	0.5600921	0.7272727	0.8695652	0.6606487	0.798419
n2_l1-0_b4_s0-0_p1-1000to1800	0.862069	0.5597247	0.6060606	0.9288538	0.6414767	0.7674572
n2_l2-0_b4_s1-2_p1-1200to1800	0.8714734	0.5571603	0.5757576	0.9486166	-	0.7621871
n1_l1-0_b4_s1-4_p1-1200to1800	0.8432602	0.5571262	0.7121212	0.8774704	0.655943	0.7947958
n0_l2-0_b8_s1-3_p1-1000to1800	0.8777429	0.5568751	0.5	0.9762846	0.6216713	0.7381423
n3_l2-0_b8_s1-4_p1-1000to1800	0.8526646	0.556261	0.6515152	0.9051383	0.647619	0.7783267
n0_l1-0_b4_s1-3_p1-1200to1800	0.8401254	0.5533281	0.6818182	0.8814229	0.6529921	0.7816206

n0_l0-0_b1_s1-4_p1-1200to1800	0.8714734	0.5528742	0.530303	0.9604743	0.624864	0.7453887
n3_l0-0_b4_s1-3_p1-1200to1800	0.8557994	0.5504227	0.5909091	0.9249012	0.637072	0.7579051
n0_l2-0_b2_s1-2_p1-1200to1800	0.8495298	0.5495883	0.6666667	0.8972332	0.6441195	0.7819499
n1_l0-0_b1_s1-4_p1-1200to1800	0.8557994	0.5464795	0.6212121	0.916996	0.633856	0.7691041
n1_l2-0_b4_s1-3_p1-1000to1800	0.830721	0.5452847	0.7727273	0.8458498	0.6522455	0.8092885
n1_l0-0_b4_s1-2_p1-1200to1800	0.8275862	0.5450624	0.7727273	0.8418972	0.6542278	0.8073123
n2_l0-0_b2_s1-4_p1-1200to1800	0.8338558	0.5411106	0.7272727	0.8616601	0.6446316	0.7944664
n3_l1-0_b4_s1-3_p1-1200to1800	0.815047	0.5410151	0.8030303	0.8181818	0.6568059	0.8106061
n1_l2-0_b2_s1-2_p1-1200to1800	0.8401254	0.5357673	0.6818182	0.8814229	0.6363213	0.7816206
n0_l1-0_b4_s1-3_p1-1000to1800	0.8526646	0.5351708	0.6212121	0.9130435	0.6204923	0.7671278
n0_l2-0_b4_s1-3_p1-1200to1800	0.8369906	0.5350227	0.6969697	0.8735178	0.6352135	0.7852437
n2_l0-0_b4_s1-3_p1-1200to1800	0.8746082	0.5348123	0.4848485	0.9762846	0.5971861	0.7305665
n0_l0-0_b2_s1-3_p1-1200to1800	0.8495298	0.5345926	0.6212121	0.9090909	0.6280417	0.7651515
n1_l2-0_b8_s0-0_p1-1000to1800	0.8589342	0.5339241	0.5757576	0.9328063	0.6160536	0.7542819
n3_l1-0_b4_s1-4_p1-1200to1800	0.846395	0.5314692	0.6363636	0.9011858	0.6227329	0.7687747
n1_l1-0_b4_s1-3_p1-1200to1800	0.8714734	0.5313889	0.4848485	0.972332	0.5975075	0.7285903
n1_l2-0_b8_s1-3_p1-1200to1800	0.8432602	0.5280296	0.6515152	0.8932806	0.6196915	0.7723979
n1_l1-0_b4_s1-2_p1-1200to1800	0.8087774	0.5278049	0.7878788	0.8142292	0.6458796	0.801054
n3_l1-0_b4_s0-0_p1-1200to1800	0.8557994	0.5273934	0.5606061	0.9328063	0.6129608	0.7467062
n0_l1-0_b4_s1-4_p1-1200to1800	0.830721	0.5270823	0.7121212	0.8616601	0.6339407	0.7868906
n0_l2-0_b4_s1-2_p1-1200to1800	0.846395	0.5264629	0.6212121	0.9051383	0.6214876	0.7631752
n1_l0-0_b4_s1-4_p1-1000to1800	0.7899687	0.525957	0.8787879	0.7667984	0.6536246	0.8227931
n0_l2-0_b1_s1-4_p1-1200to1800	0.8369906	0.5235235	0.6818182	0.8774704	0.6248756	0.7796443
n0_l1-0_b4_s1-2_p1-1200to1800	0.8056426	0.5232485	0.8333333	0.798419	0.6443412	0.8158762
n1_l1-0_b1_s1-2_p1-1200to1800	0.8432602	0.5200658	0.6363636	0.8972332	0.6173735	0.7667984
n0_l2-0_b8_s1-4_p1-1000to1800	0.8369906	0.5200327	0.6515152	0.8853755	0.6224957	0.7684453

Table A3.4 –Top 10 LDA models from pre-processing grid search, with sensitivity and specificity results from 51 resamples. Optimal results in bold.

Model Name	**Pre-processing**					**Sampling**			
	Norm	Deriv	Bin	Smooth	Cut	No	Up	Down	Smote
	-					Sensitivity / Specificity (%)			
n0_l1-0_b4_s0-0_p1-1200to1800	0	1	4	0	1200-1800	67.3/86.5	69.9/84.6	82.3/76.6	82.3/77.6
n0_l1-0_b4_s1-2_p1-1200to1800	0	1	4	2	1200-1800	76.1/83.5	89.5/72.0	87.9/70.4	81.7/78.4
n0_l2-0_b2_s1-4_p1-1200to1800	0	2	2	4	1200-1800	78.4/73.0	80.4/70.4	78.4/70.0	78.4/70.0
n1_l0-0_b4_s1-4_p1-1200to1800	1	0	4	4	1200-1800	76.5/81.3	**82.4/83.4**	78.1/85.0	80.7/79.5
n1_l0-0_b4_s1-4_p1-1000to1800	1	0	4	4	1000-1800	89.2/62.0	79.7/77.3	83.0/72.5	76.5/80.3
n2_l0-0_b2_s1-3_p1-1200to1800	2	0	2	3	1200-1800	86.6/68.7	82.7/72.7	80.1/76.8	79.7/75.2
n2_l0-0_b4_s1-3_p1-1000to1800	2	0	4	3	1000-1800	81.7/67.0	74.5/77.2	75.2/78.4	79.7/75.7
n2_l0-0_b4_s1-4_p1-1200to1800	2	0	4	4	1200-1800	82.0/75.1	88.6/71.7	88.2/69.5	87.6/73.1
n3_l1-0_b4_s1-2_p1-1000to1800	3	1	4	2	1000-1800	85.0/65.5	71.2/83.5	88.6/63.5	83.7/73.6
n3_l2-0_b4_s1-2_p1-1200to1800	3	2	4	2	1200-1800	81.7/78.3	87.3/73.8	80.7/76.2	76.8/79.4

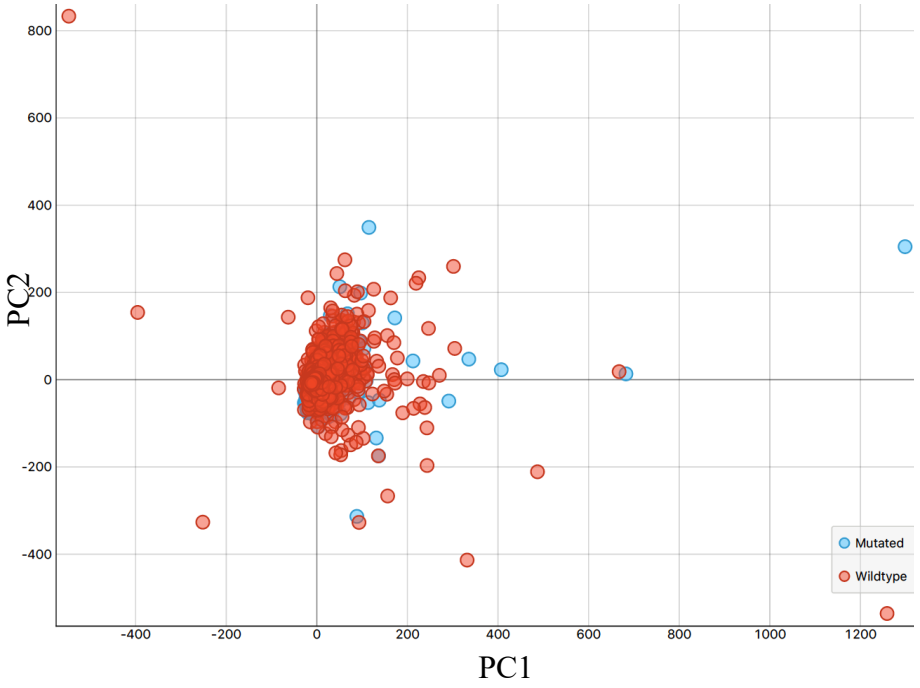

Figure A3.1 - PCA-based quality test: PCA scores plot of PC1 and PC2 before selection of central cluster.

a)

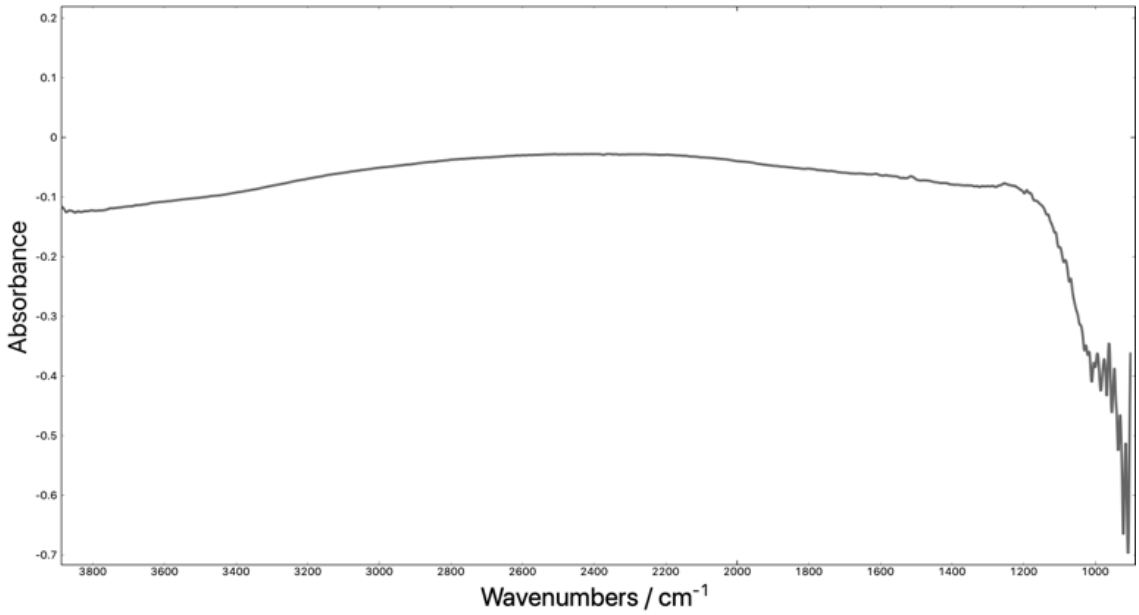

b)

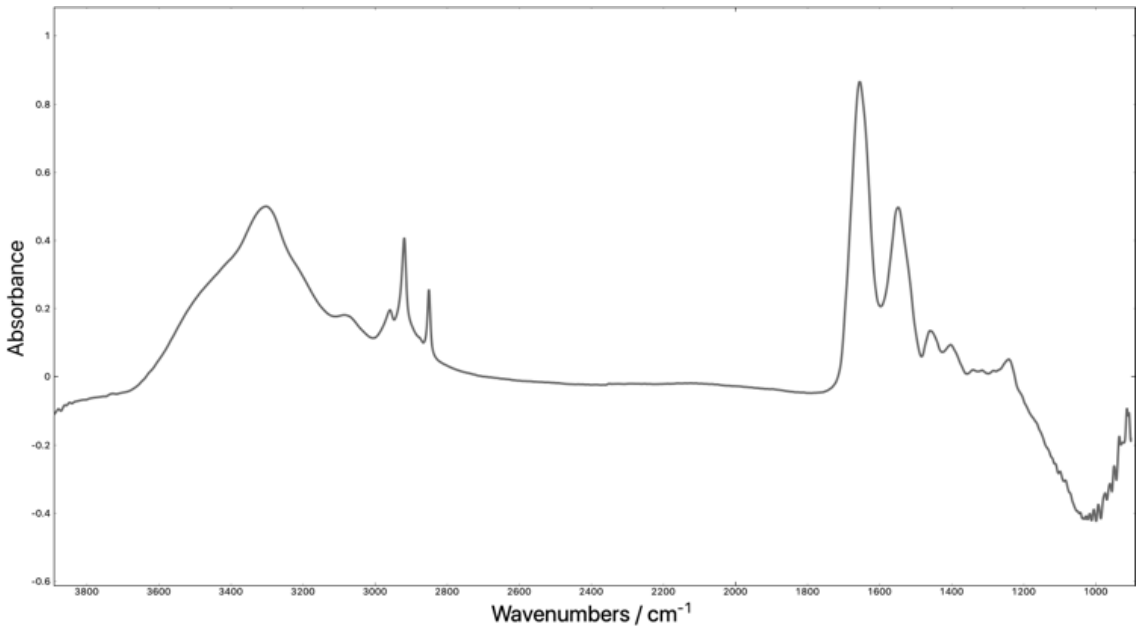

Figure A3.2 – a) Absorbance spectrum of blank CaF_2 substrate and b) raw sample spectra affected by drop in absorbance <1200 cm^{-1}.

Figure A3.3 – Microscope image of a dehydrated ‘concentrate’ sample. As the sample dries it begins to crack and then lifts off the SIRE surface.

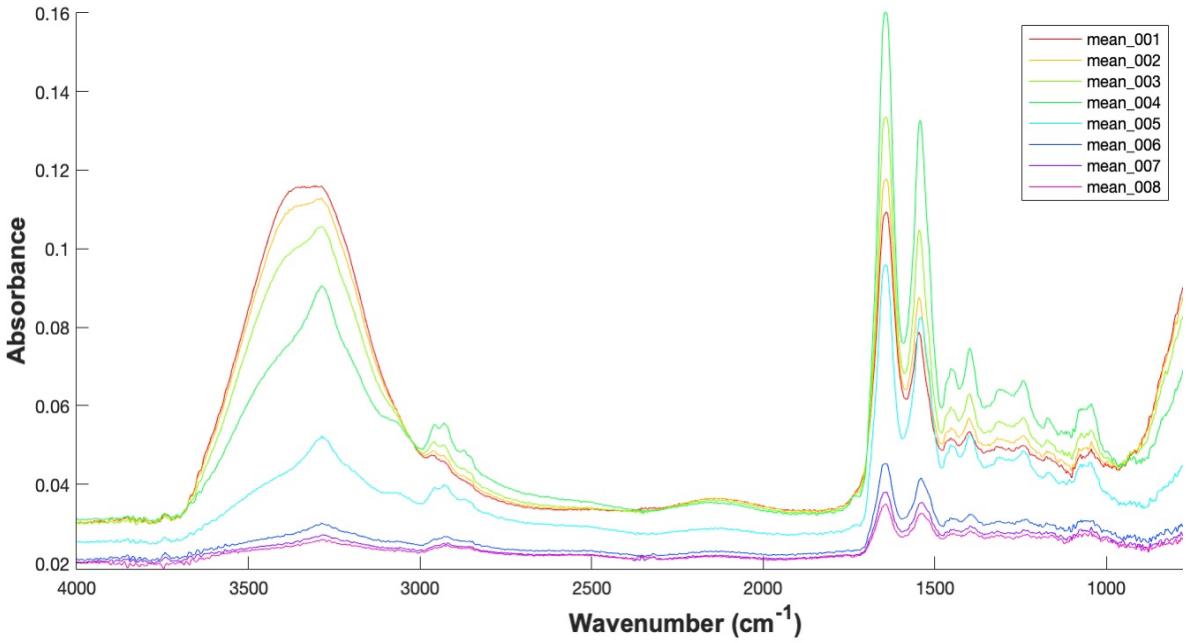

Figure A3.4 – Raw spectra describing the drying process of a concentrate sample. After 4 minutes the absorbance begins to decrease as the sample lifts off of the substrate surface.

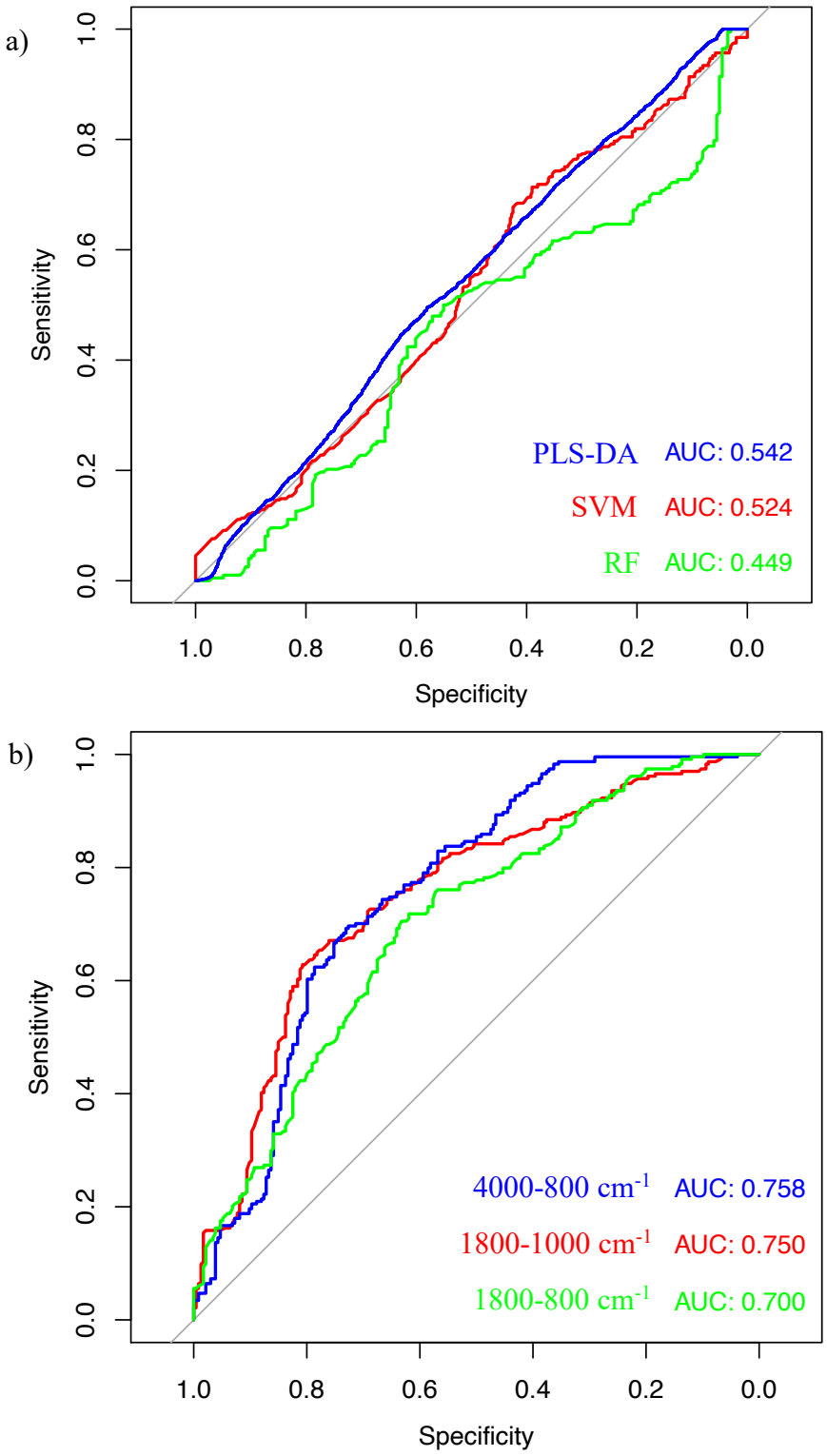

Figure A3.5 - Single model receiver operator characteristic (ROC) graphs for the a) whole serum dataset displaying the PLS-DA (blue), SVM (red) and RF (green) classifiers; and b) the best performing model for each of the tested filtrate fractions: the full spectrum (4000-800 cm^{-1}, blue), the fingerprint region (1800-1000 cm^{-1}, red) and the extended fingerprint region (1800-800 cm^{-1}, green).

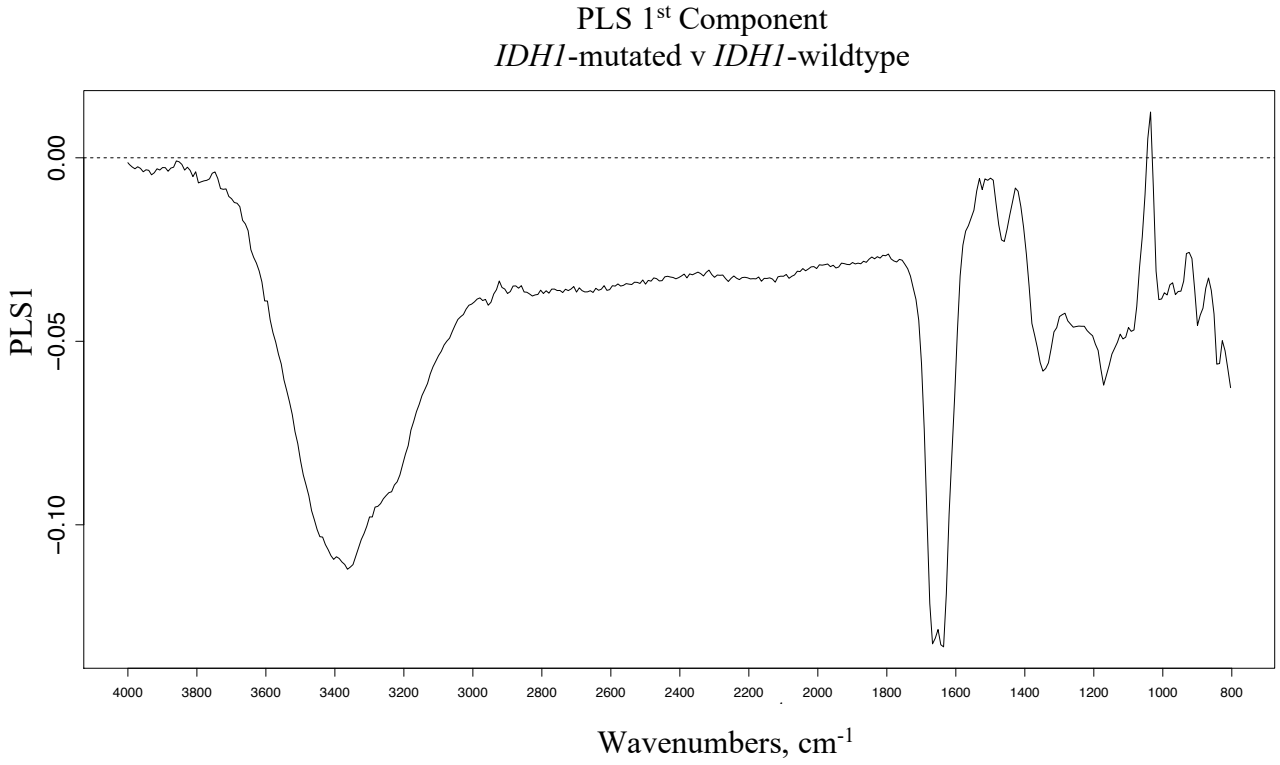

Figure A3.6 - The loadings plot for the 1st PLS component highlighting differences between *IDH1*-mutated and *IDH1*-wildtype, for the <3kDa serum filtrate (4000-800 cm^{-1}) dataset.

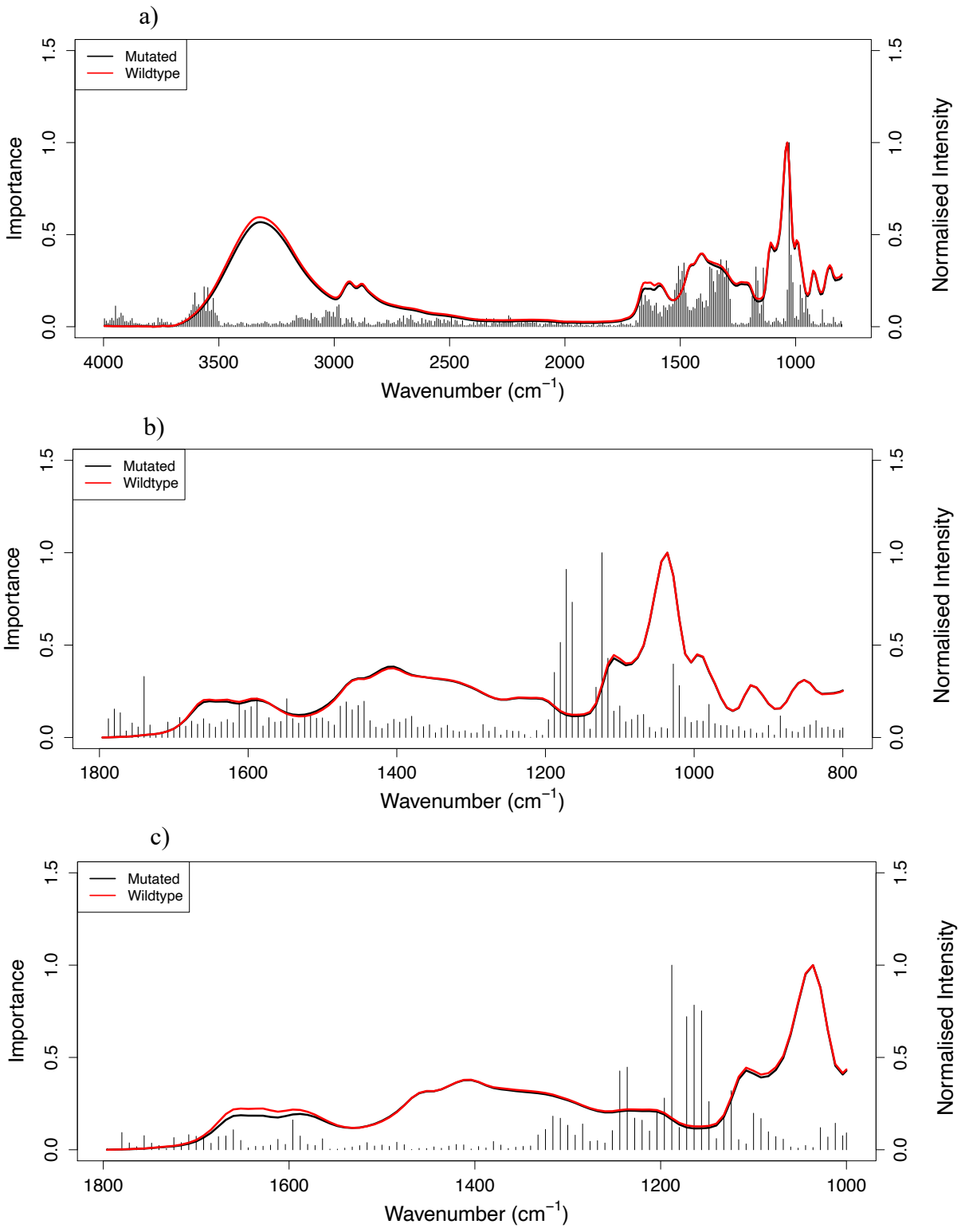

Figure A3.7 – Random forest Gini importance plots for the <3kDa filtrate datasets, showing the most important wavenumbers responsible for the IDH1-muated versus IDH1-wildtype classifications; a) 4000-800 cm^{-1}, b) 1800-800 cm^{-1} and c) 1800-1000 cm^{-1}.

Appendix 4 - Presentation List

Oral Presentations

Biofluid Disease Diagnostics: A High-throughput Method for the Detection of Brain Tumours (FLASH)

SPEC 2018 Conference, Glasgow, June 2018.

Developing Infrared Spectroscopic Detection for Stratifying Brain Tumour Patients: Glioblastoma Multiforme vs. Lymphoma

Federation of Analytical Chemistry and Spectroscopy Societies (FACSS) presents SciX2019 (The Great Scientific Exchange) Conference, Palm Springs, California, October 2019.

Developing Infrared Spectroscopic Detection for Stratifying Brain Tumour Patients: Glioblastoma Multiforme vs. Lymphoma

7th Analytical Biosciences Early Career Researchers Meeting, Glasgow, March 2020

Poster Presentations

The Royal Society of Chemistry Twitter Poster Conference, March 2018.

Biofluid Disease Diagnostics: A High-throughput Method for the Detection of Brain Cancer

James M. Cameron, Holly J. Butler, Matthew J. Baker, David S. Palmer

WestCHEM, Department of Pure and Applied Chemistry, Technology and Innovation Centre, University of Strathclyde, 99 George St, Glasgow G1 1RD, UK

University of Strathclyde Science

Introduction

Brain cancer patients lose on average 20.1 years of life, which is the highest of all other cancers. A reported 38% of patients living with a brain tumour visited their GP with headaches on 5 or more occasions before being finally diagnosed. Due to the lack of symptoms specific to brain tumours, 62% of patients were diagnosed as emergency presentations.[1] As early detection can have a huge impact on the effectiveness on treatment, the implementation of a rapid diagnostic tool into GP clinics would greatly reduce diagnosis times, improve patient prognosis and ultimately lower mortality rates. Research has shown spectroscopic techniques, such as attenuated total reflection Fourier transform infrared (ATR-FTIR), to be sensitive to the hallmarks of cancer,[2] specifically brain cancer.[3]. We have collected over 700 blood serum samples that have been obtained from brain cancer and control patients, contributing to the largest spectroscopic study to date. The project explores a high-throughput alternative to traditional ATR-FTIR, which should accelerate the translation of a quick diagnostic tool into the clinic.

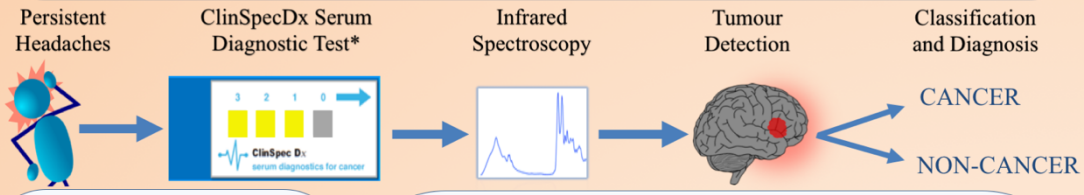

Methodology

- ATR-FTIR serum spectroscopy
- Diamond crystal traditionally used as internal reflection element (IRE)

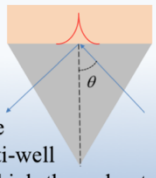

- ClinSpecDx have developed a multi-well silicon IRE* for high-throughput analysis
- Well 0 left blank for background, 3µl of serum onto wells 1, 2 and 3 → 9 spectra per patient

What Next?

- Finish remaining samples to complete the dataset
- Look at different pre-processing parameters to enhance sensitivity and specificity values
- Validate with an external test set – clinical feasibility study

Initial Results

- 509 Cancer (C) vs 232 Non-cancer (NC) patients; total of 741 samples.
- Matlab has been used for principal component analysis (PCA). The supervised PRFFECT toolbox within R Studio has been used for classifications - random forest (RF).
- a) mean spectra of whole dataset cut to fingerprint region (1800-1000cm^{-1}) b) PCA plot showing C/NC separation c) PC3 loadings – biggest variance in amide I/II region (1650-1500cm^{-1}), which correlates with d) RF importance

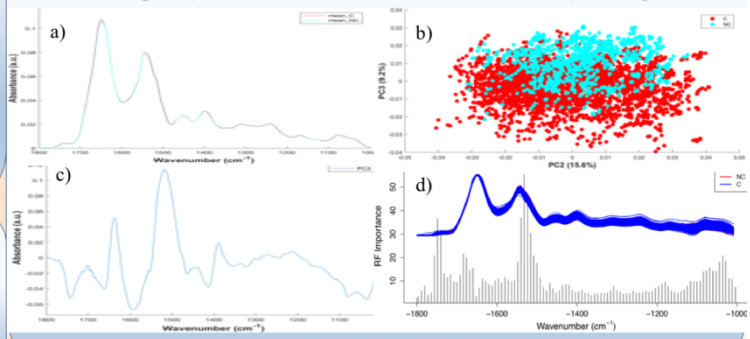

- The current classification output differentiating the cancer and non-cancer patients is **87% sensitivity and 82% specificity**

Acknowledgements

Thanks go to the Walton Centre, Liverpool, and the Rosemere Cancer Foundation, Royal Preston Hospital for collecting and supplying the serum samples used in this study, and of course, the ClinSpecDx team.

rosemere CANCER FOUNDATION
The Walton Centre NHS
NHS Foundation Trust
CLINSPEC Dx
serum diagnostics for cancer

References

[1] The Brain Tumour Charity, "Finding a Better way?," Aug-2017. [Online]. Available: http://cdn.basw.co.uk/upload/basw_21512-10.pdf.
[2] M. J. Baker et al., "Developing and understanding biofluid vibrational spectroscopy: a critical review," Chem Soc Rev, vol. 45, no. 7, pp. 1803–1818, 2016.
[3] J. R. Hands et al., "Attenuated Total Reflection Fourier Transform Infrared (ATR-FTIR) spectral discrimination of brain tumour severity from serum samples: Serum spectroscopy gliomas," J. Biophotonics, vol. 7, no. 3–4, pp. 189–199, Apr. 2014.

Biofluid Disease Diagnostics: A High-throughput Method for the Detection of Brain Tumours

James M. Cameron, Holly J. Butler, David S. Palmer, Mark G. Hegarty, Matthew J. Baker

WestCHEM, Department of Pure and Applied Chemistry, Technology and Innovation Centre, University of Strathclyde, 99 George St, Glasgow G1 1RD, UK

University of Strathclyde Science

ATR-FTIR Spectroscopy | Data Analysis | Tumour Detection

Introduction

Brain tumour patients lose on average 20.1 years of life.

38% of patients visited their GP with headaches on 5 or more occasions before being diagnosed.

Ultimately, 62% of patients are diagnosed as emergency presentations.[1]

Early detection can have a huge impact on the effectiveness on treatment.

A rapid diagnostic tool in GP clinics would greatly reduce diagnosis times and lower mortality rates.

Attenuated total reflection Fourier transform infrared (ATR-FTIR), is sensitive to the hallmarks of cancer,[2] specifically brain cancer.[3]

We hold over 700 blood serum samples obtained from brain tumour and control patients, contributing to the largest spectroscopic study to date.

The project explores a high-throughput alternative to traditional ATR-FTIR, which should accelerate the translation of a quick diagnostic tool into the clinic.

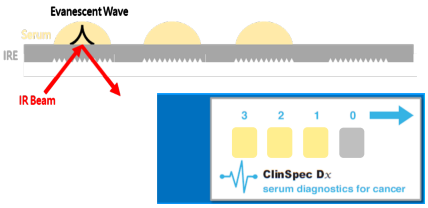

Methodology

- ClinSpecDx have developed a multi-well silicon internal reflection element (IRE) replacing traditional diamond crystal for high-throughput ATR-FTIR serum analysis.
- Well 0 left blank for background collection, 3µl of serum onto wells 1, 2 and 3. The spectra is collected on a Perkin Elmer Spectrum 2 spectrometer, and each well is analysed in triplicate, resulting in 9 spectra per patient.
- 487 brain tumour vs 237 healthy (control) patients.

Data Analysis

1) Full Brain Tumour Dataset

- Raw spectra cut to biological fingerprint region (1800-1000cm^{-1}).
- Principal component analysis (PCA) plot shows separation of the two classes.
- PC2 loadings; biggest variance in Amide I/II region (1650-1500cm^{-1}) and 1100-1000cm^{-1}.

724 *patients*

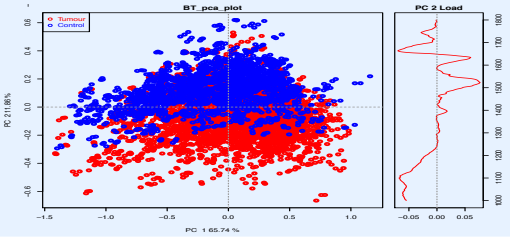

2) Brain Tumour vs Control Classification

- PRFFECT toolbox on R Studio has been used for classifications through random forest (RF).
- RF importance Gini plot suggest most important peaks arise ~1525cm^{-1} and ~1035cm^{-1}.
- Optimal RF parameters gives sensitivity and specificity result of 88.5% and 85.7% respectively.

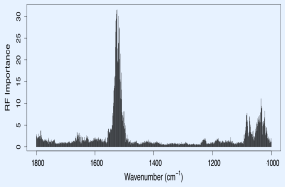

92% *sens. & spec.*

- Partial least squares-discriminant analysis (PLS-DA) combined with a genetic algorithm (GA) gave an improved result with 92% for both sensitivity and specificity.
- Raw data pre-processed using extended multiplicative signal correction (EMSC) and the GA was used to choose optimal wavenumbers.

3) Brain Tumour Differentiation

- Various brain tumour types within large dataset.
- Taken small subset of more common tumours to see if we can differentiate between them.
- Initial findings promising using RF, with most >70% sens. and spec.
- Needs explored further with more advanced machine learning techniques.

Dataset	Sensitivity/Specificity (%)
GBM vs Meningioma	**71.5/70.4**
Meningioma vs Metastasis	**72.1/68.8**
GBM vs Metastasis	**73.3/75.9**
Astrocytoma vs GBM	**85.7/78.6**
Astrocytoma vs Meningioma	**73.1/71.4**
Astrocytoma vs Metastasis	**77.8/68.0**

Future Work

Validate with an external test set, clinical feasibility study in Edinburgh Western GH.

Look into the molecular status of brain tumour patients; 1p/19q, *MGMT* and *IDH1*.

Effect of chemotherapeutic drugs on cancer classification.

Acknowledgements

Thanks to the Walton Centre and the Rosemere Cancer Foundation for collecting and supplying the blood samples used in this study and EPSRC for funding.

References

[1] The Brain Tumour Charity, "Finding a Better way?," Aug-2017. [Online]. Available: http://cdn.basw.co.uk/upload/basw_21512-10.pdf.
[2] M. J. Baker et al., "Developing and understanding biofluid vibrational spectroscopy: a critical review," Chem Soc Rev, vol. 45, no. 7, pp. 1803–1818, 2016.
[3] J. R. Hands et al., "Attenuated Total Reflection Fourier Transform Infrared (ATR-FTIR) spectral discrimination of brain tumour severity from serum samples: Serum spectroscopy gliomas," J. Biophotonics, vol. 7, no. 3–4, pp. 189–199, Apr. 2014.

Appendix 5 – Publications Abstracts

Abstracts for the peer-reviewed publications that have not been directly included in this thesis.

First Author:

JOURNAL OF BIOPHOTONICS

REVIEW ARTICLE | Open Access |

Biofluid spectroscopic disease diagnostics: A review on the processes and spectral impact of drying

James M. Cameron, Holly J. Butler, David S. Palmer, Matthew J. Baker

First published:26 January 2018 | https://doi.org/10.1002/jbio.201700299 | Citations: 21

Funding information EPSRC, Grant/Award number: EP/L505080/1
The copyright line for this article was changed on 20 April 2018 after original online publication.

SECTIONS PDF TOOLS SHARE

Abstract

The complex patterns observed from evaporated liquid drops have been examined extensively over the last 20 years. Complete understanding of drop deposition is vital in many medical processes, and one which is essential to the translation of biofluid spectroscopic disease diagnostics. The promising use of spectroscopy in disease diagnosis has been hindered by the complicated patterns left by dried biological fluids which may inhibit the clinical translation of this technology. Coffee-ring formation, cracking and gelation patterns have all been observed in biofluid drops, and with surface homogeneity being a key element to many spectroscopic techniques, experimental issues have been found to arise. A better understanding of the fundamental processes involved in a drying droplet could allow efficient progression in this research field, and ultimately benefit the population with the development of a reliable cancer diagnostic.

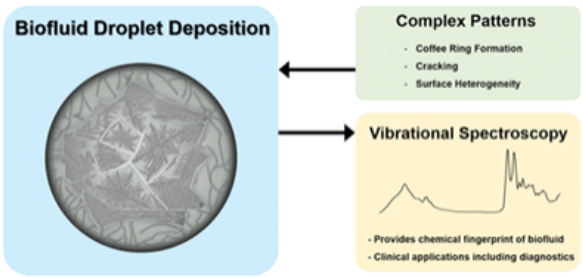

ACADEMIC PRESS

Vibrational Spectroscopy in Protein Research
From Purified Proteins to Aggregates and Assemblies
2020, Pages 269-314

Chapter 10 - Vibrational spectroscopic analysis and quantification of proteins in human blood plasma and serum

James M. Cameron [1], Clément Bruno [2, 3, 4], Drishya Rajan Parachalil [5, 6], Matthew J. Baker [1, 7], Franck Bonnier [2], Holly J. Butler [1, 7], Hugh J. Byrne [5]

Show more

https://doi.org/10.1016/B978-0-12-818610-7.00010-4

Abstract

Alterations in biomolecular components in human blood are commonly used as an indication of disease states, namely differences in protein concentration. Unfortunately, conventional test kits currently employed in hospitals suffer from long time delays, meaning patients often have to wait anxiously for their test results. Vibrational spectroscopic techniques, such as infrared and Raman, have the ability to replace current practices, as they are label-free, cost-effective, easy to operate, and require minimal sample preparation. The sensitivity to subtle changes in biochemical composition makes them ideal diagnostic tools, and recent advances in technology and data analytics means bodily fluids can be analyzed rapidly and noninvasively to detect disease-related fluctuations in protein concentration. In this chapter, we outline the current clinical procedures for blood tests, examine the capability of biomedical vibrational spectroscopy for disease diagnostics and monitoring, and discuss the potentiality for the techniques to be successfully translated into the clinic.

Vibrational Spectroscopy
Volume 109, July 2020, 103092

Exploring pre-analytical factors for the optimisation of serum diagnostics: Progressing the clinical utility of ATR-FTIR spectroscopy

James M. Cameron [a], Holly J. Butler [b], David J. Anderson [a, c], Loren Christie [b], Lily Confield [d], Katie E. Spalding [a], Duncan Finlayson [d], Stuart Murray [a], Zanib Panni [d], Christopher Rinaldi [a], Alexandra Sala [a], Ashton G. Theakstone [a], Matthew J. Baker [a, b]

Show more

https://doi.org/10.1016/j.vibspec.2020.103092

Abstract

Data quality and reproducibility are vital for robust, reliable and consistent diagnostic techniques within clinical environments. Most variance within clinical laboratories occur within the pre-analytical phase, prior to obtaining and analysing data. Herein, we investigate pre-analytical considerations for the spectroscopic analysis of blood serum for the purpose of clinical diagnostics.

Variables within sample collection, storage and preparation are explored in order to evaluate their effects on the spectral outcome, including; differences between sample collection tubes, centrifugal speed and time, short and long-term storage conditions, individual analyst technique, sample volumes, environment of sample batches, as well as various drying techniques. Exploratory data analysis using principal component analysis was implemented to unearth spectral variance not immediately observable.

Minor spectral variations were observed within each experiment; however, these were not considered significant differences as a result of these varying experimental factors. Variation between different operator techniques when preparing samples was observed, yet can be resolved with appropriate standard operating procedures, regardless of other factors such as sample volume and storage conditions. The findings within this report suggest that experimental variations within a laboratory, or between different laboratories, does not significantly affect the spectral outcome, and with good laboratory practice and careful sample handling results should be consistent and reliable.

Co-author:

nature COMMUNICATIONS

ARTICLE

https://doi.org/10.1038/s41467-019-12527-5 OPEN

Development of high-throughput ATR-FTIR technology for rapid triage of brain cancer

Holly J. Butler[1,2*], Paul M. Brennan[3], James M. Cameron[1], Duncan Finlayson[1], Mark G. Hegarty[2], Michael D. Jenkinson[4], David S. Palmer[1,2], Benjamin R. Smith[1] & Matthew J. Baker[1,2*]

Non-specific symptoms, as well as the lack of a cost-effective test to triage patients in primary care, has resulted in increased time-to-diagnosis and a poor prognosis for brain cancer patients. A rapid, cost-effective, triage test could significantly improve this patient pathway. A blood test using attenuated total reflection (ATR)-Fourier transform infrared (FTIR) spectroscopy for the detection of brain cancer, alongside machine learning technology, is advancing towards clinical translation. However, whilst the methodology is simple and does not require extensive sample preparation, the throughput of such an approach is limited. Here we describe the development of instrumentation for the analysis of serum that is able to differentiate cancer and control patients at a sensitivity and specificity of 93.2% and 92.8%. Furthermore, preliminary data from the first prospective clinical validation study of its kind are presented, demonstrating how this innovative technology can triage patients and allow rapid access to imaging.

[1] WestCHEM, Department of Pure and Applied Chemistry, University of Strathclyde, Technology and Innovation Centre, 99 George Street, Glasgow G1 1RD, UK. [2] ClinSpec Diagnostics Limited, University of Strathclyde, Technology and Innovation Centre, 99 George Street, Glasgow G1 1RD, UK. [3] Translational Neurosurgery, Department of Clinical Neurosciences, Western General Hospital, Edinburgh EH4 2XU, UK. [4] Institute of Translational Medicine, University of Liverpool & The Walton Centre NHS Foundation Trust, Lower Lane, Fazakerley, Liverpool L9 7LJ, UK. *email: holly.butler@clinspecdx.com; matthew.baker@clinspecdx.com

Clinical Spectroscopy
Volume 1, December 2019, 100003

Shining a light on clinical spectroscopy: Translation of diagnostic IR, 2D-IR and Raman spectroscopy towards the clinic

Holly J. Butler [a, b], James M. Cameron [a], Cerys A. Jenkins [c], Gordon Hithell [d], Samantha Hume [d], Neil T. Hunt [e, d], Matthew J. Baker [a, b]

Show more

https://doi.org/10.1016/j.clispe.2020.100003

Abstract

In recent years, the application of vibrational spectroscopy in biomedical research has rapidly expanded; covering aspects of pharmaceutical development, to point-of-care technologies. Vibrational spectroscopy techniques such as Fourier-transform IR (FTIR), and Raman spectroscopy have been at the forefront of this movement, with their complementary information able to shine light onto a range of medical applications. As a relative newcomer to biomedical applications, two-dimensional (2D)-IR is also gaining traction in the field. Here we describe the recent development of these techniques as analytical tools in medical science, and their relative advancements towards the clinic.

Cancer Letters
Volume 477, 1 May 2020, Pages 122-130

Mini-review

Biofluid diagnostics by FTIR spectroscopy: A platform technology for cancer detection

Alexandra Sala [a], David J. Anderson [a], Paul M. Brennan [b], Holly J. Butler [c], James M. Cameron [a], Michael D. Jenkinson [d], Christopher Rinaldi [a], Ashton G. Theakstone [a], Matthew J. Baker [a, c]

Show more

https://doi.org/10.1016/j.canlet.2020.02.020

Highlights

- A simple, rapid, cost-effective and accurate test is needed in the clinical environment.
- ATR-FTIR analysis of biofluids has obtained remarkable statistical results with the aid of machine learning algorithms.
- Clinical spectroscopy is in continuous development to achieve translation into the clinic.
- A proof-of-concept study on detection of brain tumours has recently progressed to a prospective clinical validation study.

Abstract

Fourier Transform Infrared Spectroscopy (FTIR) has been largely employed by scientific researchers to improve diagnosis and treatment of cancer, using various biofluids and tissues. The technology has proved to be easy to use, rapid and cost-effective for analysis on human blood serum to discriminate between cancer *versus* healthy control samples. The high sensitivity and specificity achievable during samples classification aided by machine learning algorithms, offers an opportunity to transform cancer referral pathways, as it has been demonstrated in a unique and recent prospective clinical validation study on brain tumours. We herein highlight the importance of early detection in cancer research using FTIR, discussing the technique, the suitability of serum for analysis and previous studies, with special focus on pre-clinical factors and clinical translation requirements and development.

Appendix 6 – Certificates

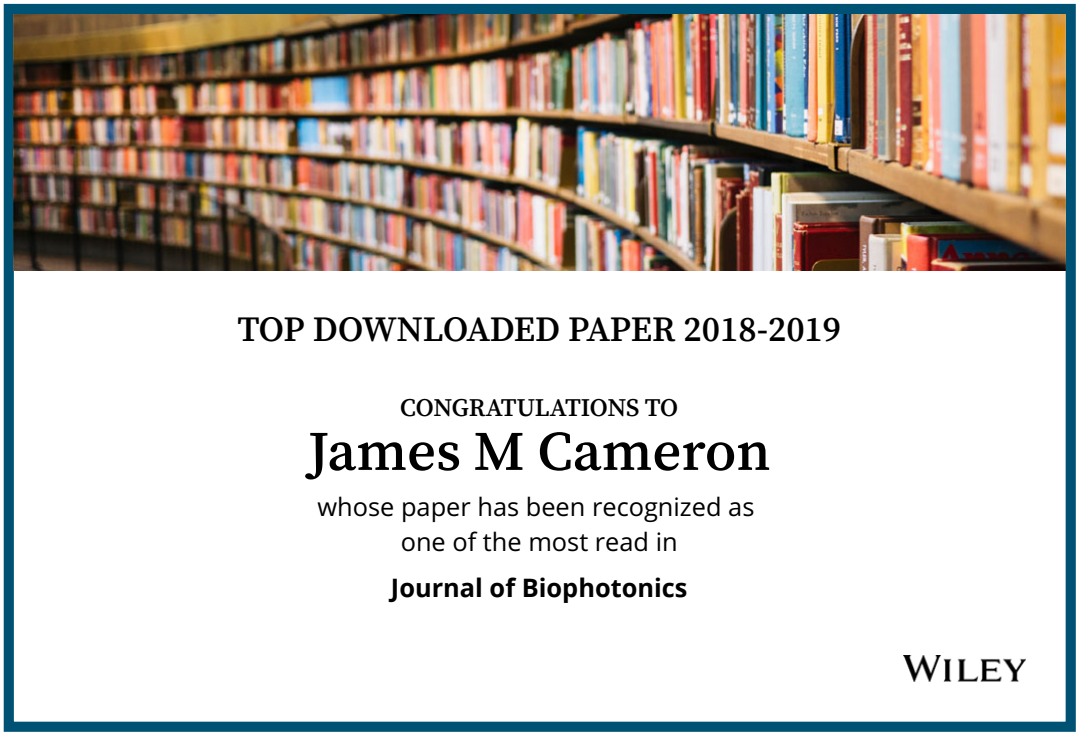

TOP DOWNLOADED PAPER 2018-2019

CONGRATULATIONS TO

James M Cameron

whose paper has been recognized as
one of the most read in

Journal of Biophotonics

WILEY

cancers

an Open Access Journal by MDPI

Indexed in: PubMed | CITESCORE 3.4 SCOPUS | IMPACT FACTOR 6.126

CERTIFICATE OF PUBLICATION

Certificate of publication for the article titled:

Stratifying Brain Tumour Histological Sub-Types: The Application of ATR-FTIR Serum Spectroscopy in Secondary Care

Authored by:

James M. Cameron; Christopher Rinaldi; Holly J. Butler; Mark G Hegarty; Paul M. Brennan; Michael D. Jenkinson;
Khaja Syed; Katherine M. Ashton; Timothy P. Dawson; David S. Palmer; Matthew J. Baker

Published in:

Cancers **2020**, Volume 12, Issue 7, 1710

MDPI Academic Open Access Publishing since 1996

Basel, July 2020

ROYAL SOCIETY OF CHEMISTRY

Analyst

This is to certify that

James Cameron

has been awarded an *Analyst* Oral Presentation Prize at the

7th Analytical Biosciences Early Career Researcher Meeting 2020

Glasgow, United Kingdom

5th – 6th March, 2020

Jeanne Andres

Jeanne Andres

Executive Editor, *Analyst*

www.rsc.org/analyst

Registered Charity Number 207890